Doctoral Dissertation
Doctoral Program in Metrology (33.th cycle)

Developing new paradigms for quantum measurements

Enrico Rebufello

* * * * *

Supervisor
Dr. Marco Genovese, Istituto Nazionale di Ricerca Metrologica

Doctoral Examination Committee:
To be defined

Politecnico di Torino
October 31, 2020

I hereby declare that, the contents and organisation of this dissertation constitute my own original work and does not compromise in any way the rights of third parties, including those relating to the security of personal data.

....

Enrico Rebufello

Turin, October 31, 2020

Summary

Ever since its inception in the early 20th century, Quantum Mechanics has led to the development of many groundbreaking technologies, such as lasers, semiconductors, and so on. These technologies, which relied on general ensemble properties of quantum systems, are usually referred to as part of the "first quantum revolution". Today, a second quantum revolution, based on specific properties of single quantum systems, is underway, and more and more technologies able to generate and manipulate individual quantum states (and exploit their peculiar quantum properties) are being developed. One of the applications of these new technologies are quantum metrology and sensing which exploit quantum effects to overcome the limits of classical systems, achieving higher precisions and better signal-to-noise ratios in several measurement scenarios. For this reason, the development of new standards and procedures for the characterization of these new quantum technologies, as well as the development new quantum-enhanced measurement protocols, are fundamental tasks for quantum metrology.

In my thesis, I tackle both tasks for single/few photons systems, presenting several works which focus on state characterization and the development of novel quantum parameter estimation techniques and quantum measurement protocols, presenting in each case the theoretical framework together with the experimental results obtained in the practical implementation. The experiments have been performed exploiting quantum optics setups able to generate, manipulate and detect single- and entangled-photon states.

The first two works I present are aimed at characterizing single- and entangled-photon sources. The first work in this context the development of a strategy to estimate the multi-photon component of a continuous wave heralded single-photon source, paving the way for a standardization of the characterization of single-photon sources as one of the key tools of several quantum technologies, some of them even already stepping foot on the market (e.g. quantum cryptography). The strategy has been successfully applied in a pilot comparison among a few European national metrological institutes (INRiM, NPL and PTB).

The second work, instead, concerns the optimal estimation of the amount of non-classical correlations (i.e. discord and entanglement) within a specific class of two-photons states, for which I introduce and test experimentally some optimal unbiased estimators for the aforementioned quantities. There, I show how such estimators perform better than their nonoptimal counterparts by allowing to achieve the minimum uncertainty possible, i.e. the one granted by the saturation of the Quantum Cramér-Rao bound.

Then, I present two works in which I investigate new quantum measurement paradigms based on weak measurements, and their possible applications to quantum metrology and other quantum technologies. The first protocol, protective measurement (PM), allows extracting the expectation value of a quantum observable even from a single detection event, something apparently in sharp contrast with the very definition of expectation value as a statistical quantity associated with an ensemble of particles. I show the first experimental implementation of such protocol, involving a single-photon-based quantum optics setup. I also analyse the statistical uncertainties of PM, showing the advantage it grants with respect to "strong" (projective) measurements. Second, I illustrate the theory and the first experimental implementation of robust weak measurement (RWM), an evolution of PM. With RWMs one can obtain a reliable estimate of the weak value of an observable with just a single detection event, instead of averaging over multiple events like for usual weak value measurements.

Finally, I present the first experimental reconstruction of a pseudo-density operator (a generalization of the usual density operator), a novel quantum mechanical tool able to describe temporal and spatial correlations on the same level. Such formalism is able to provide a satisfactory description of quantum systems even in situations with which the usual density operator formalism of quantum mechanics can present some issues, and even give rise to paradoxes . As emblematic examples, we consider its application to the optical simulation of two physical scenarios: entangled particles entering an open time-like curve, and black-hole evaporation.

Acknowledgements

I would like to express my gratitude to all who helped me in these three years.

In particular, I wish to thank Dr. Marco Genovese, who gave me the opportunity to work in this highly stimulating scientific field.

A special thanks to Dr. Fabrizio Piacentini, who spent part of his time discussing and reading my thesis drafts, and to all the quantum optics group (Alessio, Alice, Ekaterina, Elena, Ettore, Fabio, Giorgio, Giulia, Ivano, Ivo, Laura, Marco, Muriel, Paolo, Salvatore), who supported me throughout these years.

And I would also like to acknowledge Dr.s C. J. Chunnilall, M. Lopéz, R. A. Kirkwood and S. Kück, with whom I collaborated in a pilot comparison, and Dr.s E. Cohen, J. Dziewior, C. Marletto, L. Vaidman, and V. Vedral, for their constant collaboration with our research group.

Finally, a special thanks to my family and friends, for their moral support during these three years.

To the undiscovered country... the future.

Contents

x

List of Tables

List of Figures

XVII

Chapter 1

Introduction

In this chapter we introduce all the theoretical elements which are necessary for the comprehension of this thesis. In the first part, we give a general introduction of quantum mechanics and the emergent field of the new quantum technologies, which will help us contextualize this work. Then, we thoroughly describe measurements processes in quantum mechanics with both a direct and an indirect formalism. The latter will allow us to introduce the concepts of weak measurements and weak values, and their several practical applications. After that, we introduce some parameters that are able to characterize entanglement and Quantum Discord. Finally, we give a review of quantum parameter estimation, focusing, in particular, on the derivation of the Quantum Cramér-Rao bound and Quantum Van Trees bound, which define the ultimate uncertainty limit with which a parameter can be estimated.

1.1 Quantum mechanics: theory and applications

Quantum mechanics (QM) is the fundamental theory of physics, able to give an exhaustive explanation of all the microscopic phenomena and, in principle, providing the framework in which all physical theories should be included. The main differences between QM and classical mechanics are that, in QM, energy, momentum and many other quantities of a bound system are restricted to discrete values (*quantization*), quantum objects have characteristics of both wave and particles (*wave-particle duality*), there is a fundamental limit to the precision with which we can know the values for certain pairs of physical quantities, such as position and momentum (*uncertainty principle*), specific correlations (e.g. *entanglement*) exist among subsystems that cannot be reproduced by classical systems.

Quantum mechanics gradually emerged in the early 20th century, when new theories were proposed in order to explain some peculiar physical phenomena, such

as black-body radiation[1], in which Planck hypothesized that atoms could absorb and emit electromagnetic radiation only in discrete energy packets, and the photoelectric effect[2], in which Einstein argued that all electromagnetic radiation can be divided into a finite number of localized "points in space": the *energy quanta*, later renamed *photons*[3]. A few years later, Bohr applied the quantization to the hydrogen atom[4], thus explaining the behaviour of its spectral lines[5], that did not find explanation in classical models. Thanks to the effort of many physicists, these scattered theories started to coalesce into modern quantum mechanics after De Broglie theorized[6] that particles can exhibit wave characteristics and vice versa in 1923. Building on his approach, Schrödinger deduced his famous equation[7], which describes the state of a quantum-mechanical system trough the *wave-function*. Few years later, Heisenberg formulated the aforementioned uncertainty principle[8], in which he stated that the more precisely the position of some particle is determined, the less precisely its momentum can be predicted from initial conditions, and vice versa. In 1932, von Neumann formulated the rigorous mathematical basis for quantum mechanics in the theory of linear operators on Hilbert spaces[9].

Later, the application of quantum mechanics to field theory led to the birth of quantum field theory (QFT), a theory capable of unifying three of the four fundamental interactions of our universe (electromagnetic, weak and strong)[10]. Gravitational interaction, however, is still missing from the picture and the formulation of a quantum theory of gravity is one of the challenges of the century[11].

Today, quantum mechanics is heralding a new technological revolution (see Sec. 1.1.2 for further details), of which we can already see some effects, even in metrology. In new International System of Units (SI) revision[12], the realizations of many units of measurements depend on quantum mechanical effects, such as lasers and atomic transitions for the second[13], Josephson effect and quantum Hall effect for electrical units[14] and the Kibble balance for the kilogram[15].

1.1.1   Key concepts in quantum mechanics

The specific properties of quantum mechanics, that we have just summarized, derive from its mathematical formulation, of which we introduce here some key concepts that will be useful later.

The Postulates of quantum mechanics

Postulate 1. *Quantum states*
Every physical system is associated with a complex separable Hilbert space $\mathcal{H}$ with inner product. The system is fully described by its vector state, which is a normalized vector in the Hilbert space.

The simplest physical system, a two-level system, belongs to a bidimensional Hilbert space $\mathcal{H}_2$. If $|0\rangle$ and $|1\rangle$ form an orthonormal basis for $\mathcal{H}_2$, then a generic state vector can be written as:

$$|\psi\rangle = \alpha |0\rangle + \beta |1\rangle \tag{1.1.1.1}$$

where α and β are complex number, normalized such that $\langle\psi|\psi\rangle = |\alpha|^2 + |\beta|^2 = 1$. In quantum information theory, such systems are usually called *qubits*.

Postulate 2. *The observables*
Every observable quantity A is associated with a linear self-adjoint (Hermitian, i.e. $\hat{A} = \hat{A}^\dagger$) operator $\hat{A}$ on $\mathcal{H}$. The ensemble of the possible outcomes of a measurement of said quantity is given by the eigenvalues spectrum of $\hat{A}$.

The linearity of the operator ensures any non-infinite non-continue operator can be represented in matricial form, and its hermicity grants that its spectrum is composed of real eigenvalues. An operator can be represented in any arbitrary basis, however, it is often convenient to express it in the basis of its eigenstates $|\alpha\rangle$, defined as:

$$\hat{A} |\alpha\rangle = \alpha |\alpha\rangle \tag{1.1.1.2}$$

with α being the eigenvalues.

Postulate 3. *Probability of a result*
If the physical system is in a state $|\psi\rangle$, the probability of having the outcome α after measuring a quantity A is directly proportional to $|\langle\alpha|\psi\rangle|^2$, $|\alpha\rangle$ being the eigenstate corresponding to the eigenvalue α.

Since the total probability of having any result must be 1:

$$\sum_\alpha |\langle\alpha|\psi\rangle|^2 = 1 \tag{1.1.1.3}$$

It is possible to define the quantum expectation value of an observable as the average of its outcomes α weighted on their respective probabilities $p(\alpha)$:

$$\langle A \rangle = \sum_\alpha \alpha p(\alpha) \tag{1.1.1.4}$$

Starting from the formula for the mean, it is possible to define the variance:

$$(\Delta A)^2 = \langle (A - \langle A \rangle)^2 \rangle = \langle A^2 \rangle - \langle A \rangle^2 \tag{1.1.1.5}$$

Postulate 4. *Wave-function collapse*
The state of the quantum system after a measurement of the observable A, given that outcome α occurred, is projected on the eigenstate of α.

Since the overall experimental outcome probability must be 1 (postulate 3), if the measurement of A projects the state $|\psi\rangle$ into $|\alpha\rangle$, then all subsequent measurements of A must give the same result with probability 1, provided that the state did not evolve between subsequent measurements.

Another consequence is that if two operators $\hat{A}$ and $\hat{B}$ commute ($[\hat{A}, \hat{B}] = \hat{A}\hat{B} - \hat{B}\hat{A} = 0$), it is possible to find a common eigenstate basis. This means that independent measurements of these observables do not influence each other. As an example, the measurement of an observable A projects the state $|\psi\rangle$ of a system into the eigenstate $|\alpha\rangle$ of A. A subsequential measurement of B would collapse the state in $|\alpha, \beta\rangle$, belonging both to the eigenstate of A and B. Further measurements of A or B would not bring other results than α and β, respectively. Thus, the measurement of B does not influence the measurement of A and viceversa. In contrast, this is not true for non-commuting operators. Their mutual influence induces an uncertainty (denoted as ΔA and ΔB) whose minimal value is given by *Heisenberg uncertainty principle*[8]:

$$\Delta A \Delta B \geq \frac{\left|\left\langle [\hat{A}, \hat{B}] \right\rangle\right|}{2} \tag{1.1.1.6}$$

Postulate 5. *Schrödinger equation*
The evolution of a quantum state in a closed system is described by:

$$i\hbar \frac{\partial}{\partial t}|\psi(t)\rangle = \hat{H}(t)|\psi(t)\rangle \tag{1.1.1.7}$$

where $\hat{H}$ is the system's Hamiltonian operator and $\hbar$ the reduced Planck constant.

To know a system Hamiltonian means to know, at least in principle, its dynamics. From the Hamiltonian it is possible to define the *time evolution operator $\hat{U}$* such that:

$$|\psi(t)\rangle = \hat{U}(t, t_0)|\psi(t_0)\rangle \tag{1.1.1.8}$$

with the following properties:

- $\hat{U}(t_0, t_0) = \mathbb{1}$

- $\hat{U}^\dagger = \hat{U}^{-1}$ (unitary)

- $\hat{U}(t, t_0) = \hat{U}(t, t_1)\hat{U}(t_1, t_0)$ for $t < t_1 < t_0$

being $\mathbb{1}$ the identity. By substituting it into Schrödinger equation, we obtain the following differential equation for U:

$$i\hbar \frac{\partial \hat{U}(t, t_0)}{\partial t} = \hat{H}\hat{U}(t, t_0) \tag{1.1.1.9}$$

In the general case of time-dependent Hamiltonian, Eq. (1.1.1.9) is solved by a Volterra equation:

$$\hat{U}(t, t_0) = 1 - \frac{i}{\hbar} \int_{-t_0}^{t} dt_1 \hat{H}(t_1) \hat{U}(t_1, t_0) \qquad (1.1.1.10)$$

which is, in turn, solved[16] by the Dyson formula:

$$\hat{U}(t, t_0) = T \exp\left(-\frac{i}{\hbar} \int_{t_0}^{t} d\tau \hat{H}(\tau) \right) \qquad (1.1.1.11)$$

where T is the temporal order operator:

$$T[\hat{H}(t_1), \hat{H}(t_2)] = \begin{cases} \hat{H}(t_1)\hat{H}(t_2) & t_2 > t_1 \\ \hat{H}(t_2)\hat{H}(t_1) & t_2 < t_1 \end{cases} \qquad (1.1.1.12)$$

In the simpler case of time-independent Hamiltonian, Eq. (1.1.1.11) simplifies to:

$$\hat{U}(t, t_0) = T \exp\left(-\frac{i}{\hbar}(t - t_0)\hat{H} \right) \qquad (1.1.1.13)$$

Postulate 6. *Composite systems*
The state space of a composite system is described by the tensor product of the state spaces of the component physical systems. Moreover, if we have a system composed of n separate subsystems, and each subsystem i is prepared on a state $|\psi_i\rangle$, then the joint state is the tensor product $|\psi_1\rangle \otimes |\psi_2\rangle \otimes \cdots \otimes |\psi_n\rangle$.

This postulate enables us to introduce one of the most counter-intuitive aspects of quantum mechanics: the *entanglement*.

Entanglement

For simplicity, we will describe entanglement for a bipartite system, but it can be easily generalized[17].

Let A and B be two non-interacting systems with associated Hilbert spaces $\mathcal{H}_A$ and $\mathcal{H}_B$ and let $\mathcal{H} = \mathcal{H}_A \otimes \mathcal{H}_B$ be the Hilbert space of the composite system, as per postulate 6. A generic pure state $|\psi\rangle_{AB}$ on the composite system is *separable* if and only if it can be written as the product of two states $|\psi\rangle_A$ and $|\psi\rangle_B$ on the two systems A and B:

$$|\psi\rangle_{AB} = |\psi\rangle_A \otimes |\psi\rangle_B \qquad (1.1.1.14)$$

However, not all states are separable. Such states are called *entangled*. Their non-separability implies a strong correlation between the two subsystems, so strong that the measurement of an observable of one subsystem "influences" the result of a measurement of an observable of the other subsystem. Let us suppose that Alice

and Bob are the observers for the subsystems A and B, respectively, and that the state of the composed system is a singlet state of two spin $1/2$ particles:

$$|\psi\rangle = \frac{1}{\sqrt{2}} \left(|\uparrow\rangle_A \otimes |\downarrow\rangle_B + |\downarrow\rangle_A \otimes |\uparrow\rangle_B \right) \qquad (1.1.1.15)$$

where $|\uparrow\rangle$ and $|\downarrow\rangle$ represent a single particle of spin up and down, respectively.

If Alice measures the z component of the spin on the particle A, she can obtain two results, with equal probability:

- Alice measures $\uparrow$: the system collapses in $|\uparrow\rangle_A \otimes |\downarrow\rangle_B$;

- Alice measures $\downarrow$: the system collapses in $|\downarrow\rangle_A \otimes |\uparrow\rangle_B$.

Therefore, each subsequent measurement of the z spin component of the particle B performed by Bob will always provide the result $\uparrow$ or $\downarrow$, depending on Alice's result, meaning that the subsystem B has been altered by a local measurement on the subsystem A.

The fact that a measurement of one subsystem influences the other even when they are spatially separated led Einstein, Podolsky and Rosen (EPR) to the formulation of their famous paradox[18], in which they wondered whether QM is a complete theory or whether it is a statistical approximation of a deterministic theory. In order to find an answer, they introduced the concept of *element of reality*: if, without disturbing in any way a system, an observer can predict the value of a physical quantity without any uncertainty, then there is a element of reality corresponding to this quantity (*realism hypothesis*). Following special relativity, EPR also formulated the reasonable hypothesis that any non-local action is forbidden (*locality hypothesis*). Following this description, a theory is complete only when it describes any element of reality.

Returning to our example, which follows Bohm's variant of the original EPR experiment[19], after her measurement of the z spin component on A, Alice immediately knows the z spin component of particle B, without disturbing B in any way. Therefore, the z spin component of B is an element of reality, according to EPR definition. Since the singlet state is invariant under rotations, the same argument can be made for any other spin component of particle B. However, spin components on different axes are incompatible variables in QM (Post. 4, [16]). Therefore, according to EPR definition, quantum mechanics is not a complete theory, because it does not allow a prediction of all elements of reality.

Another interesting property of entangled systems is that, before any measurement is performed, the values of some specific observables of the subsystems are not defined. The measurement of the observable of one of the subsystems, however,

6

immediately fixes the value of the correlated subsystem (as seen in the previous example), independently of the distance. This phenomenon, which is often called *quantum non-locality*, does not imply, however, violation of causality. Following the previous example, by measuring the z spin, Alice's outcomes are either ↑ or ↓, with an associated probability of $1/2$ each. The same can be said about Bob, who may be space-like separated from Alice. While the two outcomes will always be correlated, without classical communication, Bob has no way to determine whether Alice has performed a measurement or not, meaning that his result is just a random spin. Therefore, Alice can not transmit information to Bob by only acting on her subsystem[20]. Nevertheless, this property of entangled systems and its implications started an hot debate, from which emerged the development of the so-called *local hidden variable* (LHV) theories, i.e. theories which propose the existence of a deterministic local theory describing nature, where the values of all observables of a physical system are fixed by some unknown *hidden variables*. Quantum mechanics, then, would only be a statistical approximation of this theory, as thermodynamics is a statistical approximation of classical mechanics.

Bell inequalities Several years after EPR published their article, after a first failed attempt by von Neumann[9], John Bell suggested an experiment to disprove the existence of hidden-variable theories. In his article[21], he showed that any realistic local hidden variable theory must satisfy certain inequalities, that are violated by quantum mechanics. Here, we briefly derive one specific Bell inequality: the *CHSH inequality*[22], introduced a few years later by John Clauser, Michael Horne, Abner Shimony, and Richard Holt.

Let us suppose that an observer named Charlie prepares identical sets of two particles A and B, sending, each time, particle A to Alice and particle B to Bob. Alice, then, can perform one of two different measurements P_Q or P_R on her particle, randomly choosing. In the frame of hidden variable theories, Suppose that particle A has values Q and R for the properties P_Q and P_R, respectively, which can take value $+1$ or -1. Q and R, then, are *elements of reality* of particle A. Similarly, we suppose that Bob can measure, randomly choosing, one of two different properties P_S or P_T, revealing an objective property of particle B. Once again, S and T can take value $+1$ or -1. Measurement timing is arranged so that Alice's and Bob's measurements are *local*, i.e. they are spacelike-separated. Therefore, the results of one measurement cannot disturb the results of the other.

Since all variables can either be $+1$ or -1, we can easily notice that:

$$QS + RS + RT - QT = (Q + R)S + (R - Q)T = \pm 2 \qquad (1.1.1.16)$$

Now, suppose that $p(q, r, s, t)$ is the probability that, before any measurement is performed, the system is in the state $Q = q$, $R = r$, $S = s$, $T = t$. Then, we can write the mean value of $QS + RS + RT - QT$ as:

$$E(QS + RS + RT - QT) = \sum_{qrst} p(q, r, s, t) \left(qs + rs + rt - qt\right) \leq 2 \sum_{qrst} p(q, r, s, t) = 2$$
(1.1.1.17)

where we denoted the classical expectation value as $E(\cdot)$ to differentiate it from the quantum expectation value (Eq. (1.1.1.4)). For this expectation value, we can also write:

$$E(QS + RS + RT - QT) = \sum_{qrst} p(q, r, s, t)qs + \sum_{qrst} p(q, r, s, t)rs + \sum_{qrst} p(q, r, s, t)rt$$
$$- \sum_{qrst} p(q, r, s, t)qt = E(QS) + E(RS) + E(RT) - E(QT)$$
(1.1.1.18)

which, combined, give us the *CHSH inequality*:

$$E(QS) + E(RS) + E(RT) - E(QT) \leq 2 \qquad (1.1.1.19)$$

that any realistic local hidden variable theory must satisfy.

It is easy to show that entangled particles violate this inequality. For instance, the measure of quantities $Q = (\sigma_z)_A$, $R = (\sigma_x)_A$, $S = -\frac{(\sigma_z)_B + (\sigma_x)_B}{\sqrt{2}}$ and $T = \frac{(\sigma_z)_B - (\sigma_x)_B}{\sqrt{2}}$, being $\sigma_x = \begin{pmatrix} 0 & 1 \\ 1 & 0 \end{pmatrix}$ and $\sigma_z = \begin{pmatrix} 1 & 0 \\ 0 & -1 \end{pmatrix}$ two Pauli matrices, for the state $|\psi\rangle = \frac{|01\rangle - |10\rangle}{\sqrt{2}}$ yields the result:

$$\langle QS\rangle + \langle RS\rangle + \langle RT\rangle - \langle QT\rangle = 2\sqrt{2} \qquad (1.1.1.20)$$

which clearly violates the CHSH inequality.

The first experimental realization of a Bell inequality experiment respecting the locality principle has been implemented by Alain Aspect et al. with entangled photons[23] in 1982, showing a Bell inequalities violation of more than 5 standard deviations. Since then, a long series of experiments has been performed, all confirming the violation of Bell inequalities[24] culminated in two experiments where any significant additional hypothesis was eliminated[25, 26]. This suggests that at least one of the assumptions on which Bell inequalities are based (locality and realism) is not correct, meaning that the world is not locally realistic. This, of course, rules out completely realistic local hidden-variables theories.

Bell inequalities violation also tells us that entanglement is a new resource, which goes beyond what classical resources can achieve. As we will see in Sec. 1.1.2, a lot of the emerging quantum technologies indeed exploit its properties.

The density operator

A more general description of a quantum system uses a tool called *density operator* or *density matrix* instead of the state vectors. The two formulations are mathematically equivalent[27], but the density operator provides a more convenient language to describe some quantum phenomena. In fact, the density operator was introduced by von Neumann[28] to describe a system of which we only have a partial description, thus using a statistical language. Let a quantum system be an ensemble of systems which can be in a certain number of pure quantum states $|\psi_i\rangle$ (i being an index) with respective probabilities p_i. Then, the density operator of such system is defined as:

$$\hat{\rho} = \sum_i p_i |\psi_i\rangle\langle\psi_i| \tag{1.1.1.21}$$

The density operator has the following properties:

- $\text{Tr}(\hat{\rho}) = 1$

- $\hat{\rho}$ is a positive operator (it has non-negative eigenvalues)

The density operator can be represented in a certain orthonormal basis $|e_n\rangle$:

$$\hat{\rho}_{mn} = \sum_i p_i \langle e_m|\psi_i\rangle \langle\psi_i|e_n\rangle \tag{1.1.1.22}$$

This representation is called *density matrix* and depends on the chosen basis.

Purity of a state A simple test can discriminate between $\hat{\rho}$ being a pure or mixed state:

$$\text{Tr}\left(\hat{\rho}^2\right) \begin{cases} = 1 & \text{if pure} \\ < 1 & \text{if mixed} \end{cases} \tag{1.1.1.23}$$

As a consequence, the density operator of a pure state is idempotent, i.e. $\hat{\rho}^2 = \hat{\rho}$.

The postulates of quantum mechanics with the density operator Some of the postulates can be modified in order to accommodate the introduction of the density operator.

Postulate 1. *Quantum states*
Every physical system is associated with a complex separable Hilbert space $\mathcal{H}$ with inner product. The system is fully described by its density operator, which is a positive operator ρ with trace one, acting on the state space of the system. If the system is in an ensemble of states ρ_i with respective probabilities p_i, then its density operator is $\sum_i p_i\rho_i$, known as Born rule.

Postulate 3. ***Probability of a result***
If the physical system is on a state $\hat{\rho} = \sum_i p_i |\psi_i\rangle\langle\psi_i|$, the probability of having the outcome α after measuring a quantity A is $p(\alpha) = \langle\psi|\hat{\rho}|\psi\rangle$.

Postulate 5. ***von Neumann equation***
The evolution of a quantum state in a closed system is described by:

$$i\hbar \frac{\partial}{\partial t}\hat{\rho}(t) = \left[\hat{H}, \hat{\rho}\right] \qquad (1.1.1.24)$$

where $\hat{H}$ is the system's Hamiltonian operator and $\hbar$ the reduced Planck constant.

It is possible to describe the time evolution with the *time evolution operator* introduced in (1.1.1.11):

$$\hat{\rho}(t) = \hat{U}(t, t_0)\hat{\rho}(t_0)\hat{U}(t, t_0)^{\dagger} \qquad (1.1.1.25)$$

Postulate 6. ***Composite systems***
The state space of a composite system is described by the tensor product of the state spaces of the component physical systems. Moreover, if we have a system composed of n separate subsystems, and each subsystem i is prepared on a state $\hat{\rho}_i$, then the joint state is the tensor product $\hat{\rho}_1 \otimes \hat{\rho}_2 \otimes \cdots \otimes \hat{\rho}_n$.

If a composite system is described by a density operator $\hat{\rho}$, then its subsystems can be described by the *reduced density operators*. Let us consider, for simplicity, a system composed of two subsystems A and B. If $\hat{\rho}^{AB}$ is the density operator of the total system, the reduced density operator of the subsystem B is

$$\hat{\rho}^B = \mathrm{Tr}_A\left(\hat{\rho}^{AB}\right) \qquad (1.1.1.26)$$

where Tr_A is called *partial trace* over A and is defined as:

$$\mathrm{Tr}_A\left(|a_i\rangle\langle a_j| \otimes |b_k\rangle\langle b_l|\right) = \mathrm{Tr}_A\left(|a_i\rangle\langle a_j|\right)|b_k\rangle\langle b_l| \qquad (1.1.1.27)$$

with $|a_i\rangle$ and $|a_j\rangle$ being any two vectors in the space of A and $|b_k\rangle$ and $|b_l\rangle$ being any two vectors in the space of B.

Entanglement with density operators   The definition of entanglement can be generalized to mixed states. A generic density operator $\hat{\rho}_{AB}$ on the composite system is *separable* if and only if it can be written as a linear convex combination of tensor product of density matrices

$$\hat{\rho} = \sum_{ij} \lambda_{ij}\hat{\rho}_A^i \otimes \hat{\rho}_B^j \qquad (1.1.1.28)$$

where $\lambda_{ij} \geq 0$ and $\sum_{ij} \lambda_{ij} = 1$.

Another important property is that, in general, a state $\hat{\rho}_{AB}$ is entangled if and only if its reduced density operators are not pure[27].

Entropy and Quantum Discord

As we have seen in the Sec. 1.1.1, quantum states of a composite system can be divided into entangled and separable states. While entanglement is a strong non-classical correlation with many interesting properties, separable states are *generally* considered as classical. However, it has been shown[29, 30] that even some separable states contain non-classical correlations, that can be exploited in quantum computation in order to perform tasks exponentially faster than any classical algorithm. Such non-classicality is measured by the Quantum Discord, which is defined as the discrepancy between the quantum versions of two classically equivalent expressions for an information theory quantity called *mutual information.*

The definition of mutual information is based on the concept of *entropy* in (quantum) information theory, that can be regarded as a measure of the degree of "disorder" (or mixedness, in the quantum case) of a physical system[27]. For this reason, in this section we give a brief overview of the role of entropy in classical and quantum information theory, from which we will be able to introduce the concept of Quantum Discord.

Classical case: Shannon entropy   In classical information theory, the amount of information contained in a random variable X is quantified by the *Shannon entropy*[27, 31]:

$$H(X) = -\sum_x p_x \log_2 p_x \qquad (1.1.1.29)$$

where p_x is the probability of occurrence of the outcome x for X. H can be interpreted as the information gainable upon measuring the random variable X or, equivalently, as the amount of uncertainty about X before we learn its value[32]. Shannon entropy was introduced as part of Shannon's noiseless coding theorem[31] in order to characterize the amount of resources needed to store information, providing a mathematical limit on how well data can be losslessly compressed onto a perfectly noiseless channel.

Shannon entropy also allows us to evaluate the correlations between variables. Let us focus on the case of two random variables X and Y in a bipartite system, which are quantified by their *mutual information.* Before defining the mutual information, however, we introduce an useful quantity, called *joint entropy.*

The joint entropy $H(X, Y)$ is a simple extension of Shannon entropy, it is defined as the Shannon entropy for the joint probability distribution $p(x, y)$:

$$H(X, Y) = -\sum_{x,y} p(x, y) \log_2 p(x, y) \qquad (1.1.1.30)$$

and can easily be extended to more variables. The joint entropy measures the total uncertainty about the pair (X, Y) and is symmetrical.

Then, we can define the mutual information content of X and Y, which quantifies the amount of information in common between X and Y, as

$$I(X : Y) = H(X) + H(Y) - H(X, Y) \tag{1.1.1.31}$$

This definition is clearly symmetrical, i.e. $I(X : Y) = I(Y : X)$, and can be easily understood by looking at Fig. 1.1.
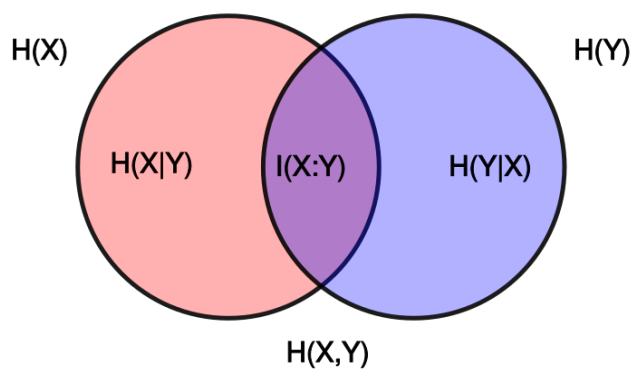
Figure 1.1: Individual ($H(X)$, $H(Y)$), joint ($H(X, Y)$) and conditional ($H(X|Y)$, $H(Y|X)$) entropies for a bipartite system with mutual information $I(X : Y)$

Another useful quantity is the conditional entropy, which quantifies the amount of knowledge that we have on Y given what we know about X or, equivalently, the uncertainty in measurement of Y when X is known, and is defined as

$$H(Y|X) = H(X, Y) - H(X) \tag{1.1.1.32}$$

This definition is not, in general, symmetrical.

Conditional entropy, allows us, thanks to Bayes' theorem[32], to reach an equivalent definition for the mutual information

$$J(X : Y) = H(X) - H(X|Y) \tag{1.1.1.33}$$

where $H(X|Y)$ is the conditional entropy. Once again, it can be easily understood by looking at Fig. 1.1.

Quantum case: von Neumann entropy In quantum systems, Shannon entropy can be generalized by replacing the probability distribution with density operators. This way, we define the entropy of a quantum state $\hat{\rho}$ as the *von Neumann entropy*[27, 33]:

$$S(\hat{\rho}) = -\operatorname{Tr}(\hat{\rho}\log_2\hat{\rho}) \tag{1.1.1.34}$$

Von Neumann entropy has the following properties[27]:

- S is non-negative and reaches zero if and only if the state is pure;

- in a d-dimensional Hilbert space, S is at most $\log_2 d$;

- if a composite system AB is in a pure state, then $S(A) = S(B)$;

- if $\hat{\rho} = \sum_i p_i\rho_i$, then

$$S(\sum_i p_i\rho_i) = H(p_i) + \sum_i p_i S(\rho_i) \tag{1.1.1.35}$$

Let us now consider a bipartite system AB in a quantum state $\hat{\rho}_{AB}$. Joint and conditional entropy can be easily defined by analogy with Eq.s (1.1.1.30) and (1.1.1.32):

$$S(\hat{\rho}_{AB}) = -\operatorname{Tr}(\hat{\rho}_{AB}\log_2\hat{\rho}_{AB}) \tag{1.1.1.36}$$
$$S(\hat{\rho}_{B|A}) = S(\hat{\rho}_{AB}) - S(\hat{\rho}_B) \tag{1.1.1.37}$$

where $\hat{\rho}_{B|A}$ is the state of the B subsystem given a measurement of A and $\hat{\rho}_{A(B)} = \operatorname{Tr}_{B(A)}(\hat{\rho}_{AB})$ is the reduced density matrix (Sec. 1.1.1) of $\hat{\rho}_{AB}$ for the subsystem $A(B)$.

The same can be done with the mutual information I, which quantifies the total amount of correlations:

$$I(\hat{\rho}_{AB}) = S(\hat{\rho}_A) + S(\hat{\rho}_B) - S(\hat{\rho_{AB}}) \tag{1.1.1.38}$$

This definition is symmetrical, like its classical counterpart reported in Eq. (1.1.1.31).

The generalization of the mutual information $J(\hat{\rho})$ to the quantum case, however, needs a bit of tinkering, because it involves the outcomes of a measurement, but quantum measurements are basis dependent and influence the state of the system (Sec. 1.2). Given the generalization of the conditional entropy in $S(\hat{\rho}_{B|A})$, we define the mutual information J_A by minimizing the entropy over all possible measurements $\left\{\hat{E}_k\right\}$ of A:

$$J_A(\hat{\rho}_{AB}) = H(\hat{\rho}_B) - \min_{\left\{\hat{E}_k\right\}}\sum_k p_k H(\hat{\rho}_{B|k}) \tag{1.1.1.39}$$

where $\hat{\rho}_{B|k} = \mathrm{Tr}_A \left(\hat{E}_k \otimes \hat{\mathbb{1}}_B \hat{\rho} \right) / \mathrm{Tr} \left(\hat{E}_k \otimes \hat{\mathbb{1}}_B \hat{\rho} \right)$ is the state of B conditioned to the outcome k of a measurement of A and $\left\{ \hat{E}_k \right\}$ is the POVM set (Sec. 1.2.1) for subsystem A, and p_k is the probability of the outcome k of a measurement $\hat{E}_k$. Note that, in contrast with the classical J, this is not, in general, a symmetric definition, i.e. $J_A(\hat{\rho}) \neq J_B(\hat{\rho})$. In quantum systems the definition for the mutual information J is not equivalent to I, and this difference quantifies the Quantum Discord.

Quantum Discord   As previously stated, Quantum Discord is a measure of non-classical correlations between two subsystems of a quantum system such as, but not limited to, entanglement. It is defined, for a bipartite system, as the discrepancy between the two expressions I (Eq. (1.1.1.38)) and J (Eq. (1.1.1.39)) for mutual information:

$$\mathcal{D}_A(\hat{\rho}) = I(\hat{\rho}_{AB}) - J_A(\hat{\rho}_{AB}) \tag{1.1.1.40}$$

which has the following properties:

- $\mathcal{D}$ is always non-negative.

- $\mathcal{D}$ is not, in general, symmetrical, i.e. $\mathcal{D}_A \neq \mathcal{D}_B$.

- A state is said to be completely classically correlated if $\mathcal{D}_A = \mathcal{D}_B = 0$

Non-zero Quantum Discord, then, indicates the presence of non-classical correlations.

1.1.2   New quantum technologies

Quantum technologies are an emerging field of physics and engineering which relies on quantum mechanics in order to beat classical limits in many practical applications.

Today, there already are many technologies available to the public that rely on quantum mechanical effects, such as lasers[34], semiconductor devices and transistors[35] and magnetic resonance imagers[36]. These technologies, based on generic ensemble properties of quantum mechanical systems, are usually said to belong to the *first quantum revolution in technology*. A *second quantum revolution* based on specific properties, such as entanglement, of single quantum systems, however, is underway, promising new practical applications spanning several research fields, such as telecommunications, computation, metrology and imaging. Let us briefly describe some of these new technologies.

Quantum computers[27] are devices that can process quantum data, taking advantage of the properties of quantum mechanics. Whereas classical computers

encode all data in the bit, a binary digit that can assume either the value 0 or 1, quantum computers employ *qubits* ("quantum bits") as basic units of information, which can be 0, 1 or a superposition of both. It has been showed that this difference, together with non-classical correlations such as entanglement, can be exploited in order to have exponential speed-ups in certain algorithms with respect to their classical version. For instance, factorization is known to be a hard problem for classical computers, but is an easy task for quantum computers[37]. This poses a critical issue in cybersecurity, since it would make anyone possessing a quantum computer able to break the current encryption standard (RSA), which relies on the inability of classical computers to factorize a large number in a short time.

Quantum communication[38] concerns the realization of new communication schemes based on peculiar properties of quantum systems. In particular, it could provide "quantum safe" communication techniques, quantum key distribution (QKD) [39, 40]. Another well known property is quantum teleportation[41, 42]. In QKD, the cryptographic key is transmitted using quantum light in a way that makes obvious for both the sender and the receiver to detect an eventual eavesdropper. In particular, in order to obtain information on the key, the eavesdropper must perform a measurement on the photon, thus introducing a detectable perturbation (Postulate 4; Sec. 1.2). Once the key is safely transmitted, the encrypted message can be sent in a classical channel and, if the key is used only once, this method is inherently safe[43]. Today, QKD systems are already available on the market and, for instance, have been used during the elections in Switzerland and the Football World Championship, while many nations are implementing a quantum backbone[44], i.e. a large scale quantum communication network. Quantum teleportation, instead, is a technique which allows transmitting quantum states without having to physically transport the underlying particle. This is possible by coupling the state to be transmitted to a pair of entangled particles shared by sender and receiver. Thanks to this coupling, by performing a series of measurements and sending the results to the receiver through a classical channel, the sender makes the receiver able to obtain a particle in the same state.

Metrology is another field of research which is greatly benefiting from the advent of quantum technologies. As mentioned before, in the new SI revision[12], the the realizations of many units of measurements depend on quantum mechanical effects[13, 14, 15]. For instance, in Quantum Hall Effect[45] the electrical resistance has been found to be integer or fractional multiples of a fundamental resistance value R_K, which is independent of the device. Since R_K only depends on the Planck constant and the electrical charge, which have exact values, it is also an exact value that can be used to realize the Ohm. Similarly, Josephson junctions[46] allow defining the Volt from the quantization of the voltage flux. Beyond that, the field of quantum metrology studies ways to exploit quantum resources such as, but

not limited to, entanglement to develop "quantum enhanced" measurement techniques[47, 48, 49] that give better precision than the same measurement performed in a classical framework. For instance, entangled light can be employed to overcome the limits of classical imaging, drastically reducing the noise[50, 51].

Today, thanks to the potential of these new quantum technologies, research in the field of quantum technologies is benefiting from several government programs, such as the 10-years-long Quantum Technology Flagship of the European Commission. Many large companies have also made multiple investments in quantum technologies, such as IBM and Google.

1.2 Measurements in quantum mechanics

Measurements play a crucial role in quantum mechanics, as several postulates deal with them. Because of that, a lot of effort has been given in order to model and characterize them. In the following sections, we will describe the direct and the indirect formalisms, from which a new subclass of measurements, called *weak measurements* will emerge.

1.2.1 Strong (sharp) direct measurements: projective, POVM

The first class of measurements that we analyse is the one of strong direct measurements.

Projective measurement

Projective measurements emerge from the postulates 2, 3 and 4 and are the most intuitive and simple description of a measurement in quantum mechanics.

A projective measurement is defined by an observable A to which is associated a linear self-adjoint operator $\hat{A}$ in the space of the states of the system $\mathcal{H}$. The spectral decomposition of the operator is

$$\hat{A} = \sum_{\alpha} a\hat{\mathbb{P}}_{\alpha} \qquad (1.2.1.1)$$

where $\hat{\mathbb{P}}_{\alpha}$ is the projector on the eigenspace of $\hat{A}$ with eigenvalue α defined as

$$\hat{\mathbb{P}}_{\alpha} = |\alpha\rangle\langle\alpha| \qquad (1.2.1.2)$$

It is interesting to notice that the structure of the projector is similar to the one of density operators. In fact, a density operator may be seen as the average of the

projectors on the states $\{|\psi_i\rangle\}$ weighted on their respective probabilities.

The possible outcomes of the measurement are the eigenvalues α of the observable. The probability of obtaining the outcome α by means of a projective measurement of the state $|\psi\rangle$ (or the corresponding $\hat{\rho}$) is

$$p(\alpha) = \langle\psi|\hat{\mathbb{P}}_\alpha|\psi\rangle = \mathrm{Tr}\left(\hat{\mathbb{P}}_\alpha\hat{\rho}\right) = |\langle\alpha|\psi\rangle|^2 \qquad (1.2.1.3)$$

If the outcome is α, the state collapses in the eigenstate

$$|\alpha\rangle = \frac{\hat{\mathbb{P}}_\alpha|\psi\rangle}{\sqrt{p(\alpha)}} \qquad (1.2.1.4)$$

or its corresponding density operator $\hat{\rho}_\alpha = |\alpha\rangle\langle\alpha|$.

For two generic projectors belonging to a complete set of orthogonal projectors, it holds:

$$\hat{\mathbb{P}}_\alpha\hat{\mathbb{P}}_\beta = \delta_{\alpha,\beta}\hat{\mathbb{P}}_\alpha \qquad (1.2.1.5)$$

Expectation values

Thanks to the projective measurements, we can give a more detailed definition of *quantum expectation value*:

$$\langle A \rangle = \langle\psi|A|\psi\rangle = \langle\psi|\left(\sum_\alpha \alpha\hat{\mathbb{P}}_\alpha\right)|\psi\rangle = \sum_\alpha \alpha\langle\psi|\hat{\mathbb{P}}_\alpha|\psi\rangle = \sum_\alpha \alpha p(\alpha) \qquad (1.2.1.6)$$

Or, equivalently:

$$\langle A \rangle_\rho = \mathrm{Tr}(A\hat{\rho}) \qquad (1.2.1.7)$$

Measurement operators

It is possible to generalize[27] projective measurements in order to take into account several cases impossible to describe with such formalism. For instance, a photon passing through a polariser can either be projected onto a new polarization state or be absorbed. This absorption is not describable by projectors.
In order to introduce the new measurements, two postulates of quantum mechanics need to be modified.

Postulate 3. *Probability of a result (pure states)*
Quantum measurements are described by an ensemble of measurement operators $\left\{\hat{K}_m\right\}$. *These operators act on the measurand state space and the index m denotes one of the possible experimental outcomes.*
If the state before the measurement is $|\psi\rangle$, then the probability of the outcome m is

$$p(m) = \langle\psi|\hat{K}_m^\dagger\hat{K}_m|\psi\rangle \qquad (1.2.1.8)$$

Or, in the density operator formalism:

Postulate 3. *Probability of a result (density operator)*
Quantum measurements are described by an ensemble of measurement operators $\left\{ \hat{K}_m \right\}$. *These operators act on the measurand state space and the index m denotes one of the possible experimental outcomes.*
If for a state $|\psi_i\rangle$, the probability of the outcome m is

$$p(m|i) = \langle\psi_i|\hat{K}_m^\dagger \hat{K}_m|\psi_i\rangle = \mathrm{Tr}\left(\hat{K}_m^\dagger \hat{K}_m \, |\psi_i\rangle\langle\psi_i| \right) \tag{1.2.1.9}$$

then, if the density operator of the system is $\hat{\rho} = \sum_i p_i \, |\psi_i\rangle\langle\psi_i|$,

$$p(m) = \sum_i p_i p(m|i) = \sum_i p_i \, \mathrm{Tr}\left(\hat{K}_m^\dagger \hat{K}_m \, |\psi_i\rangle\langle\psi_i| \right) = \mathrm{Tr}\left(\hat{K}_m^\dagger \hat{K}_m \hat{\rho} \right) \tag{1.2.1.10}$$

Thanks to the fact that $\sum_m p(m) = 1$, it is easy to show that:

$$\sum_m \hat{K}_m^\dagger \hat{K}_m = \mathbb{1} \tag{1.2.1.11}$$

Postulate 4. *The state after a measurement*
The state after a measurement is

$$\frac{\hat{K}_m \, |\psi\rangle}{\sqrt{\langle\psi|\hat{K}_m^\dagger \hat{K}_m|\psi\rangle}} \tag{1.2.1.12}$$

or, equivalently

$$\hat{\rho}_m = \frac{\hat{K}_m \hat{\rho} \hat{K}_m^\dagger}{\mathrm{Tr}\left(\hat{K}_m^\dagger \hat{K}_m \hat{\rho} \right)} \tag{1.2.1.13}$$

It is easy to notice that, by evaluating the case $\hat{K}_m = \hat{\mathbb{P}}_m$, measurement operators include projective measurements.

POVM

The postulates give us rules to describe the statistics of the measurements and the state after a measurement. However, in some applications, only the probabilities of the outcomes may be of interest. In those cases, it is possible to use the *POVM* (Positive Operator-Valued Measure) formalism. Let us suppose that the measurement of a system is described by the operators $\hat{K}_m$ and that the probability of the outcome m is $p(m) = \langle\psi|\hat{K}_m^\dagger \hat{K}_m|\psi\rangle$. Then, by defining

$$\hat{E}_m = \hat{K}_m^\dagger \hat{K}_m \tag{1.2.1.14}$$

we know, from both the postulates and linear algebra[52], that $\hat{E}_m$ is a positive operator such that $\sum_m \hat{E}_m = 1$ and $p(m) = \langle\psi|\hat{E}_m|\psi\rangle$.

The operators $\hat{E}_m$ are called *POVM elements*, whereas their ensemble is called POVM. A POVM is sufficient to determine the probabilities of the different outcomes.

Projective measurements are a special case of POVM. Since, for projectors belonging to a complete set of orthogonal projectors, $\hat{\mathbb{P}}_m\hat{\mathbb{P}}_n = \delta_{m,n}\hat{\mathbb{P}}_m$ and $\sum_m \hat{\mathbb{P}}_m = 1$ hold for any projector $\hat{\mathbb{P}}_m$, all the POVM elements correspond to the projectors, since $\hat{E}_m = \hat{\mathbb{P}}_m^\dagger\hat{\mathbb{P}}_m = \hat{\mathbb{P}}_m$. Note that this is only true for projective measurements.

1.2.2 Indirect measurements and the von Neumann protocol

The direct measurements formalism is a really simple and powerful framework but it is inadequate to describe real measurements because we do not usually directly measure the system. Instead, we perform a coupling between the system and a measurement apparatus (usually called *meter*) and observe the measurement effects on the meter. This is similar to what happens in the classical world, where, for instance, the measurement of the weight of an object is carried out by coupling it with the measurement apparatus (the balance) and then reading the effect of the interaction on the needle of the balance (usually called *pointer*).

In order to keep track of these factors, we introduce the indirect measurements formalism[53]. This formalism describes the measurement procedure of a system by introducing a second system (the meter). The interaction between the initial system and the meter entangles them. Thus, by reading the meter through the *pointer*, one can obtain information about the value of the system observable under test.

Let us start by describing in detail the system $\mathcal{S}$, the meter $\mathcal{M}$ and the total system $\mathcal{T}$, i.e. the one formed by the entanglement of $\mathcal{S}$ and $\mathcal{M}$:

System $\mathcal{S}$

The system lives in a Hilbert space $\mathcal{H}_\mathcal{S}$, in which it is defined the operator $\hat{S}$, corresponding to the observable S that we want to measure. Its eigenstates $\{|s_i\rangle\}$ (with $i = 1, 2, \cdots, d_S$; $d_S = \dim \mathcal{H}_\mathcal{S}$) form a complete orthonormal basis for $\mathcal{H}_\mathcal{S}$.

The Hamiltonian of the system $\hat{H}_\mathcal{S}$ is usually assumed to vanish.

The projectors on $\mathcal{H}_S$ are called $\hat{\mathbb{P}}_{s_i}$.

For simplicity, we assume that the system is on a generic state $\hat{\sigma}_0$.

Meter $\mathcal{M}$

The meter is described as a quantum device living in a Hilbert space $\mathcal{H}_{\mathcal{M}}$, in which the operator $\hat{M}$, called *pointer variable*, is defined. Its eigenstates $\{|m_k\rangle\}$ (with $k = 1, 2, \cdots, d_S$; $d_M = \dim \mathcal{H}_{\mathcal{M}}$) are called *pointer states*.

As per the system, the Hamiltonian of the meter $\hat{H}_{\mathcal{M}}$ is assumed to vanish in most cases.

The projectors on $\mathcal{H}_{\mathcal{M}}$ are called $\hat{\Pi}_{m_k}$.

We assume that the meter is prepared in the initial state $\left|m^{(0)}\right\rangle$, which may or may not be an eigenstate of the pointer. Thus, the initial density operator of the pointer is $\hat{\mu}_0 = \left|m^{(0)}\right\rangle\!\!\left\langle m^{(0)}\right|$.

Total system $\mathcal{T}$

The total system encompasses both the system $\mathcal{S}$ and the meter $\mathcal{M}$. Its Hilbert space is the direct product $\mathcal{H}_{\mathcal{T}} = \mathcal{H}_{\mathcal{S}} \otimes \mathcal{H}_{\mathcal{M}}$. The initial state is $\hat{\tau}_0 = \hat{\sigma}_0 \otimes \hat{\mu}_0$, in which system and meter are assumed to be uncorrelated (not entangled). The only non-vanishing term in the total Hamiltonian is assumed to be the interaction one: $\hat{H}_{\mathcal{T}} = \hat{H}_{int}$.

The first step of the measurement is the coupling between the system and the meter, carried out by a unitary temporal evolution operator $\hat{U}$. This procedure is also known as *pre-measurement*. The total system evolves from its initial *pre-selected* state $\hat{\tau}_0$ in:

$$\hat{\tau}_1 = \hat{U}\hat{\tau}_0\hat{U}^\dagger = \hat{U}\hat{\sigma}_0 \otimes \hat{\mu}_0 \hat{U}^\dagger \tag{1.2.2.1}$$

where, as per (1.1.1.13),

$$\hat{U} = \exp\left(-\frac{i}{\hbar}\int dt \hat{H}_{\mathcal{T}}\right) \tag{1.2.2.2}$$

An easy way to calculate the time evolution is to evolve $\mathcal{T}$ when $\mathcal{S}$ is in one of its eigenstates:

$$\hat{U}\left(|s_i\rangle \otimes \left|m^{(0)}\right\rangle\right) = |s_i\rangle \otimes \left|m^{(i)}\right\rangle \tag{1.2.2.3}$$

where $i = 0, 1, \cdots, d_{\mathcal{S}}$. This shows that the interaction does not change a pure eigenstate of the system.

As for $\left|m^{(0)}\right\rangle$, $\left|m^{(i)}\right\rangle$ are not, in general, eigenstates of the meter operator $\hat{M}$, but normalized superpositions of them. Therefore, they are not mutually orthogonal and they do not form a complete set in $\mathcal{H}_{\mathcal{M}}$. Furthermore, a meter state $\left|m^{(i)}\right\rangle$ acts as a kind of marker for the eigenstate $|s_i\rangle$, as we will see later.

Since $\hat{U}$ is a linear operator, we can extend the above time evolution to the case in which the system initial state is a superposition $|s\rangle$ of its eigenstates:

$$\hat{U}\left(|s\rangle \otimes \left|m^{(0)}\right\rangle\right) = \sum_{i=1}^{d_{\mathcal{S}}} |s_i\rangle \otimes \left|m^{(i)}\right\rangle \tag{1.2.2.4}$$

which is not separable anymore. The interaction entangles the system and the meter.

From Eq. (1.2.2.4), we can calculate the evolution of the density operator $\hat{\tau}_0$:

$$
\begin{aligned}
\tau_1 &= \hat{U}\hat{\tau}_0\hat{U}^\dagger = \hat{U}\hat{\sigma}_0 \otimes \hat{\mu}_0\hat{U}^\dagger \\
&= \sum_{i,j}(|s_i\rangle \otimes \left|m^{(i)}\right\rangle \langle s_i|\hat{\sigma}_0|s_j\rangle \langle s_j| \otimes \left\langle m^{(j)}\right|) \\
&= \sum_{i,j}(\left|m^{(i)}\right\rangle \hat{\mathbb{P}}_{s_i}\hat{\sigma}_0\hat{\mathbb{P}}_{s_j} \left\langle m^{(j)}\right|)
\end{aligned}
\tag{1.2.2.5}
$$

which allows us to obtain the partial state of the system after the interaction, thanks to the partial trace:

$$
\begin{aligned}
\hat{\sigma}_1 &= \mathrm{Tr}_\mathcal{M}\,\hat{\tau}_1 = \sum_k \langle m_k|\hat{\tau}_1|m_k\rangle \\
&= \sum_{i,j,k} \left\langle m_k\middle|m^{(i)}\right\rangle \hat{\mathbb{P}}_{s_i}\hat{\sigma}_0\hat{\mathbb{P}}_{s_j} \left\langle m^{(j)}\middle|m_k\right\rangle \\
&= \sum_{i,j} \left(\hat{\mathbb{P}}_{s_i}\hat{\sigma}_0\hat{\mathbb{P}}_{s_j} \left\langle m^{(j)}\middle|m^{(i)}\right\rangle\right)
\end{aligned}
\tag{1.2.2.6}
$$

If there is no overlap between the meter states $\left|m^{(i)}\right\rangle$ and $\left|m^{(j)}\right\rangle$, then $\left\langle m^{(i)}\middle|m^{(j)}\right\rangle = \delta_{i,j}$ would imply that $\hat{\sigma}_1$ is diagonal, meaning that this indirect measurement would be analogous to a projective one. However, in general, $\left\langle m^{(i)}\middle|m^{(j)}\right\rangle \neq 0$ for $i \neq j$, because, as it has been previously mentioned, the meter states $\left|m^{(i)}\right\rangle$ are not eigenstates of $\hat{M}$, nor orthogonal with respect to each other. This means that, in general, the meter states can overlap.

Analogously, we can calculate the meter state after the interaction:

$$
\hat{\mu}_1 = \mathrm{Tr}_\mathcal{S}\,\hat{\tau}_1 = \sum_i \langle s_i|\hat{\tau}_1|s_i\rangle = \sum_i \left|m^{(i)}\right\rangle \langle s_i|\hat{\sigma}_0|s_i\rangle \left\langle m^{(i)}\right|
\tag{1.2.2.7}
$$

with matrix elements

$$
\langle m_k|\hat{\mu}_1|m_l\rangle = \sum_i \left\langle m_k\middle|m^{(i)}\right\rangle \langle s_i|\hat{\sigma}_0|s_i\rangle \left\langle m^{(i)}\middle|m_l\right\rangle
\tag{1.2.2.8}
$$

expressed in terms of the wave-function $\left\langle m_k\middle|m^{(i)}\right\rangle$. Notice that we can efficiently distinguish between the different eigenvalues s_i of $\hat{S}$ if and only if there is no overlap between the wave-functions $\left\langle m_k\middle|m^{(i)}\right\rangle$.

The read-out

Now we measure the pointer observable M, obtaining the eigenvalue m_k of the operator $\hat{M}$ using the projector $\hat{\Pi}_{m_k} = |m_k\rangle\langle m_k|$:

$$\hat{\tau}_2 = \frac{\left(\hat{\mathbb{1}}_{\mathcal{S}} \otimes \hat{\Pi}_{m_k}\right) \hat{\tau}_1 \left(\hat{\mathbb{1}}_{\mathcal{S}} \otimes \hat{\Pi}_{m_k}\right)}{p(m_k|\hat{\tau}_1)} \tag{1.2.2.9}$$

where $p(m_k|\hat{\tau}_1)$ is the probability of obtaining the eigenvalue m_k from the state $\hat{\tau}_1$.

$$\begin{aligned}
p(m_k|\hat{\tau}_1) &= \text{Tr}\left[\left(\hat{\mathbb{1}}_{\mathcal{S}} \otimes \hat{\Pi}_{m_k}\right) \hat{\tau}_1\right] \\
&= \sum_i \left(\left|\left\langle m^{(i)} \middle| m_k \right\rangle\right|^2 \langle s_i|\hat{\sigma}_0|s_i\rangle\right) \\
&= \sum_i p(m_k|m^{(i)})p(s_i|\hat{\sigma}_0)
\end{aligned} \tag{1.2.2.10}$$

One again we notice that the m_k distribution reflects the s_i one if and only if the meter wave-functions do not overlap. Let us see what happens to the system after the read-out of the meter, by performing a partial trace over the meter:

$$\begin{aligned}
\hat{\sigma}_2 &= Tr_{\mathcal{M}}(\hat{\tau}_2) \\
&= \frac{1}{p(m_k|\hat{\tau}_1)} Tr_{\mathcal{M}}\left[\left(\hat{\mathbb{1}}_S \otimes \hat{\Pi}_{m_k}\right) \hat{\tau}_1 \left(\hat{\mathbb{1}}_S \otimes \hat{\Pi}_{m_k}\right)\right] \\
&= \frac{1}{p(m_k|\hat{\tau}_1)} \langle m_k| \hat{U}\hat{\sigma}_0 \otimes \hat{\mu}_0 \hat{U}^\dagger |m_k\rangle \\
&= \frac{1}{p(m_k|\hat{\tau}_1)} \langle m_k| \hat{U} \left| m^{(0)} \right\rangle \hat{\sigma}_0 \left\langle m^{(0)} \right| \hat{U}^\dagger |m_k\rangle \\
&= \frac{1}{p(m_k|\hat{\tau}_1)} \hat{K}_k \hat{\sigma}_0 \hat{K}_k^\dagger
\end{aligned} \tag{1.2.2.11}$$

where the operators $\hat{K}_k$ are the *measurement operators* that we introduced in section 1.2.1. It is easy to see that they act only on $\mathcal{H}_{\mathcal{S}}$ and are defined as:

$$\begin{aligned}
\hat{K}_k &= \left\langle m_k \middle| \hat{U} \middle| m^{(0)} \right\rangle \\
&= \sum_i \left\langle m_k \middle| m^{(i)} \right\rangle |s_i\rangle\langle s_i| \\
&= \sum_i \left\langle m_k \middle| m^{(i)} \right\rangle \hat{\mathbb{P}}_{s_i}
\end{aligned} \tag{1.2.2.12}$$

This means that, by carefully choosing the interaction and the meter, we can use an indirect measurement to reproduce any measurement operator, including, of course, projectors and POVMs.

For completeness, let us calculate the density operator of the meter after the measurement:

$$\hat{\mu}_2 = \frac{\hat{\Pi}_{m_k} \hat{\mu}_1 \hat{\Pi}_{m_k}}{p(m_k|\hat{\tau}_1)} \tag{1.2.2.13}$$

It is important to notice that, after the read-out, system and meter are disentangled.

The von Neumann protocol

So far, we have given a general description of the indirect measurement protocol. A special case of indirect measurement protocol is the von Neumann protocol[9] (not to be confused with the von Neumann scheme, an alternative name for projective measurements), which has the advantage of giving a detailed description of the meter and uses a very specific interaction Hamiltonian. For this reason, the von Neumann protocol is the one describing most experiments.

Let us describe the total system in detail:

System $\mathcal{S}$

The system retains the same definition as for the general indirect measurement protocol. For simplicity, however, we assume that the system is on a pure initial state $|s\rangle$.

Meter $\mathcal{M}$

The meter is described as quantum device living in a *continuous* Hilbert space $\mathcal{H}_M$.

$\left|m^{(0)}\right\rangle$ denotes the initial wave-function of the measuring device. It can be expressed in the position basis as

$$\left|m^{(0)}\right\rangle = \int dq\, |q\rangle \left\langle q\middle|m^{(0)}\right\rangle = \int dq\, |q\rangle\, \phi_0(q) \tag{1.2.2.14}$$

where q is the position of the measuring needle, i.e. the *pointer* and $\phi_0(q)$ is the pointer wave-function. Thus, $|q\rangle$ are called *pointer states*. They are eigenstates of $\hat{Q}$, which is, in turn, called *pointer variable*. $|q\rangle$ and $\hat{Q}$ replace, respectively, $|m_k\rangle$ and $\hat{M}$ from the indirect measurement.

We also assume that the wave-function $\phi_0(q)$ is centred in 0, with variance σ^2:

$$\phi_0(q) = \left[\frac{1}{\sqrt{2\pi\sigma^2}} \exp\left(-\frac{q^2}{2\sigma^2} \right) \right]^{\frac{1}{2}} \tag{1.2.2.15}$$

meaning that $\left\langle \hat{Q} \right\rangle_0 = 0$.

The Hamiltonian of the meter $\hat{H}_M$ is assumed to vanish in most cases.

Total system $\mathcal{T}$

The only non-vanishing term in the total Hamiltonian is assumed to be the interaction one.

As mentioned before, von Neumann protocol defines a very specific interaction Hamiltonian:

$$\hat{H}_{int} = \gamma \hat{S} \otimes \hat{P} \qquad (1.2.2.16)$$

where γ is the coupling constant and $\hat{P}$ is the variable of the meter canonically conjugated to the pointer $\hat{Q}$ ($\left[\hat{Q}, \hat{P}\right] = i\hbar$). Since we have assumed that the Hamiltonians of both the system and the meter vanish, the time evolution of the total system becomes:

$$\hat{U} = \exp\left(-\frac{i}{\hbar}\int dt\hat{H}_T\right) = \exp\left(-\frac{i}{\hbar}\int dt\hat{H}_{int}\right) = \exp\left(-\frac{i}{\hbar}g\hat{S} \otimes \hat{P}\right) \quad (1.2.2.17)$$

where $g = \int dt\gamma$ is the effective coupling constant.

In order to calculate the evolution of the total system, let us observe that, since $\hat{Q}$ and $\hat{P}$ are canonically conjugated, a generic operator $\exp\left(\frac{i}{\hbar}\lambda\hat{P}\right)$ with $\lambda \in \mathbb{R}$ acts as a translation operator for a wave-function $\phi(q)$ in the q basis:

$$\exp\left(\frac{i}{\hbar}\lambda\hat{P}\right)|\phi\rangle = \exp\left(\frac{i}{\hbar}\lambda\hat{P}\right)\int dq\,|q\rangle\,\phi(q) = \int dq\,|q\rangle\,\phi(q+\lambda) \qquad (1.2.2.18)$$

Therefore, the evolution of the total system $\mathcal{T}$ under the time evolution $\hat{U}$ for each of the system eigenvalues s_i is:

$$\begin{aligned}
|s_i\rangle\left|m^{(i)}\right\rangle &= \hat{U}\left(|s_i\rangle \otimes \left|m^{(0)}\right\rangle\right) \\
&= \exp\left(-\frac{i}{\hbar}g\hat{S} \otimes \hat{P}\right)\left(|s_i\rangle \otimes \left|m^{(0)}\right\rangle\right) \\
&= |s_i\rangle \otimes \left[\exp\left(-\frac{i}{\hbar}gs_i\hat{P}\right)\int dq\,|q\rangle\,\phi_0(q)\right] \\
&= |s_i\rangle \otimes \int dq\,|q\rangle\,\phi_0(q - gs_i)
\end{aligned} \qquad (1.2.2.19)$$

which means that for each eigenvalue, the initial state of the meter $\left|m^{(0)}\right\rangle$ evolves into a state $\left|m^{(i)}\right\rangle$:

$$\left|m^{(i)}\right\rangle = \int dq\,|q\rangle\,\langle q|m^{(i)}\rangle = \int dq\,|q\rangle\,\phi_i(q) = \int dq\,|q\rangle\,\phi_0(q - gs_i) \qquad (1.2.2.20)$$

or

$$\phi_i(q) = \phi_0(q - gs_i) \qquad (1.2.2.21)$$

This means that the interaction translates the initial state of the pointer $\phi_0(q)$, which was centred around $q = 0$, in a superposition of $\phi_i(q)$ states, which, in turn, are the initial state translated by gs_i. The read-out of the meter, then, allows to obtain one of the numbers $q = gs_i$, from which one can extract the result of the

measurement of $\hat{S}$.

This description makes it easy to visualize the meaning of the overlap of the wave-functions seen in Eq. (1.2.2.6). If the standard deviation σ of the distribution is much smaller than the effective coupling constant g, then there will be no overlap between the wave-functions ϕ_i. Once again, in this case we reproduce the projective measurement scenario.

Pre- and post-selection

Let us now introduce two important concepts: the pre- and post-selection.

Pre-selection   The pre-selection represent the choice of the initial state of an experiment. A generic incoming state $|\psi\rangle$ can be projected onto a different state $|\psi'\rangle$ which will be the initial state of the experiment.

Post-selection   If pre-selection represents the choice of the initial state, the post-selection can be seen as a choice of the final state. Let us start by describing it in the simpler case of direct measurements.

Post-selection in direct measurements   Let us suppose to perform two consecutive non-destructive projective measurements on the system.

We start by preparing the system in the initial pure state $|s\rangle$. Then, we measure the observable S by obtaining one of its *non-degenerate* eigenstates $|s_i\rangle$ ($i = 1, 2, \cdots, d_{\mathcal{S}}$) with probability $p(s_i|s) = |\langle s_i|s\rangle|^2$. Then, we measure the second observable F and we are only interested in one specific outcome $|f\rangle$. The joint probability of obtaining $|s_i\rangle$ in the first measurement and $|f\rangle$ in the second one is:

$$p(s_i, f|s) = p(f|s_i)p(s_i|s) = |\langle f|s_i\rangle|^2 |\langle s_i|s\rangle|^2 \qquad (1.2.2.22)$$

which leads to the total probability of obtaining f, regardless of the intermediate result s_i:

$$p(f|s) = \sum_i p(s_i, f|s) = \sum_i |\langle f|s_i\rangle|^2 |\langle s_i|s\rangle|^2 \qquad (1.2.2.23)$$

Thanks to Bayes' rule, these two probabilities allow us to calculate the probability of having an outcome s_i given the pre- and post-selection s and f:

$$p(s_i|f, s) = \frac{p(s_i, f|s)}{p(f|s)} = \frac{|\langle f|s_i\rangle|^2 |\langle s_i|s\rangle|^2}{\sum_i |\langle f|s_i\rangle|^2 |\langle s_i|s\rangle|^2} \qquad (1.2.2.24)$$

which is known as Aharonov-Bergman-Lebowitz (ABL) rule[54]. From the ABL rule we can calculate the expectation value of the observable S conditioned to the outcome f of the post-selection:

$$\langle \hat{S} \rangle_f = \sum_i s_i p(s_i|f, s) = \sum_i s_i \frac{|\langle f|s_i\rangle|^2 |\langle s_i|s\rangle|^2}{\sum_i |\langle f|s_i\rangle|^2 |\langle s_i|s\rangle|^2} \qquad (1.2.2.25)$$

Post-selection in indirect measurements Since S is not directly measured in the indirect measurement protocols, we cannot directly derive the ABL rule. Nevertheless, in the limit of projective measurements (no overlap between the different meter states), it is possible to retrieve the ABL rule. Let us start from a generic $\hat{\tau}_0 = \hat{\sigma}_0 \otimes \hat{\mu}_0$ and evolve it with the interaction $\hat{U}$:

$$\hat{\tau}_1 = \hat{U}\hat{\sigma}_0 \otimes \hat{\mu}_0 \hat{U}^\dagger = \sum_{i,j} \left(\left| m^{(i)} \right\rangle \hat{\mathbb{P}}_{s_i} \hat{\sigma}_0 \hat{\mathbb{P}}^\dagger_{s_j} \left\langle m^{(i)} \right| \right) \tag{1.2.2.26}$$

and post-select by projecting the system onto $|f\rangle$:

$$\begin{aligned} \hat{\tau}_2 &= \frac{(\hat{\mathbb{P}}_f \otimes \mathbb{1}_\mathcal{M})\hat{\tau}_1(\hat{\mathbb{P}}_f \otimes \mathbb{1}_\mathcal{M})}{p(f|\tau_1)} = \frac{(\hat{\mathbb{P}}_f \otimes \mathbb{1}_\mathcal{M})\left(\hat{U}\hat{\sigma}_0 \otimes \hat{\mu}_0 \hat{U}^\dagger\right)(\hat{\mathbb{P}}_f \otimes \mathbb{1}_\mathcal{M})}{p(f|\tau_1)} \\ &= \frac{(\hat{\mathbb{P}}_f \otimes \mathbb{1}_\mathcal{M}) \sum_{i,j} \left(\left| m^{(i)} \right\rangle \hat{\mathbb{P}}_{s_i} \hat{\sigma}_0 \hat{\mathbb{P}}_{s_j} \left\langle m^{(j)} \right| \right) (\hat{\mathbb{P}}_f \otimes \mathbb{1}_\mathcal{M})}{p(f|\tau_1)} \end{aligned} \tag{1.2.2.27}$$

Then, the total probability of obtaining f regardless of the intermediate result is:

$$\begin{aligned} p(s_i, f|s) &= Tr_\mathcal{T}\left[(\hat{\mathbb{P}}_f \otimes \mathbb{1})\hat{\tau}_2\right] \\ &= \sum_{i,j,k} (\langle s_i| \otimes \langle m_k|)(\hat{\mathbb{P}}_f\hat{\mathbb{P}}_{s_i}\hat{\sigma}_0\hat{\mathbb{P}}_{s_j}\hat{\mathbb{P}}_f \otimes \left\langle m^{(i)} \middle| m^{(j)} \right\rangle)(|s_i\rangle \otimes |m_k\rangle) \\ &= \sum_{i,j,k} \left\{ \left[\langle s_i| \hat{\mathbb{P}}_f\hat{\mathbb{P}}_{s_i}\hat{\sigma}_0\hat{\mathbb{P}}_{s_i}\hat{\mathbb{P}}_f |s_i\rangle \right] \left[\langle m_k| \hat{\mathbb{P}}_{m_k} \left| m^{(i)} \right\rangle \left\langle m^{(j)} \right| \hat{\mathbb{P}}_{m_k} |m_k\rangle \right] \right\} \\ &= \sum_{i,j,k} \{ [\langle s_i|f\rangle \langle f|s_i\rangle \langle s_i| \hat{\sigma}_0 |s_i\rangle \langle s_i|f\rangle \langle f|s_i\rangle] \\ &\quad \times \left[\langle m_k|m_k\rangle \left\langle m_k \middle| m^{(i)} \right\rangle \left\langle m^{(j)} \middle| m_k \right\rangle \langle m_k|m_k\rangle \right] \} \end{aligned} \tag{1.2.2.28}$$

Since we have asked to be in the projective measurements limit, the different meter states are separate, so $\left\langle m^{(j)} \middle| m^{(i)} \right\rangle = \delta_{i,j}$:

$$p(s_i, f|s) = |\langle f|s_i\rangle|^2 |\langle s_i|s\rangle|^2 \tag{1.2.2.29}$$

from which follows the ABL rule.

1.2.3 Strong indirect measurements: non-demolition

The indirect measurement formalism allows us to define a special type of measurement, which is called *quantum non-demolition* (QND) *measurement*[55]. A QND measurement of $\hat{A}$ is defined as a *sequence* of precise measurements of $\hat{A}$ through several measurement apparatuses $\mathcal{M}_i$, such that the result of each measurement is completely predictable from the result of the first measurement and,

eventually, some information about the initial state of the system. In mathematical terms, let $\hat{A}$ be an observable of the system $\mathcal{S}$, which is coupled to the meter $\mathcal{M}_i$ through an interaction Hamiltonian $\hat{H}_{int}$ (as in sec. 1.2.2). Between subsequent measurements, the system evolves following its free Hamiltonian $\mathcal{H}_\mathcal{S}$.

Most observables cannot be monitored in a QND way. Any measurement of the observable $\hat{A}$ creates a back-action which kicks all its non-commuting observables $\hat{C}$. In the subsequent free evolution of the system, the contamination of $\hat{C}$ may spread into $\hat{A}$, making the results of future measurements of $\hat{A}$ unpredictable. There is, however, a special class of observables, which can be immune to such feedback; they are called *QND observables*. $\hat{A}$ is a QND observable if and only if, when the system is evolving freely in the Heisenberg picture, $\hat{A}$ commutes with itself at the different times of measurement t_i:

$$\left[\hat{A}(t_i), \hat{A}(t_j)\right] = 0 \tag{1.2.3.1}$$

If this condition is satisfied $\forall t_i$, t_j, then $\hat{A}$ is a *continuous QND observable*. If it is satisfied only at special times, then $\hat{A}$ is called *stroboscopic QND observable*.
An observable which is conserved under free evolution:

$$\frac{\mathrm{d}\hat{A}}{\mathrm{d}t} = -\frac{i}{\hbar}\left[\mathcal{H}_\mathcal{S}, \hat{A}\right] = 0 \tag{1.2.3.2}$$

where $\mathcal{H}_\mathcal{S}$ is the system Hamiltonian, is automatically a continuous QND variable, because it satisfies Eq. (1.2.3.1) $\forall t_i, t_j$.

One application for QND measurements is monitoring an observable. For instance, let us monitor the QND observable $\hat{A}$ through a sequence of perfect QND measurements at times t_0, t_1, t_2, … Since all $\hat{A}(t_i)$ commute, we can prepare the system at time t_0 in the state $|\psi_0\rangle$ which is a simultaneous eigenstate of the observables $\left\{\hat{A}(t_i)\right\}$. From the results of this first measurement at t_0, we can compute all the eigenvalues $\left\{\hat{A}(t_i)\right\}$. Then, if the system evolves freely (i.e. following its free Hamiltonian $\mathcal{H}_\mathcal{S}$) the measured eigenvalues will be the computed one. Instead, if the system is perturbed, this will change the eigenvalues, allowing for a detection of such perturbation.

1.2.4 Weak measurements and weak values

So far, the measurements that we have described have one element in common: the state collapses after the measurement. For this reason, they are usually called *strong* or *sharp* measurements. It is, however, possible to generalize them into a new type of measurements, which do not cause the state of the system to collapse after the measurements, at the price of obtaining less information about the system.

These measurements are called *weak measurements*[53, 56].

Definition

In order to realize a weak measurement one has to:

1. weakly couple the system and the measurement apparatus;

2. perform a strong measurement on the pointer. The collapsed state of the measurement apparatus is the result of the weak measurement.

A measurement is considered weak if the standard deviation of the result is larger than the difference between the eigenvalues of the observable that we want to measure.

Weak measurements in the indirect measurement protocol

As per section 1.2.2, the initial state $\hat{\tau}_0 = \hat{\sigma}_0 \otimes \hat{\mu}_0$ is the direct product of the initial density operator of the system and the meter, i.e., respectively, $\hat{\sigma}_0$ and $\hat{\mu}_0 = \left| m^{(0)} \right\rangle\!\!\left\langle m^{(0)} \right|$. After the interaction $\hat{U}$, the total system is in the state $\hat{\tau}_1 = \hat{U}\hat{\tau}_0\hat{U}^\dagger$. For weak measurements, we assume that the interaction is described as in the von Neumann protocol (sec. 1.2.2):

$$\hat{U} = \exp\left(-\frac{i}{\hbar}g\hat{S} \otimes \hat{P}\right) \tag{1.2.4.1}$$

with g being the effective coupling constant between the measurand observable $\hat{S}$ and the variable $\hat{P}$ canonically conjugated to the pointer $\hat{Q}$. In contrast with the von Neumann protocol, $\hat{P}$ and $\hat{Q}$ are assumed to be generic operators.

For *weak coupling* $(g \to 0)$, we can expand the exponential:

$$\hat{U} = \exp\left(-\frac{i}{\hbar}\hat{\xi}\right) = \mathbb{1} - \frac{i}{\hbar}\hat{\xi} - \frac{1}{2\hbar^2}\hat{\xi}^2 + \mathcal{O}(\hat{\xi}^3) \tag{1.2.4.2}$$

where $\hat{\xi} = g\hat{S} \otimes \hat{P}$. Therefore:

$$\begin{aligned}
\hat{\tau}_1 = \hat{U}\hat{\tau}_0\hat{U}^\dagger &\approx \left(\mathbb{1} - \frac{i}{\hbar}\hat{\xi} - \frac{1}{2\hbar^2}\hat{\xi}^2\right)\hat{\tau}_0\left(\mathbb{1} + \frac{i}{\hbar}\hat{\xi} - \frac{1}{2\hbar^2}\hat{\xi}^2\right) \\
&\approx \hat{\tau}_0 + \frac{i}{\hbar}\left[\hat{\tau}_0, \hat{\xi}\right] - \frac{1}{2\hbar^2}\left(\hat{\xi}^2\hat{\tau}_0 + \hat{\tau}_0\hat{\xi}^2 - 2\hat{\xi}\hat{\tau}_0\hat{\xi}\right) \\
&= \hat{\tau}_0 + \frac{i}{\hbar}\left[\hat{\tau}_0, \hat{\xi}\right] - \frac{1}{2\hbar^2}\left[\left[\hat{\tau}_0, \hat{\xi}\right], \hat{\xi}\right]
\end{aligned} \tag{1.2.4.3}$$

Using the following simplifying assumptions

$$\langle \hat{P} \rangle_0 = \text{Tr}_{\mathcal{M}} \left(\hat{\mu}_0 \hat{P} \right) = 0 \tag{1.2.4.4}$$

$$\langle \hat{P}^2 \rangle_0 = \text{Tr}_{\mathcal{M}} \left(\hat{\mu}_0 \hat{P}^2 \right) \neq 0 \tag{1.2.4.5}$$

the system density operator becomes

$$\hat{\sigma}_1 = \text{Tr}_{\mathcal{M}} \, \hat{\tau}_1 \approx \hat{\sigma}_0 - \frac{1}{2\hbar^2} g^2 \, \langle \hat{P}^2 \rangle_0 \left[\left[\hat{\sigma}_0, \hat{S} \right], \hat{S} \right] \tag{1.2.4.6}$$

with elements

$$\langle s_i | \hat{\sigma}_1 | s_j \rangle \approx \langle s_i | \hat{\sigma}_0 | s_j \rangle \left[1 - \frac{1}{2\hbar} g^2 \, \langle \hat{P}^2 \rangle_0 \, (s_i - s_j)^2 \right] \tag{1.2.4.7}$$

so, the correction to the initial density matrix is of the second order in the interaction strength g. A direct comparison with Eq. (1.2.2.6) shows that:

$$\left\langle m^{(i)} \middle| m^{(j)} \right\rangle \approx 1 - \frac{1}{2\hbar} g^2 \, \langle \hat{P}^2 \rangle_0 \, (s_i - s_j)^2 \tag{1.2.4.8}$$

This means that there is a superposition of the meter states in weak measurements, therefore weak measurements are not able to efficiently distinguish the eigenvalues s_i.

The meter final state is, in the same approximation:

$$\hat{\mu}_1 = \text{Tr}_{\mathcal{S}}(\hat{\tau}_1) \approx \hat{\mu}_0 + \frac{i}{\hbar} g \, \langle \hat{S} \rangle_0 \left[\hat{\mu}_0, \hat{P} \right] - \frac{1}{2\hbar} g^2 \, \langle \hat{S} \rangle_0 \left[\left[\hat{\mu}_0, \hat{P} \right], \hat{P} \right] \tag{1.2.4.9}$$

After the measurement, the mean value of the pointer $\hat{Q}$, assuming $\langle \hat{Q} \rangle_0 = 0$, will be

$$\langle \hat{Q} \rangle_1 = g \, \langle \hat{S} \rangle_0 + \mathcal{O}(g^2) \tag{1.2.4.10}$$

This kind of relationship between mean values of system and pointer is typical of weak measurements[53].

Weak measurements in the von Neumann protocol

Weak measurements are a natural extension of the von Neumann protocol modelling strong measurements. In fact, all the results in sec. 1.2.2 are general and still hold for the weak measurements case.

Remember that, in the von Neumann protocol, we want to measure the pointer which is associated to a continuous observable $\hat{Q}$ and states $|q\rangle$ in a continuous Hilbert space $\mathcal{H}_{\mathcal{M}}$. By assuming that $\langle Q \rangle_0$ vanishes for the initial state and that

the initial state is normally distributed around $q = 0$, we get the initial wave-function of the pointer:

$$\varphi_0(q) = \left[\frac{1}{\sqrt{2\pi\sigma^2}} \exp\left(-\frac{q^2}{2\sigma^2}\right) \right]^{\frac{1}{2}} \tag{1.2.4.11}$$

Then, by assuming $H_{int} = \gamma \hat{S} \otimes \hat{P}$, the initial wave-function is transformed into a superposition of states $\varphi_i(q)$:

$$\varphi_i(q) = \varphi_0(q - gs_i) \tag{1.2.4.12}$$

which are translations of the initial state by the quantity gs_i.

In order for the measurement to weak, the standard deviation σ of the wave-functions φ_i must be much greater than the distance $g\Delta s_i$ between the eigenvalues. In this way, there will be an overlap between the wave-functions and the greater the variance, the greater the overlap. In contrast, a small variance completely separates the wave-functions, generating strong measurements. For this reason, it is possible to see the weak measurements as a generalization of the strong measurements.

Weak values: definition and applications

A new property of the system called *weak value*[57] emerges if we post-select the system after a weak interaction.
Let $\hat{S}$ be an Hermitian operator on the system $\mathcal{S}$ and let $|s\rangle$ and $|f\rangle$ be two states on the Hilbert space $\mathcal{H}_{\mathcal{S}}$ of the system. Let $\left|m^{(0)}\right\rangle$ be the initial state of the meter. Let us suppose to perform a weak measurement on a particle on the state $|s\rangle$ by using the interaction Hamiltonian $\hat{H}_{int} = \gamma \hat{S} \otimes \hat{P}$. Then, we post-select the final state of the system $|f\rangle$. The amplitude of obtaining the outcome $|f\rangle$ is

$$\langle f | \hat{U} | s \rangle \tag{1.2.4.13}$$

with $\hat{U} = \exp\left(-\frac{i}{\hbar} \int dt \hat{H}_{int}\right)$. The post-selection only selects particles which are in the state $|f\rangle$ after the interaction, therefore it can be modelled as a set of two projections:

$$\begin{aligned} \hat{\mathbb{P}}_0 &= |f\rangle\langle f| \otimes \mathbb{1}_{\mathcal{M}} \\ \hat{\mathbb{P}}_1 &= \sum_{i \neq 0} |f_i\rangle\langle f_i| \otimes \mathbb{1}_{\mathcal{M}} \end{aligned} \tag{1.2.4.14}$$

where $\{|f_i\rangle\}$ is a basis of $\mathcal{H}_{\mathcal{S}}$ and $|f\rangle = |f_0\rangle$. If we only consider the outcome 0, the state after the pre-selection, weak interaction and post-selection chain is

$$|f\rangle\langle f| \exp\left(-\frac{i}{\hbar} g \hat{S} \otimes \hat{P}\right) |s\rangle \otimes \left|m^{(0)}\right\rangle \tag{1.2.4.15}$$

which can be approximated, for $\frac{g}{\sigma} \ll 1$, to:

$$
\begin{aligned}
&|f\rangle\langle f| \exp\left(-\frac{i}{\hbar}g\hat{S}\otimes\hat{P}\right)|s\rangle \otimes \left|m^{(0)}\right\rangle \\
&\approx |f\rangle\langle f|\left(\mathbb{1}-\frac{i}{\hbar}g\hat{S}\otimes\hat{P}\right)|s\rangle \otimes \left|m^{(0)}\right\rangle \\
&\approx |f\rangle\,\langle f|s\rangle\left(1-\frac{i}{\hbar}g\,\langle\hat{S}\rangle_w\,\hat{P}\right)\left|m^{(0)}\right\rangle \\
&\approx |f\rangle\,\langle f|s\rangle\exp\left(-\frac{i}{\hbar}g\,\langle\hat{S}\rangle_w\,\hat{P}\right)\left|m^{(0)}\right\rangle
\end{aligned}
\tag{1.2.4.16}
$$

where

$$
\langle\hat{S}\rangle_w = \frac{\langle f|\hat{S}|s\rangle}{\langle f|s\rangle}
\tag{1.2.4.17}
$$

is the *weak value* of S. It is easy to see that the weak value is not bounded to the eigenvalues spectrum. Values outside the eigenvalues spectrum are called *anomalous*.

The meter wavefunction, which was centred around $q = 0$, has evolved into

$$
\varphi_f = \left\langle q\middle|m^{(f)}\right\rangle = \varphi_0\left(q - g\,\langle\hat{S}\rangle_w\right)
\tag{1.2.4.18}
$$

The weak value is a measurable property of the system and its nature has been largely debated (see [53, 56, 58, 59, 60, 61, 62, 63, 64, 65] and many others). For instance, some pondered whether weak values are a statistical artefact[60, 65], while others demonstrated a deep connection with contextuality [62, 63]. Nevertheless, several practical application of weak values have been discovered, as we will see in the following sections.

Properties

Unbounded If we use post-selection, it is easy to see that the pointer distribution could be centred onto a value very far from any of the eigenvalues of $\hat{A}$. For instance, take two qubits:

$$
\begin{aligned}
|s\rangle &= \cos(\theta)\,|H\rangle + \sin(\theta)\,|V\rangle \\
|f\rangle &= \cos(\varphi)\,|H\rangle + \sin(\varphi)\,|V\rangle
\end{aligned}
\tag{1.2.4.19}
$$

for pre- and post-selection. The measurand is the polarization:

$$
\hat{S} = |H\rangle\langle H| - |V\rangle\langle V|
\tag{1.2.4.20}
$$

It is easy to see that:

$$
\langle S\rangle_w = \frac{\cos(\theta + \varphi)}{\cos(\theta - \varphi)}
\tag{1.2.4.21}
$$

31

with

$$\langle f|s \rangle = \cos(\theta - \varphi) \tag{1.2.4.22}$$

The weak value is not bounded between -1 and 1, but it can go way beyond. For instance, take $\theta = -0.41$ rad and $\varphi = 1.16$ rad. For such angles, $\langle S \rangle_w \approx 420$ and it is possible to go even further! This amplification is due to the fact that the more the two states are orthogonal, the smaller will be their inner product and, therefore, the larger will be the weak value. However, a smaller $\langle f|s \rangle$ also implies a smaller probability of success for the post-selection ($p(f|s) = |\langle f|s \rangle|^2$). In our example, $p \approx 3 * 10^{-6}$.
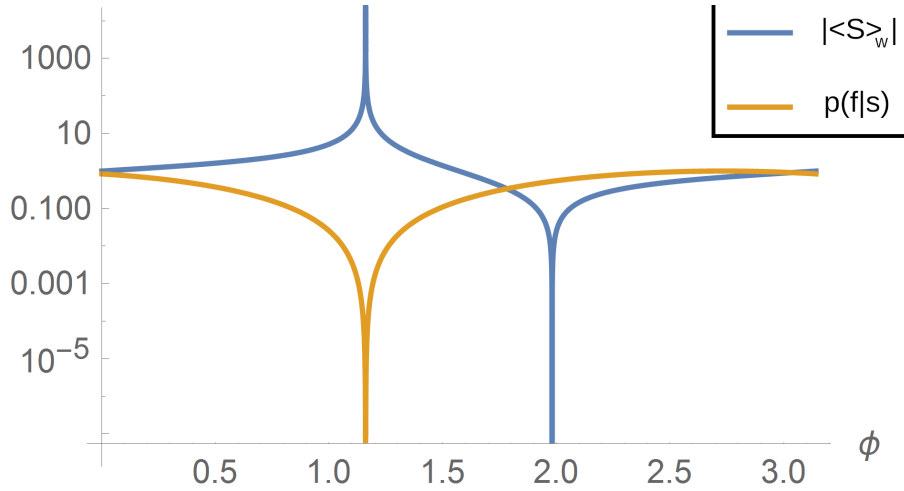
Figure 1.2: Values of $|\langle S \rangle_w|$ and the probability of success of the post-selection $p(f|s)$ as a function of φ for a fixed $\theta = -0.41 rad$. The weak value and the probability of success peak at the same angle φ.

Complex weak values   The weak value $\langle S \rangle_w$ could assume complex values. It is easy to show[66] that the real part of the weak value shifts the expectation value of the pointer position $\hat{Q}$, whereas the imaginary part shifts the expectation value of its momentum $\hat{P}$.

Applications

Signal amplification   As we have seen (sec. 1.2.4), it is possible to obtain an arbitrarily large weak value $|\langle \hat{S} \rangle_w|$ by choosing a $|f\rangle$ quasi-orthogonal to $|s\rangle$. Therefore, it is possible to use weak values to amplify small signals through Eq. (1.2.4.18). Such amplification has been first implemented in an experiment by Hosten and Kwiat[67], who managed to measure distances of the order of one tenth

of a nanometre thanks to a four orders of magnitude amplification. Subsequent experiments demonstrated the ability to measure down to 400 frad of deflection[68] and showed gains in the signal-to-noise ratio (SNR), thanks to the robustness of the amplification techniques with respect to various technical noise sources[69, 70, 71, 72, 73, 74]. Yet, the cost of such amplifications is a reduced data acquisition rate, due to the low success probability of the post-selection in high amplification regimes (e.g. Fig. 1.2). Thus, an important metrological question is whether the amplification effect can overcome the corresponding low post-selection success probability to provide an estimation at a precision surpassing optimal techniques (i.e. techniques that reach the ultimate bound on uncertainty provided by the quantum Cramér-Rao bound, see Sec. 1.4).

It can, indeed, be showed[75, 76, 77, 78, 79, 80] that, with the same amount of initial resources, the amplification effect does not carry an higher precision with respect to conventional techniques. Nevertheless, this also means that, in spite of lower collection rate, due to the post-selection, parameter estimation in amplification techniques shows similar sensitivity to optimal estimation methods with the same amount of initial resources.

As we have seen, then, the amplification technique has two important properties:

- an equivalent sensitivity to optimal estimation methods, in spite of the losses due to the post-selection;

- robustness with respect to technical noise.

The first property can be exploited, for instance, by recycling techniques[81, 82], in which the "discarded" outcomes of the post-selection are, instead, recycled and reused. Thanks to the virtual increase of the initial resources induced by the recycling, such techniques show an higher measurement precision with respect to classical and non-recycling weak values techniques[83]. The second property, instead, allows us to amplify the signal without amplifying certain types of unrelated technical noise backgrounds. Thus, both properties are of great metrological interest and can even be combined in order to achieve an high precision even with relatively modest laboratory equipment[84].

Direct measurement of the wave-function   Weak values allow performing a direct measurement of the wave-function[85]. Up until the introduction of weak values, such measurement was believed to be impossible, and the wave-function was only obtainable via indirect procedures (such as tomography).
Let us suppose that we want to measure the spatial wave-function $\psi(x) = \langle x|s \rangle$ for the state $|s\rangle$. Let $\hat{S}$ be the projector $\hat{\mathbb{P}}_x = |x\rangle\langle x|$ and we post-select on a momentum

eigenstate $|p\rangle$. Then

$$\langle \hat{S} \rangle_w = \langle \hat{\mathbb{P}}_x \rangle_w = \frac{\langle p|x \rangle \langle x|s \rangle}{\langle p|s \rangle} = \frac{\exp\left(\frac{i}{\hbar}px\right)\psi(x)}{\tilde{\psi}(p)} \qquad (1.2.4.23)$$

where $\tilde{\psi}(p)$ is the momentum wave-function. If $p = 0$:

$$\psi(x) = k \langle \hat{\mathbb{P}}_x \rangle_w \qquad (1.2.4.24)$$

where k can be obtained via normalization.

Measurement of non-commuting observables   In some cases, weak values allow us to perform measurements on two non-commuting observables[86, 87, 88, 89]. To understand how this is possible, let us star by define joint e sequential measurements of weak values.

Take two observables $\hat{A}$ and $\hat{B}$. To measure their weak value, we realize two different couplings g_x and g_y with two different momentums $\hat{P}_x$ and $\hat{P}_y$. The weak values are defined as $\langle \hat{X} \rangle = g_x \langle \hat{A} \rangle_w$ and $\langle \hat{Y} \rangle = g_y \langle \hat{B} \rangle_w$. Now we can distinguish between two cases:

- joint weak measurements
  Joint measurements allow us to realize the measurement of two observables on two entangled particles at the same time. In this case, by measuring the covariance of the pointers X and Y, we obtain

  $$\langle \hat{X}\hat{Y} \rangle = \frac{1}{4}g_x g_y Re\left[\langle \hat{A}\hat{B} + \hat{B}\hat{A} \rangle_w + 2\langle \hat{A} \rangle_w^* \langle \hat{B} \rangle_w\right] \qquad (1.2.4.25)$$

  where $\langle \hat{A}\hat{B} + \hat{B}\hat{A} \rangle_w$ is the *joint weak value.*

- sequential weak measurements
  In a sequential measurement, a first measurement of an observable A is followed by a second measurement of an observable B and so on. Limiting us to two measurements and using the interactions described for joint measurements, we can reach a similar result:

  $$\langle \hat{X}\hat{Y} \rangle = \frac{1}{2}g_x g_y Re\left[\langle \hat{A}\hat{B} \rangle_w + \langle \hat{A} \rangle_w^* \langle \hat{B} \rangle_w\right] \qquad (1.2.4.26)$$

  where $\langle \hat{A}\hat{B} \rangle_w$ is the *sequential weak value.*

Therefore, the real part of the sequential ($Re\left[\langle \hat{A}\hat{B} \rangle_w\right]$) or joint ($Re\left[\langle \hat{A}\hat{B} + \hat{B}\hat{A} \rangle_w\right]$) weak values of two non-commuting ensembles can be evaluated by measuring $\langle \hat{X}\hat{Y} \rangle$ and from the independent extraction of the weak values $\langle \hat{A} \rangle_w$ and $\langle \hat{B} \rangle_w$.

1.3 Parameters to characterize entanglement and discord

In Sec. 1.1.1 and 1.1.2 we discussed the importance of entanglement in modern quantum technologies. In quantum communication, for instance, only a maximally entangled state can teleport a qubit. Non-maximally entangled states, however, can still provide an asymptotically faithful teleportation at some rate, provided that sender and receiver share many copies of the same entangled state. This is possible thanks to a protocol called *entanglement distillation*[17, 90], which allows "distilling" maximally entangled pairs from multiple copies of non-maximally entangled ones. In order to find out how many copies are needed it is, then, important to characterize the amount of entanglement in those states[90, 91]. To do so, one may reconstruct the physical state via a process called quantum state tomography[92], but that requires a lot of measurements, especially for higher dimensions. For this reason, many methods have been implemented, such as Bell tests[22], visibility experiments[93], parameters which estimate the entanglement[17], etc. In this section, we focus on such parameters, explaining first the characteristics that they should have and, then, introducing the parameters that we will use in the rest of the thesis. For simplicity, we will restrict ourselves to the bipartite case $\hat{\rho} = \hat{\rho}_{AB}$.

1.3.1 Properties of an entanglement measure

Many of the first measures of entanglement (such as those in [90, 91]) arose from optimization of some protocols. However, any function of the quantum state can be an entanglement measure, provided that it possesses two properties[17]:

- monotonicity

- vanishing on separable states.

Let us describe them in detail.

Monotonicity

The first, and most important, property is the monotonicity under LOCC (Local Operations and Classical Communication) operations, i.e. local operations on both photons with possible classical communication[91, 94]. Mathematically, the monotonicity property can be formulated as follows:

For any LOCC operation $P(\hat{\rho})$ and function $E(\hat{\rho})$ of the quantum state:

$$E(P(\hat{\rho})) \leq E(\hat{\rho}) \tag{1.3.1.1}$$

This means that *entanglement cannot increase under local operations and classical communication.*

Vanishing on separable states

Entanglement vanishes on separable states. This means that a function of the quantum state $E(\hat{\rho})$ can be considered a valid parameter to characterize the entanglement if $E(\hat{\rho}_{sep}) = 0$ for any separable state $\hat{\rho}_{sep}$.

Since every separable state can be converted to any other separable state by LOCC, it can be showed[95] that any function E possessing the monotonicity property is constant on separable states. This also ensures that E must be minimal on separable states, because any separable state can be obtained by LOCC from any other state. Thus, in order to have this property, we only need to set this constant to zero.

Notice also that these two properties, combined, impose E to be a *non-negative* function[17].

Other properties

While the two properties above are the only two required for entanglement measures, there are many others which can be useful. Here is a brief overview of the principal ones.

Normalization   The normalization property requires that the entanglement measure returns, for maximally entangled states, the number of entangled pairs. In our simple case of bipartite entanglement:

$$E(\hat{\rho}_{ent}) = 1 \qquad\qquad (1.3.1.2)$$

This property can only be applied to entangled pairs or states consisting of several entangled pairs, and it cannot be generalized to multipartite entangled states, due to the non-existence of a maximally entangled state in that case[17].

Asymptotic continuity   It is possible to introduce some sort of continuity for the parameter function. This takes the form[95, 96, 97]

$$\|\hat{\rho} - \hat{\sigma}\|_1 \to 0 \implies |E(\hat{\alpha}) - E(\hat{\sigma})| \to 0 \qquad\qquad (1.3.1.3)$$

for states $\hat{\rho}$ and $\hat{\sigma}$ acting on the same Hilbert space and $\|X\|_1 = \mathrm{Tr}\,|X| = \mathrm{Tr}\,\sqrt{X^\dagger X}$ being the 1-norm. This property is useful in estimating transition rates[17].

Convexity Finally, convexity is a property displayed by many entanglement measures, e.g. entanglement of formation and negativity[17]. It can be expressed as

$$E\left(\sum_i p_i \hat{\rho}_i\right) \leq \sum_i p_i E(\hat{\rho}_i) \tag{1.3.1.4}$$

We can now introduce some specific entanglement measures. We focus on *entanglement of formation*, *concurrence*, *negativity* and *log-negativity*, four simple parameters with different characteristics. Then, for what concerns the Quantum Discord estimation, we introduce the Quantum Geometric Discord, not qualified as an entanglement measure since it is not monotone with entanglement.

1.3.2 Entanglement of formation

One of the most basic entanglement measures is the entanglement of formation E_F, which quantifies the resources needed to create a given entangled state[91]. For a pure state $|\psi\rangle$ of a pair of subsystems A and B, the entanglement of formation is defined as

$$E_F(|\psi\rangle) = S\left(\mathrm{Tr}_A\left[|\psi\rangle\langle\psi|\right]\right) = S\left(\mathrm{Tr}_B\left[|\psi\rangle\langle\psi|\right]\right) \tag{1.3.2.1}$$

being S the von Neumann entropy (Eq. (1.1.1.34)). This can be extended to mixtures of entangled states according to

$$E_F(\hat{\rho}) = \min \sum_i \mu_i E\left(|\psi_i\rangle\langle\psi_i|\right) \tag{1.3.2.2}$$

taking the minimum over all possible decompositions

$$\hat{\rho} = \sum_i \mu_i |\psi_i\rangle\langle\psi_i| \tag{1.3.2.3}$$

The entanglement of formation is an entanglement monotone and vanishes for separable states. Thus, it is a valid entanglement measure. E_F also has the following properties:

- E_F is normalized;

- E_F is a convex function of $\hat{\rho}$.

The importance of the entanglement of formation comes from the fact that it provides an upper bound for distillable entanglement[91], i.e. the maximal number of maximally entangled states per copy that can be distilled from many copies of a given state $\hat{\rho}$ by using LOCC operations. However, it is difficult to evaluate this quantity, in general, for mixtures of entangled states. The search for an explicit form led to the introduction of another parameter for the specific case of two-qubit states: the Concurrence[98].

1.3.3 Concurrence

Concurrence[98, 99, 100, 101, 102] is a scalar function which quantifies the amount of entanglement in the density matrix $\hat{\rho}$ of a bipartite system, and is defined as:

$$\mathcal{C}(\hat{\rho}) = \max\left(0, \lambda_1 - \lambda_2 - \lambda_3 - \lambda_4\right) \tag{1.3.3.1}$$

being λ_i the eigenvalues of the hermitian matrix

$$\hat{R} = \sqrt{\sqrt{\hat{\rho}}\tilde{\rho}\sqrt{\hat{\rho}}} \tag{1.3.3.2}$$

in descending order, where

$$\tilde{\rho} = (\hat{\sigma}_y \otimes \hat{\sigma}_y)\hat{\rho}^*(\hat{\sigma}_y \otimes \hat{\sigma}_y) \tag{1.3.3.3}$$

and $\hat{\sigma}_y$ is the Pauli matrix $\begin{pmatrix} 0 & -i \\ i & 0 \end{pmatrix}$.

Concurrence is monotone in the entanglement and vanishes for separable states hence it is a valid entanglement measure. Furthermore, it has the following properties:

- $\mathcal{C}$ is normalized;

- $\mathcal{C}$ is a convex function of $\hat{\rho}$.

Its importance stems from the fact that it allows calculating the entanglement of formation for any two-qubits state as[98]

$$E_F(\hat{\rho}) = H'\left(\frac{1 + \sqrt{1 - \mathcal{C}^2(\hat{\rho})}}{2}\right) \tag{1.3.3.4}$$

with

$$H'(x) = -x\log_2 x - (1-x)\log_2(1-x) \tag{1.3.3.5}$$

being the binary entropy.

1.3.4 Negativity

Negativity[101, 103] is defined as

$$\mathcal{N}(\hat{\rho}) = \frac{\left\|\hat{\rho}^{T_A}\right\|_1 - 1}{2} \tag{1.3.4.1}$$

where $\hat{\rho}^{T_A}$ is the partial transpose[104] of $\hat{\rho}$ with respect to A.
An equivalent definition is

$$\mathcal{N}(\hat{\rho}) = \sum_i \frac{|\lambda_i| - \lambda_i}{2} \tag{1.3.4.2}$$

where λ_i are the eigenvalues of $\hat{\rho}^{T_A}$.

Negativity is monotone in the entanglement and vanishes for separable states and, thus, it qualifies as an entanglement measure. Furthermore, Negativity has the following properties:

- $\mathcal{N}$ is normalized;

- $\mathcal{N}$ is a convex function of $\hat{\rho}$.

As it only involves a trace norm and partial transpose, the negativity is an easy to compute entanglement measure, in contrast with Concurrence and entanglement of formation, which require to compute an optimization. Its importance, however, comes from the fact that it bounds the extent to which a single copy of the state $\hat{\rho}$ can be exploited for quantum teleportation[103].

1.3.5 Log-Negativity

A possible definition for the Log-Negativity is

$$\mathcal{L}(\hat{\rho}) = \log_2 \left\| \hat{\rho}^{T_A} \right\|_1 \tag{1.3.5.1}$$

which is closely related to the Negativity

$$\mathcal{L}(\hat{\rho}) = \log_2(2\mathcal{N}(\hat{\rho}) + 1) \tag{1.3.5.2}$$

As per the Negativity, Log-Negativity[103] is monotone in the entanglement and vanishes for separable states. It also retains the normalization property.

As per E_F, Log-Negativity bounds the the amount of distillable entanglement contained in the state $\hat{\rho}$[17].

1.3.6 Quantum Geometric Discord

We have previously (Sec. 1.1.1) introduced Quantum Discord as a measure of non-classical correlations in a multipartite quantum system, including correlations which are due to quantum effects not related to entanglement. Such definition, however, is difficult to compute, a task that has been shown to be an NP-complete problem[105]. Therefore, we introduce a geometrical approximation called Quantum Geometric Discord (QGD)[106], which is defined as the minimum distance between the state $\hat{\rho}$ and the closest zero-Discord state $\hat{\chi}$.

$$\mathcal{GD}_A^{(2)}(\hat{\rho}) = \min_{\hat{\chi} \in \Omega_0} \text{Tr} \left(\hat{\rho} - \hat{\chi} \right)^2 \tag{1.3.6.1}$$

where Ω_0 is the set of zero-discord states.

The QGD has the following properties:

- $\mathcal{GD}$ is non-negative;

- $\mathcal{GD}$ reaches zero for classically correlated states.

Anyway, unlike our previous parameters, it is not monotone in the entanglement (exactly like quantum discord), hence it cannot be used as an entanglement measure.

1.4   Quantum parameter estimation

The goal of the estimation theory[107] is to determine a fixed unknown parameter θ (the *estimand*), which characterizes the population of measured data X through a probability density function (PDF) $f(x|\theta)$. We call *estimator* the function $\hat{\theta}(X)$ which estimates the value of the parameter θ from the measured data X. Since X can be described as a random variable, the same holds for the estimator $\hat{\theta}$. Estimators are not, in general, invariant under a parameter transformation[108].

A good estimator should be:

- consistent: $\forall \varepsilon > 0, \lim_{n \to \infty} p\left(\left|\hat{\theta} - \theta\right| > \varepsilon\right) = 0$ meaning that, by increasing the number of measurements n, the estimator converges to the estimand.

- robust: not too much sensitive to deviations of the actual PDF from the theoretically-expected one.

- efficient: smallest possible uncertainty associated with the estimated value.

We must pay a bit of attention to the uncertainty: the variance is defined around the mean value and, therefore, is of little use for biased estimators, i.e. estimators with average not equal to the estimand. In its stead, it is useful to introduce the *mean square error* (MSE):

$$MSE(\hat{\theta}) = E(\hat{\theta} - \theta)^2 = Var(\hat{\theta}) + b^2(\hat{\theta}, \theta) \tag{1.4.0.1}$$

where $Var(\hat{\theta})$ is the variance of $\hat{\theta}$ and $b(\hat{\theta}, \theta) = E(\hat{\theta}) - \theta$ is the bias of the estimator $\hat{\theta}$ ($E(\cdot)$ denotes the statistical average). Being defined on the random variable $(\hat{\theta} - \theta)$, the MSE takes into account the bias and allows a comparison among the estimators. An estimator is said to be more efficient than another if it has a lower MSE. It is useful, then, to introduce the *relative efficiency* of $\hat{\theta}_1$ with respect to $\hat{\theta}_2$ for the same number of measurements, defined as:

$$eff(\hat{\theta}_1|\hat{\theta}_2) = \frac{\frac{1}{MSE(\hat{\theta}_2)}}{\frac{1}{MSE(\hat{\theta}_2)}} = \frac{MSE(\hat{\theta}_2)}{MSE(\hat{\theta}_1)} \begin{cases} > 1 & \hat{\theta}_1 \text{ is more efficient} \\ = 1 & \text{same efficiency} \\ < 1 & \hat{\theta}_2 \text{ is more efficient} \end{cases} \tag{1.4.0.2}$$

The search for the most efficient estimator, i.e. the one which minimizes the MSE, can be carried out in two different ways. The first - and most common - one is the unbiased parameter estimation, which focuses on estimators without bias ($b(\hat{\theta}, \theta) = 0$), optimizing the variance (equal to the MSE in this case) to reach the lowest MSE. The other method, called biased parameter estimation, optimizes both the bias and the variance in order to achieve the least possible MSE. For simplicity, in the following sections, we introduce both methods for the single parameter case.

1.4.1 Unbiased parameter estimation

Unbiased parameter estimation focuses on estimators whose average converges to the estimand θ without any bias. In this case, the MSE is equal to the variance, which has a lower limit given by the Cramér-Rao bound[109, 110] (CRB). It is useful to introduce them in the classical form first.

Classical case: Fisher Information and Cramér-Rao bound

The Cramér-Rao bound expresses a lower bound on the variance of *unbiased* estimators for a certain parameter. For a generic parameter θ and n measurements of X, it is defined as:

$$Var(\hat{\theta}) \geq \frac{1}{nI(\theta)} \tag{1.4.1.1}$$

meaning that the variance of an estimator of parameter θ cannot go below the reciprocal of the product of the number of measurements n and the *Fisher Information*[111] $I(\theta)$, which, in turn, is defined as:

$$I(\theta) = \int dx f(x|\theta) \left(\frac{\partial \ln f(x|\theta)}{\partial \theta}\right)^2 = \int dx \frac{1}{f(x|\theta)} \left(\frac{\partial f(x|\theta)}{\partial \theta}\right)^2 \tag{1.4.1.2}$$

and measures the amount of information that an observable random variable X carries about the unknown parameter θ upon which the probability of X depends following the PDF $f(x|\theta)$ (usually called *likelihood function*). Thus, we can see the Fisher information as the curvature of $\log f(x|\theta)$, often called *log-likelihood function*. An high (low) Fisher information therefore indicates that its maximum is sharp (shallow) with respect to variations of θ. This provides an intuitive interpretation of the Fisher information, which increases when the likelihood is more sharply distributed around θ.

The Cramér-Rao bound allows us to improve our definition of efficiency, by directly comparing the variance of the unbiased estimator $\hat{\theta}$ to the bound: $eff(\hat{\theta}) = \frac{I^{-1}(\theta)}{Var(\hat{\theta})}$. Thus, the most efficient estimator is the one which saturates the bound and

has unitary efficiency. This estimator is said to be *efficient* or *optimal* and it is often dubbed as *minimal variance unbiased* (MVU) estimator. The CRB, however, does not provide a method to obtain the optimal estimator, nor a guarantee that it exists. Nevertheless, the CRB guarantees that if an optimal estimator exists, it is unique.

One method to achieve the optimal estimator is called maximum likelihood method[112], which searches for the parameter which maximizes the likelihood function over the parameter space. For particular statistical models and choices of parametrization, this method is known to provide an asymptotically efficient estimator[112, 113, 114].

Quantum case

In order to extend the Fisher Information and the Cramér-Rao bound to the quantum case, the statistical model of our system becomes an ensemble of quantum states ρ_θ (we drop the hat from the density operator in order to avoid any confusion) which depends on a parameter θ. The parameter θ is not, in general, a quantum observable, and our aim is to estimate it through the measurement of some observable on ρ_θ. The estimator $\hat{\theta}$ is a self-adjoint operator, which describes a quantum measurement followed by classical data processing.

Quantum Fisher Information In order to extract the Fisher Information in this new case, we need to obtain the PDF and introduce a new operator[114]. We can obtain the PDF by defining the measurement as an element of a POVM set $\{E_x\}$ such that $\int_x E_x = \mathbb{1}$, this way, $f(x|\theta) = \text{Tr}\,(E_x\theta)$. The next step is the introduction of the *Symmetric Logarithmic Derivative* (SLD) L_θ as the self-adjoint operator satisfying

$$\frac{L_\theta\rho_\theta + \rho_\theta L_\theta}{2} = \frac{\partial\rho_\theta}{\partial\theta} \tag{1.4.1.3}$$

from which follows $\partial_\theta f(x|\theta) = \text{Tr}\,(\partial_\theta\rho_\theta E_x) = \text{Re}\,[\text{Tr}\,(\rho_\theta E_x L_\theta)]$. The Fisher Information is then rewritten as[114]

$$I(\theta) = \int dx \frac{\text{Re}\,[\text{Tr}\,(\rho_\theta E_x L_\theta)]^2}{\text{Tr}\,(\rho_\theta E_x)} \tag{1.4.1.4}$$

This formula establishes the precision classical bound for a fixed quantum measurement (POVM element). However, in order to calculate the ultimate bound on precision, we have to maximize the Fisher Information over the possible quantum

measurements[114]:

$$
\begin{aligned}
I(\theta) &\leq \int dx \left| \frac{\text{Tr}\left(\rho_\theta E_x L_\theta\right)}{\sqrt{\text{Tr}\left(\rho_\theta E_x\right)}} \right|^2 \\
&= \int dx \left| \text{Tr}\left[\frac{\sqrt{\rho_\theta}\sqrt{E_x}}{\sqrt{\text{Tr}\left(\rho_\theta E_x\right)}} \sqrt{E_x} L_\theta \sqrt{\rho_\theta} \right] \right|^2 \\
&\leq \int dx \, \text{Tr}\left(E_x L_\theta \rho_\theta L_\theta\right) \\
&= \text{Tr}\left(L_\theta \rho_\theta L_\theta\right) \\
&= \text{Tr}\left(\rho_\theta L_\theta^2\right)
\end{aligned}
\tag{1.4.1.5}
$$

Thus, the Fisher Information $I(\theta)$ of any quantum measurement is upper-bounded by the so-called *Quantum Fisher Information $H(\theta)$*:

$$
I(\theta) \leq H(\theta) = \text{Tr}\left(\rho_\theta L_\theta^2\right)
\tag{1.4.1.6}
$$

Quantum Cramér-Rao bound   The Quantum Fisher Information allows defining the *Quantum Cramér-Rao bound*

$$
Var(\theta) \geq \frac{1}{nH(\theta)}
\tag{1.4.1.7}
$$

which provides a more general uncertainty bound, because it does not depend on the measurement, nor on the geometrical structure of the model. Note, however, that the maximization in Eq. (1.4.1.5) can be obtained only by assuming that the whole information on the estimand θ comes from the set of possible quantum states of the system, i.e. the measurement strategy aimed at estimating the parameter does not depend on its value. There are cases in which this assumption does not hold. In those cases, alternative approaches are needed[115, 116, 117].

An optimal quantum measurement for the estimation of θ, then, corresponds to the POVM with a Fisher information equal to the Quantum Fisher information. It is possible[114] to find an explicit form for the optimal estimator for the optimal POVM. This estimator, however, is not as straightforward as the maximum likelihood one to calculate, nor to understand what it actually represents in the physical system. For this reason, a common employed strategy is to identify the family of measurement which are available, and then to maximize the Fisher information over all such measurements[115].

1.4.2   Biased parameter estimation

As we have seen in the previous section, the (Quantum) Cramér-Rao bound is a powerful tool, which allows putting a constraint on the variance of unbiased

estimators. It does not, however, guarantee the existence of a MVU estimator. In fact, there are cases in which there are no MVU estimators, or where the MVU estimator provides unreliable estimations. This is the case, for instance, of inferring the odds ratio from n Bernoulli trials[118]. Furthermore, it can be showed[108, 118, 119] that introducing a small bias may allow reaching a lower MSE with respect to the one achievable by optimal unbiased estimators. More generally, Bayesian estimation[108] does not require the unbiasedness assumption about the estimator, so long as we place a prior on the parameter space. For these reasons, much effort has been put into generalizing the Fisher Information and the Cramér-Rao bound to the case of biased estimation.

In the following sections we introduce the basics of biased estimation: first, we present an extension of the Cramér-Rao bound to estimators with a generic bias, then we introduce the more general case of Bayesian estimation, from which we will derive the more general Van Trees bound[120].

Extending the Cramér-Rao bound

For an estimator $\hat{\theta}$ with a generic bias $b(\hat{\theta}, \theta)$, the Cramér-Rao bound can be easily generalized[118, 120] into:

$$Var(\hat{\theta}) \geq \frac{\left(1 + b'(\hat{\theta}, \theta)\right)^2}{nI(\theta)} \tag{1.4.2.1}$$

leading to a MSE

$$MSE(\hat{\theta}) \geq \frac{\left(1 + b'(\hat{\theta}, \theta)\right)^2}{nI(\theta)} + b(\hat{\theta}, \theta)^2 \tag{1.4.2.2}$$

where $b'(\hat{\theta}, \theta) = \frac{\partial b(\hat{\theta}, \theta)}{\partial \theta}$.

Thanks to the dependence of both therms on the bias function, we can achieve a lower MSE with respect to the unbiased case by carefully tuning our bias function. To better understand this, let us focus on the simple case of a linear Gaussian model of which we know the MVU estimator $\hat{\theta}_a$ and restrict ourselves to the subclass of estimators with a linear bias $b(\hat{\theta}, \theta) = m\theta$, for which it is easy to show[118] that the biased Cramér-Rao bound can be achieved by the estimator

$$\hat{\theta}_b = (1 + m)\hat{\theta}_a \tag{1.4.2.3}$$

where m will be chosen in order to minimize the MSE which, in turn, is

$$MSE(\hat{\theta}_b) = (1 + m)^2 Var(\hat{\theta}_a) + m^2 \theta^2 \tag{1.4.2.4}$$

44

Clearly, for $-1 \leq m < 0$, there is a trade-off between the reduction of the variance and the increase of the bias (Fig. 1.3). Thus, we need to find a value m_{opt} of m which minimizes the overall MSE. This can be done by studying the first derivative of the MSE, obtaining:

$$m_{opt} = -\frac{1}{1 + \theta^2/Var(\hat{\theta}_a)} \tag{1.4.2.5}$$

which, unfortunately, depends on the unknown estimand θ. Nevertheless, it is possible to find an optimal m in the cases in which the variance is constant or depends on θ[118, 119].
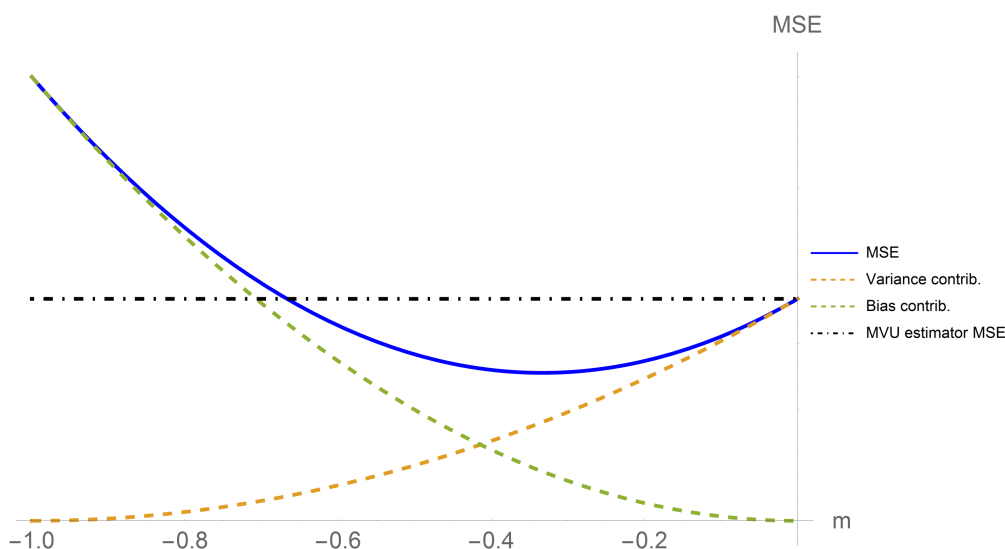
Figure 1.3: Trade-off between variance and bias to reduce the MSE. The variance component is $(1+m)^2 Var(\hat{\theta}_a)$. The bias component is $m^2\theta^2$. MSE axis: arbitrary units.

The extension to the quantum case is trivial, as it only requires to substitute the Fisher Information in Eq. (1.4.2.1) with the Quantum Fisher Information.

Notice that, again, the bound does not guarantee that the estimator exists.

Bayesian estimation: the Van Trees inequality

A more general approach is the one of the Bayesian estimation, in which we assume to have a probability density $\pi(\theta)$, representing an a priori knowledge of the estimand[120], and drop the request of unbiasedness. In this case, we can define an average MSE as

$$\overline{MSE}(\theta) = \int \mathrm{d}x \int \mathrm{d}\theta \, \pi(\theta) \left[\hat{\theta}(x) - \theta\right]^2 \tag{1.4.2.6}$$

45

which is the MSE averaged over the prior information.

In the classical case, the MSE has a lower bound given by the Van Trees inequality[120, 121], a generalization of the CRB which has the form

$$\overline{MSE}(\theta) \geq \frac{1}{nZ_I} \tag{1.4.2.7}$$

where

$$Z_I = \int \mathrm{d}x \int \mathrm{d}\theta\, p(x, \theta) \left[\frac{\partial \log p(x, \theta)}{\partial \theta}\right]^2 = \int \mathrm{d}\theta\, \pi(\theta) I(\theta) + \int \mathrm{d}\theta\, \pi(\theta) \left[\frac{\partial \log \pi(\theta)}{\partial \theta}\right]^2$$

$$= E_\pi \left[I(\theta)\right] + I(\pi(\theta))$$

$$\tag{1.4.2.8}$$

is the generalized Fisher information, which is the sum of two terms. The first term is the average of the Fisher information over the a priori distribution, while the second term is the Fisher information of the a priori distribution itself. Here, $p(x, \theta) = f(x|\theta)\pi(\theta)$ and $E_\pi(\cdot)$ represents the average over the a priori information $\pi(\theta)$.

The generalization to the quantum case requires to substitute the Fisher information I with the Quantum Fisher information H into Eq. (1.4.2.8):

$$Z_H = E_\pi \left[H(\theta)\right] + I(\pi(\theta)) \tag{1.4.2.9}$$

from which can be derived the Quantum Van Trees bound

$$\overline{MSE}(\theta) \geq \frac{1}{Z_H} \tag{1.4.2.10}$$

The (Quantum) Van Trees bound, then, generalizes the (Quantum) Cramér-Rao bound taking into account possible a priori information on the system, at the cost of dropping the unbiasedness assumption. While it can be shown that, in the asymptotic limit, the a priori distribution is no longer relevant[115], the injection of this a priori information brings benefits for small data sets, for which the Van Trees inequality may provide a lower bound with respect to the Cramér-Rao one.

Chapter 2

Single- and entangled-photons sources

Research on single and entangled photon sources (i.e., sources whose light emission is composed of just photons or entangled photon pairs, respectively) is of crucial importance for experiments on the foundations of quantum mechanics as well as for the new quantum technologies (Sec. 1.1.2). For instance, some quantum key distribution (QKD) protocols demand single photons travelling over a channel and more than one photon potentially compromise the security of the communication, allowing an eavesdropper to gain information without being noticed[122]. In this chapter, we describe the main methods to generate single- and entangled-photons, focusing, in particular, on parametric down-conversion.

2.1 The ideal single-photon source

An ideal single-photon source (SPS) should have the following properties:

- *deterministic behaviour*: single photons can be emitted arbitrarily by the user with 100% probability and with the highest possible repetition rate;

- *indistinguishability* between the photons emitted at different times;

- *zero multi-photon component.*

Similar requirements about deterministic behaviour and indistinguishability can also be made for an entangled-photons source (EPS).

Although such devices are still far from being realized, much effort and many different ideas have been invested in these sources and their improvement, resulting in the birth of several different specific on-purpose SPS and EPS prototypes, each focusing on improving the feature(s) needed for the related tasks. Such photons sources can be split in two families: deterministic and probabilistic sources.

2.2 Deterministic SPSs: single emitters

In this section we give a brief description of deterministic sources, which include quantum dots[123, 124, 125] and defects in nanodiamonds[124, 126]. Such sources are ideally able of emitting *on demand* single- and, in some cases, entangled-photons. The trade-off, however, is a reduced indistinguishability.

2.2.1 Quantum dots

Quantum dots are a central topic in nanotechnologies. They are nanoscale semi-conductors with a small band-gap, embedded in a large band-gap host crystal. The small size of quantum dots results in a discrete energy structure, which allows us to create an *exciton* (i.e. a electron-hole pair) on demand by exciting an electron of the quantum dot valence band into the conductance band of the host crystal. Such exciton is usually obtained through illumination by an ultraviolet laser (saturating the single system through photon-absorption) or by electrical means. The recombination of the electron-hole pair, then, results in a single-photon emission.

Although photoluminescence emits over all the solid angle, it is possible to collect the emitted photons with a high efficiency (nearly 80%) thanks to confined microcavities. Such cavities also allows for collection of the emitted photons into a single spatial mode and for achieving a high repetition rate, thanks to the Purcell effect[127].

QDs can also be exploited in order to generate entangled-photons. One simple way[128] would be to exploit a simple scheme involving a quantum dot SPS and a beam splitter: two subsequent single-photons are produced with the same polarization. The first one is delayed and rotated of 90°, so that the two photons enter a beam splitter (BS) at the same time and with orthogonal polarization. When the two output photons go out of the BS from two different ports, they are known to be entangled in polarization[129]. Another way to generate entangled-photons would be to generate a *biexciton* by creating two electron-hole pairs. The subsequent decay into the ground state of the biexciton causes the emission of two entangled photons[130].

Although being a deterministic SPS, quantum dots also may have in their emission a small multi-photon component. Furthermore, they need to be operated at cryogenic temperature and their photon emission is not completely indistinguishable.

2.2.2   Defects in (nano)diamonds

Diamonds contain hundreds of known optically active defects, a few of which have been investigated for single-photon generation. For this purpose, one of the most studied defect is the nitrogen-vacancy (NV) centre. A NV centre consists of a substitutional nitrogen atom (N) next to a missing carbon atom (vacancy V) in the diamond lattice. The resulting energy level structure has been found to be of great interest for magnetic field detection[131], implementation of qubits[132] and single-photons generation, as they allow for fluorescence when excited by optical[133] or electrical stimulation[134], which can be exploited in order to create a deterministic SPS.

Excitation of the energy levels of the NV centre in a (nano)diamond allows us to generate single-photons with a count rate up to $10^6 - 10^7$[135, 136] photons per second and can achieve a low multi-photon component and a very high radiative efficiency even at room temperature[137]. Indistinguishability, however, is very low, due to the broad emission spectrum[137].

2.3   Probabilistic sources: heralded single-photon sources

While promising, the deterministic SPSs are still less efficient than the probabilistic SPSs. In the following sections we will introduce some probabilistic SPSs, focusing, in particular, on the ones based on the second-order nonlinear optics phenomenon called *parametric down-conversion* (PDC).

2.3.1   General introduction

Probabilistic single-photon sources usually exploit the properties of a second- or third-order nonlinear optical medium. [34, 138]

In order to understand the nonlinearity, it is useful to introduce the energy of a classical electromagnetic field within a non-magnetic medium:

$$H = \int d^3r \frac{1}{2\mu_0} \vec{B}^2(\vec{r}, t) + \int d^3r \int_0^{\vec{D}(\vec{r},t)} \vec{E}(\vec{r}, t) \cdot d\vec{D}(\vec{r}, t) \tag{2.3.1.1}$$

where $\vec{E}$ is the electric field, $\vec{B}$ the magnetic flux density, $\vec{D}$ the electric displacement. The electric displacement is defined as:

$$\vec{D}(\vec{r}, t) = \varepsilon_0 \vec{E}(\vec{r}, t) + \vec{P}(\vec{r}, t) \tag{2.3.1.2}$$

where $\vec{P}$ is the polarization induced in the medium. For a non-dispersive medium, or when the effective frequencies of the field are not too close to the resonance frequencies of the medium, the induced polarization can be expanded in a power series in $\vec{E}$:

$$P_i = \chi_{ij}^{(1)}E_j + \chi_{ijk}^{(2)}E_jE_k + \chi_{ijkl}^{(3)}E_jE_kE_l \cdots \tag{2.3.1.3}$$

where $\chi^{(n)}$ is the electric susceptibility tensor of rank $n+1$.

Let us focus on the second order term:

$$P_i^{(2)} = \chi_{ijk}^{(2)}E_jE_k \tag{2.3.1.4}$$

The second order nonlinear response can also be rewritten in a more compact form by observing that the fields E_j and E_k can be permuted without changing the polarization[139]. This way, the 27 elements of the $\chi^{(2)}$ tensor can be reduced to a 18-elements matrix d_{ij} called *nonlinear optical coefficient tensor*:

$$\begin{pmatrix} P_x^{(2)} \\ P_y^{(2)} \\ P_z^{(2)} \end{pmatrix} = \begin{pmatrix} d_{11} & d_{12} & d_{13} & d_{14} & d_{15} & d_{16} \\ d_{21} & d_{22} & d_{23} & d_{24} & d_{25} & d_{26} \\ d_{31} & d_{32} & d_{33} & d_{34} & d_{35} & d_{36} \end{pmatrix} \begin{pmatrix} E_xE_x \\ E_yE_y \\ E_zE_z \\ 2E_yE_z \\ 2E_zE_x \\ 2E_xE_y \end{pmatrix} \tag{2.3.1.5}$$

Usually, the nonlinear susceptibilities have small magnitude, meaning that they are negligible for weak electric field amplitudes. In contrast, when the electric field is large, the nonlinear terms give rise to several interesting phenomena[34, 124, 139]. Here we briefly describe some of the most common nonlinear effects.

Second-order nonlinear phenomena

If the medium is excited by waves at angular frequencies ω_1 and ω_2 with amplitudes E_1 and E_2, respectively, then the second-order nonlinear polarization (i.e. the second term of Eq. (2.3.1.3)) will be:

$$P_i^{(2)} = \chi^{(2)}E_1E_2\frac{1}{2}\left[\cos(\omega_1 + \omega_2)t + \cos(\omega_1 - \omega_2)t\right] \tag{2.3.1.6}$$

which tells us that the second-order nonlinear response generates an oscillating polarization at the sum and difference frequencies of the input fields. These phenomena take the names of *sum frequency mixing* (SFM) and *difference frequency mixing* when $\omega_{sum} = \omega_1 + \omega_2$ and $\omega_{diff} = \omega_1 - \omega_2$ are produced, respectively. In the special case of $\omega_1 = \omega_2$, the sum frequency doubles the input frequency and the effect is called *second harmonic generation* (SHG) or *frequency doubling*.
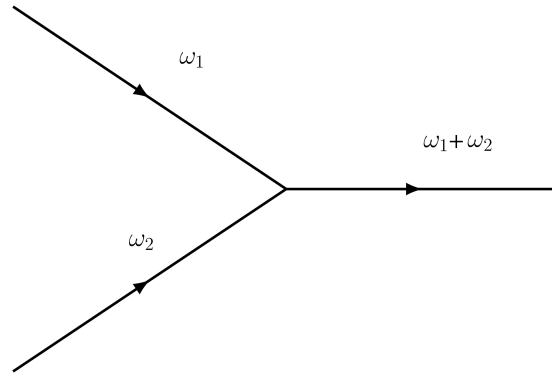
Figure 2.1: Diagram for sum frequency mixing

Another important second-order nonlinear phenomenon is *spontaneous parametric down-conversion* (SPDC). SPDC is a quantum phenomenon which can be seen as a reverse of SFM. It is a process in which a photon from a *pump* beam interacting with a second-order nonlinear crystal is spontaneously converted in two correlated photons, usually called *signal* and *idler*, under conservation of energy and momentum.
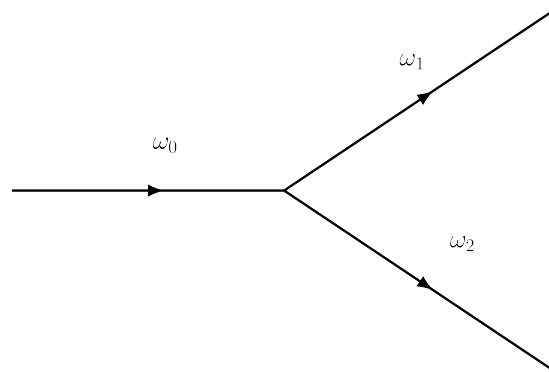
Figure 2.2: Diagram for PDC. ω_0: pump frequency. ω_1: signal frequency. ω_2: idler frequency.

Today, PDC is one of the most widely used techniques for generating single (and entangled) photons, because it is well understood, simple to implement and produces photons in well defined modes at high rates. We will give a more detailed description of PDC in Sec. 2.3.2.

Third-order nonlinear phenomena

Similarly to the second-order phenomena, in a medium excited by three incoming waves of frequencies ω_1, ω_2 and ω_3, the third-order nonlinear response

generates an oscillating polarization at the sum and difference frequencies of the input fields. The outputs are $\omega_{sum} = \omega_1 + \omega_2 + \omega_3$ for *sum frequency mixing* and $\omega_{diff} = \omega_1 + \omega_2 - \omega_3$ for *difference frequency mixing*. In the special case of $\omega_1 = \omega_2 = \omega_3$, the sum frequency triples the input frequency and the effect is called *third harmonic generation* (THG).

Third order phenomena also allow for a phenomenon analogous to SPDC: the *spontaneous four-wave mixing* (SFWM). SFWM is a process in which the absorption of two photons from two intense pump fields at frequencies ω_1 and ω_2 causes the emission of two correlated photons ω_3 and ω_4 usually called signal and idler, under conservation of energy and momentum.
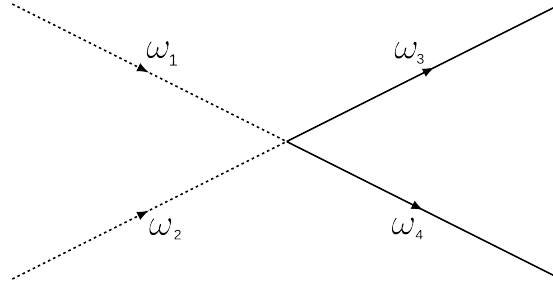
Figure 2.3: Diagram for four wave mixing. ω_1 and ω_2: pump frequencies. ω_3: signal frequency. ω_4: idler frequency.

Third-order phenomena are usually observed in isotropic materials, such as silica glass, in which the second-order term vanishes due to symmetry constraints. As such, they are particularly suited for fibre applications.

2.3.2 Spontaneous parametric down-conversion

In this section, we focus on the aforementioned phenomenon of *spontaneous parametric down-conversion* (SPDC). First, we will introduce the general theory of PDC, then, see its applications in single-photon and entangled photons sources.

General theory

Recalling sec. 2.3.1, PDC is a second-order nonlinear non-classical phenomenon in which one incident photon of frequency ω_0 and wave vector $\vec{k}_0$ in a nonlinear crystal is converted into two lower-frequency photons, known as *signal* and *idler*. In general, such photons have different frequencies ω_1, ω_2 and wave vectors $\vec{k}_1$,

$\vec{k}_2$, under conservation of the four-momentum, which imposes the so-called *phase-matching conditions*:

$$\omega_0 = \omega_1 + \omega_2$$
$$\vec{k}_0 = \vec{k}_1 + \vec{k}_2 \tag{2.3.2.1}$$
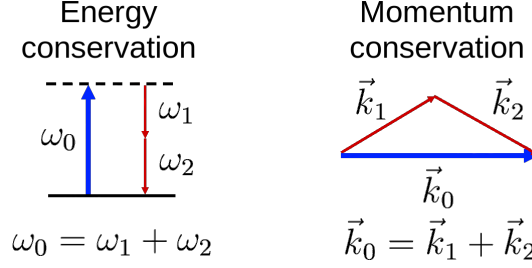
Figure 2.4: The phase-matching conditions.

We can distinguish three types of PDC:

- Type-I PDC, in which signal and idler share the same polarization, which is orthogonal to the pump field;

- Type-II PDC, in which signal and idler polarizations are orthogonal;

- Type-0 PDC, in which pump, signal and idler fields are coplanar and share the same polarization.

Methods of achieving the phase-matching condition for these different types of PDC are described in the next sections of this chapter.

Quantum mechanical description The Hamiltonian for single-mode PDC can be written in the following form:

$$\hat{H} = \sum_{i=0}^{2} \hbar\omega_i \left(\hat{n}_i + \frac{1}{2} \right) + \hbar g \left[\hat{a}_1^\dagger \hat{a}_2^\dagger \hat{a}_0 + h.c. \right] \tag{2.3.2.2}$$

where $\hat{a}_i(\hat{a}_i^\dagger)$ are the annihilation (creation) operators for the photon i and g is the real-mode coupling constant, which contains $\chi^{(2)}$. Subscript $0, 1, 2$ refer, respectively, to pump, signal and idler.

Since PDC is a nonlinear phenomenon, only a small fraction (10^{-12} to 10^{-5}) of the pump photons gets down-converted[140]. Therefore, the pump field should be intense, meaning that the pump mode $\hat{a}_0$ can be described classically as a field of complex amplitude $a_0 = v_0 e^{-i\omega_0 t}$. This only holds when the depletion of the pump field is negligible, i.e. when $\langle \hat{n}_1(t) \rangle \ll |v_0|^2$ and $\langle \hat{n}_2(t) \rangle \ll |v_0|^2$. With this

approximation, usually called *parametric approximation*, the Hamiltonian only has two quantized fields modes, corresponding to the signal and idler photons:

$$\hat{H} = \sum_{i=0}^{2} \hbar\omega_i \left(\hat{n}_i + \frac{1}{2} \right) + \hbar g \left[\hat{a}_1^\dagger \hat{a}_2^\dagger v_0 e^{-i\omega_0 t} + h.c. \right] \tag{2.3.2.3}$$

for which $\hat{n}_1 - \hat{n}_2$ is a constant of motion:

$$\left[\hat{n}_1 - \hat{n}_2, \hat{H} \right] = 0 \tag{2.3.2.4}$$

meaning that signal and idler photons are always created together.

In order to solve the Heisenberg equations of motions, it is useful to introduce the operators $\hat{A}_i = \hat{a}_i(t)e^{-i\omega_i t}$ for $i = 1, 2$. This way, they take the form:

$$\frac{d\hat{A}_1(t)}{dt} = \frac{i}{\hbar}\left[\hat{H}, \hat{A}_1 \right] = -igv_0 \hat{A}_2^\dagger$$
$$\frac{d\hat{A}_2(t)}{dt} = \frac{i}{\hbar}\left[\hat{H}, \hat{A}_2 \right] = -igv_0 \hat{A}_1^\dagger \tag{2.3.2.5}$$

By differentiating a second time and defining $v_0 = |v_0|e^{i\theta}$ and $\zeta = g|v_0|$, we obtain:

$$\frac{d^2\hat{A}_1(t)}{dt^2} = \zeta^2 \hat{A}_1^\dagger$$
$$\frac{d^2\hat{A}_2(t)}{dt^2} = \zeta^2 \hat{A}_2^\dagger \tag{2.3.2.6}$$

The general solutions are:

$$\hat{A}_1(t) = \hat{A}_1(0)\cosh(\zeta t) - ie^{i\theta}\hat{A}_2^\dagger(0)\sinh(\zeta t)$$
$$\hat{A}_2(t) = \hat{A}_2(0)\cosh(\zeta t) - ie^{i\theta}\hat{A}_1^\dagger(0)\sinh(\zeta t) \tag{2.3.2.7}$$

This result allows us to extract the photon statistics, by calculating the expectation value of the number operator $\hat{n}_i = \hat{a}_i^\dagger \hat{a}_i$ with respect to the initial state of the signal and idler modes, that, for *spontaneous* PDC, is the two-mode vacuum state $|vac\rangle_{12} = |0\rangle_1 \otimes |0\rangle_2$. Remembering that $\hat{A}_i(0) |vac\rangle_{12} = 0$, the expectation value of signal and idler photon number is:

$$\langle \hat{n}_1(t) \rangle = \langle \hat{n}_2(t) \rangle = \sinh^2 (\zeta t) \tag{2.3.2.8}$$

The average number of down-converted photons grows quadratically in time as long as $\zeta t \ll 1$, which is a typical working condition if we take t as the propagation time

through the nonlinear crystal, which is usually very short.

The cross-correlation of the photon number fluctuations is given by:

$$
\begin{aligned}
\langle \hat{n}_1 \hat{n}_2 \rangle &= \left\langle \hat{A}_1^\dagger(t) \hat{A}_2^\dagger(t) \hat{A}_1(t) \hat{A}_2(t) \right\rangle \\
&= \langle \left[\left(c\hat{A}_2^\dagger(0) + ie^{-i\theta} s\hat{A}_1(0) \right) \left(c\hat{A}_1^\dagger(0) + ie^{-i\theta} s\hat{A}_2(0) \right) \right] \\
&\quad \times \left[\left(c\hat{A}_2(0) - ie^{i\theta} s\hat{A}_1^\dagger(0) \right) \left(c\hat{A}_1 - ie^{i\theta} s\hat{A}_2^\dagger(0) \right) \right] \rangle \\
&= s^2 c^2 + s^4 \langle vac|_{12} \, \hat{A}_1(0) \hat{A}_2(0) \hat{A}_1^\dagger(0) \hat{A}_2^\dagger(0) \, |vac\rangle_{12} \\
&= \langle \hat{n}_1 \rangle \left(1 + 2 \langle \hat{n}_1 \rangle \right)
\end{aligned}
\tag{2.3.2.9}
$$

where $s = \sinh(\zeta t)$ and $c = \cosh(\zeta t)$. This expression violates Schwartz inequality, an important evidence of non-classical behaviour[34].

Multimodal treatment of SPDC   Even if the sum of the signal and idler frequencies is fixed by the phase-matching conditions, each signal and idler photon can have a certain frequency bandwidth. This can be described by a more general Hamiltonian that we restrict, for ease of notation, only to the propagation direction z

$$
\hat{H}_I(t) = \hbar g \int_{-L/2}^{L/2} dz \iiint d\omega_0 d\omega_1 d\omega_2 e^{-i(\omega_0 - \omega_1 - \omega_2)t} e^{i(k_0 - k_1 - k_2)z} v_0 a_{k_1 \omega_1}^\dagger a_{k_2 \omega_2}^\dagger + h.c.
\tag{2.3.2.10}
$$

where k_0 and ω_0 are the wave-vector and frequency of the classical monochromatic pump of vector amplitude v_0. The integral length is taken over the active region L of the nonlinear medium. We can use this Hamiltonian to evolve an initial vacuum state $|\psi(0)\rangle = |vac\rangle_{12}$ in the Schrödinger picture:

$$
|\psi\rangle_{12} = \exp \left[-\frac{i}{\hbar} \int_0^t dt' \hat{H}_I(t') \right] |vac\rangle_{12}
\tag{2.3.2.11}
$$

by assuming the production of only one photon pair, we can expand the exponential, finding:

$$
\begin{aligned}
|\psi(t)\rangle &= |0\rangle_1 |0\rangle_2 + \mathcal{N} \int_0^t dt' \int_{-L/2}^{L/2} dz \iiint d\omega_0 d\omega_1 d\omega_2 e^{-i(\omega_0 - \omega_1 - \omega_2)t'} e^{i(k_0 - k_1 - k_2)z} \\
&\quad \times v_0 a_{k_1 \omega_1}^\dagger a_{k_2 \omega_2}^\dagger |0\rangle_1 |0\rangle_2
\end{aligned}
\tag{2.3.2.12}
$$

where $\mathcal{N}$ is the product of several constants. Performing the integration over z and letting the creation operators act, we obtain

$$
\begin{aligned}
|\psi(t)\rangle &= |0\rangle_1 |0\rangle_2 + \mathcal{N}' \int_0^t dt' \iiint d\omega_0 d\omega_1 d\omega_2 e^{-i(\omega_0 - \omega_1 - \omega_2)t'} \\
&\quad \times L \frac{\sin \left[\frac{L\Delta k}{2} \right]}{\frac{L\Delta k}{2}} v_0 |k_1 \omega_1\rangle |k_2 \omega_2\rangle
\end{aligned}
\tag{2.3.2.13}
$$

where $\Delta k = k_0 - k_1 - k_2$ and, again, $\mathcal{N}'$ is the product of several constants. Finally, integration over t[124] yields the delta function $\delta(\omega_0 - \omega_1 - \omega_2)$, which depicts the energy conservation. Afterwards, a subsequent integration of ω_0 gives us the result

$$|\psi(t)\rangle = |0\rangle_1 |0\rangle_2 + \mathcal{N}'' \iint d\omega_1 d\omega_2 L \frac{\sin\left[\frac{L\Delta k}{2}\right]}{\frac{L\Delta k}{2}} v_0 |k_1\omega_1\rangle |k_2\omega_2\rangle \qquad (2.3.2.14)$$

where $\mathcal{N}''$ is the product of several constants and which is maxed when $\Delta k = k_0 - k_1 - k_2 = 0$, i.e. when momentum is conserved and phase-matching conditions are fulfilled. From this expression it clearly emerges that wave-vectors and frequencies are not fixed, but strictly correlated, meaning that the two photons are entangled in frequency and momentum.

Bulk crystal SPDC: birefringent phase-matching The majority of PDC sources has been realized in bulk crystals, i.e., standard nonlinear crystals without poling or embedded waveguides. In this paragraph, we describe how phase-matching can be achieved in such crystals.

To generate SPDC, we have to respect the phase-matching conditions(2.3.2.1):

$$\begin{aligned} \omega_0 &= \omega_1 + \omega_2 \\ \vec{k}_0 &= \vec{k}_1 + \vec{k}_2 \end{aligned} \qquad (2.3.2.15)$$

where the wave-vectors $\vec{k}_i$ depend on the frequencies ω_i by a dispersion relation which, for birefringent crystals, is[141, 142]

$$\vec{k}_i = n_i(\rho_i, \varphi_i)\frac{\omega_i}{c}\hat{s}_i \qquad (2.3.2.16)$$

where $i = 0, 1, 2$; n_i is the refraction index for the i-th single photon in its respective polarization and propagation direction $\hat{s}_i$ and c is the speed of light. Here and in the rest of this paragraph, the hat indicates an unit vector. In the laboratory reference frame (Fig. 2.5), ρ_0 is the angle between $\hat{s}_0$ and the Z axis, φ_0 is the azimuthal angle between the X axis and $\hat{s}_0$ in the $X - Y$ plane. For the down-converted photons, ρ_i indicates the angle between $\hat{s}_i$ and $\hat{s}_0$, while φ_i is a rotation on the $\hat{s}_0$ normal plane.

Equation (2.3.2.16) show how the wavelength of down-converted photons variates following the variation of the exit angles.

The relative directions of wave vectors can be either collinear (scalar phase-matching) or non-collinear (vector phase-matching). In this second case, the phase-matching conditions can only be fulfilled in anisotropic crystals, in which fields of
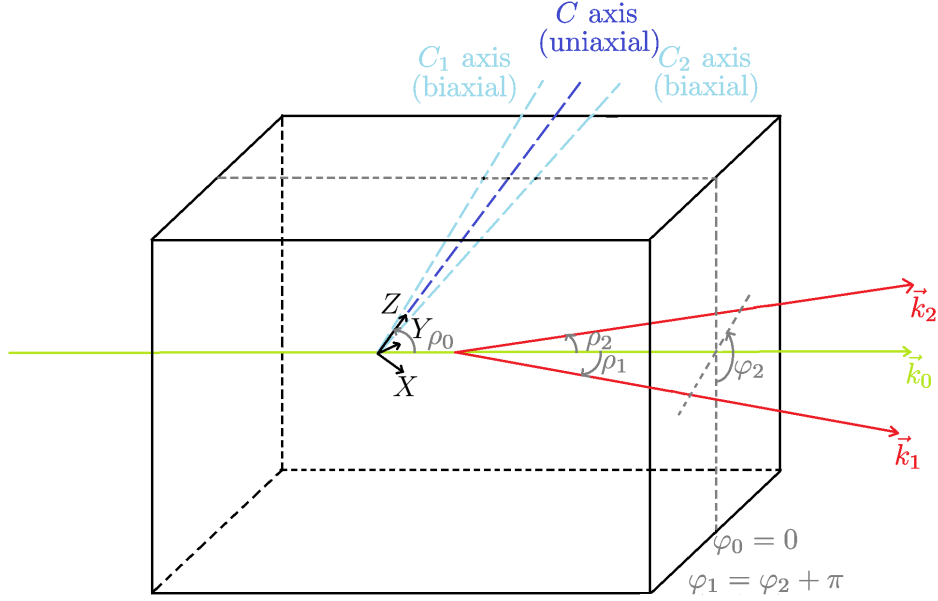
Figure 2.5: View of the crystal in the laboratory reference frame in a typical configuration. In this picture, the plane $X - Z$ (corresponding to $\varphi_0 = 0$ is the plane of the page). This choice can always be made in uniaxial crystals. In biaxial crystals, this choice can be made only if the crystal axes C_1, C_2 and the pump beam are on the same plane. In this case, the azimuthal angles φ_1 and φ_2 are measured within the plane $X - Z$.

different polarizations experience different refractive indices. For instance, in uniaxial crystals, we can define the plane containing the optical axis and the pump wave vector as the *principal plane*. A light beam polarized orthogonally to that plane is called *ordinary* (*o*-beam), a beam polarized within the plane, instead, is called *extraordinary* (*e*-beam). The refractive index n_o for *o*-beams is independent of the field orientation in the crystal, whereas the refractive index n_e for *e*-beams does. This difference is known as birefringence. An uniaxial crystal is defined positive if $n_o \leq n_e$ and negative otherwise.

Birefringent crystals allow us to reach phase-matching conditions in different beam configurations. We call Type-I phase-matching the cases in which signal and idler photons have the same polarization, which is orthogonal to the one of the pump beam:

$$\vec{k}_0(o) = \vec{k}_1(e) + \vec{k}_2(e) \text{ (positive crystals)} \tag{2.3.2.17}$$

$$\vec{k}_0(e) = \vec{k}_1(o) + \vec{k}_2(o) \text{ (negative crystals)} \tag{2.3.2.18}$$

In this case, 3D phase-matching conditions tell us that signal and idler photons exit the crystal in the opposite sides of two concentric cones centred on the propagation axis of the pump beam. Proper spatial and frequency filters allow us to select such pairs of photons and send them to the appropriate optical paths.
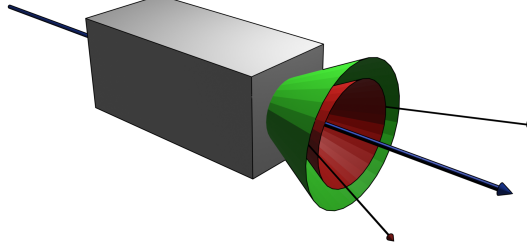
Figure 2.6: Type-I SPDC: photons from the pump beam (blue) are converted into signal and idler photons emerging from the crystal along different directions (red and green). The possible directions form an ensemble of concentric cones.

We call Type-II phase-matching, instead, the cases in which signal and idler photons have orthogonal polarizations (one of which is the same as the pump beam):

$$\vec{k}_0(o) = \vec{k}_1(e) + \vec{k}_2(o) \text{ (positive crystals)} \tag{2.3.2.19}$$

$$\vec{k}_0(o) = \vec{k}_1(o) + \vec{k}_2(e) \text{ (positive crystals)} \tag{2.3.2.20}$$

$$\vec{k}_0(e) = \vec{k}_1(e) + \vec{k}_2(o) \text{ (negative crystals)} \tag{2.3.2.21}$$

$$\vec{k}_0(e) = \vec{k}_1(o) + \vec{k}_2(o) \text{ (negative crystals)} \tag{2.3.2.22}$$

This means that the photons are emitted on two cones, one for the ordinary wave (o) and one for the extraordinary wave (e) (Fig 2.7a), of orthogonal polarizations. Thus, at the intersections between two cones of photons at the same wavelength there will be ambiguity about the polarization of the incoming photons (Fig. 2.7b), which can be written as:

$$\left|\psi^+\right\rangle = \frac{1}{2}\left(|V\rangle_1 |H\rangle_2 + |H\rangle_1 |V\rangle_2\right) \tag{2.3.2.23}$$

which is an entangled state.

Type-0 phase matching, instead, cannot generally be implemented in bulk crystals, but it is often achieved through periodically-poled crystals.

Periodically-poled crystal SPDC: quasi-phase-matching   Quasi-phase-matching (QPM)[124, 143] is a way to achieve efficient energy transfer between interacting

(a) Non-collinear Type-II SPDC: the two photons emerge distributed on two intersecting cones thanks to the crystal birefringence.

(b) It is impossible to determine from which cone a photon in the intersections is coming. Therefore, the intersections between the *e*-*o*-cone can be used as a source of photons entangled in polarization.
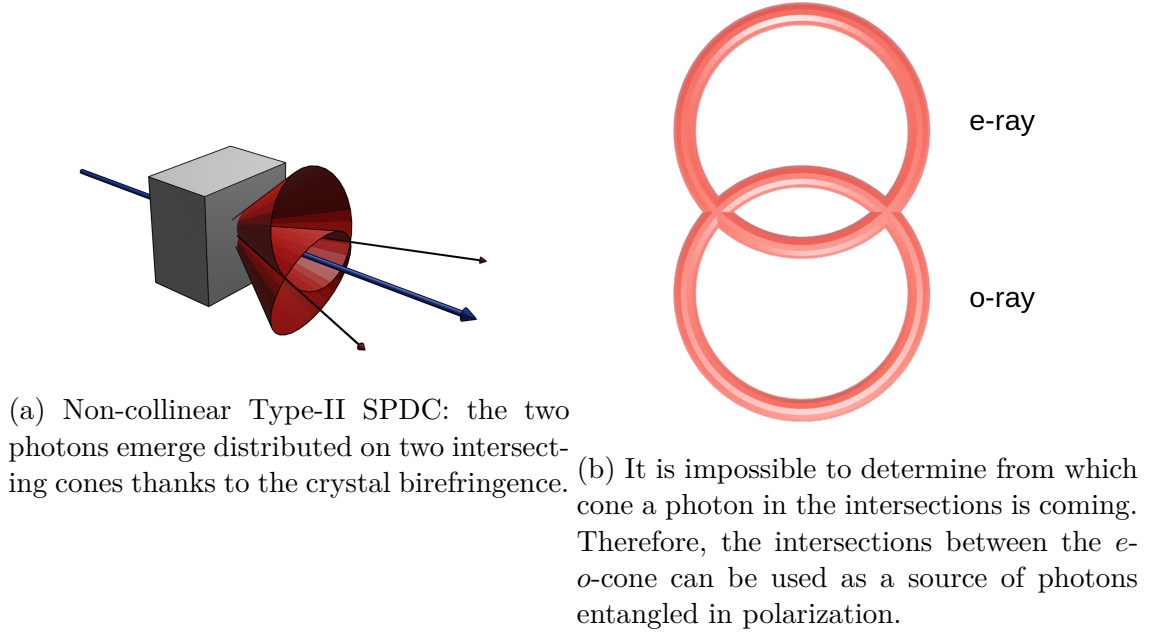
Figure 2.7: Type-II SPDC

waves in nonlinear media. Such result is achieved thanks to a spatial modulation of the nonlinear properties along the propagation direction, usually implemented by periodically alternating the orientation of the crystal domain. The interacting fields propagate with different phase velocities inside the crystal, but the sign of the nonlinear susceptibility is changed every time the phase mismatch reaches π. This way, the fields never interfere destructively, creating a step-wise growth in the output power along the crystal length.

In order to understand this phenomenon, let us write the longitudinal varying nonlinear susceptibility $d(z)$ as a Fourier series

$$d(z) = d_{bulk} \sum_m F_m \exp\left(-ik_m z\right) \tag{2.3.2.24}$$

where d_{bulk} is the nonlinear coefficient of the bulk material, F_m are the Fourier coefficients, $k_m = 2\pi m/\Lambda$ is the grating vector of the m-th Fourier component and Λ is the poling periodicity.

Now, we assume that only one Fourier component is phase-matched, therefore we only have one significant contribution to the PDC process. This assumption allows us to obtain an expression for the field E_1 after a length L[124]:

$$E_1 \propto L d_Q \frac{\sin\left(\Delta k_Q \frac{L}{2}\right)}{\left(\Delta k_Q \frac{L}{2}\right)} \tag{2.3.2.25}$$

where d_Q is the effective nonlinear coefficient in QPM. In our case, we can model the effective nonlinear coefficient as a square-wave modulation from $-d_{bulk}$ to $+d_{bulk}$:

$$d_Q = 2d_{bulk}\frac{\sin(\pi D)}{m\pi} \qquad (2.3.2.26)$$

where $D = \frac{l}{\Lambda}$, usually called *duty factor*, is the ratio between the length l of a single reversed domain and the period Λ. The order of the QPM is given by m. As the efficiency is proportional to $1/m^2$, a low-order QPM is usually desired. However, since $\Lambda = w\pi m/k$, lowering the order m has the downside of reducing the period Λ.
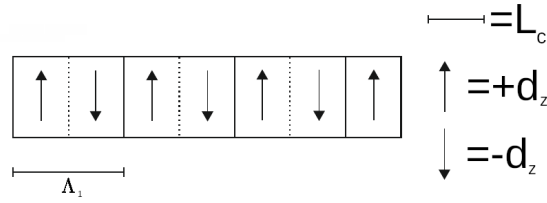
Figure 2.8: First-order QPM. The period Λ_1 is twice as long as the coherence length $L_c = \pi/\Delta k$.

The largest nonlinear coefficient for QPM is obtained for a first-order process ($m = 1$, Fig. 2.8) with duty cycle $D = 0.5$:

$$d_Q = \frac{2}{\pi}d_{bulk} \qquad (2.3.2.27)$$

meaning that whenever we perform a QPM, we reduce effective nonlinearity by *at least* a factor $2/\pi$ with respect to the value for birefringent phase-matching in the bulk medium.

Due to quasi-phase-matching, the effective wave-vector mismatch (see Eq. (2.3.2.14)) becomes

$$\Delta k_Q = k_0 - k_1 - k_2 - k_m = \Delta k_{bulk} - k_m \qquad (2.3.2.28)$$

This means that QPM allows us to reach a fully phase-matched interaction even when the wave-vector mismatch is non-zero in the bulk material, thanks to the grating vector k_m, which is independent of material properties and easily tunable during fabrication[124]. Furthermore, the phase-matching can be tuned by using the temperature dependence of the refractive index n, which implies the temperature dependence of the wave vectors (see Eq. 2.3.2.16). Since the poling period Λ depends on the thermal expansion of the medium, also the grating vector k_m displays a temperature dependency. For each type of medium, the refractive index with respect to temperature and wavelength can be easily derived thanks to Sellmeier equations[144] (see, for instance, [145]).

Heralded single-photon sources with SPDC

First introduced by Klysko[146], heralded single-photon sources (HSPSs) are probabilistic sources, which usually employ Type-0 and Type-I SPDC to generate time-correlated pairs of photons. The detection of one photon heralds the presence of of its twin, allowing it to be exploited for the task we want to perform.

In Type-I SPDC, the constraints posed by the phase-matching conditions present both an advantage and a disadvantage. While the highly directional emission is generally useful, we have limited control on the inherent dispersion of transparent materials, putting some constraints on the wavelengths that a given crystal can produce. In Type-0 PDC, instead, we can produce a crystal tailored to the specific wavelengths that we want to produce, at the price of collinear emission.

Regardless of the phase-matching type, these are probabilistic sources, a feature that inherently limits our control over the system. In order to overcome this issue, we can use a pulsed pump or a continuous pump with some special electronics. With a pulsed pump, the production of the two photons is limited to each pulse. This way, by tuning the repetition rate of such pulses, we achieve a better control of the system. Usually, pulsed pumps are generated by a mode-locked laser[147], which has a pulse duration of the order of the a hundred femtoseconds, very close to the SPDC coherence time. When working with continuous pumps, instead, one can employ dedicated electronics which accept an heralding signal only at a specific time interval (Sec. 3.1.2). Note, however, that this does not influence the emission rate.

Entangled-photon sources with SPDC

SPDC allows us to generate photons pairs entangled in polarization. Here we describe some methods.

As, previously described, in Type-II SPDC, signal and idler are emitted in two intersecting cones, and with orthogonal polarizations.. After a proper time-compensation, at the two intersections between the cones (Fig. 2.7a), it is impossible to distinguish whether the photon belongs to the *e*- or *o*-cone. Thus, the state of two photons belonging to the intersection regions is

$$|\psi\rangle = \frac{1}{\sqrt{2}} \left(|HV\rangle + e^{i\theta} |VH\rangle \right) \tag{2.3.2.29}$$

Being θ the relative phase between ordinary and extraordinary polarized light.

In degenerate Type-I SPDC, instead, signal and idler have the same wavelength and parallel polarization. Suppose, without loss of generality, that the photons are

produced in horizontal $|H\rangle$ polarization. Then, if we rotate the polarization of one of the two photons by 90°, and then combine them in a beam splitter and only select the events in which the two photons separate into the two output ports, the resultant two-photons polarization state is[129]

$$|\psi\rangle = \frac{1}{\sqrt{2}} \left(|HV\rangle + |VH\rangle \right) \tag{2.3.2.30}$$

which is an entangled state. Unfortunately, the post-selection procedure is probabilistic, with a success probability of 0.5.

Another method to generate entangled photons by exploiting Type-I SPDC is to use two Type-I crystals oriented with perpendicular optical axes[148], i.e. one on the plane X-Y and the other on the plane Y-Z, Z being the beam direction. This can be realized either way in optical condensers[149] or with two thin crystals in contact[150]. When they are illuminated by a pump beam in the state $|+\rangle = 1/\sqrt{2} \left(|H\rangle + |V\rangle \right)$, signal and idler photons are emitted either by the first or the second crystal in horizontal or vertical polarization, respectively. If the two crystals are sufficiently thin, the two cones in which photons are emitted are indistinguishable, therefore, the polarization state of the emitted photons is in the superposition

$$|\psi\rangle = \frac{1}{\sqrt{2}} \left(|HH\rangle + e^{i\theta} |VV\rangle \right) \tag{2.3.2.31}$$

θ being a phase between the two terms.

There are many other methods to exploit SPDC to produce entangled states (e.g. Type-II SPDC in a Mach-Zender interferometer[151]). In this thesis, however, we will only exploit the one we described for Type-II SPDC in bulk crystals.

Chapter 3

Characterization of quantum resources for technological and scientific applications

Part of the work described in this chapter has been previously published in [152] *and* [153].

Quantum mechanics has a pivotal role in modern metrology, science and industry (Chap. 1). In particular, the growth of quantum technologies, that exploits quantum resources such as entanglement or squeezing, prompt the development of characterization and standardization methods. The necessity of precise characterization of the used resources in SPSs is also fundamental in research experiments, as the ones we will present in Chap. 4. Therefore, the characterization of quantum resources is becoming an important metrological task. In this chapter, we focus on the characterization of single- and entangled photons sources.

First, we present a strategy to characterize the multi-photon component of a single-photon source (SPS) at telecom wavelength (1550 nm)[152]. The multi-photon component in SPSs emission is one of the key parameters of such devices (Sec. 2.1) and its characterization is a crucial metrological task, both for fundamental research and for commercial implementations (e.g. quantum communication, in which the difference between one or two photons makes the difference between secure and insecure communication).

Second, we present a method allowing to estimate the amount of entanglement and discord between two photons[153]. The ability to estimate non-classical aspects in two-qubit systems is relevant not only for experiments on quantum mechanics foundations, but also for quantum information technologies.

3.1 Single-photon sources characterization

In this section we describe a joint effort among three metrological institutes (INRiM, NPL and PTB) to provide a robust procedure suited for the characterization of the multi-photon emission of extremely faint light continuous wave (CW) heralded SPS (HSPS). First, we introduce the parameter that characterizes the multi-photon component of a generic SPS. Second, we present the particular SPS prototype under test and, finally, the results obtained in a pilot study (involving three different metrological institutes) in which a strategy for the estimation of the aforementioned parameter has been applied to our HSPS prototype.

3.1.1 The second-order autocorrelation function $g^{(2)}(\tau)$

The multi-photon component is usually evaluated through the second-order autocorrelation function $g^{(2)}(\tau)$[34] introduced by Glauber[154] in 1963.

Classical case

In the classical case, the second-order autocorrelation is defined as

$$g^{(2)}(\tau) = \frac{\langle E^*(t)E^*(t+\tau)E(t+\tau)E(t)\rangle}{\langle E^*(t)E(t)\rangle \, \langle E^*(t+\tau)E(t+\tau)\rangle} = \frac{\langle I(t)I(t+\tau)\rangle}{\langle I(t)\rangle \, \langle I(t+\tau)\rangle} \tag{3.1.1.1}$$

where $E(t)$ and $I(t)$ represent, respectively, the electric field and the intensity at the time t. The symmetry of the definition implies $g^{(2)}(\tau) = g^{(2)}(-\tau)$.
Since the variance of the intensity is defined as $\Delta I^2 = \langle I^2\rangle - \langle I\rangle^2$, the second-order autocorrelation can be rewritten, for the time distance $\tau = 0$, as

$$g^{(2)}(0) = \frac{\Delta I^2}{\langle I\rangle^2} + 1 \tag{3.1.1.2}$$

which is always greater than 1, since $\Delta I^2 \geq 0$. There are no upper bounds.

To evaluate the $\tau > 0$ case, we observe that the Schwartz inequality implies:

$$\langle I(t)I(t+\tau)\rangle^2 \leq \langle I(t)^2\rangle \, \langle I(t+\tau)^2\rangle \tag{3.1.1.3}$$

Furthermore, for ergodic or stationary systems, we know that $\langle I(t)\rangle = \langle I(t+\tau)\rangle$, therefore:

$$\langle I(t)I(t+\tau)\rangle \leq \langle I(t)^2\rangle \tag{3.1.1.4}$$

which leads to

$$g^{(2)}(\tau) \geq g^{(2)}(0) \tag{3.1.1.5}$$

The second-order autocorrelation for a time distance $\tau > 0$ is always equal or greater than the one at $\tau = 0$ in the classical case (blue curve in Fig. 3.1).

Quantum case

By quantizing the electric field, Eq. (3.1.1.1) becomes:

$$g^{(2)}(0) = \frac{\langle \hat{n}(\hat{n} - 1) \rangle}{\langle \hat{n} \rangle^2} \qquad (3.1.1.6)$$

where $\hat{n}$ is the number operator of the incoming photons. If the input state is a Fock state $|n\rangle$ (n being the number of photons), the correlation becomes:

$$g^{(2)}(0) = \frac{n(n - 1)}{n^2} < 1 \qquad (3.1.1.7)$$

So, quantum sources have a second-order autocorrelation $g^{(2)}(\tau) < 1$, which reaches $g^{(2)}(0) = 0$ for SPSs ($n = 1$) (orange curve in Fig. 3.1).

Coherent sources

It can be shown[34] that coherent sources, such as the laser, have a poissonian behaviour. Therefore, $\Delta n^2 = \langle \hat{n} \rangle$, with Δn^2 being the variance of the photon number. After a small manipulation, substituting this into Eq. (3.1.1.6), we obtain

$$g^{(2)}(0) = \frac{\langle \hat{n}(\hat{n} - 1) \rangle}{\langle \hat{n} \rangle^2} = \frac{\Delta n^2 + \langle \hat{n} \rangle^2 - \langle \hat{n} \rangle}{\langle \hat{n} \rangle^2} = 1 \qquad (3.1.1.8)$$

Therefore, the second-order autocorrelation for coherent sources is always equal to 1 (green curve in Fig. 3.1).

Measuring $g^{(2)}(\tau)$

The Hanbury-Brown and Twiss interferometer[155] (HBT, Fig. 3.2) is conventionally used to measure the $g^{(2)}(\tau)$[34]. In this device, initially introduced in radio astronomy, incoming light encounters a $50 : 50$ beam splitter, followed by two single-photon detectors. Coincidence electronics allows us to count the number of coincidences between a photon on the first detector at time t and a photon on the second detector at time $t + \tau$. So, the second-order autocorrelation can be evaluated as:

$$g^{(2)}(\tau) = \frac{\langle n_1(t) n_2(t + \tau) \rangle}{\langle n_1(t) \rangle \langle n_2(t + \tau) \rangle} \qquad (3.1.1.9)$$

3.1.2 Low-noise CW 1550 nm SPS prototype and $g^{(2)}(0)$ measurement devices

In this subsection we present the prototype of a low-noise CW HSPS with an extremely low level of background and multi-photon component[156] and the HBTs that we will use to characterize its multi-photon component.
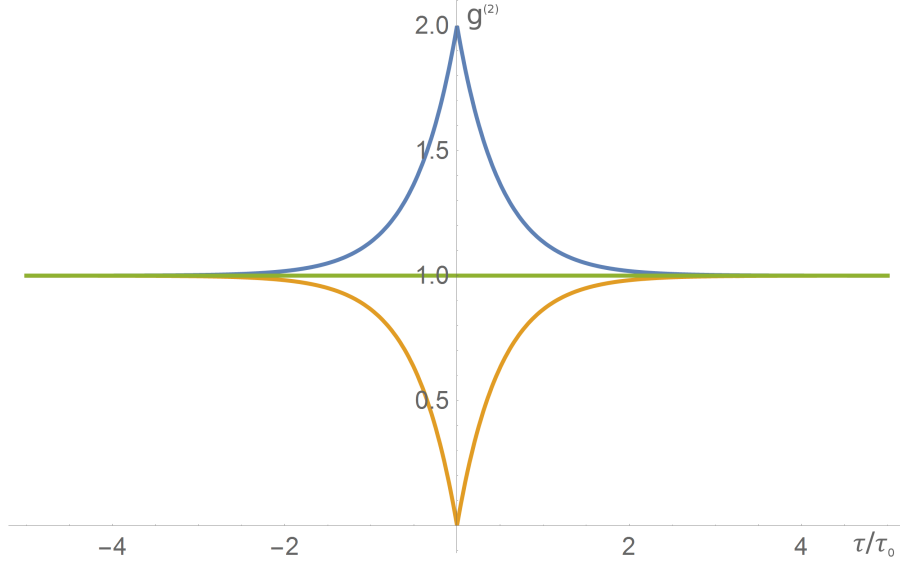
Figure 3.1: $g^{(2)}$ as a function of the normalized delay over the coherence time τ/τ_c, i.e. the time interval over which appreciable amplitude and phase correlations of the light vibrations of an optical field in a specific point in space persist[34]. The blue curve describes an example of thermal (classical) source. The green curve describes coherent light, as, for instance, the laser. The orange curve describes an example of (quantum) single-photon source.
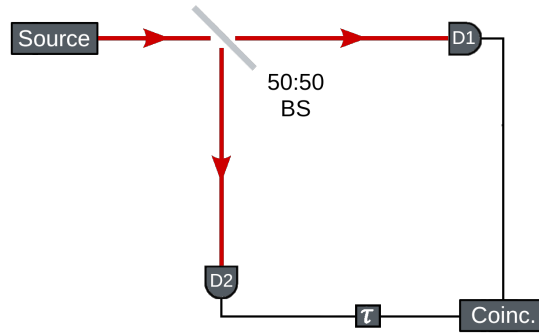
Figure 3.2: Experimental implementation of the HBT experiment. Incoming light is split and detected by the detectors D1 and D2. The output of one of the detectors can be delayed before going to the coincidence electronics.

In our prototype (section 1 of Fig. 3.3), a CW laser ($\lambda = 532$ nm) pumps a 10 mm $\times$ 1 mm $\times$ 10 mm periodically-poled lithium niobate (PPLN) crystal, producing non-degenerate Type-0 SPDC (Sec. 2.3.2). We tune the system in order to have signal and idler photons at $\lambda_s = 1550$ nm and $\lambda_i = 810$ nm, respectively. A

66
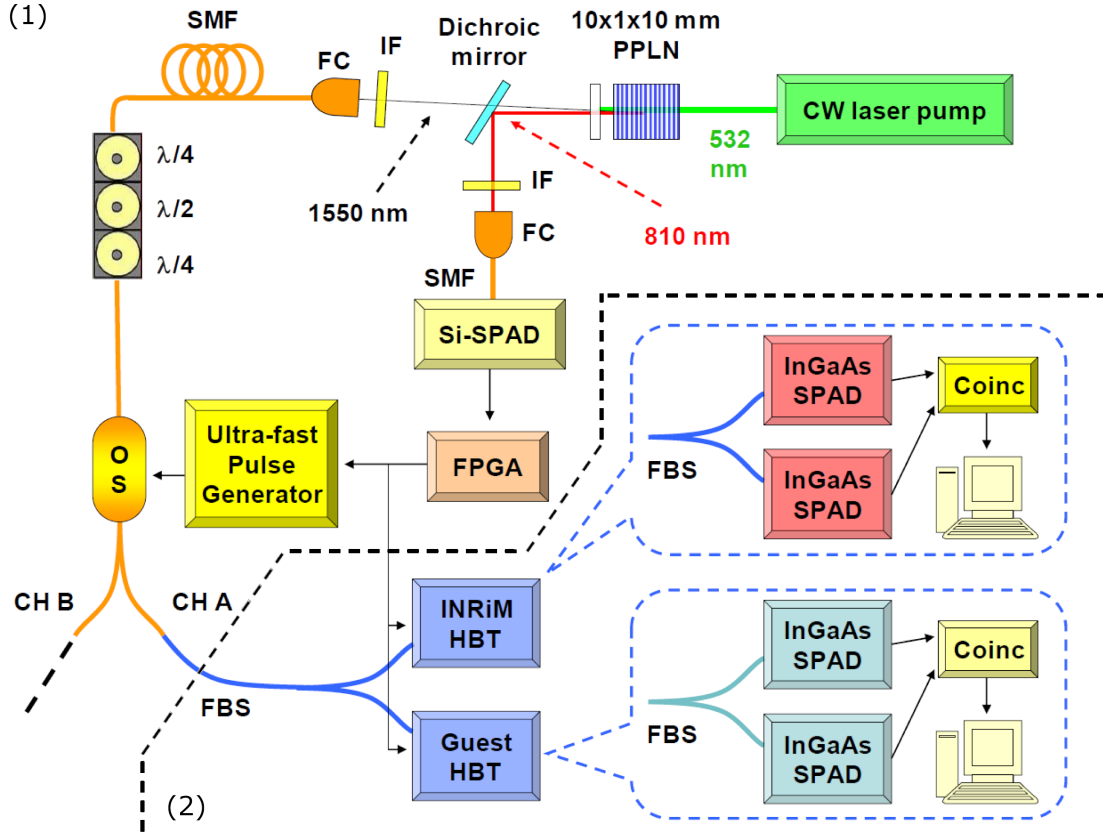
Figure 3.3: Experimental Setup. (1) SPS prototype. (2) HBT interferometers. PPLN: periodically-poled lithium niobate. FC: fibre coupler. SMF: single-mode fibre. $\lambda/4$: quarter-wave fibre paddle. $\lambda/2$: half-wave fibre paddle. OS: optical shutter. FPGA: field programmable gate array. FBS: fibre beam splitter. HBT: Hanbury-Brown and Twiss interferometer. Coinc: time-tagging coincidence electronics. ⓒⓘ E. Rebufello et al., Towards a standard procedure for the measurement of the multi-photon component in a CW telecom heralded single-photon source, Metrologia **56** (2019) 025004, https://doi.org/10.1088/1681-7575/ab022e

dichroic mirror separates the two photons.

The idler photon is sent to an interference filter (IF), centred at 810 nm and with a full width at half maximum (FWHM) of 10 nm, then, it is fibre-coupler and sent to a silicon single-photon avalanche diode (Si-SPAD). Successful detection of the idler photon heralds the arrival of the signal photon on the correlated branch.

The signal photon is addressed to a 30 nm FWHM IF centred at 1550 nm, and coupled to a 20 m long single-mode optical fibre (SMF) connected to an electro-optical shutter (OS) operated by a fast pulse generator controlled by a field programmable

gate array (FPGA). The OS is a ultra-high-speed 2×2 polarization-dependent optical switch, based on a LiNbO$_3$ Mach-Zender interferometer.

When receiving a heralding signal, the FPGA triggers a fast pulse generator with 50 ps rise-time, whose signal opens the OS channel A for a time interval $\Delta t_{switch} = 7$ ns corresponding to the passage of the signal photon. Then, the OS switches back to channel B for a tunable 'sleep' time $t_{dead} \simeq 11$ μs before accepting a new heralding. This way, we can tune the single-photons emission rate in order to avoid dead time issues with the detectors, by granting a minimum time between subsequent photons. Since, as we will see in the following, our infrared detectors have a dead time of 10 μs, we choose $t_{dead} \simeq 11$ μs.

HBT interferometers

The output of our source (channel A) is then sent to the devices involved in our multi-photon component characterization experiment (second part of Fig. 3.3). In our experiment, this is done by means of a $50 : 50$ fibre beam splitter (FBS) whose outputs are sent to two HBT interferometers, one belonging to INRiM and one to a guest national metrology institute (PTB or NPL). This configuration allows us to perform simultaneous data collection, avoiding any mismatch due to eventual drifts in the SPS output over time.

Every HBT is composed of two InGaAs-InP SPADs, either gated by the same FPGA signal which goes to the OS or free-running. Their outputs are sent to appropriate coincidence electronics. These are the configurations:

- INRiM: two calibrated MPD gated SPADs (30 ns detection window); Hydra-Harp 400 + time-to-amplitude converter (TAC);

- NPL: one id210 (gated, 25 ns) and one id230 (free-running); HydraHarp 400;

- PTB: one id210 (gated, 25 ns) and one id201 (gated, 50 ns); PicoHarp 300.

Let us take a closer look to the typical temporal histogram of one of the INRiM HBT SPADs (fig. 3.4). We can distinguish three different regions, corresponding to:

- $N^{(Her)}$ = true heralded photon counts;

- $N^{(Bkg)}$ = counts due to unheralded background photons passing through the optical switch;

- $N^{(Dark)}$ = dark counts of the detector.
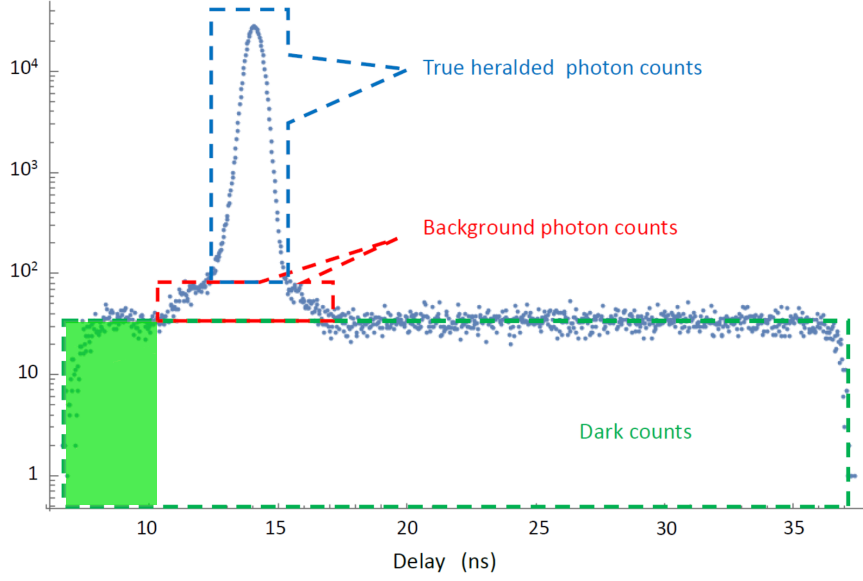
Figure 3.4: Histogram of the detections acquired in one run by one of the INRiM HBT gated SPADs (30 ns detection window). We can clearly see the true heralded photons (Her), background photons (Bkg) and dark counts (Dark). The green shaded area indicates the dark counts forbidding the SPAD to detect a photon from the HSPS (Null). ⓒ① E. Rebufello et al., Towards a standard procedure for the measurement of the multi-photon component in a CW telecom heralded single-photon source, Metrologia **56** (2019) 025004, https://doi.org/10.1088/1681-7575/ab022e

Therefore, the total number of counts of the detector can be written as:

$$N^{(Tot)} = N^{(Her)} + N^{(Bkg)} + N^{(Dark)} \tag{3.1.2.1}$$

It is possible, then, to define the total photon detection probability $P_i^{(Ph)}$ for the detector i of each HBT ($i = 1, 2$):

$$P_i^{(Ph)} = \frac{N_i^{(Ph)}}{N_i^{(Trig)}} = \frac{N_i^{(Her)} + N_i^{(Bkg)}}{N_i^{(Trig)}} = \frac{N_i^{(Tot)} - N_i^{(Dark)}}{N_i^{(Trig)}} \tag{3.1.2.2}$$

where $N_i^{(Trig)}$ is the total number of trigger signals from the FPGA.

Analogously, we can define the dark count probability as $P_i^{(Dark)} = \frac{N_i^{(Dark)}}{N_i^{(Trig)}}$, so that the overall detection probability will be $P_i^{(Tot)} = P_i^{(Ph)} + P_i^{(Dark)}$. Operatively, the number $N_i^{(Ph)}$ can be extracted as the difference between the counts of

69

the photon peak region ($N_i^{(Peak)}$, integrated on a $10ns$ time window) and the dark count belonging to a corresponding number of time bins in the dark counts region ($N_i^{(Dark=Peak)}$): $N_i^{(Ph)} = N_i^{(Peak)} - N_i^{(Dark=Peak)}$. Having extracted $N_i^{(Ph)}$, it is easy to compute the number of dark counts: $N_i^{(Dark)} = N_i^{(Tot)} - N_i^{(Ph)}$.

By carefully tuning the sleep time of the FPGA, in case of gated SPADs we can always have both detectors ready for each accepted heralding, like with dark-count-free detectors, therefore $N_1^{(Trig)} = N_2^{(Trig)} = N^{(Trig)}$. With free-running detectors, instead, $N^{(Trig)}$ only represents the number of heralding signals accepted by the FPGA and, unless dark counts are negligible (like in our case), a dead-time correction must be introduced.

3.1.3 A metrological procedure to determine the multi-photon component of a single-photon source

In order to evaluate the multi-photon component of our SPS, we want to estimate the second-order autocorrelation function $g^{(2)}(\tau = 0)$. For low total detection probabilities ($P_i^{(Tot)} \ll 1$), the second-order autocorrelation function can be approximated by the parameter α[157]:

$$\alpha = \frac{P_{12}^{(Ph;Ph)}}{P_1^{(Ph)} P_2^{(Ph)}} \simeq g^{(2)}(0) \tag{3.1.3.1}$$

where $P_{12}^{(Ph;Ph)}$ is the probability of having a coincidence photon count between the two HBT SPADs (dark counts subtracted). Since the probability of having more than one heralded photon within a 1 ns time interval (a generous estimate of the detector jitter time) is below 10^{-9}, the coincidence probability can be written as

$$P_{12}^{(Ph;Ph)} = P_{12}^{(Tot;Tot)} - P_1^{(Tot)} P_2^{(Dark)} - P_1^{(Dark)} P_2^{(Tot)} + P_1^{(Dark)} P_2^{(Dark)} \tag{3.1.3.2}$$

Where thee total coincidence probability is defined as $P_{12}^{(Tot;Tot)} = \frac{N^{(Coinc)}}{N^{(Trig)}}$, with $N^{(Coinc)}$ being the number of coincidence events between the two detectors.

Following Eq. (3.1.3.2), Eq. (3.1.3.1) can be rearranged as

$$\alpha = \frac{P_{12}^{(Tot;Tot)} - P_1^{(Tot)} P_2^{(Tot)} \left(Q_1^{(Dark)} + Q_2^{(Dark)} - Q_1^{(Dark)} Q_2^{(Dark)} \right)}{\left(P_1^{(Tot)} \left(1 - Q_1^{(Dark)} \right) \right) \left(P_2^{(Tot)} \left(1 - Q_2^{(Dark)} \right) \right)} \tag{3.1.3.3}$$

where $Q_i^{(Dark)} = \frac{N_i^{(Dark)}}{N_i^{(Tot)}}$ is the dark counts ratio on the i-th detector.

70

Null events influence on the estimation of α

The α parameter evaluation may be further refined by observing fig. 3.4: the portion of dark counts on the left of the photon peak (green shaded area) occurs before the arrival of the heralded photons. Therefore, such events forbid the SPAD to detect the heralded photons. Hence, we name them *null events.*

Null events $N_i^{(Null)}$ ($i = 1,2$), in principle, must be taken into special consideration when evaluating the α parameter, by removing them from the valid trigger events and from the SPAD counts. Then, the true valid trigger counts, dark counts and total counts will be, respectively: $N_i'^{(Trig)} = N^{(Trig)} - N_i^{(Null)}$, $N_i'^{(Dark)} = N^{(Dark)} - N_i^{(Null)}$ and $N_i'^{(Tot)} = N^{(Tot)} - N_i^{(Null)}$.
Starting from Eq. (3.1.3.1), the new formula for the parameter α will then be:

$$\alpha = \frac{P_{12}'^{(Ph;Ph)}}{P_1'^{(Ph)} P_2'^{(Ph)}} \tag{3.1.3.4}$$

Now, let us observe that, by introducing the coefficient $q_i = \frac{N^{(Trig)}}{\left(N^{(Trig)} - N_i^{(Null)}\right)}$, we can write the single-photon detection probabilities as $P_i'^{(Ph)} = q_i P_i^{(Ph)}$. Analogously, we can derive the relation $P_{12}'^{(Ph;Ph)} = q_1 q_2 P_{12}^{Ph;Ph}$ for the coincidence count probability. Substituting it into the formula for the α parameter we obtain

$$\alpha = \frac{P_{12}'^{(Ph;Ph)}}{P_1'^{(Ph)} P_2'^{(Ph)}} = \frac{q_1 q_2 P_{12}^{(Ph;Ph)}}{q_1 P_1^{(Ph)} q_2 P_2^{(Ph)}} = \frac{P_{12}^{(Ph;Ph)}}{P_1^{(Ph)} P_2^{(Ph)}} \tag{3.1.3.5}$$

which shows that these null events do not affect α. For this reason, we do not perform null events correction for the estimation of α.

Measurement procedures

In our experiment we perform two direct comparisons: one between INRiM and NPL and one between INRiM and PTB, in which both institutes perform simultaneous measurements. Let us now thoroughly analyse the different measurement procedures that we employ in this comparison.

INRiM   INRiM's HBT comprises a $50 : 50$ FBS and two calibrated MPD single-photon counters based on InGaAs/InP gated SPADs, with a $30ns$ detection window. Their outputs, together with the FPGA gating signal, are addressed to a time-tagger (HydraHarp400) with a $2.5ps$ time-bin resolution and to a time-to-amplitude converter (TAC), in order to evaluate single counts and coincidence counts separately. This way, each acquisition can host both the single- and two-photon counts.

In order to avoid missing any coincidence, coincidence windows of both the time-tagger and the TAC are set to 100 ns.

Recalling Eq. (3.1.3.3)

$$\alpha = \frac{P_{12}^{(Tot;Tot)} - P_1^{(Tot)} P_2^{(Tot)} \left(Q_1^{(Dark)} + Q_2^{(Dark)} - Q_1^{(Dark)} Q_2^{(Dark)} \right)}{\left(P_1^{(Tot)} \left(1 - Q_1^{(Dark)} \right) \right) \left(P_2^{(Tot)} \left(1 - Q_2^{(Dark)} \right) \right)}$$

the total detector and coincidence probabilities are obtained from the TAC counts (indicated by the $\sim$ symbol), acquired in 40 $100s$ sets: $P_i^{(Tot)} = \frac{\left\langle \tilde{N}_i^{(Tot)} \right\rangle}{\left\langle \tilde{N}_i^{(Trig)} \right\rangle}$, where the $\langle \tilde{N} \rangle$ are mean values over these repeated acquisitions. The dark count ratios, instead, are extracted from the multi-channel analyser (MCA) histograms of the two detectors forming the HBT integrating all the counts registered by the time-tagger within the whole acquisition time: $Q_i^{(Dark)} = \frac{N_i^{(Dark)}}{N_i^{(Tot)}}$.

NPL and PTB   NPL HBT hosts a 50 : 50 FBS and two ID Quantique detectors: a gated InGaAs/InP SPAD (ID210, with a 25 ns detection window) and a low-noise free-running InGaAs/InP SPAD (ID230). Their outputs, together with the FPGA gating signal, are addressed to a HydraHarp400 time-tagger. For the comparison, we opted to perform three measurements:

1. a 1000 s acquisition using the FPGA as external clock and feeding the HydraHarp400 with the two detector outputs;

2. a 2000 s acquisition in which the ID210 acts as the external clock and the ID230 is the only input of the time-tagger;

3. a second 1000 s acquisition, with the same settings as the first one.

This method allows us to make a time-correlated evaluation of the HBT coincidences, while minimizing the eventual temporal fluctuations and drifts. Since one of the detectors of the HBT is free-running, we set a larger time window of 200 ns on the time-tagger, in order not to loose any significant event.

PTB HBT, instead, hosts a 50 : 50 FBS and two ID Quantique gated infrared detectors (one ID210 and one ID201, with, respectively, 25 ns and 50 ns detection windows). The time-tagging system, however, is a PicoHarp300, which hosts only one input channel, plus an external clock. Such time-tagger makes it impossible to evaluate simultaneously the single- and two-photon counts, therefore, we opt for the same method described for NPL HBT. In the first and last run, both detectors are evaluated at once, by feeding both outputs of the detectors to the single

PicoHarp300 input channel, by adding a proper delay to one of the two outputs. In the central run, the ID210 acts as external clock for the ID201. Since the sum of both SPADs detection windows is around 75 ns, we set a 100 ns window in the time-tagging electronics.

In both HBTs, the total single count probabilities are evaluated as $P_i^{(Tot)} = \frac{N_i^{(Tot)}}{N_S^{(Trig)}}$, where $N_S^{(Trig)}$ is the number of FPGA valid gates for the two single-photon events acquisitions. The two-photon count probability, instead, is $P_{12}^{(Tot;Tot)} = \frac{N^{(Coinc)}}{N_C^{(Trig)}}$, where $N_S^{(Trig)}$ is the number of FPGA valid gates for the two-photon events acquisitions. The dark counts ratios estimation is the same as the one described for INRiM.

Results

Session	α (INRiM)	α (NPL)	α (PTB)
INRiM-NPL	0.013 ± 0.008	0.02 ± 0.02	-
INRiM-PTB	0.016 ± 0.006	-	0.04 ± 0.05

Table 3.1: Experimental results obtained within the pilot comparison. Coverage factor: $k = 1$.

Table 3.1 hosts the results obtained by INRiM, NPL and PTB during the different measurement session of the $g^{(2)}(0)$ of the HSPS. As we can see, all measurements are in agreement between each other even with a coverage factor $k = 1$.

Uncertainty budgets

In this section, we thoroughly analyse the uncertainty contributions to the estimation of the parameter α.

INRiM Three elements contribute to the INRiM uncertainty budget (Tabs. 3.2, 3.3):

- $u_{(P)}(\alpha)$: uncertainty derived from the double and single total photon count probabilities ($P_{12}^{(Tot;Tot)}$ and $P_i^{(Tot)}$), given by the TAC counts;

- $u_{(Q_i)}(\alpha)$: uncertainty derived from the dark counts fraction $Q_i^{(Dark)}$ of each SPAD, evaluated from the HydraHarp400 histograms.

The first contribution is evaluated as

$$u_{(P)}(\alpha) = \sqrt{\sum_{l,m=0}^{3} C_{l,m} \left(\frac{\partial \alpha}{\partial \tilde{N}_l} \right) \left(\frac{\partial \alpha}{\partial \tilde{N}_m} \right) u\left(\tilde{N}_l \right) u\left(\tilde{N}_m \right)} \qquad (3.1.3.6)$$

$$C_{l,m} = \frac{\langle \tilde{N}_l \tilde{N}_m \rangle - \langle \tilde{N}_l \rangle \, \langle \tilde{N}_m \rangle}{u(\tilde{N}_l) u(\tilde{N}_m)} \tag{3.1.3.7}$$

where $\tilde{N}_0 = \tilde{N}^{(Trig)}$, $\tilde{N}_i = \tilde{N}_i^{(Tot)}$ $(i = 1, 2)$, $\tilde{N}_3 = \tilde{N}^{(Coinc)}$ and $u(\tilde{N}_k)$ being the uncertainty on the average $\langle \tilde{N}_k \rangle$. The measured correlation coefficients $C_{i,j}$ $(i, j = 0, \cdots, 3)$ among the $\tilde{N}_i$ are reported in Tab. 3.4.

Evaluating the second and third contributions $(u_{Q_i}(\alpha))$ by merely extracting them from the HydraHarp400 histograms would lead to an overestimation of the total uncertainty $u(\alpha)$. Therefore, we need a better strategy. Knowing that $Q_i^{(Dark)} = \frac{N_i^{(Dark)}}{N_i^{(Tot)}} = 1 - \frac{\tilde{N}_i^{(Ph)}}{\tilde{N}_i^{(Tot)}}$, we can write:

$$
\begin{aligned}
u^2(Q_i^{(Dark)}) =& \left(\frac{1}{\tilde{N}_i^{(Tot)}} \right)^2 u^2(\tilde{N}_i^{(Ph)}) + \left(\frac{\tilde{N}_i^{(Ph)}}{(\tilde{N}_i^{(Tot)})^2} \right)^2 u^2(\tilde{N}_i^{(Tot)}) \\
&- 2 \left(\frac{1}{\tilde{N}_i^{(Tot)}} \right) \left(\frac{\tilde{N}_i^{(Ph)}}{(\tilde{N}_i^{(Tot)})^2} \right) \left(\langle \tilde{N}_i^{(Tot)} \tilde{N}_i^{(Ph)} \rangle - \langle \tilde{N}_i^{(Tot)} \rangle \, \langle \tilde{N}_i^{(Ph)} \rangle \right)
\end{aligned}
\tag{3.1.3.8}
$$

Since $\tilde{N}_i^{(Tot)} = \tilde{N}_i^{(Ph)} + \tilde{N}_i^{(Dark)}$, it is easy to see that

$$\left(\langle \tilde{N}_i^{(Tot)} \tilde{N}_i^{(Ph)} \rangle - \langle \tilde{N}_i^{(Tot)} \rangle \, \langle \tilde{N}_i^{(Ph)} \rangle \right) = u^2(\tilde{N}_i^{(Ph)}) \leq u^2(\tilde{N}_i^{(Tot)}) \tag{3.1.3.9}$$

therefore

$$u(Q_i^{(Dark)}) \leq \frac{Q_i^{(Dark)}}{\tilde{N}_i^{(Tot)}} u(\tilde{N}_i^{(Tot)}) \tag{3.1.3.10}$$

which provides us an upper bound for the uncertainty contributions:

$$u_{(Q_i)}(\alpha) = \left| \frac{\partial \alpha}{\partial Q_i^{(Dark)}} \right| u(Q_i^{(Dark)}) \tag{3.1.3.11}$$

Since no correlation exists among these three contribution, the total uncertainty on α can be expressed as:

$$u(\alpha) = \sqrt{u_{(Q_1)}^2(\alpha) + u_{(Q_2)}^2(\alpha) + u_{(P)}^2(\alpha)} \tag{3.1.3.12}$$

NPL and PTB Since they share the acquisition method, NPL and PTB measurement uncertainties are evaluated in the same way:

$$u(\alpha) = \sqrt{\sum_{l=0}^{6} \left(\frac{\partial \alpha}{\partial N_l} \right)^2 u^2(N_l)} \tag{3.1.3.13}$$

	Quantity	Unc.	Sens. Coeff	Unc. Contr.
$Q_1^{(Dark)}$	0.05604	0.00008	1.0461	0.00010
$Q_2^{(Dark)}$	0.05607	0.00008	1.0462	0.00010
$\tilde{N}^{(Trig)}$	6.0133×10^6	2.6×10^3	2.242×10^{-8}	0.00006
$\tilde{N}_1^{(Tot)}$	18261	31	7.382×10^{-6}	0.0002
$\tilde{N}_2^{(Tot)}$	19396	32	6.950×10^{-6}	0.0002
$\tilde{N}^{(Coinc)}$	7.1	0.4	0.01905	0.008
α	0.013	0.008		

Table 3.2: INRiM uncertainty budget related to the INRiM-NPL measurement session. Coverage factor: $k = 1$. Unc.: uncertainty. Sens. Coeff.: sensitivity coefficient. Unc. Contr.: contribution to the global uncertainty on α.

	Quantity	Unc.	Sens. Coeff.	Unc. Contr.
$Q_1^{(Dark)}$	0.04525	0.00008	1.0302	0.00008
$Q_2^{(Dark)}$	0.04875	0.00009	1.0340	0.00009
$\tilde{N}^{(Trig)}$	6.1885×10^6	2.4×10^3	1.898×10^{-8}	0.00005
$\tilde{N}_1^{(Tot)}$	22490	41	5.223×10^{-6}	0.0002
$\tilde{N}_2^{(Tot)}$	23407	42	5.018×10^{-6}	0.0002
$\tilde{N}^{(Coinc)}$	9.1	0.5	0.01294	0.006
α	0.016	0.006		

Table 3.3: INRiM uncertainty budget related to the INRiM-PTB measurement session. Coverage factor: $k = 1$.

with $N_0 = N_S^{(Trig)}$, $N_i = N_i^{(Tot)}$ and $N_{2+i} = N_i^{(Dark)}$ ($i = 1, 2$), $N_5 = N_C^{(Trig)}$ and $N_6 = N^{(Coinc)}$.

Since both NPL and PTB did not have repeated measurements, we had to provide a sensible upper bound to the uncertainties, by means of physical and statistical considerations on the source and measurement device. Since the dark counts of the detectors are known to follow a Poissonian distribution and the distribution of a multi-mode PDC is almost indistinguishable from a Poissonian distribution, we can assume the fluctuations of the N_j quantities to be Poissonian. Therefore, we assign the value $u(N_j) = \zeta \sqrt{N_j}$ to the uncertainties related to the quantities N_j, being ζ a coefficient which takes into account the eventual super-poissonian behaviour of the system. In our case we opted for a conservative $\zeta = 2$, because of some unexpected fluctuations in the CW pump power. NPL and PTB uncertainty budgets are reported in Tabs. 3.5 and 3.6, respectively.

	INRiM-NPL	INRiM-PTB
$C_{0,1}$	0.326	0.857
$C_{0,2}$	0.445	0.891
$C_{0,3}$	0.269	0.133
$C_{1,2}$	0.650	0.824
$C_{1,3}$	0.00261	-0.000155
$C_{2,3}$	-0.000909	0.00161

Table 3.4: Correlation coefficients related to the INRiM measurements in both sessions.

	Quantity	Unc.	Sens. Coeff.	Unc. Contr.
$N_S^{(Trig)}$	1.20348×10^8	$\zeta \cdot 1.1 \times 10^4$	1.042×10^{-9}	$\zeta \cdot 0.00002$
$N_1^{(Tot)}$	304900	$\zeta \cdot 600$	1.726×10^{-7}	$\zeta \cdot 0.00010$
$N_2^{(Tot)}$	283300	$\zeta \cdot 600$	1.003×10^{-7}	$\zeta \cdot 0.00005$
$N_1^{(Dark)}$	3100	600	3.256×10^{-6}	0.00018
$N_2^{(Dark)}$	9600	100	3.590×10^{-6}	0.0004
$N_C^{(Trig)}$	1.20184×10^8	$\zeta \cdot 1.1 \times 10^4$	5.218×10^{-10}	$\zeta \cdot 0.00001$
$N^{(Coinc)}$	43	$\zeta \cdot 7$	0.00146	$\zeta \cdot 0.010$
α	0.02	0.02		

Table 3.5: NPL uncertainty budget related to the INRiM-NPL measurement session. Coverage factor: $k = 1$. We set $\zeta = 2$.

3.1.4 Conclusion

In this section we illustrated a strategy to evaluate the multi-photon component of a CW HSPS and applied it to a low-noise prototype fibre HSPS at 1550 nm. Then, we showed the results of a pilot comparison, carried out with different measurement setups and data collection methodologies; these results are all in agreement with each other within the experimental uncertainties, even with a coverage factor $k = 1$, certifying the flexibility, reliability and robustness of our strategy.

We believe that our proposed strategy, which is adaptable to a large variety of detectors and coincidence electronics, may pave the way to a standardization of the characterization of single-photon sources, one of the most important tasks of present and future quantum metrology for the widespread diffusion of incoming quantum technologies.

	Quantity	Unc.	Sens. Coeff.	Unc. Contr.
$N_S^{(Trig)}$	1.23807×10^8	$\zeta \cdot 1.1 \times 10^4$	1.031×10^{-8}	$\zeta \cdot 0.00011$
$N_1^{(Tot)}$	453500	$\zeta \cdot 700$	1.140×10^{-6}	$\zeta \cdot 0.0008$
$N_2^{(Tot)}$	474200	$\zeta \cdot 700$	4.4884×10^{-7}	$\zeta \cdot 0.0004$
$N_1^{(Dark)}$	50700	300	2.390×10^{-6}	0.0006
$N_2^{(Dark)}$	140800	400	2.888×10^{-6}	0.0011
$N_C^{(Trig)}$	1.23733×10^8	$\zeta \cdot 1.1 \times 10^4$	5.158×10^{-10}	$\zeta \cdot 0.00006$
$N^{(Coinc)}$	690	$\zeta \cdot 30$	0.0009224	$\zeta \cdot 0.03$
α	0.04	0.05		

Table 3.6: PTB uncertainty budget related to the INRiM-PTB measurement session. Coverage factor: $k = 1$. We set $\zeta = 2$.

3.2 Optimal measurement of Entanglement and Discord in two-photon states

In this section we focus on the problem of evaluating the amount of entanglement (Sec. 1.1.1) and *Quantum Discord* (Sec. 1.1.1) in two-photon states generated by entangled-photon sources (Sec. 2.3.2). A robust way to perform such evaluation would be to completely reconstruct the quantum state of the two photons, via a process called quantum tomography (Sec. 3.2.3). Unfortunately, while this reconstruction technique provides all the information on the physical system under analysis, it is also a demanding procedure due the high number of measurements required on identical copies of the system, especially for large Hilbert spaces. Furthermore, being based on optimization algorithms, tomography does not allow to perform a direct estimation of the uncertainty associated with the reconstructed density matrix, nor the reconstructed density matrix provides an immediate quantification of the amount of entanglement or Quantum Discord, that need to be quantified with some parameters (Sec. 1.3). For these reasons, several methods have been proposed to speed up the evaluation, such as Bell tests[22], visibility experiments[93], etc.

There are, however, more efficient ways to estimate the amount of entanglement and Quantum Discord in a multipartite system when one has a small a-priori information on the state under investigation. We decide to focus on the estimation of some of the parameters which characterize the entanglement and Quantum Discord. In the following sections, we introduce a set of unbiased estimators for a selection of parameters able to characterize entanglement and Discord for a specific class of two-qubit states. Then, we present an experiment in which we measure such estimators as well as the uncertainties associated with them, comparing them with the theoretical predictions.

3.2.1 Parameters estimators

In this section, we introduce two unbiased estimators, one optimal and one non-optimal, for four parameters of interest: Concurrence (Sec. 1.3.3), Negativity (Sec. 1.3.4), Log-Negativity (Sec. 1.3.5) and Quantum Geometric Discord (Sec. 1.3.6). We only focus on unbiased estimation because we assume a simple "prepare and measure" experiment, in which we have no a priori knowledge of the produced state, except the family of states to which it belongs.

We define our estimators for the specific family of states that we are going to test. These are the quantum states whose density matrix can be expressed in the following form:

$$\hat{\rho} = (1-p) \begin{pmatrix} 0 & 0 & 0 & 0 \\ 0 & q & 0 & 0 \\ 0 & 0 & 1-q & 0 \\ 0 & 0 & 0 & 0 \end{pmatrix} + p \begin{pmatrix} 0 & 0 & 0 & 0 \\ 0 & q & -\sqrt{q(1-q)} & 0 \\ 0 & -\sqrt{q(1-q)} & 1-q & 0 \\ 0 & 0 & 0 & 0 \end{pmatrix} \quad (3.2.1.1)$$

where p and q are unknown variables in the interval $[0,1]$. This density matrix describes a wide range of states, from the maximally entangled singlet state ($p = 1$, $q = 1/2$) to a completely decoherent mixture ($p = 0$, $q = 1/2$). These are typical quantum states involved in several real-world scenarios in which entangled states (such as the ones produced by Type-II SPDC) are exposed to decoherence, due to coupling with the environment, which degrades the quantum resources available for the task we want to execute. Thus, their characterization plays an important role for the scientific and industrial community.

Let us now define the unbiased estimators for each entanglement parameter and their corresponding theoretical minimal uncertainty, thanks to the Quantum Cramér-Rao bound (QCRB), introduced in Sec. 1.4.1. These definitions were reached by trying different combinations of measurable parameters for our system. In particular, we focused on the coincidence probabilities for the four possible combination of measured diagonal polarizations.

Negativity estimators

For our family of states, the Negativity becomes:

$$\mathcal{N} = 2p\sqrt{q(1-q)} \quad (3.2.1.2)$$

From which we can calculate the QCRB for estimating the Negativity with a single measurement:

$$\text{QCRB}_{\mathcal{N}} = 1 - \mathcal{N}^2 \quad (3.2.1.3)$$

thus, the optimal estimation of Negativity has an associated uncertainty:

$$\text{unc}_{\mathcal{N}} = \frac{\sqrt{\text{QCRB}_{\mathcal{N}}}}{\sqrt{n}} = \frac{\sqrt{1 - \mathcal{N}^2}}{\sqrt{n}} \tag{3.2.1.4}$$

where n is the number of repeated measurements.
First, we define a non-optimal estimator $\varepsilon\mathcal{N}_1$ as

$$\varepsilon\mathcal{N}_1 = 1 - 4P(++) \tag{3.2.1.5}$$

where $P(X)$ is the probability of the coincidence event X and the symbol $+(-)$ indicates projection onto the state $|+(-)\rangle = \frac{|H\rangle + (-)|V\rangle}{\sqrt{2}}$, $|H\rangle$ and $|V\rangle$ being the horizontal and vertical polarization, respectively. The probability of finding a pair of photons both with diagonal polarization is calculated as:

$$P(++) = N(++)/(N(++) + N(+-) + N(-+) + N(--)) \tag{3.2.1.6}$$

where N is the number of detected photon pairs.

The theoretical minimum uncertainty associated with the non-optimal estimator $\varepsilon\mathcal{N}_1$ is

$$\text{unc}_{\varepsilon\mathcal{N}_1} = \frac{\sqrt{-(\mathcal{N}^2 + 2\mathcal{N} - 3)}}{\sqrt{n}} \tag{3.2.1.7}$$

Second, we define the optimal estimator $\varepsilon\mathcal{N}_2$ as

$$\varepsilon\mathcal{N}_2 = P(+-) + P(-+) - P(++) - P(--) \tag{3.2.1.8}$$

which has a theoretical minimum uncertainty equal to the one set by the saturation of the QCRB (Eq. (3.2.1.4)).

Log-Negativity estimators

As previously described, the Log-Negativity is the base-2 logarithm of the Negativity. Therefore, we can easily derive its expression for our family of states:

$$\mathcal{L} = \log_2(2p\sqrt{q(1-q)} + 1) \tag{3.2.1.9}$$

and the corresponding QCRB:

$$\text{QCRB}_{\mathcal{L}} = -\frac{2^{-\mathcal{L}}(2^{\mathcal{L}} - 2)}{\log^2(2)} \tag{3.2.1.10}$$

Similarly, we define the non-optimal and optimal estimators $\varepsilon\mathcal{L}_1$ and $\varepsilon\mathcal{L}_2$ as the base-2 logarithm of their corresponding Negativity estimators:

$$\varepsilon\mathcal{L}_1 = \log_2\left[1 - 4\left(P(++) - \frac{1}{4}\right)\right] \tag{3.2.1.11}$$

$$\varepsilon\mathcal{L}_2 = \log_2\left[1 - (P(+-) + P(-+) - P(++) - P(--))\right] \tag{3.2.1.12}$$

with associated uncertainties

$$\text{unc}_{\varepsilon\mathcal{L}_1} = \sqrt{-\frac{4^{-\mathcal{L}}(4^{-\mathcal{L}} - 4)}{\log^2(2)}\frac{1}{\sqrt{n}}} \tag{3.2.1.13}$$

$$\text{unc}_{\varepsilon\mathcal{L}_2} = \sqrt{-\frac{2^{-\mathcal{L}}(2^{\mathcal{L}} - 2)}{\log^2(2)}\frac{1}{\sqrt{n}}} \tag{3.2.1.14}$$

where n is the number of measurements. The second estimator $\varepsilon\mathcal{L}_2$ saturates the QCRB.

Concurrence estimators

For our family of states, the Concurrence becomes:

$$\mathcal{C} = 2p\sqrt{q(1-q)} \tag{3.2.1.15}$$

which is identical to the expression for the Negativity (Eq. (3.2.1.2)). Therefore, we can exploit the QCRB and the estimators introduced for the Negativity to evaluate the Concurrence. Note, however, that the equivalence between Negativity and Concurrence only holds for our specific family of states, and is not true in general.

Quantum Geometric Discord estimators

Since our states are symmetric under exchange of subsystems, the two definitions of Quantum Discord are equivalent, i.e. $\mathcal{D}_A = \mathcal{D}_B = \mathcal{D}$. Therefore, the QGD for our family of states is:

$$\mathcal{GD} = 2p^2(1-q)q \tag{3.2.1.16}$$

that can be rearranged as a function of the Negativity:

$$\mathcal{GD} = \frac{\mathcal{N}^2}{2} \tag{3.2.1.17}$$

Again, this result, which ties QGD and Negativity, is only true for our family of states and not in general. From the Negativity QCRB, we can calculate the QGD one:

$$\text{QCRB}_{\mathcal{GD}} = 2(1 - 2\mathcal{GD})\mathcal{GD} \tag{3.2.1.18}$$

The non-optimal estimator $\varepsilon\mathcal{GD}_1$ and the optimal estimator $\varepsilon\mathcal{GD}_2$ also follow from the Negativity ones:

$$\varepsilon\mathcal{GD}_1 = \frac{1}{2}(1 - 4P(++))^2 \tag{3.2.1.19}$$

$$\varepsilon\mathcal{GD}_2 = \frac{1}{2}(P(+-) + P(-+) - P(++) - P(--))^2 \tag{3.2.1.20}$$

with associated theoretical uncertainties:

$$\text{unc}_{\varepsilon\mathcal{GD}_1} = \sqrt{-2\mathcal{GD}(2\mathcal{GD} + 2\sqrt{2}\sqrt{\mathcal{GD}} - 3)}\frac{1}{\sqrt{n}} \qquad (3.2.1.21)$$

$$\text{unc}_{\varepsilon\mathcal{GD}_2} = \sqrt{2(1 - 2\mathcal{GD})\mathcal{GD}}\frac{1}{\sqrt{n}} \qquad (3.2.1.22)$$

where n is the number of measurements. The second one saturates the QCRB.

3.2.2 Experimental apparatus
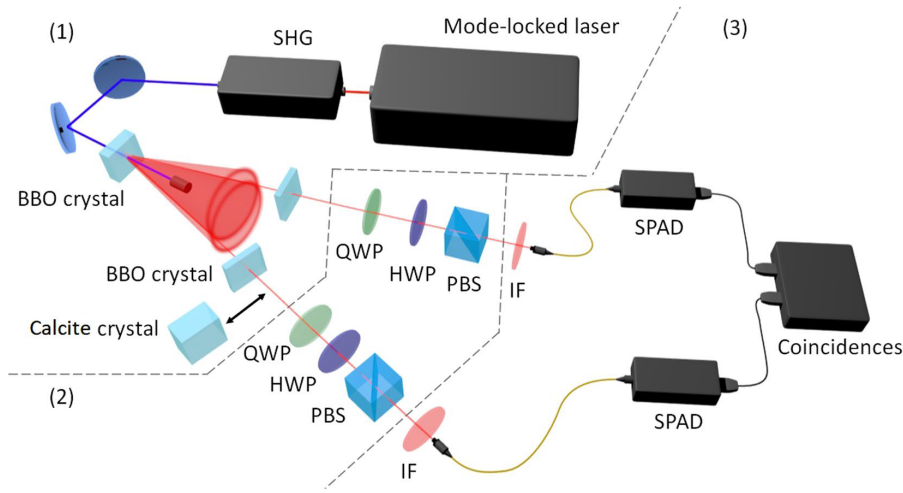
Figure 3.5: Experimental apparatus. SHG: second harmonic generator. BBO: β-Barium Borate non-linear crystal. QWP: quarter wave plate. HWP: half wave plate. PBS: polarising beam splitter. IF: interference filters. SPAD: single-photon avalanche diode. ⓒⓘ S. Virzì et al., Optimal estimation of entanglement and discord in two-qubit states, Scientific Reports **9**, 3030 (2019) https://doi.org/10.1038/s41598-019-39334-8

In order to reproduce the states in Eq. (3.2.1.1), we exploit the phenomenon of Type-II spontaneous parametric down conversion (SPDC) (Sec. 2.3.2), producing two-photon polarization-entangled states.

The first part of the setup (region 1 of Fig. 3.5) is our source of biphoton states. A Ti:Sapphire mode-locked laser, emitting pulses with duration of 150 fs at a wavelength centred on 808 nm, pumps a second harmonic generation (SHG) crystal, which produces a 404 nm pulsed beam. Such beam pumps a 0.5 mm long β-barium borate (BBO) non-linear crystal, in which type-II SPDC occurs, generating photon pairs. We spatially select the photons belonging to the intersection region of the two cones with two irises, and address them to two 0.25 mm thick BBO

crystals with the optical axis rotated of 90° with respect to the one of the PDC crystal on the orthogonal plane to the propagation direction. This crystals allow us to compensate the temporal delay between the horizontally- and the vertically-polarized photons induced by the birefringence within the SPDC crystal. This way, we produce a state:

$$|\psi_\varphi\rangle = \frac{|HV\rangle + e^{i\varphi}|VH\rangle}{\sqrt{2}} \tag{3.2.2.1}$$

where H and V represent, respectively, the horizontal and vertical polarization components and φ is the relative phase between the ordinary and extraordinary polarized light. By performing a fine tilting of one of the two crystals, we can tune the parameter φ to a chosen value (0, in our case).

Decoherence can be induced by introducing, in one of the two paths, a 2.7 mm thick birefringent calcite crystal with the optical axis orthogonal to the propagation direction, introducing temporal walk-off without modifying the photons spatial degree of freedom.

The second part of the setup (region 2) is a quantum tomography apparatus, in which each path is equipped with a quarter wave plate (QWP), a half wave plate (HWP) and a polarizing beam splitter (PBS). Together, they allow us to project each photon onto any polarisation state belonging to the surface of the Bloch sphere[27].

The third part of the setup (region 3) is dedicated to photon detection. In each path, an interference filter (IF) centred on 808 nm spectrally selects the photons. One filter has a 3 nm FWHM, while the other a 20 nm FWHM. The filtered photons, then, are fibre coupled and sent to a Silicon single-photon avalanche diode (SPAD) for the detection. A dedicated time-tagging system performs temporal post-selection on photon counts.

3.2.3 State reconstruction

Our setup is able to produce either pure singlet states $|\psi_-\rangle$ or completely decoherent states ρ_{mix}:

$$\rho^{th}_{|\psi_-\rangle} = \begin{pmatrix} 0 & 0 & 0 & 0 \\ 0 & \frac{1}{2} & -\frac{1}{2} & 0 \\ 0 & -\frac{1}{2} & \frac{1}{2} & 0 \\ 0 & 0 & 0 & 0 \end{pmatrix} \quad \rho^{th}_{mix} = \begin{pmatrix} 0 & 0 & 0 & 0 \\ 0 & \frac{1}{2} & 0 & 0 \\ 0 & 0 & \frac{1}{2} & 0 \\ 0 & 0 & 0 & 0 \end{pmatrix} \tag{3.2.3.1}$$

States with different amounts of decoherence described in Eq. (3.2.1.1) are reproduced by realizing a statistical mixture of our data in post-processing. The

procedure consists of performing all the measurements required by our four estimators for both the singlet and the completely decoherent state, with an appropriate redundancy. Then, in post-processing, we mix the results in different percentages, in order to simulate several states, each with a different amount of decoherence.

The first step of our data analysis, however, is to evaluate the quality of the produced states. To do so, we need to reconstruct the quantum state. Such reconstruction is performed through quantum state tomography[92, 158], a process which allows to completely characterize, through a set of measurements mapping the whole Bloch sphere, the density matrix of the system under investigation. In our case, we measure all 36 combinations of the following six states, which correspond to the three mutually unbiased bases constituting the three orthogonal axes of the Bloch sphere:

$$
\begin{aligned}
&|H\rangle \\
&|V\rangle \\
&|+\rangle = \frac{1}{\sqrt{2}}(|H\rangle + |V\rangle) \\
&|-\rangle = \frac{1}{\sqrt{2}}(|H\rangle - |V\rangle) \\
&|R\rangle = \frac{1}{\sqrt{2}}(|H\rangle + i\,|V\rangle) \\
&|L\rangle = \frac{1}{\sqrt{2}}(|H\rangle - i\,|V\rangle)
\end{aligned}
\tag{3.2.3.2}
$$

This allows us to reconstruct the 15 Stokes parameters which characterize the polarization state of a bipartite system through a minimization algorithm[92]. From them, then, we extract the reconstructed density matrix (Fig. 3.6).

In order to evaluate the distance between theoretical and reconstructed states, we calculate Uhlmann's Fidelity (App. A):

$$
F = \mathrm{Tr}\left(\sqrt{\sqrt{\rho^{exp}}\rho^{th}\sqrt{\rho^{exp}}}\right)
\tag{3.2.3.3}
$$

where ρ^{exp} and ρ^{th} are, respectively, the reconstructed and theoretical density matrix. From the reconstruction (Fig. 3.6), we obtain the values $F_{\psi_-} = 0.975$ and $F_{\rho_{mix}} = 0.985$, certifying the compatibility between our experimental states and the theoretical ones.

3.2.4   Results

Fig. 3.7 shows the results of our work. There, we plot the experimental points for each estimator as a function of the mixing parameter p, which ranges between
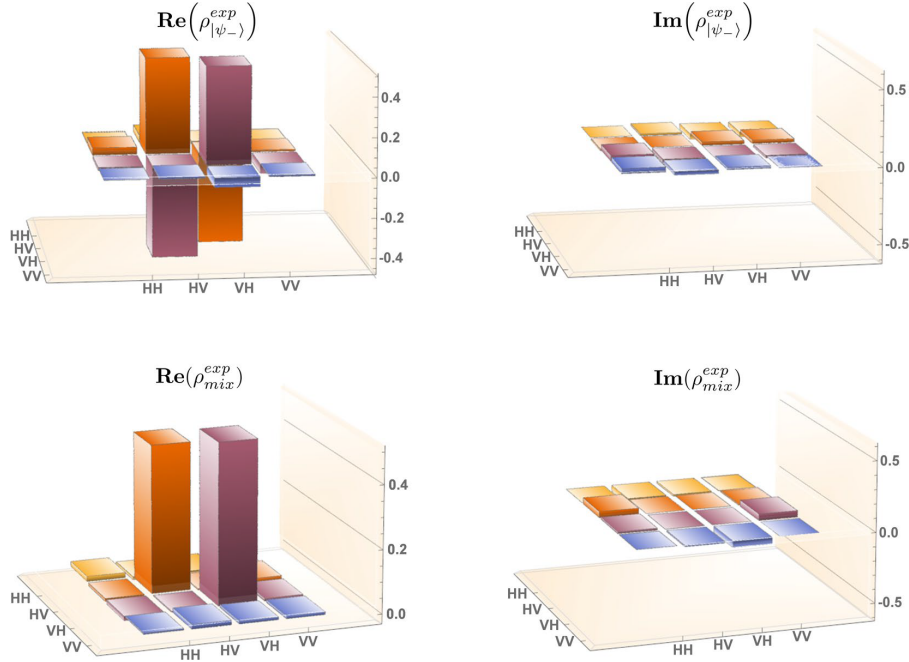
Figure 3.6: Real (left) and imaginary (right) part of the tomographically reconstructed density matrix for the singlet, maximally-entangled state (top) and the completely decoherent mixture (bottom). ⓒⓘ S. Virzì et al., Optimal estimation of entanglement and discord in two-qubit states, Scientific Reports **9**, 3030 (2019) https://doi.org/10.1038/s41598-019-39334-8

0 (completely decoherent mixture) and 1 (maximally entangled state).

The effective value of p of each point is evaluated by exploiting the tomographical reconstruction of the density matrix of the corresponding quantum state. Each point is the result of the average of 10 independent estimations on different data sets. The uncertainty bars are obtained by propagating the standard deviation of the measurement results statistical distribution. Therefore, they represent the uncertainty of a single estimation.

As for p, the parameter q is obtained from the tomographical reconstruction of the density matrices of the physical systems involved in the experiment.
The theoretical value of the estimand parameter is represented by a dotted line, while the theoretical values for the Cramér-Rao bound and the theoretical uncertainty of the non-optimal estimator are represented by the continuous and dashed curves, respectively.

Our results (Fig. 3.7) show a good agreement between theory and experiment for each estimator, both for the value and the associated statistical uncertainty. In
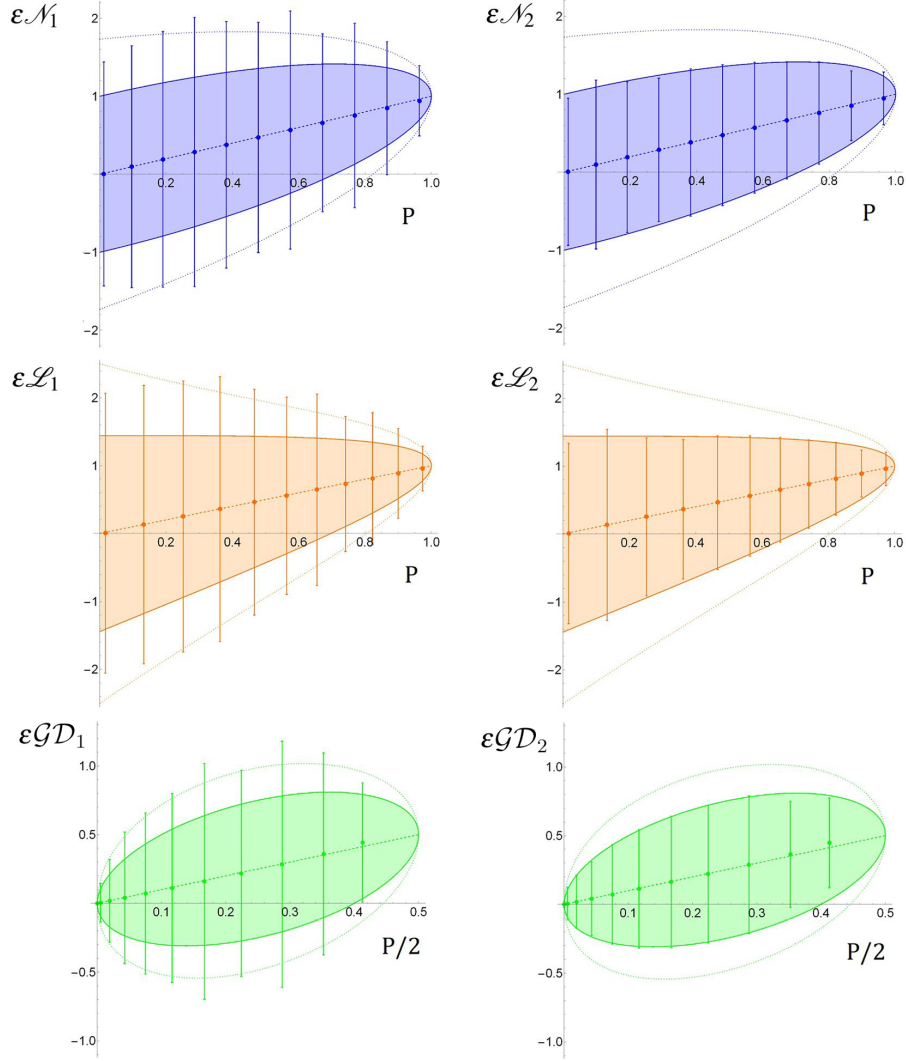
Figure 3.7: Results for Negativity and Concurrence (blue), Log-Negativity (orange) and Quantum Geometric Discord (green) with respect to *p*. Left: non-optimal estimators. Right: optimal estimators. Dashed lines: theoretical values of the quantity to estimate. Dotted lines: theoretical uncertainty for non-optimal estimators. Solid curve: theoretical uncertainty from the quantum Cramér-Rao bound. ©① S. Virzì et al., Optimal estimation of entanglement and discord in two-qubit states, Scientific Reports **9**, 3030 (2019) https://doi.org/10.1038/s41598-019-39334-8

the case of optimal estimators, this demonstrates the saturation of the Quantum Cramér-Rao bound. Furthermore, it is possible to notice an important reduction of uncertainties between optimal and non-optimal estimators, a clear confirmation of the difference between optimal and non-optimal measurements.

3.2.5 Conclusion

In this section, we proposed six unbiased estimators for the evaluation of some parameters which quantify the amount of entanglement (Negativity, Concurrence and Log-Negativity) and Discord (Quantum Geometric Discord) for a restricted family of states of particular interest in the filed of quantum information and quantum technologies. We calculated their theoretical minimum uncertainties, showing that three of them are optimal, i.e. they saturate the quantum Cramér-Rao bound. Then, we experimentally tested our prediction, finding a good agreement between theoretical expectations and experimental results. In particular, we demonstrated that our optimal estimators reach the ultimate theoretical precision limit on unbiased estimators represented by the QCRB. The agreement between the uncertainty bars and the theoretical curves for the non-optimal estimators is a further consistency test between theory and experiment.

Other interesting and unexpected results are the identity between the estimators of Negativity and Concurrence and the monotone relation between the ones of Negativity and Quantum Geometric Discord, for our family of quantum states. The direct relations between the estimators and, consequently, between the QCRB, implies that, for our family of quantum states, knowledge of the optimal estimator and the associated QCRB for Negativity allows for an immediate derivation of such quantities also for Log-Negativity, Concurrence and Quantum Geometric Discord.

Possible extensions of this work may explore the possibilities given by biased estimation, in order to define biased estimators able to achieve a lower bound on the mean square error, and estimators for other parameters that characterize entanglement and Discord.

For the above reasons, we believe that these results will pave the way to a diffuse use of these estimators in quantifying resources for quantum technologies, one of the most important issues of this field.

Chapter 4

Novel weak-interaction-based measurement protocols

Part of the work described in this chapter has been previously published in [159, 160, 161, 162, 163, 164, 165].

Weak measurements and weak values are one of the most promising research tools in quantum mechanics (Sec. 1.2.4). In particular, their properties allow for applications both in fundamental science (e.g. direct measurements of the wavefunction, measurement of non-commuting observables onto the same quantum system - Sec. 1.2.4) and metrology (e.g. tiny parameters amplification techniques - Sec. 1.2.4). For this reason, research on new weak-interaction-based measurement protocols is a task of utmost importance in quantum metrology and quantum mechanics foundations investigation.

In the first part of this section, we present a first example of a measurement protocol that can be regarded as a step beyond weak measurements: *protective measurement* (PM)[159, 160, 161, 162, 165]. One disruptive feature of PMs is that they allow us to extract the expectation value of a quantum observable, a statistical property of an ensemble of quantum systems, even from a single experiment on a single particle. We will show the first experimental implementation of PM, and a theoretical analysis of the statistical uncertainties achievable with such protocol, showing the advantage it presents with respect to traditional measurement protocols based on "strong" (projective) measurements, which consists in a strong reduction of the statistical uncertainty, with possible applications, for instance, in test of unknown state preparations.

In the second part, then, we present an iterative weak-interaction-based measurement protocol called *robust weak measurement* (RWM)[163, 164], which can be regarded as an extension of PMs to general weak values. We will show that, with

RWMs, one can obtain a reliable estimate of the weak value of an observable from just a single detection event, instead of averaging over multiple events like for usual weak value measurements. This is already a conceptual paradigm shift, since weak values have always been considered as quantities arising from a statistical ensemble of event, a feature that has covered a primary role in the decades-long debate on their quantum (or classical) intrinsic nature. When considering the advantages that the detection of a (anomalous) weak value brings in metrological contexts (Sec. 1.2.4), the metrological usefulness of this protocol, which allows extracting a weak value even from single detection events, becomes clear.

4.1 Protective measurements

The expectation value of an observable (Sec. 1.2.1) is defined as the average of its eigenvalues, weighted on their respective probabilities. Therefore, it has always been considered a statistical property of an ensemble of quantum systems. In this chapter, we show the first implementation of a *protective measurement*[166, 167], a novel measurement protocol combining weak measurements with a sort of "protection mechanism" preserving the quantum state coherence. Although originally introduced as an argument supporting the reality of the wavefunction[166], PMs present many other fascinating features, e.g. the possibility to extract the expectation value of a quantum observable even from a single detection event. In the following sections, we define traditional (projective) and protective measurements, and present the results obtained in a single-photon experiment able to implement both measurement protocols. Then, we perform a theoretical analysis of the statistical uncertainties for both procedures, showing that PM has a significant advantage over projective measurements in terms of precision.

4.1.1 Theory and properties

In this section, we describe two methods to measure the expectation value of an observable A with the von Neumann protocol (Sec. 1.2.2): the traditional one, based on projective measurements, and protective measurements. First, following our usual description, let us define the system $\mathcal{S}$, the meter $\mathcal{M}$ and the total system $\mathcal{T}$:

- System $\mathcal{S}$
  The *system* lives in a Hilbert space $\mathcal{H}_\mathcal{S}$ in which it is defined the measurand operator $\hat{A}$ corresponding to the observable of interest A. By decomposing it in the $\hat{A}$ eigenbasis $\{|a_i\rangle\}$, the initial state of the system can be described as

$$|\psi\rangle = \sum_i \alpha_i |a_i\rangle \tag{4.1.1.1}$$

- Meter $\mathcal{M}$
  The *meter* $\mathcal{M}$ has a continuous pointer value described by an operator $\hat{Q}$ whose initial wavefunction is supposed to follow the normal distribution:

$$\phi_0(x) = \langle x|\phi_0\rangle = \frac{1}{\sqrt[4]{2\pi\sigma^2}} \exp\left(-\frac{(x-x_0)^2}{4\sigma^2}\right) \qquad (4.1.1.2)$$

- Total system $\mathcal{T}$
  The only non-vanishing term in the total Hamiltonian is assumed to be the interaction one:

$$\hat{H}_{int} = g\hat{A} \otimes \hat{P} \qquad (4.1.1.3)$$

with $\hat{P}$ being the canonically conjugated operator to the pointer $\hat{Q}$.

The associated time evolution operator is

$$\hat{U} = \exp\left(-\frac{i}{\hbar}g\hat{A} \otimes \hat{P}\right) \qquad (4.1.1.4)$$

With this coupling, we can obtain the expectation value of A in two different ways. The first one is the traditional (projective) method, in which the expectation value is extracted from the statistics obtained from repeated projective measurements of an ensemble of identically-prepared particles in the state $|\psi\rangle$. The second method, instead, exploits the PM protocol, which allows us to directly extract the expectation value from a single measurement of a particle in the state $|\psi\rangle$.

Projective measurements

After a von Neumann coupling, the total system $\mathcal{T}$ evolves in the state

$$\sum_i \alpha_i |a_i\rangle |\varphi(x - ga_i)\rangle \qquad (4.1.1.5)$$

For strong coupling ($g/\sigma \gg 1$), the eigenstates of A are completely spatially separated and, therefore, distinguishable. Hence, the expectation value can be evaluated as

$$\langle \hat{A}\rangle = \sum_i |\alpha_i|^2 a_i = \frac{\sum_i a_i N_i}{\sum_i N_i} \qquad (4.1.1.6)$$

where N_i is the number of count events obtained for the eigenvalue a_i. This is a well known technique, first experimentally implemented in 1922 by W. Stern and O. Gerlach[168] for spin measurements.

Protective measurements

Initially introduced as procedure to measure the wavefunction[166], PM is a protocol in which we add a mechanism to protect the quantum state of the system during the (weak) measurement procedure, preserving the state from the (eventually small) decoherence due to the von Neumann interaction.

This protection can be carried out either by means of an adiabatic potential (passive protection), when the state is in a non-degenerate energy eigenstate[166], or by quantum Zeno effect (QZE, active protection)[169], which consists in projecting the state after each interaction onto the initial state (or, more generally, by projecting onto the initial state in the subspace in which the evolution Hamiltonian is acting). From the quantum information perspective, we can think of this as a protocol in which Alice produces a known state and transmits it to Bob together with a proper protection, which Bob implements as a black box.

Regardless of the protection, we can describe PM with a standard von Neumann measurement where, instead of an instantaneous interaction, we perform a long and adiabatic one, described by the coupling $g = g(t)$. The interaction Hamiltonian, in this case is

$$\hat{H}'_{int} = g(t)\hat{A} \otimes \hat{P} \qquad (4.1.1.7)$$

where the interaction $g(t) = 1/T$ is activated for a period of time T and smoothly goes to zero before and after. For a smooth enough $g(t)$, we obtain the adiabatic limit, in which the state $|\psi\rangle$ of the system cannot change, thanks to the protection. For bounded $\hat{P}$, in the limit $T \to \infty$, the interaction Hamiltonian goes to zero while the state $|\psi\rangle$ remains unchanged. The energy of the eigenstate, then, shifts by an infinitesimal amount given by first-order perturbation theory[166]:

$$\delta E = \langle \hat{H}'_{int} \rangle = \frac{\langle \hat{A} \rangle \hat{P}}{T} \qquad (4.1.1.8)$$

From Eq. 1.1.1.11 we can calculate the time evolution associated to $\hat{H}'_{int}$ in the limit $T \to \infty$:

$$\hat{U} = \lim_{T \to \infty} \exp\left(-\frac{i}{\hbar} \int_{-\infty}^{\infty} dt \frac{\langle \hat{A} \rangle \hat{P}}{T}\right) = \exp\left(-\frac{i}{\hbar} \langle \hat{A} \rangle \hat{P}\right) \qquad (4.1.1.9)$$

which results in a shift of the pointer wavefunction equal to the expectation value $\langle \hat{A} \rangle$.

An equivalent protection mechanism, used in our case, employs a series of K instantaneous weak interactions, described by the coupling constant g. By applying an active protection, realized by the projector

$$\hat{\Pi}_\psi = |\psi\rangle\langle\psi| \qquad (4.1.1.10)$$

the system evolves, for each step, of

$$|\psi\rangle \, \langle\psi|\hat{U}|\psi\rangle \otimes |\varphi(x)\rangle = |\psi\rangle \otimes \left|\varphi(x - g \langle\hat{A}\rangle)\rangle\right\rangle \qquad (4.1.1.11)$$

since, for a small g,

$$\langle\psi|\exp\left(-\frac{i}{\hbar}g\hat{A}\otimes\hat{P}\right)|\psi\rangle \approx \langle\psi|\left(\mathbb{1} - \frac{i}{\hbar}g\hat{A}\otimes\hat{P}\right)|\psi\rangle = \mathbb{1} - \frac{i}{\hbar}g \langle\hat{A}\rangle \hat{P} \quad (4.1.1.12)$$

So, for weak couplings, the protection causes, for each step, a shift in the meter wavefunction which is directly proportional to the expectation value $\langle\hat{A}\rangle$. Furthermore, in the $g \ll 1$ limit, the decoherence induced on the initial state by the interaction $\hat{U}$ is so small that the state survival probability after the projection $\hat{\Pi}_\psi$ is close to 1. Thus, the projection "protects" the particle, restoring its initial state without risk of destroying it. As an example of application, let us consider a quantum mint, that should produce a certain state, whose faithfulness one has to check. Then, one can construct the protection on the basis of the expected state and check if the average value is correct.

Protective measurements, then, allow us to estimate, for each particle undergoing them, directly the expectation value, so far only believed to be statistically obtainable from an ensemble of identical particles. Furthermore, it can be showed[166] that, by performing protective measurement of expectation values of projection operators on small regions of space of volume V, the outcome will be $V \langle\psi|\psi\rangle$, meaning that PMs can measure a stationary wavefunction. Thus, PM can provide new perspectives in the hot debate[170, 171, 172, 173] about the ontic or epistemic nature of the wavefunction, i.e. on whether the wavefunction has an objective, physical existence, or it only provides knowledge of a phenomenon, respectively.

4.1.2 Protective measurements in the lab

Protective measurements of polarization

In our experiment, we want to measure the expectation value of the polarization of single photons. The polarization operator is

$$\hat{A} = |H\rangle\langle H| - |V\rangle\langle V| \qquad (4.1.2.1)$$

while the initial state is in the linearly-polarized state

$$|\psi\rangle = \cos(\theta) \, |H\rangle + \sin(\theta) \, |V\rangle \qquad (4.1.2.2)$$

and the initial pointer wavefunction is the one in Eq. (4.1.1.2), where x is the photon position along one of the axes of the transverse plane with respect to the

photon propagation direction (z axis).

Our implementation consists of a series of K weak von Neumann couplings, in which the horizontal component of the polarization $\hat{\Pi}_H = |H\rangle\langle H|$ is weakly coupled to the transverse momentum P of the photon via a thin birefringent crystal (with coupling strength $g/\sigma \ll 1$). This is mathematically equivalent to a von Neumann coupling of strength $g/2$ between the pointer and the polarization operator $\hat{A}$. Each weak von Neumann coupling is followed by the protection $\hat{\Pi}_\psi$ in the protected case.

Let us now analyse the difference between projective and protective measurements in this case.

Projective case Without protection, the K von Neumann interactions (Eq. (4.1.1.4)) result in a strong interaction with strength $g' = Kg$, after which the system evolves in the state

$$\alpha_H |H\rangle |\varphi(x - a)\rangle - \alpha_V |V\rangle |\varphi(x + a)\rangle \tag{4.1.2.3}$$

being $a = g'/2$, and $\alpha_{H(V)} = +1(-1)$ is the eigenvalue corresponding to the $H(V)$ polarization.

The resulting strong interaction completely separates the spatial components of the two polarizations (Fig. 4.1), as in a Stern-Gerlach experiment[168] (Fig. 4.1). Hence, the expectation value can be evaluated as

$$\langle \hat{A} \rangle = \frac{N_H - N_V}{N_H + N_V} \tag{4.1.2.4}$$

where N_x is the the number of counts in the region corresponding to the polarization x.

Protective case The introduction of the protection $\hat{\Pi}_\psi$, instead, induces a shift of the pointer proportional to the expectation value of the polarization (Eq. (4.1.1.11), Fig. 4.2). Therefore, the expectation value of the polarization can be extracted by the formula

$$\langle \hat{A} \rangle = \frac{x - x_0}{a} \tag{4.1.2.5}$$

with $x_0 = \frac{x_H + x_V}{2}$, being x_H (x_V) the centre of the horizontally-(vertically-)polarised photon distribution in the unprotected case.

In contrast with the unprotected case, in which the expectation value can only be extracted statistically by measuring an ensemble of identical photons, in the PM picture each photon carries information about the expectation value, allowing
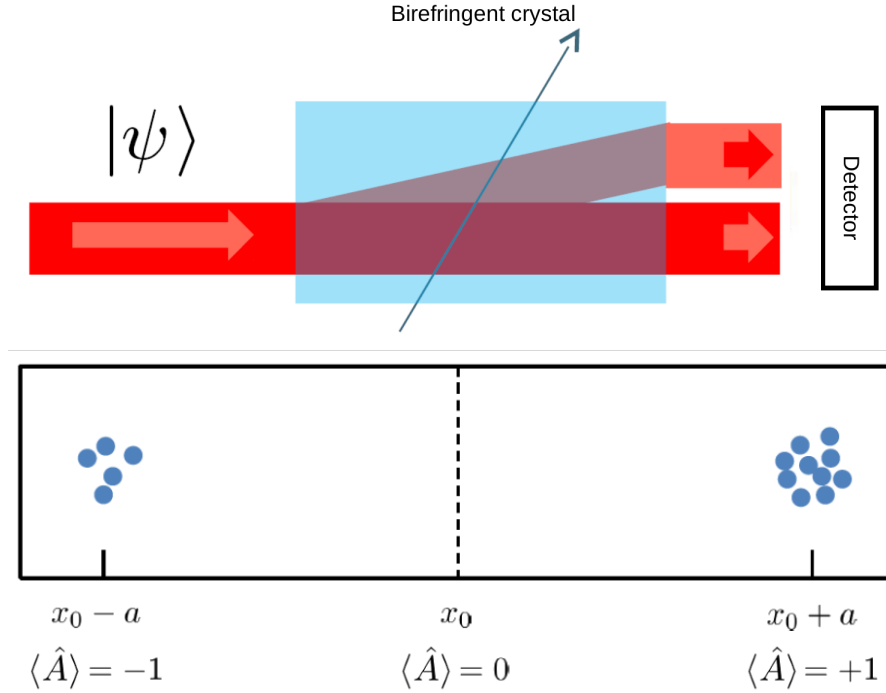
Figure 4.1: Projective case. The two polarization components are completely separated. The expectation value is evaluated as the weighted average of the events. (Despite only one polarization component is deviated, we chose to define a centre as the point in the middle between the centre of the two distributions.)

to extract it even by a single experiment on a single photon (Fig. 4.2). This is a revolutionary feature, apparently in contrast with the definition of expectation value, i.e. an intrinsically statistical quantity.

Experimental setup

Our setup (Fig. 4.3) is divided in three parts. The first part is dedicated to production of heralded single photons. A mode-locked laser with a second harmonic at 398 nm and a 76 MHz repetition rate pumps a $10 \times 10 \times 5$ mm $LiIO_3$ non-linear crystal in which Type-I PDC (Sec. 2.3.2) produces signal-idler photon pairs. The idler photons (920 nm) are filtered by an interference filter (IF) centred at 702 nm and with a FWHM of 10 nm, and coupled to a single-mode fibre (SMF) and then addressed to a Silicon Single-Photon Avalanche Diode (SPAD), heralding the presence of the correlated signal photons (702 nm). The signal photons, instead, are filtered with an IF centred at 702 nm and with a FWHM of 10 nm, fibre coupled and addressed to the second part of the setup, where the PM
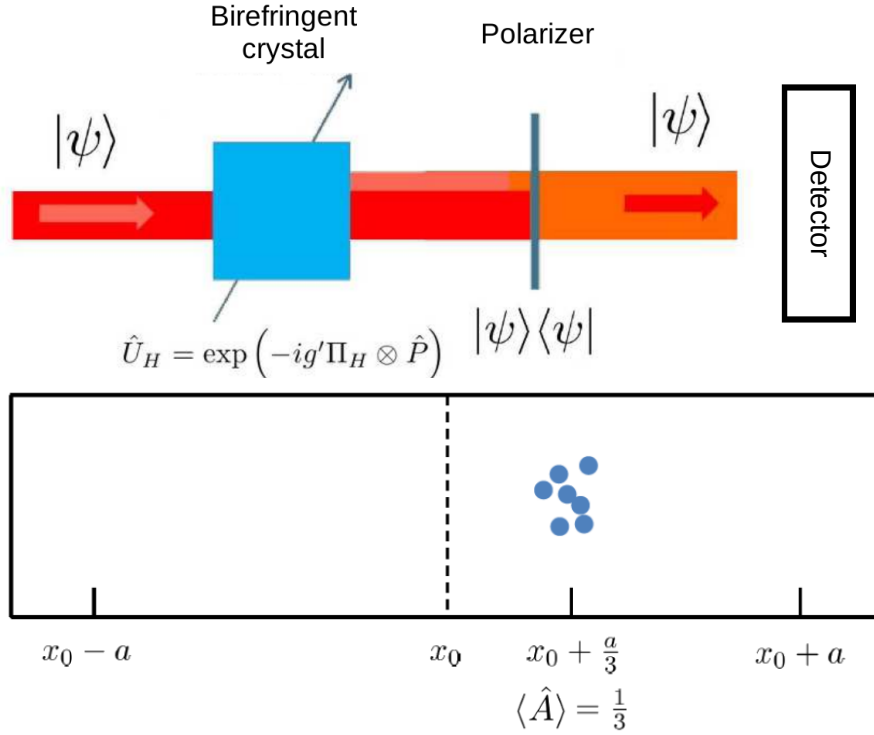
Figure 4.2: Protective case: the photons fall all in the same region, whose position is proportional to the expectation value.

takes place. We estimated the quality of our single-photon emission with a HBT interferometer (Sec. 3.1.1), obtaining a value of $\alpha = 0.13 \pm 0.01$ without any background or dark count subtraction, testifying the quality of our single photon source.

The second part is the optical path, where the signal photon, decoupled and collimated with a spatial mode close to a Gaussian, is pre-selected in the polarization state $|\psi\rangle$ by means of a calcite polariser followed by a half-wave plate. Then, the photon interacts with $K = 7$ weak interaction units, each composed of two birefringent crystals. In each unit, the first 2 mm long birefringent calcite crystal has an extraordinary (e) optical axis lying in the x - z plane, having an angle of $\pi/4$ with respect to the z direction. This generates displacement of the beam in the transverse direction x. The second (1.1 mm) calcite crystal has the optical e-axis oriented along the y-axis, compensating the phase and time decoherence induced by the first crystal. The combined effect of all the 7 units allows for complete separation of orthogonal polarizations. The protection of the quantum state is implemented exploiting the quantum Zeno effect, realized by inserting a polariser after each weak interaction unit. The polariser projects the state outgoing the von Neumann interaction into the same polarization of the initial state $|\psi\rangle$, cancelling

94
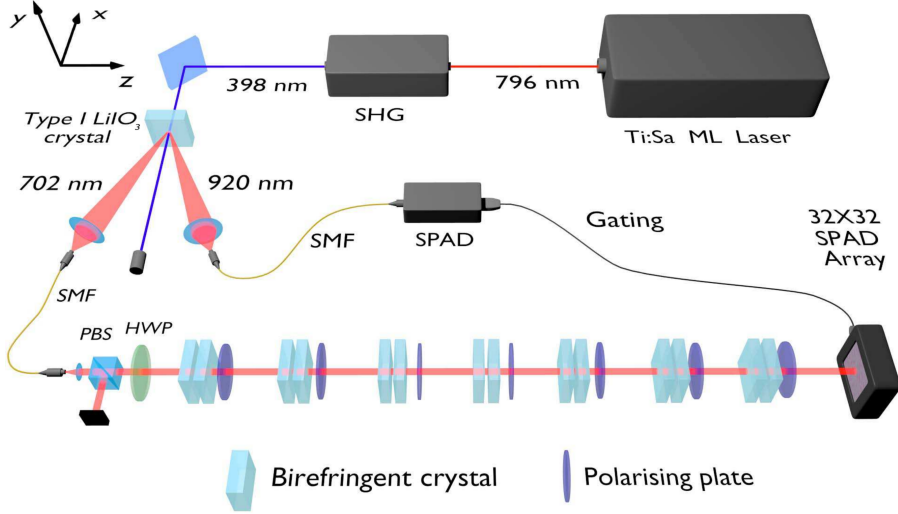
Figure 4.3: Experimental setup. Material from: 'F. Piacentini et al., Determining the Quantum Expectation Value by Measuring a Single Photon, Nat. Phys., 2017, Nature Research'

the (tiny) decoherence induced by the birefringent crystals.

At the end of the optical path, the photons are detected by a 2D spatial-resolving single-photon detector prototype, i.e. a two-dimensional array of 32x32 "smart pixels", each hosting a SPAD detector with dedicated front-end electronics[174]. The SPAD array is gated with a 6 ns detection window by the detection of the idler photon (920 nm). An optional tomography apparatus (Sec. 3.2.3), comprising a half-wave plate, a quarter-wave plate and a polariser, can be inserted before the SPAD array to reconstruct the density matrix of the state emerging from the measurement procedure.

We chose the number of units $K = 7$ from practical considerations approximating the ideal case of large K: because of losses originating from optical elements imperfections and the detector characteristics, a larger K would result in a low signal-to-noise ratio at the detector.

4.1.3 Results

We acquire data sets for three different states: the state $|+\rangle = \frac{1}{\sqrt{2}}(|H\rangle + |V\rangle)$, which should be subjected to the maximum decoherence, and two intermediate states $\left|\frac{17}{60}\pi\right\rangle = \cos\left(\frac{17}{60}\pi\right)|H\rangle + \sin\left(\frac{17}{60}\pi\right)|V\rangle$ and $\left|\frac{\pi}{8}\right\rangle = \cos\left(\frac{\pi}{8}\right)|H\rangle + \sin\left(\frac{\pi}{8}\right)|V\rangle$.

For each state, we perform a first acquisition with $|\psi\rangle = |H\rangle$ or $|\psi\rangle = |V\rangle$ and only the crystals in the optical path, which allows us to calibrate the system. Then, we perform acquisitions for the state under test both in the unprotected (only crystals) and protected (crystals + polarisers) case. Last, we perform an acquisition with only polarisers plus one with a free optical path, in order to compensate for unwanted polariser deviations of the beam.

PM output state verification

In order to verify the correct execution of the PM protocol and its difference with respect to projective measurements, we perform a tomographic reconstruction of the states at the end of the system. Obviously, we expect two very different states at the end of the two measurement procedures. In the protected case, the protection should be able to preserve the initial polarization state $\hat{\rho}_{in}$, therefore, the final state is $\hat{\rho}_{prot} = \hat{\rho}_{in}$, whereas in the unprotected case the shifts of one polarization component cause decoherence on $\hat{\rho}_{in}$, and we expect a final state $\hat{\rho}_{dec}$:

$$\hat{\rho}_{in} = \begin{pmatrix} \cos^2(\theta) & -\sin(\theta)\cos(\theta) \\ \sin(\theta)\cos(\theta) & \sin^2(\theta) \end{pmatrix} \tag{4.1.3.1}$$

$$\hat{\rho}_{dec} = \begin{pmatrix} \cos^2(\theta) & -\sin(\theta)\cos(\theta)\exp\left(-\frac{g'^2}{(2\sigma)^2}\right) \\ \sin(\theta)\cos(\theta)\exp\left(-\frac{g'^2}{(2\sigma)^2}\right) & \sin^2(\theta) \end{pmatrix} \tag{4.1.3.2}$$

g' can be obtained as $g' = \langle x_H \rangle - \langle x_V \rangle$, being $\langle x_I \rangle$ the average positions of photons in the polarization I on the horizontal axis (see next section), while σ is the average of the distribution widths obtained by Gaussian fits of our acquisitions. In our experiment, $g' = 11.56 \pm 0.07$ px (pixels) and $\sigma = 4.17 \pm 0.02$ px.

Let us now analyse the reconstruction results for each state. We will denote the reconstructed density matrices as $\hat{\rho}_{PM}^{rec}$ and $\hat{\rho}_{Pj}^{rec}$ for protective and projective measurements, respectively:

$|+\rangle$ **state** The Fidelity (App. A) between the theoretical protected state and the reconstructed one $\hat{\rho}_{PM}^{rec}$ (Fig. 4.4b) is:

$$F(\hat{\rho}_{PM}^{rec}, \hat{\rho}_{in}) = 0.999 \tag{4.1.3.3}$$

with a purity (Sec. 1.1.1) of

$$P(\hat{\rho}_{PM}^{rec}) = 0.998 \tag{4.1.3.4}$$

the protection, then, preserved the state and its purity. This confirms that the protection "freezes" the evolution of the initial state, as we described in Sec. 4.1.1.

We can also compare the reconstructed decoherent state $\hat{\rho}_{PJ}^{rec}$ (Fig. 4.4a) with the decoherent theoretical one:

$$F(\hat{\rho}_{PJ}^{rec}, \hat{\rho}_{dec}) = 0.998 \tag{4.1.3.5}$$

which fits well the theoretical predictions.

We also compute the purity of $\hat{\rho}_{PJ}^{rec}$:

$$P(\hat{\rho}_{PJ}^{rec}) = 0.504 \tag{4.1.3.6}$$

which tells us that, as expected, without protection the induced decoherence piles up step by step, lowering the purity of the state.

Finally, a comparison between the two reconstructed states

$$F(\hat{\rho}_{PJ}^{rec}, \hat{\rho}_{PM}^{rec}) = 0.720 \tag{4.1.3.7}$$

tells us that the decoherence made the two states incompatible. This, combined with the previous results, tells us that PM protects the initial state, while, instead, in projective measurements, the combined effect of the 7 von Neumann interactions degrades the state to the point that it is incompatible with the initial state and the protected one.

$\left|\frac{17}{60}\pi\right\rangle$ **state**   As before, we compare the reconstructed protected state $\hat{\rho}_{PM}^{rec}$ (Fig. 4.5b) with the theoretical one and analyse its purity:

$$F(\hat{\rho}_{PM}^{rec}, \hat{\rho}_{in}) = 0.996 \quad P(\hat{\rho}_{PM}^{rec}) = 0.992 \tag{4.1.3.8}$$

Again confirming that the protection preserves the state and its purity.

Then, we compare the reconstructed decoherent state $\hat{\rho}_{PJ}^{rec}$ (Fig. 4.5a) with the theoretical decoherent one and compute its purity:

$$F(\hat{\rho}_{PJ}^{rec}, \hat{\rho}_{dec}) = 0.999 \quad P(\hat{\rho}_{PJ}^{rec}) = 0.520 \tag{4.1.3.9}$$

again confirming our prediction and showing the action of the decoherence on the purity.

At last, the comparison between the two reconstructed states

$$F(\hat{\rho}_{PJ}^{rec}, \hat{\rho}_{PM}^{rec}) = 0.751 \tag{4.1.3.10}$$

tells us, again, that the decoherence made the two states incompatible.
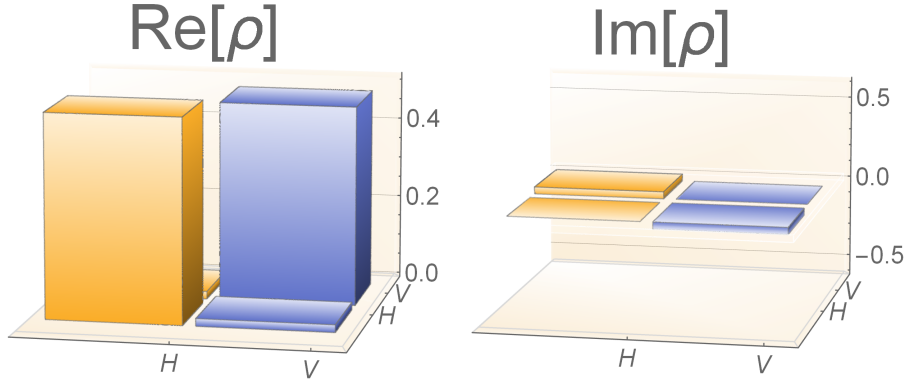
(a) Decoherent state
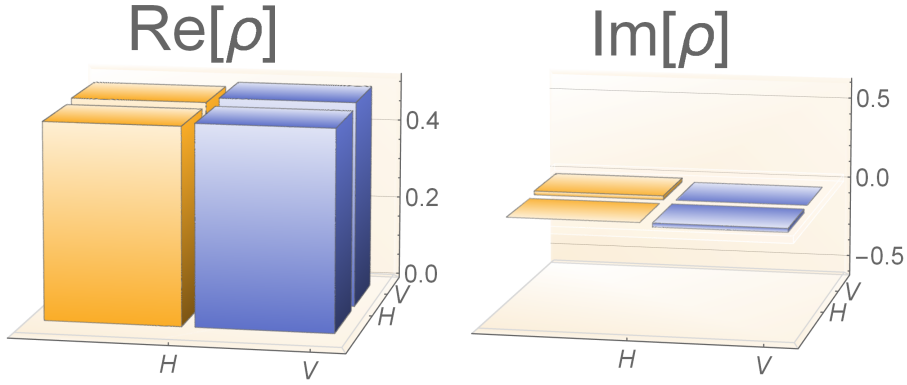
(b) Protected state

Figure 4.4: Reconstructed density matrices for the protected and unprotected states with $|\psi\rangle = |+\rangle$.

$\left|\frac{\pi}{8}\right\rangle$ **state** Once again, we perform the comparison described above in this interesting case of an highly unbalanced state. The purity of the reconstructed protected state $\hat{\rho}_{PM}^{rec}$ (Fig. 4.6b) and its Fidelity with respect to the initial state are

$$F(\hat{\rho}_{PM}^{rec}) = 0.992 \quad P(\hat{\rho}_{PM}^{rec}) = 0.992 \tag{4.1.3.11}$$

certifying again the preserving action of the protection. The lower fidelity is caused by the fact that the two polarization components, in this case, are not perfectly balanced as in the previous one.

The purity of the reconstructed decoherent state $\hat{\rho}_{PJ}^{rec}$ (Fig. 4.6a) and its Fidelity
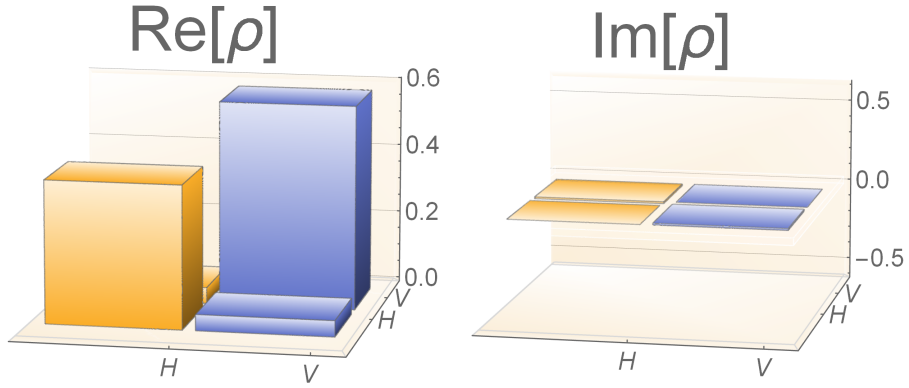
(a) Decoherent state
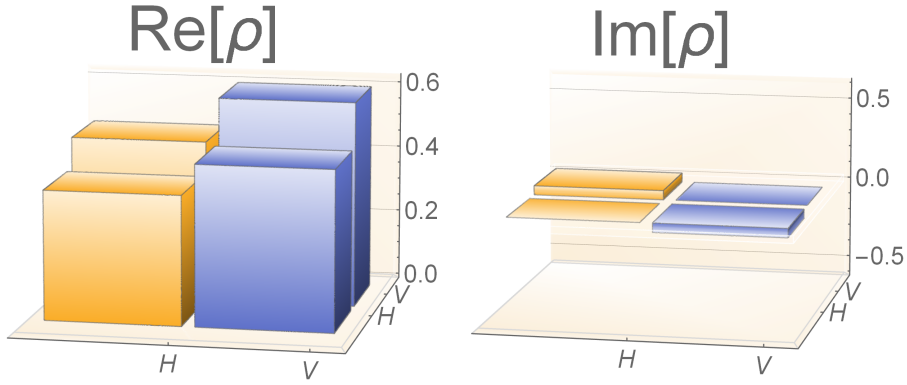
(b) Protected state

Figure 4.5: Reconstructed density matrices for protected and unprotected states with $|\psi\rangle = \left|\frac{17}{60}\pi\right\rangle$.

with respect to the theoretical decoherent state, instead, are

$$F(\hat{\rho}_{PJ}^{rec}, \rho_{dec}) = 0.999 \quad P(\hat{\rho}_{PJ}^{rec}) = 0.789 \tag{4.1.3.12}$$

again confirming our previous observations. Once again, the higher purity is due to the higher unbalance between the H and V polarization components.

At last, the Fidelity between the two reconstructed states

$$F(\hat{\rho}_{PJ}^{rec}, \hat{\rho}_{PM}^{rec}) = 0.894 \tag{4.1.3.13}$$

once again confirms that the decoherence made the two states incompatible. Again, the higher Fidelity is due to the higher unbalance between the two polarization

components.
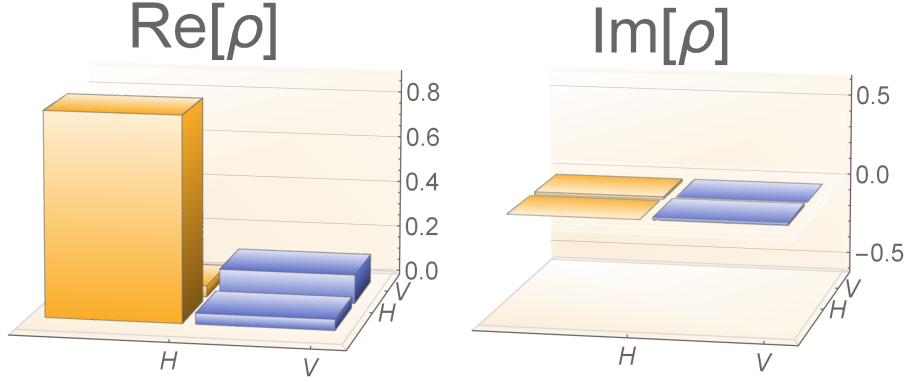
(a) Decoherent state
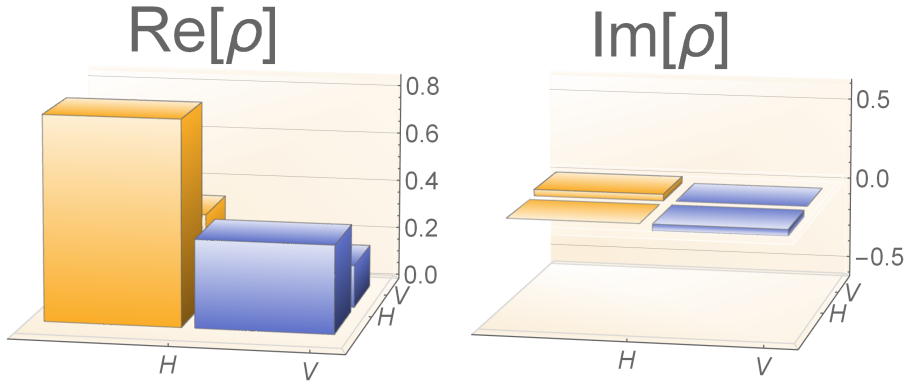
(b) Protected state

Figure 4.6: Reconstructed density matrices for protected and unprotected states with $|\psi\rangle = \left|\frac{\pi}{8}\right\rangle$.

We conclude, then, that the protection mechanism has indeed protected the initial state from the decoherence induced by the K von Neumann couplings. These results certify the correct execution of the PM protocol, allowing us to proceed with the analysis of the expectation values.

Expectation values analysis

Let us now move to the core of the experiment: the evaluation of the expectation values of the polarization.

First of all, we need to clean our raw data (Fig. 4.7). In the first step, we compare each pixel with the average of its nearest neighbours, rejecting it if its value is greater than such average multiplied by a properly chosen coefficient (ranging from 1.6 to 1.8). This allows us to exclude the so-called "hot-pixels" of the SPAD array, i.e. pixels hosting a SPAD presenting an abnormal dark count rate (even several orders of magnitude above the normal level). Such pixels, obviously impossible to physically remove from the array, would otherwise lead to a highly inaccurate and unreliable measurement. Then, we perform a linear regression with a fit function consisting of one or two Gaussians (depending on the case) plus a common bias. The fit results allow us to "fill" the gaps in output matrix caused by the hot-pixel rejection.
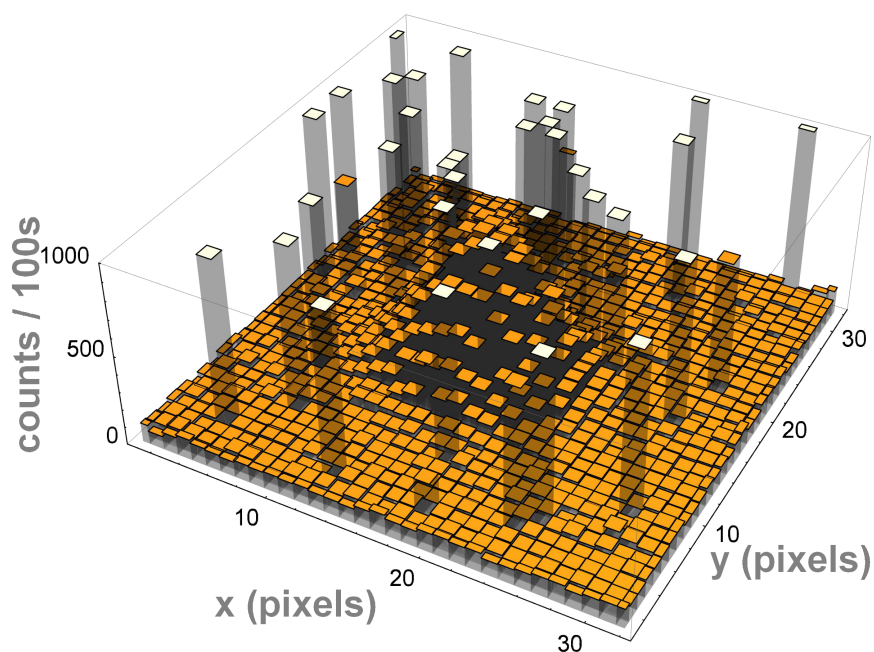
Figure 4.7: Raw data sample from one acquisition: we distinguish the signal (the Gaussian distribution) and the so-called "hot-pixels", i.e. the pixels with an abnormal dark count rate.

From the linear regression of the acquisition for the states $|H\rangle$ and $|V\rangle$, we extract the centres x_H and x_V of the photon distributions corresponding to the horizontally- and vertically-polarized photons, respectively. Remembering Fig.s 4.1 and 4.2, these are the points corresponding to the $\hat{A}$ eigenvalues ± 1. Averaging over multiple acquisitions, we obtain both their value and their respective associated uncertainties σ_{x_H} and σ_{x_V}. Then, we define the centre, in which $\langle \hat{A} \rangle = 0$, as

$$x_0 = \frac{x_H + x_V}{2} \tag{4.1.3.14}$$

and the distance between the centre and one of the two extremes as

$$a = \frac{x_H - x_V}{2} \tag{4.1.3.15}$$

with an associated uncertainty of

$$\sigma_a = \sigma_{x_0} = \frac{\sqrt{\sigma_{x_H}^2 + \sigma_{x_V}^2}}{2} \tag{4.1.3.16}$$

Let us now analyse the evaluation of the expectation values with both measurement procedures.

Projective measurement In the unprotected case, the one realizing the traditional projective measurement, we extract the expectation value with the formula in Eq. (4.1.2.4). Thus, we need to know how many detected photons have given as measurement result the eigenvalue $1(-1)$, i.e. how many photons have fallen in the SPAD array regions corresponding to the $H(V)$ polarization component. This is carried out by dividing the acquired image (Fig. 4.8) in two regions with a cut corresponding to x_0, rounded up to its closest pixel (red line in Fig. 4.8). This way, counts in the left(right) region are associated with the polarization $V(H)$.

To evaluate dark and background counts contributions $N_V^{(dark)}$ and $N_H^{(dark)}$, we perform two other cuts (horizontal white lines), which allow us to separate the regions of interest (regions 3 and 4 in Fig. 4.8) from the ones (regions 1, 2, 5 and 6) in which we only have dark and background counts. By averaging the counts in regions 1 and 5(2 and 6), we obtain an estimate of dark and background counts for each pixel in the region with polarization $V(H)$, which we multiply for the number of pixels in region 3(4), obtaining: $N_V^{(dark)}$ ($N_H^{(dark)}$). Thus, by subtracting them, we obtain the expectation value of the polarization $\hat{A}$:

$$\langle \hat{A} \rangle = \frac{N_H - N_V - N_H^{(dark)} + N_V^{(dark)}}{N_H + N_V - N_H^{(dark)} - N_V^{(dark)}} \tag{4.1.3.17}$$

which has an associated uncertainty

$$\sigma_{\langle \hat{A} \rangle} = \sqrt{\sum_{k=1}^{4} \left(\frac{\partial \hat{A}}{\partial N_k} \right)^2 \sigma_{N_k}^2} \tag{4.1.3.18}$$

with $N_1 = N_V$, $N_2 = N_H$, $N_3 = N_V^{(dark)}$, $N_4 = N_H^{(dark)}$. The uncertainties on the number of dark and background counts $\sigma_{N_V^{(dark)}}$ and $\sigma_{N_H^{(dark)}}$ are evaluated by assuming a poissonian behaviour (i.e. $\sigma_{N_{V(H)}^{(dark)}} = \sqrt{N_{V(H)}^{(dark)}}$), while the uncertainties on the number of photons in the two regions are evaluated as

$$\sigma_{N_H} = \sqrt{N_H + (c_H \ N_H)^2 + (c_V \ N_V)^2} \tag{4.1.3.19}$$

$$\sigma_{N_V} = \sqrt{N_V + (c_H \ N_H)^2 + (c_V \ N_V)^2} \tag{4.1.3.20}$$

The two coefficients $c_{(H)V}$ come from an ad hoc evaluation, based on how regions 3 and 4 are identified, of the influence of the distribution tails (small, but still relevant) on the number of photon counts due to the fact that the two distributions are separated, but not completely.

Protective measurements   In the protected case, we define the region of interest with the same method as before (horizontal white lines in Fig. 4.9). Dark and background counts subtraction is carried out by a conservative method, in which we search for the minimum of pixel counts and subtract such value from every pixel. In this case, each photon carries information about the expectation value. Following Eq. (4.1.2.5):

$$\langle \hat{A} \rangle = \frac{x - x_0}{a} \tag{4.1.3.21}$$

we can extract it from every pixel (px) and then average these results, weighting on the number of counts:

$$\langle \hat{A} \rangle = \frac{1}{\sum_{px} N_{px}} \sum_{px} N_{px} \frac{x_{px} - x_0}{a} \tag{4.1.3.22}$$

The uncertainties are evaluated as:

$$\sigma_A = \left[\left(\frac{\sum_{\{px\}} (A_{px} - \langle \hat{A} \rangle)^2 N_{px}}{\sum_{\{px\}} N_{px}} \right) \right. $$
$$ + \left(\frac{1}{x'_H + x'_V} + \frac{\langle \hat{A} \rangle}{x'_H - x'_V} \right)^2 \sigma_{x'_H}^2 \tag{4.1.3.23}$$
$$ \left. + \left(\frac{1}{x'_H + x'_V} - \frac{\langle \hat{A} \rangle}{x'_H - x'_V} \right)^2 \sigma_{x'_V}^2 \right]^{1/2}$$
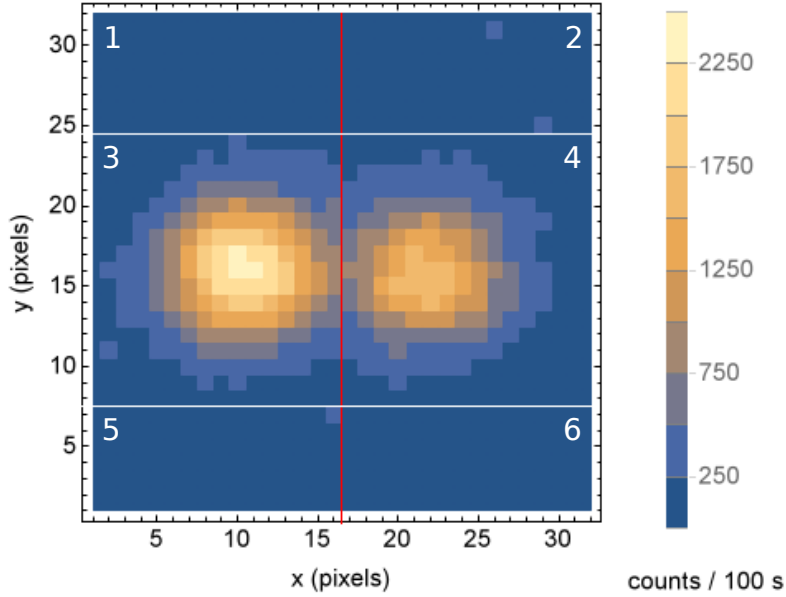
Figure 4.8: Example of the procedure for the state $\left|\frac{17}{60}\pi\right\rangle$. Here, $x_0 = 16.25 \pm 0.04$, therefore, the cut (red line) divides the graphics in two regions, one at $x \leq 16$ (V polarization) and the other at $x > 16$ (H polarization). For each region, we perform two additional cuts (white lines) to separate the regions of interest (3 and 4) for the regions in which we only have dark and background counts (1, 2, 5, 6).

where the first term is the standard deviation of the mean, while second and third terms are the uncertainties on parameters $x'_H = x_H + x_{pol} - x_{void}$ and $x'_V = x_H + x_{pol} - x_{void}$, being x_{void} and x_{pol} the positions of the beam in the acquisition with a free optical path and with only the polarisers inserted, respectively. This way, we compensate for the deviation induced by the polarisers. The variances of such parameters are $\sigma^2_{x'_{H(V)}} = \sigma^2_{x_{H(V)}} + \sigma^2_{x_{pol}} + \sigma^2_{x_{void}}$.

The results obtained for the measurements of the three states $|+\rangle$, $\left|\frac{17}{60}\pi\right\rangle$ e $\left|\frac{\pi}{8}\right\rangle$ with and without protection are summarized in Fig. 4.10. In the unprotected case (Fig. 4.10, left column), the photon counts accumulate around the positions $x = \pm a$. The expectation values, extracted with the methodology related to the usual projective measurement framework, are all in good agreement with the theoretical expectations.

In the protected case, instead (Fig. 4.10, right column), we notice that all the photons accumulate a specific position, corresponding to $x = a\langle\hat{A}\rangle$. The expectation values extracted with the two procedures are in excellent agreement with

104
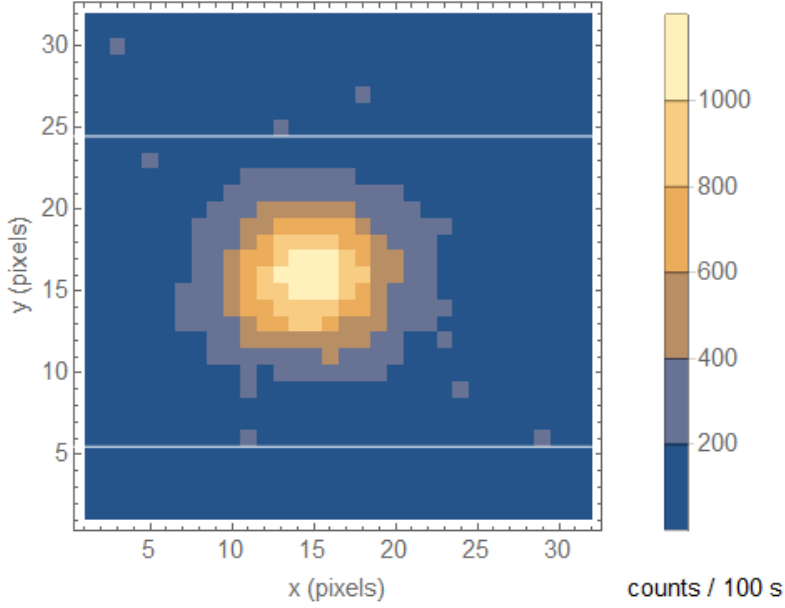
Figure 4.9: Example of region of interest for a protected $\left|\frac{17}{60}\pi\right\rangle$ state.

each other within the experimental uncertainties, as well as with the theoretical predictions for the polarization states tested. This means that, with protective measurements, each single photon carries information about the expectation value of its polarisation, granting the possibility of extracting such value even in a one-shot experiment with just a single photon.

This is further confirmed by Fig. 4.11, in which we present typical photon detection maps for the state $\left|\frac{17}{60}\pi\right\rangle$ for a small number of detected photons, obtained by extracting the first detection events from each data set. Despite the non-negligible dark count level of our non-ideal SPAD array, we notice that the photons fall in the two regions around $x = \pm a$ in the unprotected case (Fig. 4.11a) and close to the position corresponding to $\langle\hat{A}\rangle$ in the protected case (Fig. 4.11b).

Furthermore, we can calculate the expectation value of the first detection event in the protected case (white pixel in Fig. 4.11b), obtaining the value $\langle\hat{A}\rangle = -0.3 \pm 0.3$, where the uncertainty is estimated from the width of the photon counts distribution presented in Fig. 4.10, this result is in agreement with the theoretical value of $\langle\hat{A}\rangle = -0.208$. This is a final, clear demonstration of the capability of extracting the expectation value from just few detection events (even one, in the ideal case) of protective measurements.

$\left|\frac{17}{60}\pi\right\rangle$ unprotected state

$\langle\hat{A}\rangle = -0.21(2) \ (\langle\hat{A}\rangle_{th} = -0.208)$

$\left|\frac{17}{60}\pi\right\rangle$ protected state

$\langle\hat{A}\rangle = -0.19(2) \ (\langle\hat{A}\rangle_{th} = -0.208)$

$|+\rangle$ unprotected state

$\langle\hat{A}\rangle = -0.03(4) \ (\langle\hat{A}\rangle_{th} = 0)$

$|+\rangle$ protected state

$\langle\hat{A}\rangle = 0.0012(14) \ (\langle\hat{A}\rangle_{th} = 0)$

$\left|\frac{\pi}{8}\right\rangle$ unprotected state

$\langle\hat{A}\rangle = 0.72(2) \ (\langle\hat{A}\rangle_{th} = 0.707)$

$\left|\frac{\pi}{8}\right\rangle$ protected state

$\langle\hat{A}\rangle = 0.72(2) \ (\langle\hat{A}\rangle_{th} = 0.707)$

Figure 4.10: Contour plots of the photon counts distributions obtained for the unprotected (left) and protected state (right) and corresponding expectation values. First row 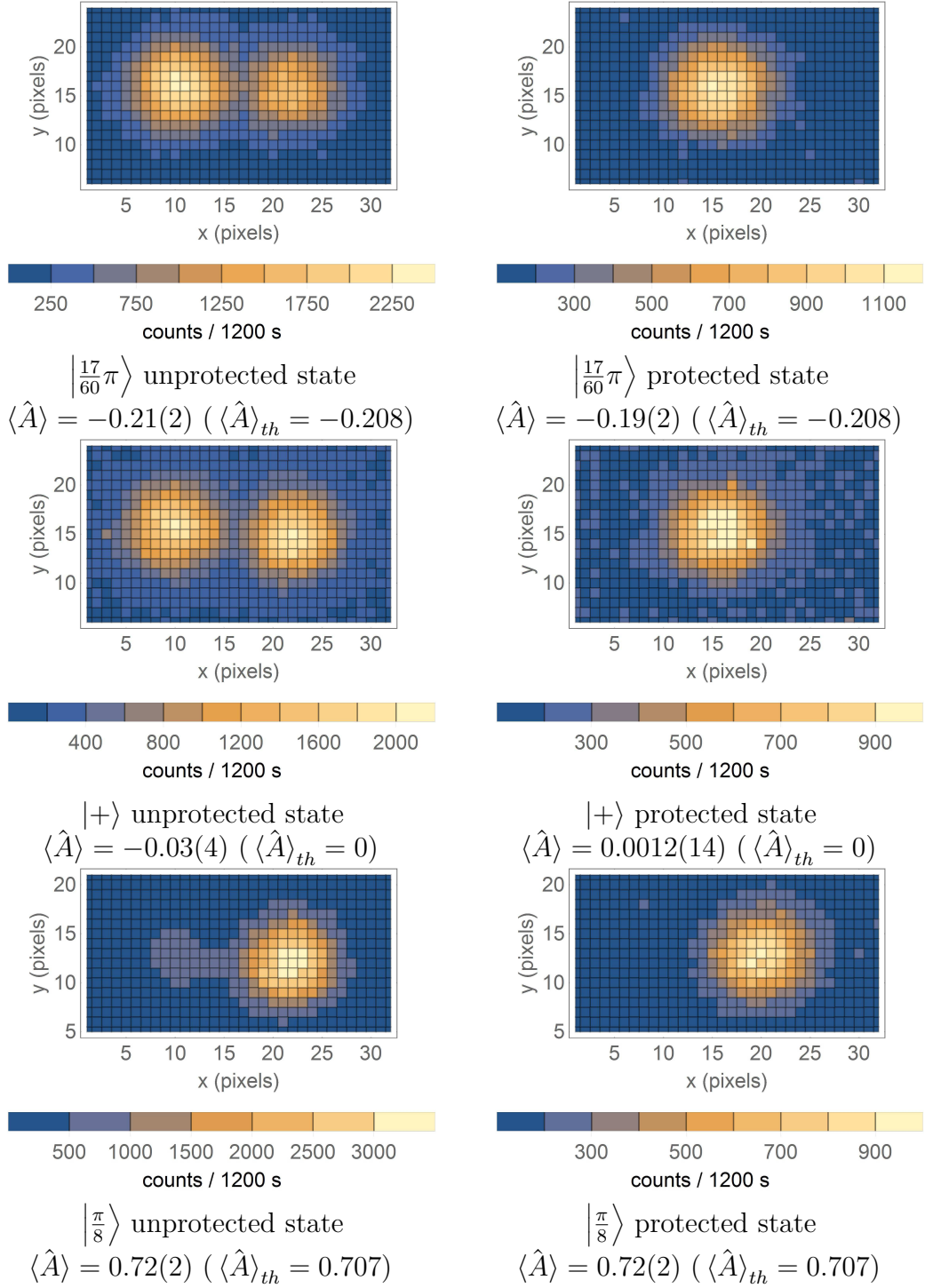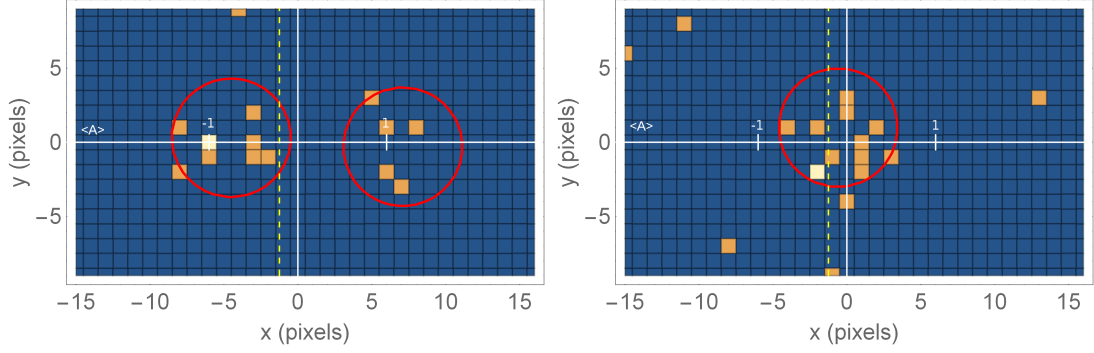images: material from: 'F. Piacentini et al., Determining the Quantum Expectation Value by Measuring a Single Photon, Nat. Phys., 2017, Macmillan Publishers Limited'

106

(a) Unprotected case (14 detection events). (b) Protected case (17 detection events).

Figure 4.11: Results for the input state $\left|\frac{17}{60}\pi\right\rangle$ obtained from a small number of detected photons. The first detection event is marked in white. Yellow dashed line: position corresponding to the theoretical expectation value of the polarization $\langle\hat{A}\rangle_{th} = -0.208$. Red circles: FWHM of the corresponding distributions for the state $\left|\frac{17}{60}\pi\right\rangle$ reported in Fig. 4.10. Material from: 'F. Piacentini et al., Determining the Quantum Expectation Value by Measuring a Single Photon, Nat. Phys., 2017, Macmillan Publishers Limited'

4.1.4 Comparison between protective and projective measurements

In this section we illustrate in detail the theory behind the protective measurement technique, in order to understand whether this new measurement protocol carries an advantage over traditional quantum measurements. To do so, let us analyse in depth both measurement protocols.

PM theoretical framework

Our implementation of PM consists of a sequence of identical interactions, corresponding to the unitary transformation $\hat{U} = \exp\left(-\frac{i}{\hbar}g\hat{\Pi}_H \otimes \hat{P}\right)$, each followed by a QZE-based protection realized by the projector $\hat{\Pi}_\psi = |\psi\rangle\langle\psi|$.

After K interaction-protection steps, the non-normalized output state is

$$|\Psi_{\text{out}}\rangle = \left(\hat{\Pi}_\psi U\right)^K |\Psi_{\text{in}}\rangle = \left(\langle V|\hat{\Pi}_\psi|V\rangle \mathbb{1}_x + \langle H|\hat{\Pi}_\psi|H\rangle e^{-ig\hat{P}}\right)^K |\Psi_{\text{in}}\rangle \quad (4.1.4.1)$$

where our initial state is $|\Psi_{\text{in}}\rangle = |\psi\rangle \otimes |f_x\rangle$, with $|\psi\rangle = \cos(\theta)|H\rangle + \sin(\theta)|V\rangle$ and $|f_x\rangle = \int dx f(x)|x\rangle$, where $f(x) = (2\pi\sigma^2)^{\frac{1}{4}}\exp\left(-\frac{x^2}{4\sigma^2}\right)$. $\mathbb{1}_x$ is the identity.

Thus, the survival probability of a photon after K steps is

$$p_{\text{sur}}(K) = \text{Tr} \left(|\Psi_{\text{out}}\rangle\langle\Psi_{\text{out}}| \right) \tag{4.1.4.2}$$

while the probability of finding a single protected photon in a specific position x_1 is

$$
\begin{aligned}
F_K(x_1) &= p_{\text{sur}}(K)^{-1} \, \text{Tr} \left(|x_1\rangle\langle x_1|\Psi_{\text{out}}\rangle\langle\Psi_{\text{out}}| \right) \\
&= \left(\sum_{k=0}^{K} \binom{K}{k} \langle V|\hat{\Pi}_\psi|V\rangle^k \langle H|\hat{\Pi}_\psi|H\rangle^{K-k} f(x_1 - kg) \right)^2
\end{aligned}
\tag{4.1.4.3}
$$

which leads us to the uncertainty on the position:

$$u(x) = \sqrt{\varepsilon(x^2) - \varepsilon(x)^2} \tag{4.1.4.4}$$

with $\varepsilon(x^n) = \int \mathrm{d}x \; x^n F_K(x)$.

By noticing that there exists a relation between expectation value $\langle\hat{A}\rangle$ and the average position $\varepsilon(x)$, we can obtain the uncertainty on $\langle\hat{A}\rangle$. In particular, we notice that polarization V corresponds to $\langle\hat{A}\rangle = -1$ and to the position $\varepsilon(x) = 0$ (since the polarization V is not deviated), while the polarization H corresponds to $\langle\hat{A}\rangle = 1$ and to the position $\varepsilon(x) = Kg$ (since every interaction shifts the polarization H of g). Therefore, the uncertainty on $\langle\hat{A}\rangle$ given by the detection of a single photon can be easily obtained by rescaling the spatial uncertainty $u(x)$:

$$u(\langle\hat{A}\rangle) = u(x)\frac{2}{Kg} \tag{4.1.4.5}$$

Comparison with the traditional (projective) measurement

Let us now compare the performance of the PM technique with the traditional one, which involves a single strong (projective) measurement realized, for instance, by a polarizing beam splitter (PBS). Measuring the polarization $\hat{A}$ of M photons in the polarization $|\psi\rangle$ with a PBS, the probability of observing m H-polarized (and $M - m$ V-polarized) photons is binomial[175] in the parameter $\cos^2(\theta)$. Therefore, the estimator of $\hat{A}$ is $A = \frac{2m}{M} - 1$ with associated uncertainty:

$$u_{\text{PBS}}(\langle\hat{A}\rangle) = \sqrt{\langle A^2\rangle - \langle A\rangle^2} = \frac{|\sin(2\theta)|}{\sqrt{M}} \tag{4.1.4.6}$$

Then, in case of one detected photon ($M = 1$), the uncertainty becomes $u_{\text{PBS}}(\langle\hat{A}\rangle) = |\sin(2\theta)|$. It is easy to show that this estimator saturates the quantum Cramér-Rao bound (Eq. 1.4.1.7). First, we re-parametrize the state $|\psi\rangle$ by defining $\alpha = \langle A\rangle$,

obtaining $|\psi_1\rangle = \sqrt{\frac{1+\alpha}{2}}\,|H\rangle + \sqrt{\frac{1-\alpha}{2}}\,|V\rangle$ (i.e. $\cos\theta = \sqrt{\frac{1+\alpha}{2}}$). Thus, the quantum Fisher information is

$$I(\alpha) = \mathrm{Tr}\left[\hat{\rho}_\alpha \hat{L}_\alpha^2\right] = 2\sum_{a,b=1}^{2} \frac{|\langle\psi_a|\partial_\alpha\hat{\rho}_\alpha|\psi_b\rangle|^2}{\alpha_a + \alpha_b} \tag{4.1.4.7}$$

where $\hat{\rho}_\alpha = |\psi_1\rangle\langle\psi_1|$, being $\{|\psi_1\rangle, |\psi_2\rangle\}$ an eigenbasis of $\hat{A}$ and α_1 and α_2 the eigenvalues of $\hat{\rho}_\alpha$. For our $|\psi_1\rangle$, we obtain $I(\alpha) = \frac{1}{(1-\alpha)(1+\alpha)} = \sin(2\theta)^{-2}$, which leads to the QCRB:

$$u(\langle A\rangle) \geq \sqrt{\frac{1}{MI(\alpha)}} = \frac{|\sin(2\theta)|}{\sqrt{M}} \tag{4.1.4.8}$$

which is saturated by u_{PBS}. We also notice that, in contrast with our practical implementation of PM, the projective one does not suffer losses in the ideal case. Since this measurement does not assume previous information on the system, we do not calculate the Van Trees bound.

In order to provide a fair comparison between projective measurements and PMs, we need to consider the same amount of initial photons. In PMs, we considered the uncertainty associated to the detection of one protected single-photon. Since not every photon survives the protection procedure, we need, in average, $1/p_{\mathrm{sur}}$ initial photons to have one protected photon arriving to our detector. Therefore, we set $M = 1/p_{\mathrm{sur}}$ in the PBS measurement case and define the ratio:

$$R = \frac{u_{\mathrm{PBS}}(\langle\hat{A}\rangle)}{u(\langle\hat{A}\rangle)} \tag{4.1.4.9}$$

We notice that this ratio is independent of the number of detected photons. In fact, if we detect $\mathcal{N}$ photons in the protective case, the uncertainty scales as $\mathcal{N}^{-1/2}$. Then, for a fair comparison, the number of initial photons in the PBS case should be $M = \mathcal{N}/p_{\mathrm{sur}}(K)$, corresponding to a $(\mathcal{N}/p_{\mathrm{sur}(K)})^{1/2}$, proving our point.

The ratio R is plotted in Fig. 4.12. We note that PM almost always outperforms projective measurements, becoming disadvantageous only for extremely weak interactions (e.g., for $K = 100$, $\xi = g/\sigma = 0.02$ and $|\psi\rangle = |+\rangle$, we have $R = 0.996$). In our case of $K = 7$ interaction, we can reach an impressive advantage $R \sim 3$ for $\xi \sim 1$. This advantage grows with the number of steps and, for $K = 100$ interactions, we get the surprising $R \sim 8.5$ advantage for $\xi \sim 0.4$ (almost one order of magnitude). For higher interaction strength, the ratio is reduced to $R \sim 1.6$ ($R \sim 4$) for $K = 7(100)$, which still makes PM better in terms of uncertainty.

This surprising result tells us that PM outperforms an optimal measurement, i.e. a measurement which saturates the QCRB. This happens because when we
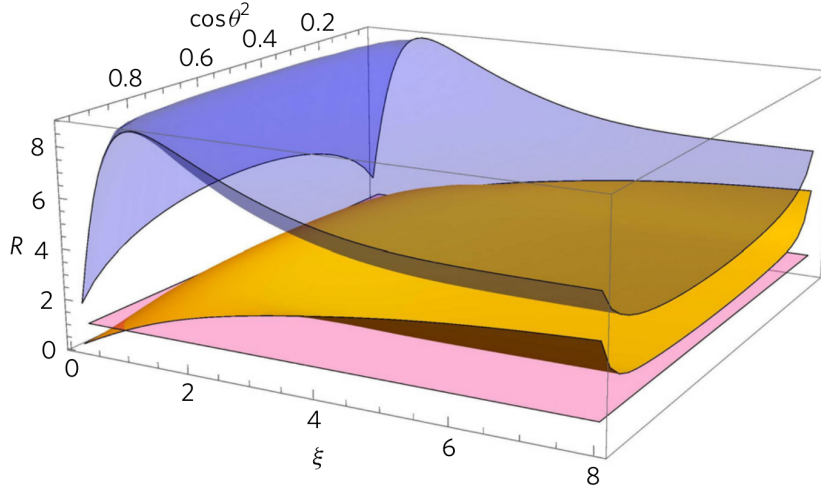
Figure 4.12: Ratio R in Eq. (4.1.4.9) plotted versus the interaction strength $\xi = g/\sigma$ and the H polarization component $(\cos\theta)^2$ of the single-photon state $|\psi\rangle$. Magenta surface: $R = 1$, discriminating the part where PM is advantageous (above) and disadvantageous (below) with respect to projective measurements. Yellow surface: ratio R for $K = 7$. Blue surface: ratio R for $K = 100$. Material from: 'F. Piacentini et al., Determining the Quantum Expectation Value by Measuring a Single Photon, Nat. Phys., 2017, Macmillan Publishers Limited'

calculate the QCRB we make the implicit assumption that the measurement apparatus does not depend on the parameter to be estimated[115]. Our protection scheme, however, exploits the state preparation procedure, making PM inherently parameter dependent and, therefore, not limited by the QCRB. Attempts to find a bound for PM have been made in [176].

R can also be seen as a quantity which identifies the necessary amount of resources needed to achieve the same level of precision with the two measurement techniques. In particular, the initial amount of photons needed with a projective measurement to achieve a certain precision is R^2 the one needed by PM (this derives from $u_{\text{PBS}}(\langle \hat{A} \rangle) \propto 1/\sqrt{M}$). This advantage can be extremely useful for quantum systems when states produced have "great value" (i.e. are hard to produce). Note, however, that the resources are not exactly identical: in PMs each photon passes through K polarisers, while in projective measurements they are sensed only by a single polariser.

The high efficiency of the PM technique comes from the surprisingly high survival probability of the protected photon, as showed in Fig. 4.13, in which one can

appreciate that, with $K = 100$ interactions and $\xi \sim 0.4$, we have $p_{\text{sur}} > 0.57$.
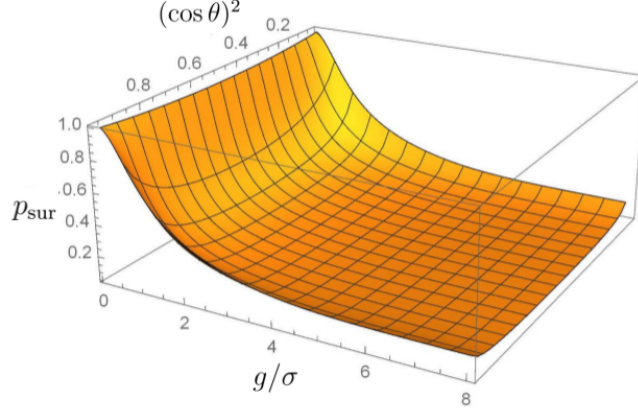

Figure 4.13: Photon survival probability $p_{\text{sur}}(K = 100)$ in a PM scheme plotted versus the interaction strength $\xi = g/\sigma$ and the H polarization component $(\cos \theta)^2$ of the single-photon state $|\psi\rangle$. Material from: 'F. Piacentini et al., Determining the Quantum Expectation Value by Measuring a Single Photon, Nat. Phys., 2017, Macmillan Publishers Limited'

We note, however, an high survival probability, $p_{\text{sur}} > 0.23$, even for strong interactions ($\xi = 6$), where the PMs approximation does not hold anymore. We can understand this by looking at Fig. 4.14 in which we see that the relative probability of losing a photon in a protection step, because of unsuccessful selection measurement, decreases with the single photon advancing in the sequence since photons are more likely on the "right path". This "natural selection" recalls genetic algorithms[177]. In particular, we can see each interaction as a mutation, followed by a crossover (the coherent recombination) and the selection, carried by the protection. This "genetic quantum measurement" protocol has been further investigated in [176].

Furthermore, we can investigate the scaling of the uncertainty in PMs versus the initial resources, by considering the number of photon-projection interactions instead of the number of initial photons. To do so, we consider a situation in which we perform the detection of a photon at each projection stage. Our initial resources in this case, then, are the K initial photons, each individually interacting with only one of the K identical polarisers. This way, we can define the ratio

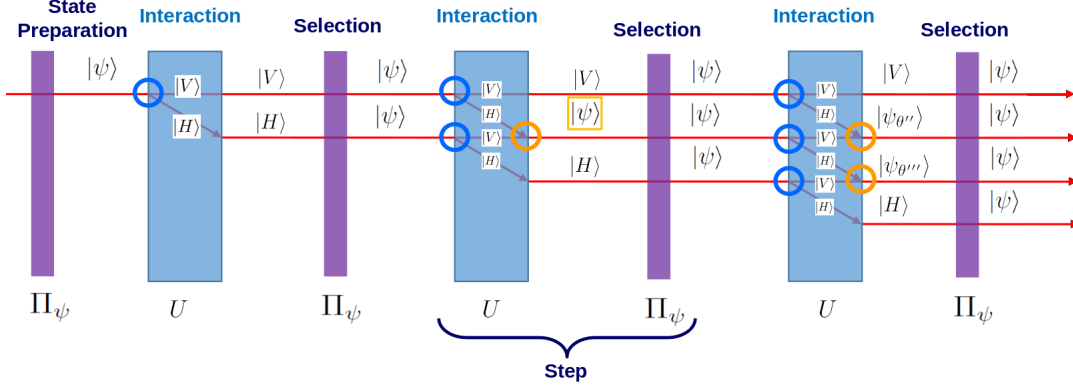$$R' = \frac{u'_{\text{PBS}}(\langle \hat{A} \rangle)}{u(\langle \hat{A} \rangle)} \tag{4.1.4.10}$$

Figure 4.14: Analogous of the PM scheme for strong interaction $\xi \gg 1$. The first interaction unit (composed of a birefringent crystal pair, as described in Sec. 4.1.2) completely separates the H and V polarization components which are then projected onto the initial state $|\psi\rangle$ with a certain probability p_{sur}. From the second interaction unit onwards, the H and V beams coherently recombine in some spots (indicated by the yellow circle), forming a state with non-zero survival probability in the subsequent protection stage. This results in a reduction of the photon losses in the paths close to the expectation value $\langle \hat{A} \rangle$, granting an advantage with respect to traditional projective measurements even without weak interaction.

between the uncertainty $u(\langle \hat{A} \rangle)$ associated with a single detected photon in a PM with K stages, and the uncertainty $u'_{\text{PBS}}(\langle \hat{A} \rangle)$ associated with the projective measurement carried on $M = K$ photons. From Fig. 4.15 we note that the value of R' associated with strong interactions ($\xi \gg 1$) does not depend on K. This means that the PM uncertainty in (Fig. 4.15) scales with the number of interactions as $1/\sqrt{K}$, which is the same scaling of the projective measurement exploiting $M = K$ initial photons. Furthermore, being $\max R' \sim 1.5$, we understand that PMs with a single detected photon (which, on average, corresponds to $1/p_{\text{sur}}$ initial photons) and projective measurements exploiting K (instead of $M = 1/p_{\text{sur}}$) photons provide almost the same uncertainty. The advantage of PM, then, comes from the fact that its related uncertainty scales as $1/\sqrt{K}$, instead of $1/\sqrt{M} = \sqrt{p_{\text{sur}}(K)}$, since $1/p_{\text{sur}} < K$.

The above considerations about the advantage of PM with respect to projective measurement have been made in the ideal case, neglecting all losses except for the ones due to the protection. In the specific case of our experiment, the optical losses greatly reduce the advantage we discussed so far. These, however, are just present technological limitations, which can be overcome by introducing more efficient optical components or by implementing this measurement in atomic or solid
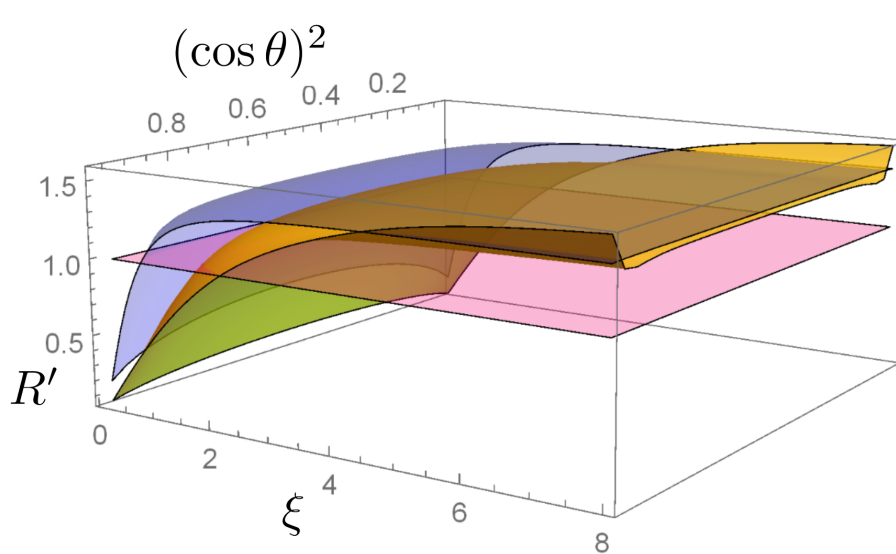
Figure 4.15: Ratio R' in Eq. (4.1.4.10) plotted versus the interaction strength $\xi = g/\sigma$ and the H polarization component $(\cos \theta)^2$ of the single-photon state $|\psi\rangle$. Magenta surface: $R' = 1$, again discriminating the part where PM is advantageous (above) and disadvantageous (below) with respect to PBS measurement. Yellow surface: R' for $K = 7$. Blue surface: R' for $K = 100$. Material from: 'F. Piacentini et al., Determining the Quantum Expectation Value by Measuring a Single Photon, Nat. Phys., 2017, Macmillan Publishers Limited'

state quantum system, where losses are typically lower than the ones experienced in optics experiments.

4.1.5   Conclusions

Protective measurements are a groundbreaking new measurement paradigm in which Alice sends Bob a state and a "protection" and in which Bob obtains a measurement of the expectation value of an observable by exploiting such resources. We described the first experimental implementation of protective measurements, showing that they can indeed extract the expectation value of an observable, a quantity so far considered purely statistical, even with just one measurement on a single (protected) particle. The results we obtained with this protocol were all in agreement with the values obtained with the traditional (projective) measurements, as well as with the theoretically-expected ones.

We also verified one fundamental property of protective measurement, i.e. that the protection procedure preserves the coherence of the initial state, as certified by the high Fidelities between the initial state and the reconstructed protected state.

Finally, we theoretically demonstrated how protective measurements outperform the projective ones, even allowing for an uncertainty reduction of almost one order of magnitude for $K = 100$ interaction-protection stages. This advantage may lead to significant applications, for instance, when testing an unknown state preparation procedure in which the produced states have "great value" (i.e., they are difficult to produce).

Our results do not only represent an important metrological advancement, but may also shed important insights on the foundations of quantum mechanics, especially in the hot debate about the ontic or epistemic nature of the wavefunction[170, 171, 172, 173]. Possible future extensions of this work regard a calculation of the effective bound on the uncertainty and an investigation of the strong measurement regime.

4.2   Robust weak measurements

Weak values (Sec. 1.2.4) are one of the most interesting new quantum measurement paradigms, with several important applications both in fundamental physics and metrology. In spite of that, weak values are still controversial. Since they rely on a weak coupling, weak values can only be observed after averaging over a very large number of readings of the pointer variable. The legitimacy of this statistical analysis has, however, been questioned (Sec. 1.2.4), since weak values also rely on post-selection, a non-standard experimental practice. In an attempt to shine some light on this matter, we introduce the *robust weak measurements* (RWMs), a natural evolution of PMs. In particular, RWMs are an iterative measurement protocol in which even a single reading of the measuring device provides a reliable estimate of a weak value, even for anomalous weak values, i.e. the ones lying outside the eigenvalue spectrum of the measured observable. While the post-selection still has a crucial role, with RWM the anomalous outcome no longer arises from a statistical analysis. In the following section, we will theoretically introduce RWMs and describe a quantum optics experiment able to implement them, presenting the obtained results.

4.2.1   Theory

RWM allows extracting in a single shot the weak value of an observable A. In order to describe them, let us first define, following our usual description, the system $\mathcal{S}$, the meter $\mathcal{M}$ and the total system $\mathcal{T}$:

- System $\mathcal{S}$
  The *system* is defined as in PMs (Sec. 4.1.1). By decomposing it in the

eigenbasis $|a_i\rangle$ of $\hat{A}$, the initial state of the system can be described as

$$|\psi\rangle = \sum_i \alpha_i |a_i\rangle \qquad (4.2.1.1)$$

- Meter $\mathcal{M}$
  The *meter* $\mathcal{M}$ has a continuous pointer value described by an operator $\hat{Q}$ whose initial wavefunction is supposed to follow the normal distribution:

$$f_x(x) = \frac{1}{\sqrt{\sigma\sqrt{2\pi}}} \exp\left(-\frac{x^2}{4\sigma^2}\right) \qquad (4.2.1.2)$$

- Total system $\mathcal{T}$
  As per PMs (Sec. 4.1.1), the only non-vanishing term in the total Hamiltonian is assumed to be the interaction one:

$$\hat{H}_{int} = g\hat{A} \otimes \hat{P} \qquad (4.2.1.3)$$

with $\hat{P}$ being the canonically conjugated operator to the pointer $\hat{Q}$.

Within this framework, we follow a procedure similar to the one described for PMs, i.e. an iterative protocol in which the photon is pre- and post-selected before and after every weak coupling with the measuring device. We also note that performing N steps of this procedure is equivalent to coupling N particles of a pre- and post-selected system with a single measurement device, a procedure first described in [178].

Intuitively, one may think that each step of RWM procedure generates a shift on the pointer which is proportional to the weak value $\langle A\rangle_w$. However, real world couplings $g/\sigma > 0$ have been showed to affect the state evolution, making the weak value less anomalous[179, 180]. Therefore, before proceeding with the experiment, we need study such effects on our polarization-based implementation of this iterative weak value measurement protocol.

Robust weak measurement of polarization

In our experiment, we want to measure (anomalous) weak values of the polarization observable

$$\hat{A} = |H\rangle\langle H| - |V\rangle\langle V| \qquad (4.2.1.4)$$

with a N-steps RWM protocol, i.e., a series of N weak couplings, each sandwiched between pre- and post-selections.

In order to provide a mathematical description of RWM, let us define the pre-selected ($|\psi_\alpha\rangle$) and post-selected ($|\psi_\beta\rangle$) states:

$$|\psi_\alpha\rangle = \cos\alpha\,|H\rangle + \sin\alpha\,|V\rangle \tag{4.2.1.5}$$

$$|\psi_\beta\rangle = \cos\beta\,|H\rangle + \sin\beta\,|V\rangle \tag{4.2.1.6}$$

Thus, the pre-(post-)selection process can be described by the projectors $\hat{\Pi}_{\alpha(\beta)} = \left|\psi_{\alpha(\beta)}\right\rangle\!\left\langle\psi_{\alpha(\beta)}\right|$ and the effective interaction Hamiltonian by

$$\hat{H}_{int} = g\hat{A} \otimes \hat{P} \tag{4.2.1.7}$$

which is realized, as in Sec. 4.1.2, by a birefringent crystal with an interaction Hamiltonian $\hat{H}'_{int} = 2g\hat{\Pi}_H \otimes \hat{P}$, being $\hat{\Pi}_H = |H\rangle\langle H|$ the projector onto the horizontal component of the polarization. The two formulations only differ by a translation.

Lastly, we introduce the rotation operator $\hat{R}$, which is defined as

$$\hat{R}\,|\psi_\beta\rangle = |\psi_\alpha\rangle \tag{4.2.1.8}$$

and, since we're dealing with linearly-polarized states, can be experimentally implemented with a half-wave plate, which allows us to perform any rotation on the linear polarization plane.

Now, we can define the RWM protocol as a succession of N "interaction blocks" $\hat{\mathcal{U}}$, each consisting in a pre-selection $\hat{\Pi}_\alpha = |\psi_\alpha\rangle\langle\psi_\alpha|$ followed by a weak interaction $\hat{U} = \exp\left(-\frac{i}{\hbar}\hat{H}'_{int}\right)$, a post-selection $\hat{\Pi}_\beta = |\psi_\beta\rangle\langle\psi_\beta|$ and the rotation $\hat{R}$, which transforms the post-selected state $|\psi_\beta\rangle$ in $|\psi_\alpha\rangle$, in order to avoid losses due to the pre-selection process. This interaction block, then, has the following mathematical expression

$$\hat{\mathcal{U}} = \hat{R}\hat{\Pi}_\beta\hat{U}\hat{\Pi}_\alpha \tag{4.2.1.9}$$

which allows us to write the state after N interactions as

$$|\Psi_{\text{out}}\rangle = \hat{\mathcal{U}}^N\,|\psi_\alpha\rangle \otimes |f_x\rangle = \sum_k \binom{N}{k} Z_H^k e^{-i2gk\hat{P}} Z_V^{N-k}\,|\psi_\alpha\rangle \otimes |f_x\rangle \tag{4.2.1.10}$$

being $Z_{H(V)} = \langle\psi_\beta|\hat{\Pi}_{H(V)}|\psi_\alpha\rangle$.

Thus, the probability of finding a photon in the position x after a RWM measurement of N steps is

$$F_N(x,\alpha,\beta,N) = |(\langle x_0| \otimes \langle\psi_\alpha|)\,|\Psi_{\text{out}}\rangle|^2 = \left|\sum_{k=0}^{N} \binom{N}{k} Z_H^k Z_V^{N-k} f_x(x-2kg)\right|^2 \tag{4.2.1.11}$$

116

Integrating F_N, we get the survival probability

$$
\begin{aligned}
p_{\text{sur}}(\alpha, \beta, N) &= \int dx F_N(x, \alpha, \beta, N) \\
&= \sum_{k=0}^{N} \sum_{k'=0}^{N} \binom{N}{k} \binom{N}{k'} Z_H^{k+k'} Z_V^{2N-k-k'} \exp\left[-\frac{g^2}{2\sigma^2}(k - k')^2\right]
\end{aligned}
\tag{4.2.1.12}
$$

and, finally, the expectation value of the pointer position

$$
\begin{aligned}
\langle x \rangle &= \int dx\, x \frac{F_N(x, \alpha, \beta, N)}{p_{\text{sur}}(\alpha, \beta, N)} \\
&= \frac{1}{p_{\text{sur}}(\alpha, \beta, N)} \sum_{k=0}^{N} \sum_{k'=0}^{N} \binom{N}{k} \binom{N}{k'} Z_H^{k+k'} Z_V^{2N-k-k'} \left(g(k + k')\right) \times \\
&\quad \times \exp\left(-\frac{g^2}{2\sigma^2}(k - k')^2\right)
\end{aligned}
\tag{4.2.1.13}
$$

and the standard deviation of the pointer

$$
\sigma_x = \sqrt{\langle x^2 \rangle - \langle x \rangle^2}
\tag{4.2.1.14}
$$

$$
= \frac{1}{p_{\text{sur}}(\alpha, \beta, N)} \sum_{k=0}^{N} \sum_{k'=0}^{N} \binom{N}{k} \binom{N}{k'} Z_H^{k+k'} Z_V^{2N-k-k'} \sigma^2 \times
$$

$$
\times \exp\left(-\frac{g^2}{2\sigma^2}(k - k')^2\right)
\tag{4.2.1.15}
$$

In this framework, the weak value is defined as

$$
\langle A \rangle_w = \frac{\langle x \rangle}{Ng} - 1
\tag{4.2.1.16}
$$

with an associated standard deviation of

$$
\sigma_{\langle A \rangle_w} = \frac{\sigma_x}{Ng}
\tag{4.2.1.17}
$$

From Eq.s (4.2.1.16) and (4.2.1.13), we notice that weak values obtained through RWMs not only depend upon the pre- and post-selected state, but also on the number of steps N and the g/σ parameter, reaching the correct value for $g/\sigma \to 0$. Moreover, this effect is eventually perfectly predictable and can be corrected. In fact, for anomalous weak values, the RWM outcome shrinks as the interaction strength g/σ increases (an effect already observed for weak values in[179, 180]). This effect does not scale linearly with the number of steps, as can be clearly appreciated in Fig. 4.16a, in which we can see the predicted weak value as a function of the interaction parameter $\eta = \exp\left(-\frac{g^2}{2\sigma^2}\right)$, with $\eta = 1$ being the ideal adiabatic

117

case. This happens because, as η deviates from the ideal case, the post-selection causes distortions of the pointer distribution (examples in Fig. 4.17). These distortions start as a shrinking of the pointer width for $\eta \sim 1$ (Fig. 4.17a), but, as η decreases, they deform the pointer into multilobate structures (as in Fig. 4.17b). Furthermore, both these effects grow stronger as the anomaly (i.e. the distance between the theoretical weak value $\langle \hat{A} \rangle_w = \langle \psi_\alpha | \hat{A} | \psi_\beta \rangle / \langle \psi_\alpha | \psi_\beta \rangle$ and the closest eigenvalue of $\hat{A}$) increases, as can be appreciated by comparing the two plots in Fig. 4.16.
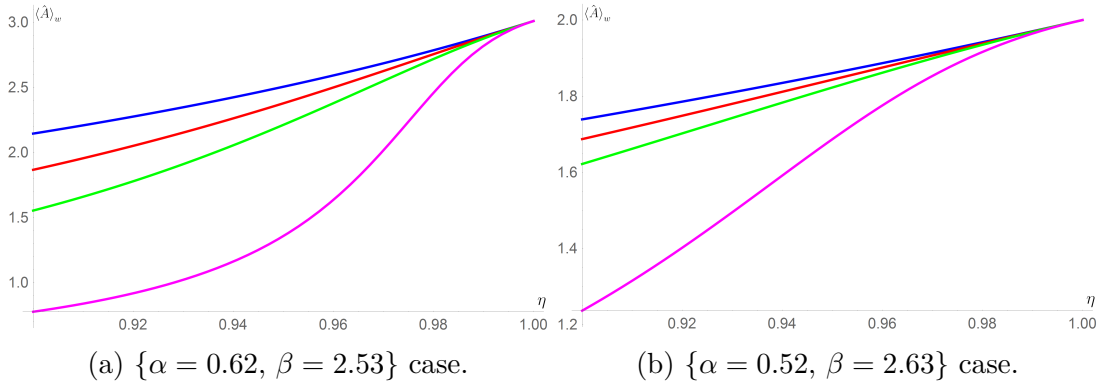

(a) $\{\alpha = 0.62,\ \beta = 2.53\}$ case. (b) $\{\alpha = 0.52,\ \beta = 2.63\}$ case.

Figure 4.16: Robust weak value for fixed α and β as a function of the parameter η. Blue line: $N = 1$. Red line: $N = 2$. Green line: $N = 3$. Magenta line: $N = 7$.

In the non-anomalous regime, instead, we notice that the weak value slightly enlarges as η parts from the ideal case. This is the case, for instance, of Fig 4.18, where we fixed $\alpha = 0.52$ and $\beta = 0.88$. The pointer distribution, in this case, only experiences a widening of its width on the x axis as η decreases.

For these reasons, we need to carefully take into account the influence of each parameter on each weak value we want to measure. In the next section, we illustrate our experimental RWM implementation.

4.2.2   Experiment

Setup

Our experimental setup is shown in Fig. 4.19. Our photons source (section (a) of Fig. 4.19) is composed by a 76 MHz mode-locked laser whose second harmonic (398 nm) pumps a $10 \times 10 \times 5$ mm LiIO$_3$ crystal, in which Type-I SPDC takes place. The signal photons are spectrally filtered by an IF centred at 702 nm and with a FWHM of 10 nm, and coupled to a single-mode fibre. At the end of the single-mode fibre, the photons are collimated in a Gaussian mode with width σ,
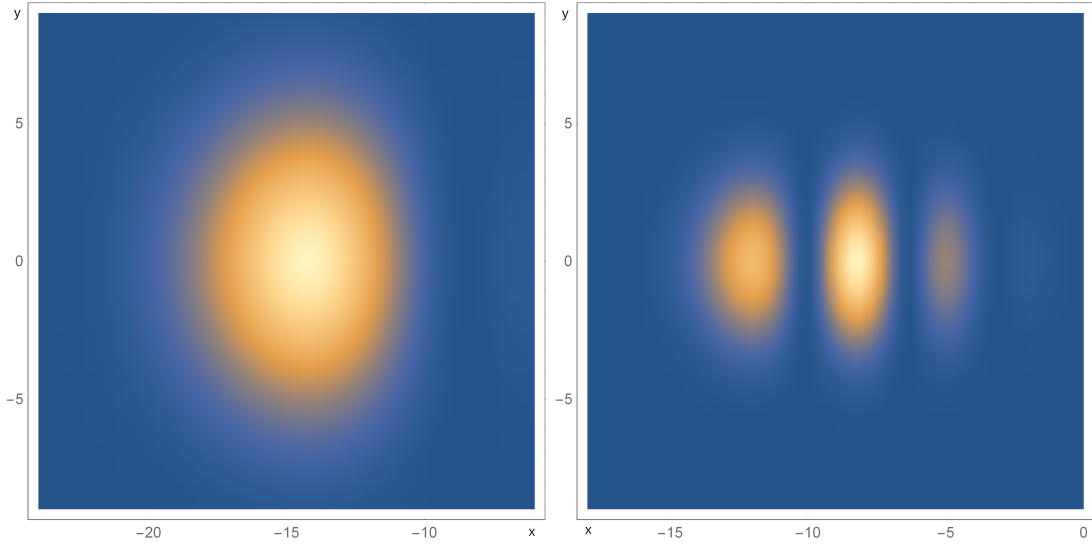
(a) $\eta = 0.986$, we notice a shrinking of the pointer width on the x axis.

(b) $\eta = 0.952$, we observe a large, multilobate pointer spatial distribution.

Figure 4.17: Pointer distributions of RWV in the non-ideal regime for $\{\alpha = 0.62,\ \beta = 2.53,\ N = 7\}$. x and y axis: arbitrary units.
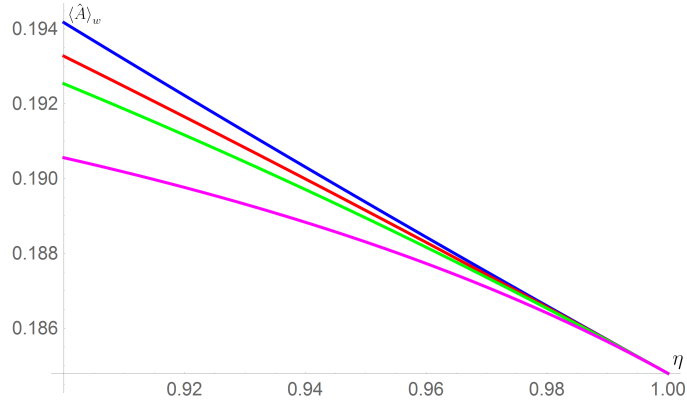
Figure 4.18: Robust weak value for $\{\alpha = 0.52,\ \beta = 0.88\}$ as a function of the parameter η. Blue line: $N = 1$. Red line: $N = 2$. Green line: $N = 3$. Magenta line: $N = 7$.

as defined in Eq. (4.2.1.2) and sent to the free-space path where the robust weak measurement experiment occurs. The idler photons are spectrally filtered by an IF centred at 920 nm and with a FWHM of 10 nm, fibre coupled, and sent to a SPAD, whose output helps us monitor any eventual fluctuations in the source intensity. Photons produced this way are in a multi-thermal distribution with a mean photon

119
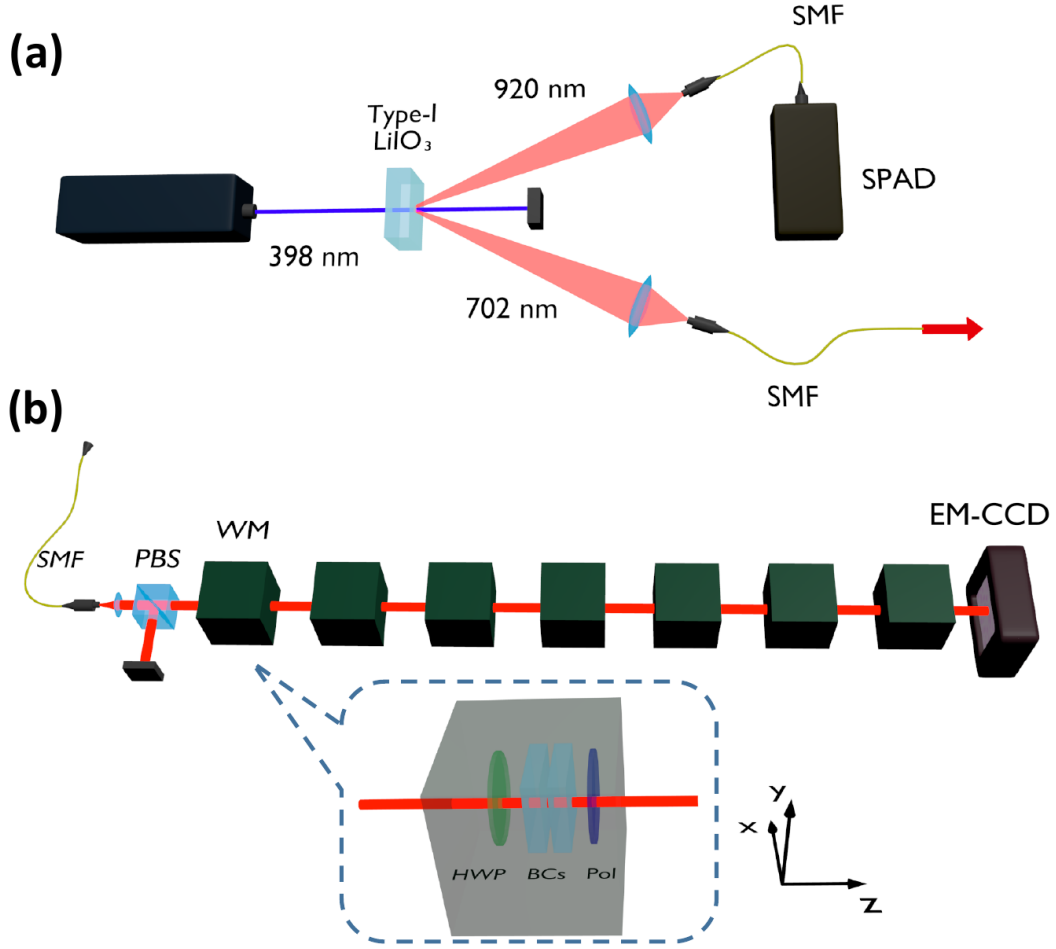
Figure 4.19: Experimental setup. PBS: polarizing beam splitter. SMF: single-mode fibre. WM: weak measurement block. HWP: half-wave plate. BCs: birefringent crystals units. Pol: polariser. EM-CCD: electron-multiplying CCD. SPAD: single-photon avalanche diode.

number per pulse $\ll 1$. This guarantees a short coherence time (~ 150 fs), which allows avoiding self-interference effects due to internal reflections in the many optical elements needed for our RWM.

In the RWM path, a polarizing beam splitter filters any residual polarization component. Then, the signal photons interact with $N = 7$ consecutive identical weak measurement blocks (WM), each of them implementing the three weak measurement phases, i.e. pre-selection, weak coupling and post-selection. The photon enters in a linear polarization, either thanks to the PBS or to the post-selection of

the previous block. The pre-selection stage consists in a half-wave plate, rotating the photon polarization to the desired $|\psi_\alpha\rangle$ polarization. The weak interaction is realized by a pair of birefringent crystals, which create a slight displacement on the x axis between the H and V polarization components. In each pair, the crystal roles are the same described in 4.1.2 for PMs, generating here a displacement of $g = 0.575 \pm 0.007$ px (note that here we define g in a different way and we use a different set of crystals and detector with respect to PM). The post-selection is executed by a polariser, projecting the photons in the state $|\psi_\beta\rangle$. This configuration is equivalent to the one described in Sec. 4.2.1. Finally, photons are detected by a 2D spatially-resolving electron-multiplying CCD (EM-CCD) device, able to work both in linear analog regime and in photon counting regime[181].

We choose to employ this specific 2D photon detector instead of the one used for PM (Sec. 4.1.2) because the low photon survival probability in the anomalous weak value regime limits us to a signal-to-noise which is too small for the SPAD camera.

4.2.3 Results

We decide to acquire data sets for four different parameters sets, shown in Tab. 4.1. For each of these sets, the number of steps is $N = 7$ and the interaction strength is the aforementioned $g = 0.575 \pm 0.007$ px.

	α (rad)	β (rad)	σ (px)
(a)	0.62	2.53	3.30
(b)	0.62	2.53	1.80
(c)	0.52	2.62	1.66
(d)	0.52	0.88	1.78

Table 4.1: Parameters of the measurement setup.

For each set, we perform a first acquisition with $|\psi_\alpha\rangle = |H\rangle$ and $|\psi_\alpha\rangle = |V\rangle$ and only the crystals in the optical path, to calibrate the system. Then, we perform an acquisition with $|\psi_\alpha\rangle$ and $|\psi_\beta\rangle$ in the desired state and all polarisers and wave-plates in the optical path. Last, we perform an acquisition with only the polarisers and wave-plates and one with a free optical path, to compensate the deviations induced by those optics.

Weak values extraction

Let us now look at the analysis techniques we employed to evaluate the RWMs of the polarization.

In contrast with the previously-exploited SPAD array (Sec. 4.1.3), our EM-CCD does not have hot pixels. Therefore, we only need to perform a linear regression of the data in order to determine and remove the dark counts. In the rare event of pixels outside the region of interest, we opted to remove them with a mask.

After that, we extract the centres x_H, x_V, x_{pol} and x_{void} of the distributions obtained with the input states $|H\rangle$ and $|V\rangle$, with only polarisers and wave-plates, and with a free optical path, respectively. Such values and their uncertainties are obtained by averaging linear regressions of multiple acquisitions. In this case, each photon carries information about the weak value, which can be extracted from the formula

$$\langle \hat{A} \rangle_w = \frac{2(x - x_{pol} + x_{void}) - x_V - x_H}{x_H - x_V} \tag{4.2.3.1}$$

where x is the position in which the photon has been detected. We can, then, extract $\langle \hat{A} \rangle_w$ directly from a single photon detection. The associated uncertainty is evaluated as

$$\sigma_{\langle \hat{A} \rangle} = \sqrt{\sigma_{px}^2 + \sigma_{angles}^2 + \sum_{i=1}^{5} \left| \frac{\partial \langle \hat{A} \rangle}{\partial x_i} \right|^2 \sigma_{x_i}^2} \tag{4.2.3.2}$$

where $x_1 = x$, $x_2 = x_H$, $x_3 = x_V$, $x_4 = x_{pol}$ and $x_5 = x_{void}$.
σ_{px} is the type-B uncertainty due to the discretization of the EM-CCD camera used for the experiment. We estimate it to be the size of half a pixel of the EM-CCD, and then we propagate it through the subsequent formulas extracting the weak value.
σ_{angles} is the type-B uncertainty associated with the sensitivity of the rotating stages hosting the polarisers and the half-wave plates determining α and β. It is taken as 1 degree (a good estimation of the precision we can reach in setting these angles, considering the 2 degrees resolution of the rotators used).

The uncertainties σ_{x_i} of x_i are evaluated as the statistical uncertainties in the case of x_{pol} and x_{void}, and as:

$$\sigma_x = \sqrt{\sigma_{x,\text{stat}}^2 + \sigma_{inhom}^2 + \langle \hat{A} \rangle_{w,\text{th}}^2 \sigma_g^2 + \sigma_{threshold}^2} \tag{4.2.3.3}$$

$$\sigma_{x_{H(V)}} = \sqrt{\sigma_{x_{H(V)},\text{stat}}^2 + \sigma_{inhom}^2 + \sigma_g^2} \tag{4.2.3.4}$$

for x, x_H and x_V. $\langle \hat{A} \rangle_{w,\text{th}}$ is the theoretically-expected RWM result for our parameters.
$\sigma_{x_i,\text{stat}}$ indicates the statistical uncertainty on x_i.
σ_{inhom} is the type-B contribution accounting for the inhomogeneities within the birefringent crystals, causing distortion and broadening on the final photon distributions. To estimate it, for each case a-d we take the V distribution (the one

theoretically unaffected by the birefringence in our setup) and extract its average value and the centre of the Gaussian fit, evaluating the discrepancies between them and choosing such value as type-B uncertainty.

σ_g is the type-B contribution related to the determination of the coupling constant g between quantum state and measurement device. To obtain this, we evaluate g for each crystal pair, and then calculate the uncertainty on the obtained g values. $\sigma_{threshold}$ is the type-B contribution accounting for the threshold chosen to discriminate between signal photons and noise (unwanted background photons and dark counts). It is estimated as some confidence level on the threshold applied.

#	1	2	3	4	5	6	7	8
	α (rad)	β (rad)	σ (px)	η	$\langle\hat{A}\rangle_{w,\text{th}}$	$\langle\hat{A}\rangle_{w,\text{exp}}$	$\langle\hat{A}\rangle_w^{1\text{P}}$	$\sigma_{\langle\hat{A}\rangle_w^{1\text{P}}}$
(a)	0.62	2.53	3.30	0.985	2.67	2.66 ± 0.12	3.1 ± 0.7	0.7
(b)	0.62	2.53	1.80	0.952	1.40	1.50 ± 0.10	1.6 ± 0.6	0.7
(c)	0.52	2.62	1.66	0.945	1.64	1.58 ± 0.07	2.0 ± 0.5	0.4
(d)	0.52	0.88	1.78	0.949	0.19	0.14 ± 0.05	-0.4 ± 0.7	0.6

Table 4.2: Results for the four cases under test. Columns 1-5: preparation parameters α, β, σ and η and the corresponding theoretical RWV $\langle\hat{A}\rangle_{w,\text{th}}$. Column 6: experimental values results. Column 7: results for a single-detection experiment. Column 8: theoretical prediction of the uncertainty for the single-detection experiment.

Column 6 of Tab. 4.2 and Fig. 4.20 host our results for the four different parameter configurations. As we can see, all measurements are in agreement with the theoretical predictions, even with a coverage factor $k = 1$. This means that, with RWM, each single photon carries information about the weak value of its polarisation, granting the possibility of extracting such value even in a one-shot experiment with just a single photon.

Furthermore, we can calculate the RWM outcome of the first detection event (black boxes in Fig. 4.20), obtaining the values in column 7 of Tab. 4.2, where the uncertainty corresponds to the width of the final pointer wavefunction in the x-direction and is estimated from the standard deviation of the pointer (as in Eq. (4.2.1.17)), calculated for the parameters α, β and the initial width of the pointer σ. These values are all in agreement with our theoretical expectations and their uncertainties are close to the ones theoretically predicted. This is a further demonstration that RWMs allow us to extract a (anomalous) weak value even from one single detection event, an impossible task in usual weak value estimation procedures.
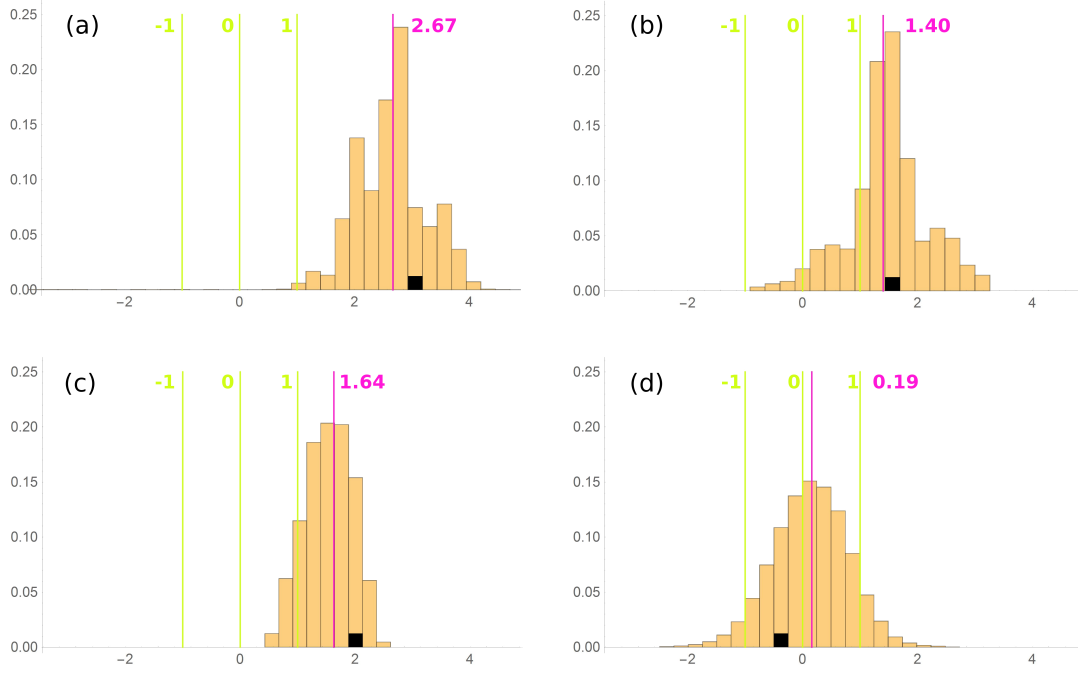
Figure 4.20: Marginals of the normalized photon counts distributions. Green lines: extremes and centre of the eigenvalues spectrum. Purple lines: theoretically expected RWM outcome. Black square: first click of the run. Results are reported in Table 4.2

.

Let us now analyse more in detail these results.

Cases a and b

Fig. 4.21 reports the behaviour of the anomalous weak value, obtained from Eq. (4.2.1.16), for the parameters $\alpha = 0.62$, $\beta = 2.53$, as a function of the parameter η for different numbers of steps N (already showed in Fig. 4.16a) and our experimental points, noticing a good agreement even with a coverage factor $k = 1$, confirming the connection between the shrinking of the weak value and the interaction strength predicted by our model.

We also notice that case b shows a trilobate structure (Fig. 4.20b), as we predicted in Sec. 4.2.1 and Fig. 4.17. In this case, the evaluation of the statistical uncertainties has been carried out with the Monte Carlo method[182].
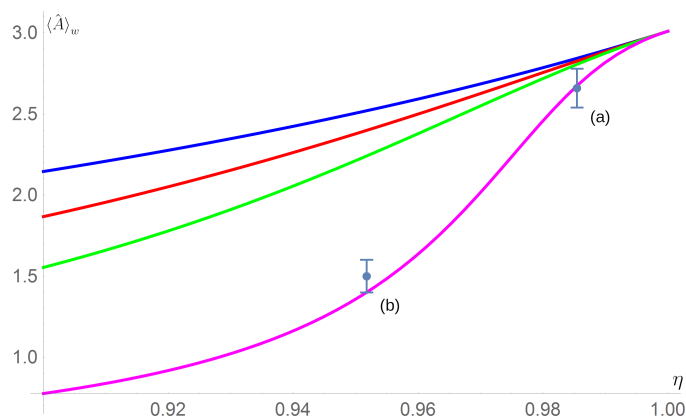
Figure 4.21: RWM for $\{\alpha = 0.62,\ \beta = 2.53\}$ as a function of the parameter η. Blue line: $N = 1$. Red line: $N = 2$. Green line: $N = 3$. Magenta line: $N = 7$. Azure points: experimentally-obtained weak values with our RWM procedure, reported with the associated uncertainties (azure vertical bars).

Case c

In Fig. 4.22 we report the behaviour of the anomalous weak value as a function of the parameter η for different numbers of steps N and $\alpha = 0.52$, $\beta = 2.63$ (already showed in Fig. 4.16a). We notice a good agreement between our experimental value and the theoretical magenta curve even for a coverage factor $k = 1$.
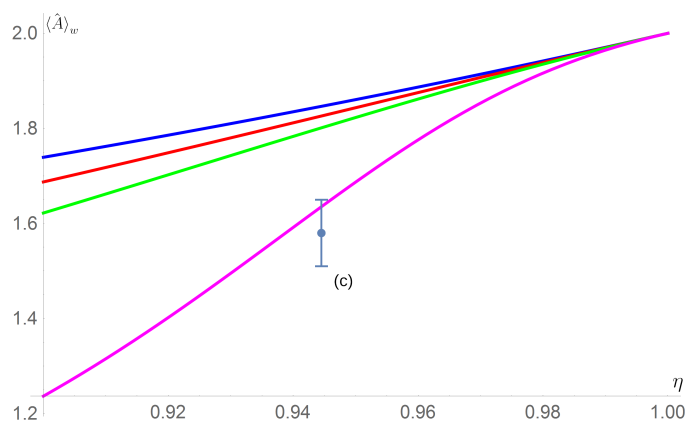

Figure 4.22: Robust weak value as a function of the parameter η for $\{\alpha = 0.52,\ \beta = 2.62\}$. Blue line: $N = 1$. Red line: $N = 2$. Green line: $N = 3$. Magenta line: $N = 7$. Azure point: experimentally-obtained weak value with our RWM procedure, reported with the associated uncertainties (azure vertical bars).

Furthermore, by looking at Fig. 4.20c, we notice that, despite having a similar η with respect to case b (Fig. 4.20b), the pointer distribution does not exhibit a

multilobate structure, a direct evidence of the dependency of the intensity of the distortion with respect to the anomaly of the weak value.

Case d

In Fig. 4.23 we report the behaviour of the non-anomalous weak value for the parameters $\alpha = 0.52$, $\beta = 0.88$, as a function of the parameter η for different numbers of steps N (already showed in Fig. 4.18). We notice, again, a good agreement between theory and experiment even with a coverage factor $k = 1$.
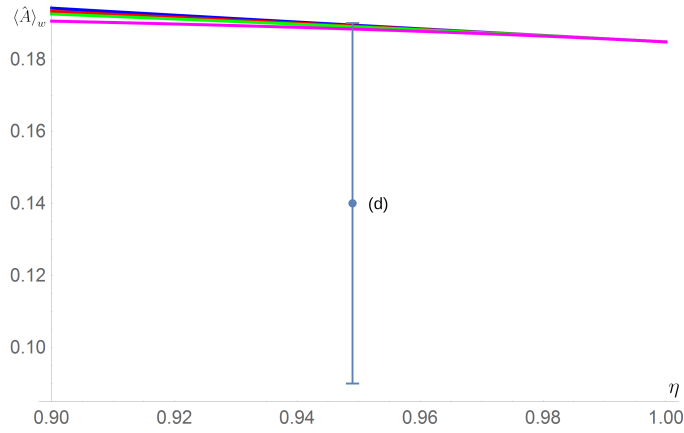

Figure 4.23: Robust weak value as a function of the parameter η for $\{\alpha = 0.52, \beta = 0.88\}$. Blue line: $N = 1$. Red line: $N = 2$. Green line: $N = 3$. Magenta line: $N = 7$. Azure point: experimentally-obtained weak value with our RWM procedure, reported with the associated uncertainties (azure vertical bars).

We have, thus, demonstrated, for the first time, the capability of extracting the weak value from even one detection event of RWM, a huge novelty with respect to the traditional weak value measurement procedures, which require averaging over a very large number of readings of the pointer variable. Furthermore, our experimental data fit the theoretical model for RWM, confirming our predictions about the "shrinking" effect and the distortion of the pointer distribution.

4.2.4 Conclusions

Robust weak measurements are a novel measurement protocol which exploits repeated couplings with the same pointer to directly extract the weak value even from a single detection event. We described the first experimental implementation of RWM, demonstrating how they allow us to extract the weak value of an observable even from a single measurement on a single particle, even in case of

anomalous weak values, i.e. the ones lying outside the measured observable eigen-value spectrum. Our experimental results are all in agreement with the theoretical predictions within a coverage factor $k = 1$, certifying the reliability of our quantum optical implementation of RWM. We believe that our analysis will offer a deeper understanding of the meaning of weak values, stressing their non-statistical, single-particle nature, and of the nature of the anomalous ones.

Furthermore, the unprecedented measurement capability of RWMs, able to extract single-shot (anomalous) weak values, will surely pave the way for future practical applications to quantum metrology and other quantum technologies.

Chapter 5

Novel quantum mechanical tools and related reconstruction techniques

Part of the work described in this chapter has been previously published in [183] *and* [184].

In this chapter, we introduce the theoretical concept and illustrate the reconstruction technique for the pseudo-density operator (PDO), an extension of the traditional density matrix formalism able to describe spatial and temporal correlations on an equal footing. Such a tool can be used to model physical scenarios that the usual density operator cannot cope with. For instance, situations were we have to add some "ad hoc" nonlinearity in the evolution of quantum systems (something in contrast with the linearity of traditional quantum mechanics). We will then show the first reconstruction of a PDO, obtained in a quantum optics experiment simulating the behaviour of a three qubit system impossible to describe with traditional quantum mechanical tools (i.e. density matrices). Since PDOs cannot be obtained by usual tomographical techniques, our results mark a relevant milestone both for the physics and metrology communities.

5.1 Beyond the density operator: the pseudo-density operator

In quantum theory, the complete specification of the state of a physical system is given at any one time by its density operator, and the initial conditions; the density operator of a composite system contains all the possible spatial correlations among its subsystems. Such operator, however, cannot describe temporal correlations among systems measured at multiple times, even though relativity[185, 186], has

revealed that many distinctions between space and time are not as fundamental as we previously thought. This prompts the question of whether it could be possible to eliminate this asymmetry between spatial and temporal correlation, by introducing a more general formalism. For this reason, several attempts to generalize quantum theory and, in particular, the density operator, have been made[187, 188]. We focus on the pseudo-density operator[189], a generalization of the density operator which treats space and time indiscriminately. As we will see in the following sections, this new formalism allows describing many physical phenomena involving space-time correlations, such as black holes and closed (open) time-like curves, which traditional quantum mechanical formalism finds difficult to describe.

5.1.1 Pseudo-density operator: definition and properties

A density operator (Sec. 1.1.1) can be viewed as a collection of all possible statistics ensuing from measurements of observables on a system of interest. For a n-qubit system, for instance, we can write a general density operator as[27, 189]:

$$\hat{\rho}_n = \frac{1}{2^n} \sum_{i_1=0}^{3} \cdots \sum_{i_n=0}^{3} \langle \bigotimes_{j=1}^{n} \hat{\sigma}_{i_j} \rangle \bigotimes_{j=1}^{n} \hat{\sigma}_{i_j} \qquad (5.1.1.1)$$

where

$$\begin{aligned}
\hat{\sigma}_0 = \mathbb{1} = \begin{pmatrix} 1 & 0 \\ 0 & 1 \end{pmatrix} \qquad \hat{\sigma}_1 = \hat{X} = \begin{pmatrix} 0 & 1 \\ 1 & 0 \end{pmatrix} \\
\hat{\sigma}_2 = \hat{Y} = \begin{pmatrix} 0 & -i \\ i & 0 \end{pmatrix} \qquad \hat{\sigma}_3 = \hat{Z} = \begin{pmatrix} 1 & 0 \\ 0 & -1 \end{pmatrix}
\end{aligned} \qquad (5.1.1.2)$$

$\langle \bigotimes_{j=1}^{n} \hat{\sigma}_{i_j} \rangle$ is the expectation value of the product of the outcomes of measurements of the n operators $\hat{\sigma}_{i_j}$.

PDOs generalise these operators into covering statistics that pertain to the time domain. In this case, then, the tensor product combines both space-like or time-like separated systems. Then, the general PDO for n qubits is defined as:

$$\hat{R}_n = \frac{1}{2^n} \sum_{i_1=0}^{3} \cdots \sum_{i_n=0}^{3} \langle \{\hat{\sigma}_{i_j}\}_{j=1}^{n} \rangle \bigotimes_{j=1}^{n} \hat{\sigma}_{i_j} \qquad (5.1.1.3)$$

which differs from the expression for the density operator (Eq. (5.1.1.1)) because $\langle \{\hat{\sigma}_{i_j}\}_{j=1}^{n} \rangle$ now denotes the expected value given by the outcomes of a set of *independently-performed* (i.e. not influenced by the outcome of the other measurement events) Pauli measurements, which, in contrast with the usual density operator, can be performed at different times on the same particle. PDO, thus,

generalizes the traditional density operator formalism to describe space-time correlations.

PDO shares the following properties[189] with the density operator:

- $\hat{R}$ is Hermitian ($\hat{R} = \hat{R}^\dagger$);

- $\mathrm{Tr}\,\hat{R} = 1$.

Furthermore, we can define the reduced PDOs of a system in the same way we do for the density operator formalism (Sec. 1.1.1), e.g., given a the PDO $\hat{R}_{AB}$ defined over two systems A and B, we can obtain the PDO for the system A with the partial trace $\hat{R}_A = \mathrm{Tr}_B\,\hat{R}_{AB}$.

Differences appear, however, when considering time correlations. Let us, for instance, imagine a physical system composed of a single qubit initially in the maximally mixed state ($\hat{R} = \mathbb{1}/2$) which can be measured at two different time instants t_1 and t_2, with no time evolution between them. Each measurement can be performed in any of the three Pauli operators $\hat{X}$, $\hat{Y}$ and $\hat{Z}$. We can represent such state with the following PDO:

$$\hat{R}_{12} = \frac{1}{4}\{\mathbb{1}_{12} + \hat{X}_1\hat{X}_2 + \hat{Y}_1\hat{Y}_2 + \hat{Z}_1\hat{Z}_2\} \qquad (5.1.1.4)$$

where 1 and 2 indicate t_1 and t_2, respectively. It is simple to show that $\hat{R}_{12}$ has at least one negative eigenvalue, therefore it is not positive and, as a consequence, it is not a density operator. Interestingly, the reduced PDOs of such systems are

$$\hat{R}_{1(2)} = \mathrm{Tr}_{2(1)}\,\hat{R}_{12} = \frac{\mathbb{1}}{2} \qquad (5.1.1.5)$$

which correspond to the density operators of a maximally-mixed state. So the marginals of this generalised operator are actually both perfectly allowed density operators, but the overall time-correlated PDO describing such a bipartite state is not.

Being able to naturally merge spatial and temporal correlations, PDOs are suited to describe a wide class of physical phenomena which involve predictions of space-time correlations violating the standard properties of quantum theory, such as superpositions of different space-time geometries in quantum gravity, resulting in superposing different causal orders [190]; or the physics of black holes [191]. This makes them an innovative and precious tool, because the aforementioned physical scenarios can not be described by the density matrix formalism without generating paradoxes to be reconciled, eventually, by adding nonlinear terms in the quantum

state evolution (something in sharp contrast with the linearity of quantum mechanics shown in Chapter 1). Therefore, the development of a technique allowing for PDO reconstruction is a high-profile metrological challenge, very likely to produce a major impact on fundamental science. In the next sections, we describe the reconstruction technique for a three-qubit PDO and briefly show the results obtained applying it to two quantum optical systems simulating the behaviour of the two physical systems mentioned above: entanglement near open time-like curves and the black hole information loss paradox.

5.1.2 Case 1: reconcile the black hole information loss paradox

One of the most interesting properties of black holes[192] is the Hawking radiation[193], i.e. black-body radiation spontaneously emitted by black holes, which is due to the steady conversion of quantum vacuum fluctuations into pairs of particles, one of which escapes at infinity while the other is trapped inside the black hole horizon. This radiation reduces the mass of black holes and is therefore also known as black hole evaporation.

The possibility of black hole evaporation, however, poses a problem from the quantum mechanical perspective[194, 195, 196, 197], as well as other cosmological aspects[198, 199, 200, 201]. This happens because, if the process is unitary (as prescribed by quantum theory), then entanglement must be created between the exterior and the interior of the black hole as particle pairs are generated through the process of Hawking radiation [202, 203, 204, 205]. In an elementary model of evaporation based on a finite number of qubits, we should presumably, at some point, reach a situation in which all the qubits left inside the black hole are maximally entangled with the qubits outside of it, assuming thermal radiation has been emitted. As the black hole continues to evaporate, then, Hawking radiation would imply the generation of even more entanglement between the interior and the exterior of the black hole. However this cannot be further, since qubits already maximally entangled cannot be entangled with anything else. This fact, that a system cannot be maximally entangled to more than one other system, is known as the monogamy of entanglement principle [17, 206]. To solve this contradiction, known as *black hole information loss paradox*[207], we either have to drop the unitary description of black hole evaporation, or allow the violation of the monogamy of entanglement [208]. PDO formalism allows describing the latter.

Black hole evaporation and PDO

Following the Schwarzschild metric[209], that describes space-time in the presence of a non-rotating black hole[210], crossing the horizon for a particle is equivalent to swapping the signatures of the spatial and temporal components of the metric [211]. Now, if we think of a typical quantum phase factor $e^{i(kx-\omega t)}$, the change of the sign of space and time simply corresponds to complex conjugation of the phase factor. In this sense, the effect on the density operator of an in-falling quantum system should be described by the operation of transposition (which swaps the off-diagonal elements and therefore implements the complex conjugation). However, transposition is a positive, but not completely positive, operation. This means that, if we perform transpose on just one of two entangled systems, the overall state may not end up being a valid density operator but it is, however, a valid PDO. In particular, we can describe the process of one particle of an entangled pair in the state $|\phi_+\rangle = \frac{1}{\sqrt{2}}(|00\rangle + |11\rangle)$ with the partial transpose $\mathbb{1} \otimes \hat{T}$. The outcome of such operation is the state $\hat{R}^{bh}$, described in Eq. (5.1.1.4), which can be used to describe the state of a pair of qubits, with one of them falling into the black hole.

The PDO formalism, then, allows modelling the process of black hole evaporation. Suppose to have a maximally-entangled state created just above the event horizon of a black hole, as in the process of Hawking radiation. One of the particles (Q2), falls onto the black hole. This process creates time-like correlations between Q2 and the other particle (Q3), described by the state $\hat{R}^{bh}$, as defined above. When Q2 becomes entangled with another particle (Q1), this leads to a three-qubit entangled pseudo-state, which can be written as

$$\hat{R}_{123} = \frac{1}{8}\{\mathbb{1}_{123} - \Sigma_{12} + \Sigma_{23} - \Sigma_{13})\} \tag{5.1.2.1}$$

where $\Sigma_{ij} = X_i X_j I_k + Y_i Y_j I_k + Z_i Z_j I_k$. The reduced states are $\hat{R}_{12} = \frac{1}{4}(\mathbb{1}_{12} - \Sigma_{12})$, $\hat{R}_{13} = \frac{1}{4}(\mathbb{1}_{13} - \Sigma_{13})$, and $\hat{R}_{23} = \frac{1}{4}(\mathbb{1}_{23} + \Sigma_{23})$. Now we can see that Q2 and Q3 are maximally correlated (in time), while Q1 and Q3, as well as Q1 and Q2, are maximally entangled (in space). Therefore, correlations described by PDOs need not obey the principle of monogamy of entanglement. We conjecture this PDO could be used to describe the elementary step involved in the black hole evaporation.

5.1.3   Case 2: entangled particles in an open time-like curve

Einstein's general relativity (GR)[186, 212, 213] allows for particular solutions which involve time travel. This is the case, for instance, of closed time-like curves (CTCs)[214], which allow observers to travel backwards in time and, possibly, even to interact with their former selves. However, these solutions have been argued to be unphysical in classical general relativity, because they lead to paradoxes, such

as the grandfather's paradox [215, 216]. Somebody even invokes a chronology-protection principle to rule out their existence in physical reality [192]. Possible solutions to these paradoxes come from merging general relativity with quantum theory, by considering the dynamics of a quantum object in proximity of CTCs [217, 218, 219]. While this approach seems to resolve the classical paradoxes, it requires the dynamical evolution on each of the qubit copies to be non-linear[217]. Because of non-linearity, CTCs can be used to perform perfect discrimination of non-orthogonal states and other tasks that violate quantum theory [220, 221, 222, 223, 224]. This nonlinear evolution has also been experimentally simulated [225].

In open time-like curves (OTCs), instead, the observer travels backwards in time, avoiding any contact with his former self. Interestingly, even in this case there can be violations of basic properties of entanglement. In fact, if we consider a time-travelling qubit Q2 which is initially maximally entangled with another, chronology respecting qubit Q1, in the chronology-violating region, we have that the qubit Q1 is both maximally entangled with Q2 and with its future copy Q3, thus violating the monogamy of entanglement[224, 226]. In the usual description, based on traditional density operators, the monogamy of entanglement is preserved at the expenses of introducing a nonlinear evolution. PDOs, instead, allow us to provide a consistent description for the three-qubit system within the chronology violating region, while maintaining the violation of the monogamy of entanglement without giving up on linearity.

In particular, we can describe an OTC with a model (Fig. 5.1) in which a maximally entangled pair of qubits (Q1 and Q2) is created in the distant past of the region of space-time that contains the OTC; qubit Q2 is then sent into the OTC. The copy which emerges from the OTC is represented by a third qubit (Q3). In the distant past and the distant future, the state of the qubits is just a maximally entangled pair. However, in the chronology-violating region, Q1 has to be maximally entangled both with the qubit that emerges from the OTC (Q3) and with the qubit entering it (Q2). This can be described by the PDO:

$$\hat{R}_{123} = \frac{1}{8}\{\mathbb{1}_{123} - \Sigma_{12} + \Sigma_{23} - \Sigma_{13})\} \tag{5.1.3.1}$$

The two reduced states $\hat{R}_{12} = \frac{1}{4}(\mathbb{1}_{12} - \Sigma_{12})$ and $\hat{R}_{13} = \frac{1}{4}(\mathbb{1}_{13} - \Sigma_{13})$ are two density operators, representing each a maximally entangled pair, while the marginal $\hat{R}_{23} = \frac{1}{4}(\mathbb{1}_{23} + \Sigma_{23})$ is, instead, a PDO describing the (maximal) temporal correlations between qubits Q2 and Q3 (and not a proper physical state, like the ones corresponding to $\hat{R}_{12}$ and $\hat{R}_{13}$). $\hat{R}_{123}$, then, describes a system of three qubits which are maximally anti-correlated in every basis, which is also unphysical. This description can be easily generalized in order to allow any unitary transformation on the qubit entering the OTC. As per the black holes case, this shows again that

the PDO describes correlations that need not obey the entanglement monogamy, thus being a viable tool to linearly describe an OTC. We also note that, from the mathematical point of view, the structure of this PDO is equal to the one describing the black hole case (Eq. (5.1.2.1)).
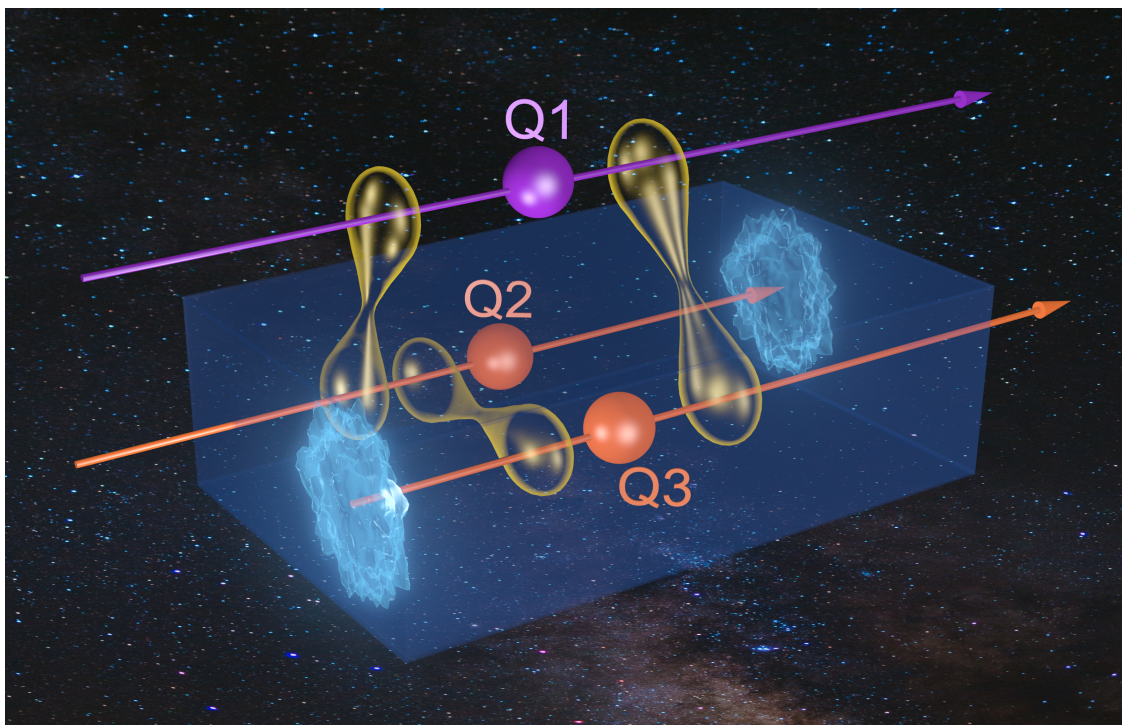

Figure 5.1: OTC circuit (pictorial representation). Qubits Q1 and Q2 are initially in a singlet state. Qubit Q2 enters a chronology-violating region (blue shaded box), emerging as qubit Q3. In the chronology-violating region, qubits Q1 and Q2 must be in a singlet state, and so are qubits Q1 and Q3. Furthermore, since Q2 and Q3 are, respectively, the past and future copy of the same qubit, they are also maximally correlated. This situation violates monogamy of entanglement: this is why it cannot be described by ordinary density operators, while it can be modelled by PDOs. Background photo taken by Franco Ruggiero.

5.1.4   PDO reconstruction techniques

In order to reconstruct the PDOs described by Eq.s (5.1.2.1) and (5.1.3.1), we perform a quantum-optical experiment simulating the behaviour of the three qubits of these systems, and we reconstruct all the statistics contained in the related PDOs, by constructing different sub-ensembles of entangled pairs of photons (A and B), on which different measurements are realised. In our system, photon A can be

measured at two different times (t_1 and t_2) while photon B can only be measured once at time t_1. Then, photon A measured at two different times represents qubits Q2 and Q3, while photon B represents qubit Q1. Note that the simulation consists of reproducing all the statistics belonging to the OTC/black hole physical scenario by performing the relevant measurements on different sub-ensembles - the quantum systems in each of these sub-ensembles obeying quantum theory.

Let us now describe our experimental setup.

Setup
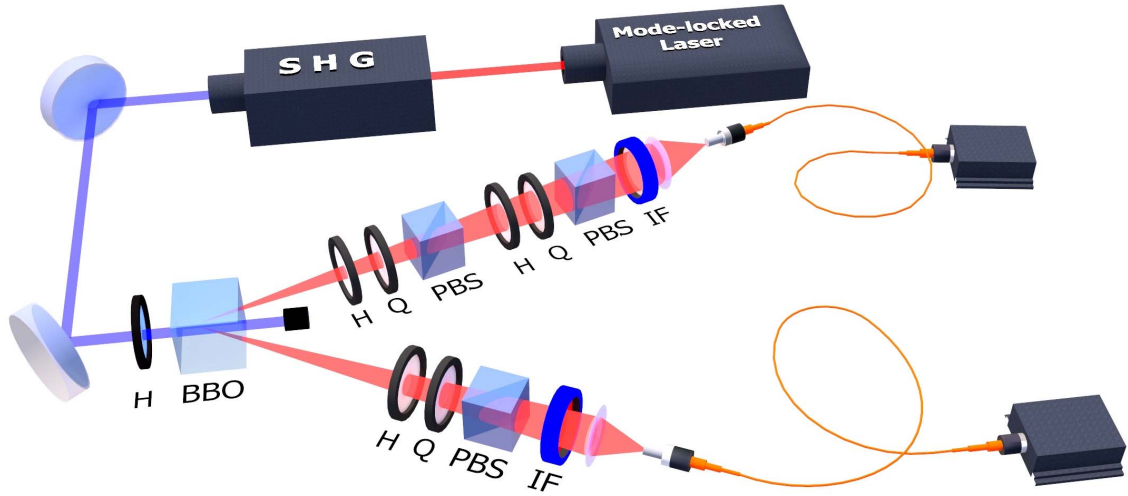
Figure 5.2: Experimental setup. H: half-wave plate. Q: quarter-wave plate. PBS: polarizing beam splitter. IF: interference filter. SHG: second harmonic generation. BBO: β-Barium borate. ⓒⓘ C. Marletto et al., Theoretical description and experimental simulation of quantum entanglement near open time-like curves via pseudo-density operators. *Nat Commun* **10**, 182 (2019). https://doi.org/10.1038/s41467-018-08100-1.

In the first part of our setup we produce maximally-entangled states. A CW laser at 532 nm pumps a Ti:Sapphire crystal in an optical cavity, generating a mode-locked laser at 808 nm with a 76 MHz repetition rate. The pulsed laser is frequency-doubled by second harmonic generation (SHG) and then injected into a 0.5 mm thick β-Barium borate (BBO) crystal, where degenerate non-collinear type-II SPDC occurs (Sec. 2.3.2). We spatially select the photons belonging to the intersections of the two SPDC cones with two irises, and properly compensate the temporal delay between the horizontally- and the vertically-polarized photons induced by the birefringence within the SPDC crystal by adding two 0.25 mm thick

BBO crystals with the optical axis rotated of 90° with respect to the one of the SPDC crystal (as already described in Sec. 3.2.2). This way, we generate the (maximally entangled) singlet state $|\psi_-\rangle = \frac{1}{\sqrt{2}}(|HV\rangle - |VH\rangle)$.

The second part of our setup is, instead, the one in which the PDO reconstruction is performed. To be able to evaluate both spatial and temporal correlations, in photon A path, two polarization measurements occur in cascade (Q1 and Q2), each carried by a half-wave plate (H) and a quarter-wave plate (Q) followed by a polarizing beam splitter (PBS). Between the two measurements, a half-wave plate and quarter-wave plate are put in order to compensate the polarization projection occurred in Q1. Photon B, instead, undergoes a single polarization measurement (Q3) performed by the same H+Q+PBS unit used for Q1 and Q2.

After these measurements, photons A and B are filtered by bandpass interference filters (centred at $\lambda = 808$ nm, with a 20 nm FWHM on path A and a 3 nm FWHM on path B) and coupled to multi-mode optical fibres connected to Si-SPADs, whose outputs are sent to coincidence electronics.

PDO reconstruction and entanglement monogamy violation

To perform the reconstruction of the PDO we realise different measurements on different sub-ensembles, collecting the 3-fold and the 2-fold correlations on the two photons. We need, however, to properly "choose" the measurements to be performed in order to form a minimum quorum allowing for a full reconstruction[227] of $\hat{R}_{123}$. This is needed because, in our experimental simulation, it would be impossible to perform a standard three-qubit quantum tomography (Sec. 3.2.3) procedure able to reconstruct $\hat{R}_{123}$, since a measurement of the photon A at t_1 (Q2) would influence the subsequent measurement at time t_2 (Q3), in contrast with the very definition of PDO. For this reason, we restrict ourselves to a sub-sample of the standard three-qubit tomographic measurements quorum, in which we measure only commuting observables in subsequent measurements on photon A (i.e. for Q2 and Q3). This way, we are able to avoid the issues derived from the measurement temporal ordering.

In particular, we can describe the PDO reconstruction procedure in four steps:

1. Prepare an ensemble where we measure the whole set $\{\hat{X}, \hat{Y}, \hat{Z}\}$ on photon A at time t_1 (Q2) followed by measurements of the same observables at time t_2 (Q3) (including all cross-correlations between different observables). This provides the full reconstruction of the reduced time-correlated pseudo-state $\hat{R}_{23} = \frac{1}{4}(I + \Sigma_{23})$.

2. Prepare an ensemble and measure the whole set $\{\hat{X}, \hat{Y}, \hat{Z}\}$ on photon A and on photon B at time t_1 (Q2 and Q1) - this provides the space-correlated state $\hat{R}_{12}$.

3. Prepare an ensemble and measure the whole set $\{\hat{X}, \hat{Y}, \hat{Z}\}$ on photon B at time t_1 (Q1) and on photon A at time t_2 (Q3) - this provides the space-correlated state $\hat{R}_{12}$.

4. Prepare an ensemble and measure the whole set $\{\hat{X}, \hat{Y}, \hat{Z}\}$ on photon A and on photon B at time t_1 (Q2 and Q1), followed by a measurement on photon A at time t_2 (Q3) identical to the one occurred at time t_1. This provides the three-point correlations which we expect, from the definition of $\hat{R}_{123}$, to be all zero.

Fig. 5.3 reports the tomographic reconstruction of $\hat{R}_{123}$, as well as the ones of its marginals $\hat{R}_{12}$, $\hat{R}_{13}$, $\hat{R}_{23}$, compared with the theoretical expectations. Unfortunately, we can only compute the Fidelity (App. A) between theoretically-predicted and experimentally-reconstructed PDO marginals $\hat{R}_{12}$ and $\hat{R}_{13}$, which are the only reconstructions corresponding to physical density operators. The fidelities for these two marginals are, respectively, $F_{12} = 0.964$ and $F_{13} = 0.963$, certifying an excellent agreement between theory and experiment.

This procedure also highlights an interesting property. As we have previously seen, the reduced PDO of some subsystem can be obtained as the a partial trace of the total system PDO, for instance, in our case $\hat{R}_{13} = \text{Tr}_2 \hat{R}_{123}$. $\hat{R}_{13}$ cannot, however, be experimentally reconstructed by using the measurements obtained for the three-point correlations and then averaging over the results of the measurements on Q2. This is because the trace over a temporal degree of freedom is not equivalent to averaging with respect to all possible values of the observables that can be measured at that time. Indeed, $\text{Tr}(\hat{P}\hat{R}_{123})$ where $\hat{P}$ is a generic projector could be negative, so that it cannot be generally interpreted as a probability. This is a general property of PDOs: they are not always positive operators because the subsystems do not always represent spatially-correlated subsystems, but they can, instead, as in the case of qubits Q2 and Q3, represent time-like separated systems. The full tomographic reconstruction of a PDO is, therefore, different from reconstructing a standard density operator, as we have seen above.

This experiment also allows us to show that $\hat{R}_{123}$ accounts for a phenomenon that would be considered paradoxical in the density operator framework, i.e. the violation of entanglement monogamy among the three qubits of our system. On the other hand, PDO formalism allows describing situations, as the aforementioned
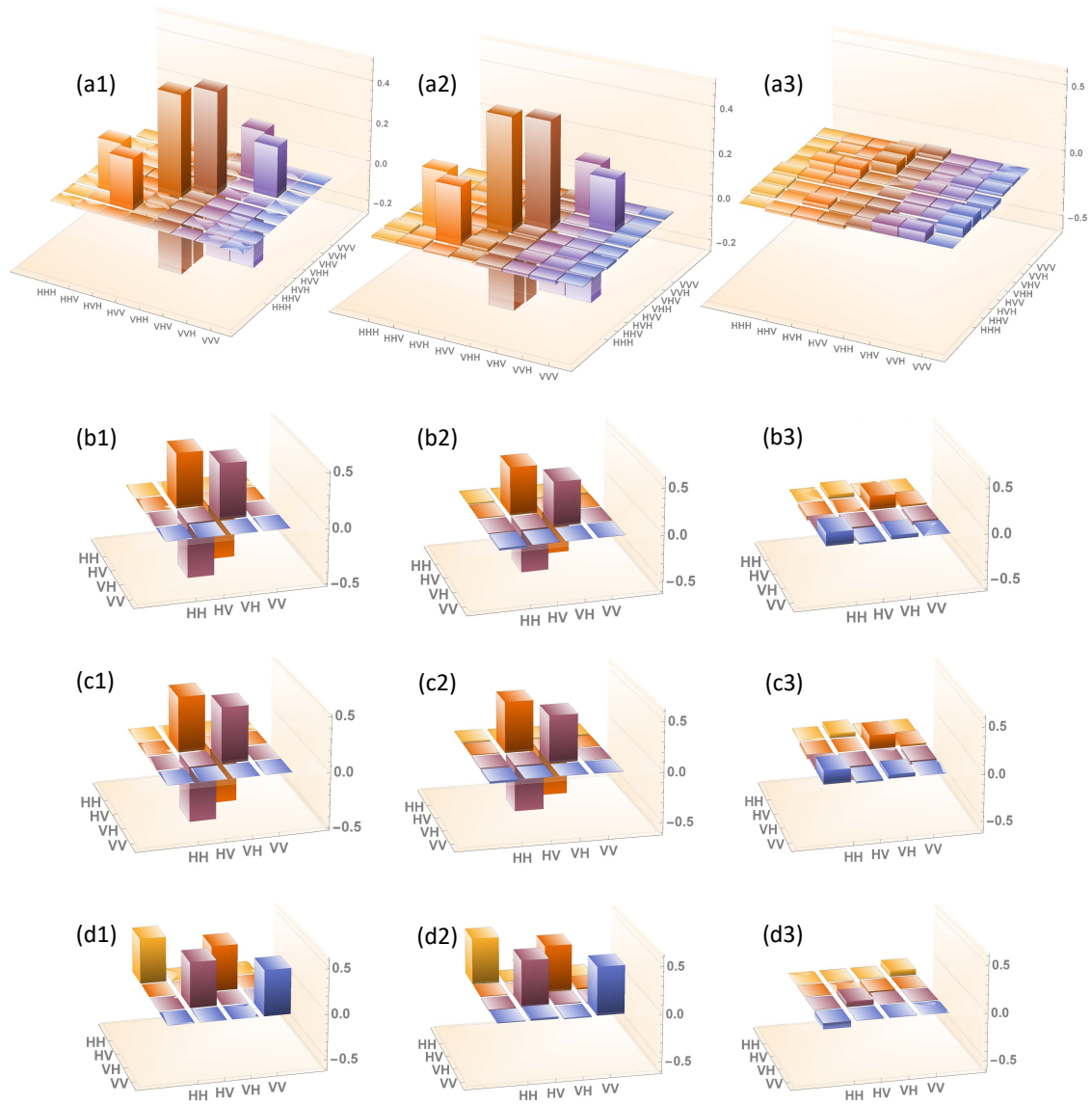
Figure 5.3: Pseudo-density operator tomographic reconstruction. Theoretical $\hat{R}_{123}$ PDO (a1) compared with the real (a2) and imaginary (a3) part extracted by quantum state tomography. Below, theoretical $\hat{R}_{12}$, $\hat{R}_{13}$ and $\hat{R}_{23}$ marginals (plots b1, c1 and d1, respectively) compared with the real (plots b2, c2 and d2) and imaginary (plots b3, c3 and d3) part of their tomographically-reconstructed counterparts. Since in our model $\text{Im}[\hat{R}_{123}]=\text{Im}[\hat{R}_{12}]=\text{Im}[\hat{R}_{13}]=\text{Im}[\hat{R}_{23}]=0$, the corresponding theoretical plots have been omitted. 🅭🅯 C. Marletto et al., Theoretical description and experimental simulation of quantum entanglement near open time-like curves via pseudo-density operators. *Nat Commun* **10**, 182 (2019). https://doi.org/10.1038/s41467-018-08100-1.

black hole and OTC ones, where the entanglement is developed among more particles in situations where different times are involved. A simple way to test such violation is to use the violation of Bell's inequalities (Sec. 1.1.1). More specifically, by setting $C_{ij} = \text{Tr}\left(\hat{R}_{ij}\hat{B}_{ij}\right)$, where $\hat{B}_{ij} = \sqrt{2}(\hat{X}_i\hat{Z}_j + \hat{Z}_i\hat{X}_j)$ is the observable that is used in the CHSH inequality (Sec. 1.1.1 - Eq. 1.1.1.19) tests on qubits i, j, we can define entanglement monogamy as[206]:

$$C_{mk} + C_{nk} \leq 4 \tag{5.1.4.1}$$

i.e., quantum states of three qubits m, n, k cannot violate Bell's inequalities in more than one pair of qubits.

In our case, we theoretically expect such violation, since $\hat{R}_{12}$ and $\hat{R}_{13}$ describe each a maximally entangled pair, $C_{12} = 2\sqrt{2} = C_{13}$, and the same is also true for $\hat{R}_{12}$ and $\hat{R}_{23}$, given that the latter also describes perfect correlations in all basis ($C_{12} = 2\sqrt{2} = C_{23}$).

Experimentally, we can reconstruct the statistics from a CHSH test on the photon A at times t_1 and t_2, and on the photons A and B at time t_1, to show the predicted violation of monogamy. To this end, we evaluate the CHSH inequality on qubits Q2 and Q3, that is, on photon A at times t_1 and t_2 (temporal domain), obtaining the value $C_{23}^{exp} = 2.84 \pm 0.02$, in perfect agreement with the predicted violation. Then, we measure the CHSH on photons B and A at time t_1 (qubits Q1 and Q2, spatial domain), achieving $C_{12}^{exp} = 2.69 \pm 0.02$, a good violation of the classical bound. From these results, it follows:

$$C_{12}^{exp} + C_{23}^{exp} = 5.52 \pm 0.03 \tag{5.1.4.2}$$

demonstrating a 160 standard deviations violation of the entanglement monogamy bound (Eq. (5.1.4.1)).

C_{13}, instead, must be extracted from the reconstructed PDO marginal $\hat{R}_{13}$ because, in our simulation setup, a direct CHSH inequality measurement for Q1 and Q3 would be possible only leaving Q2 untouched, thus forbidding the possibility of measuring C_{12}. The extracted CHSH value is $C_{13}^{rec} = 2.73$, which allows us to compute the remaining monogamy violations:

$$C_{12}^{exp} + C_{13}^{rec} = 5.42 \pm 0.07 \tag{5.1.4.3}$$
$$C_{23}^{exp} + C_{13}^{rec} = 5.55 \pm 0.07 \tag{5.1.4.4}$$

where we evaluated the uncertainty on C_{13}^{rec} as the 99% confidence interval on the experimental data. These results, then, show that the usual paradoxes due to violations of entanglement monogamy do not arise in this formalism, as the

PDO can accommodate and describe correlations that violate monogamy, thus demonstrating how such violation can naturally emerge in the proposed frameworks of black holes evaporation and open time-like curves.

5.2   Conclusions

In this section we proposed a strategy to efficiently simulate and reconstruct a pseudo-density operator, a generalization of the traditional density operator, and applied such procedure to two cases of physical interest that the traditional density operator formalism fails to properly describe, namely, the evaporation of black holes and open time-like curves. The results of the simulation are in good agreement with theoretical predictions and allow us to verify the predicted violation of entanglement monogamy, thus proving that the usual paradoxes due to such violation within the density operator framework do not arise with the PDO formalism.

Thus, PDO allows us to provide an alternative description of the evaporation of black holes and open time-like curves which preserves linearity of quantum evolution. More in general, PDO represents a general formalism able to describe measurements in quantum mechanics in a way allowing new insights and able to cope situations where the usual formalism meets difficulties. We believe, then, that PDOs can lead to a theory that retains linearity of quantum mechanics in a more general sense, while relaxing certain assumptions about the states of physical systems (e.g. entanglement monogamy) for certain specific situations. For this reason, our first PDO reconstruction marks a relevant milestone both in physics and metrology, paving the way to future applications to other interesting physical scenarios involving both temporal and spatial correlations.

Chapter 6

Conclusions

In this dissertation, I presented the most relevant projects I have been involved with during my PhD. The common thread is the development of a quantum metrology at single/few photons level. My studies concerned, in particular, single- and two-photon states characterization, the realization of new quantum-enhanced measurement paradigms and the study of physical systems needing a quantum mechanical description beyond the traditional density operator formalism. First, I illustrated a strategy to evaluate the multi-photon component of a CW heralded single-photon source, and successfully applied it to a low-noise fibre heralded single-photon source prototype within a pilot comparison among three European national metrology institutes (INRiM, NPL, PTB). The good agreement of the comparison results certified the flexibility, reliability and robustness of such strategy, which we believe may pave the way to a much needed standardization of single-photon sources characterization procedure.

Then, I presented some estimators for the evaluation of key parameters for quantifying the amount of non-classical correlations (i.e. entanglement and discord) in a family of bipartite states of particular interest for nowadays quantum technologies. Our results showed that, for each parameter, we found the optimal unbiased estimators, i.e. the ones saturating the quantum Cramér-Rao bound and, thus, achieving the ultimate theoretical precision limit on the unbiased estimation of such parameters. We believe that these estimators will be extremely important for resources quantification in quantum technologies.

Both these results were also preparatory for the characterization of the resources that we employed in the following experiments, which were aimed to the development of novel weak-interaction-based measurement protocols and to the reconstruction of a three-qubit pseudo-density operator, a recently-introduced extension of the usual density operator formalism.

The first measurement protocol I presented was Protective Measurement (of which we realized the first experimental implementation), a groundbreaking new measurement paradigm combining weak interaction and a mechanism "protecting" the state coherence. Protective measurement allows us not only to extract the expectation value of a quantum observable even from a single experiment on a single particle, something apparently in contrast with the very definition of expectation value, but also to largely outperform traditional projection-based protocols in terms of precision.

Then, I introduced the natural evolution of such protocol, called Robust Weak Measurement, and showed the experimental results obtained in their first realization. Somehow in analogy with protective measurements, robust weak measurements allow extracting the weak value of an observable even from a single detection event, something completely unprecedented in the weak values framework, traditionally estimated by averaging on multiple detection events due to identically prepared and measured particles. Our results will definitely have implications in the field of quantum metrology, in which weak values already play an important role.

The last work I presented, instead, is the first experimental reconstruction of a pseudo-density operator, an extension of the traditional density operator formalism able to describe spatial and temporal correlations on an equal footing. We applied this tool in an experimental simulation of two cases of physical interest that traditional density operators fail to properly describe, namely, the evaporation of black holes and open time-like curves, obtaining a good agreement between experimental results and theoretical predictions. We believe that our strategy to efficiently simulate and reconstruct a pseudo-density operator will pave the way to future applications of such formalism to other interesting physical scenarios involving both temporal and spatial correlations, where the usual density operator might even give rise to (apparent) paradoxes.

Possible continuations of these works are the extension of the optimal entanglement estimation experiment to the biased case, finding estimators able to reach the Van Trees bound, and a further study of iterative measurement protocols (like our implementation of protective measurement) in the strong interaction regime. Furthermore, protective measurements offer the challenging task of finding a bound on their uncertainty, since the usual Quantum Cramér-Rao bound does not hold in this case. Finally, another intriguing possibility is the extension of PDO formalism to other interesting physical scenarios involving time correlations, which we may simulate in our laboratories.

In conclusion, all the works illustrated in my dissertation can be regarded as crucial tasks in nowadays quantum metrology, and the results obtained in my PhD

could become relevant milestones in this field as well as for other quantum technologies, further promoting the (already running) second quantum revolution.

Chapter 7

Scientific output

7.1 Published works

Articles published in peer reviewed journals:

- F. Piacentini et al. Determining the quantum expectation value by measuring a single photon. In: Nature Physics 13.12 (Dec. 2017), pp. 1191–1194.[160]

- C. Marletto et al. Theoretical description and experimental simulation of quantum entanglement near open time-like curves via pseudo-density operators. In: Nature Communications 10.1 (Jan. 2019), 182.[184]

- E. Rebufello et al. Towards a standard procedure for the measurement of the multi-photon component in a CW telecom heralded single-photon source. In: Metrologia 56.2 (Feb. 2019), 025004.[152]

- S. Virzì et al. Optimal estimation of entanglement and discord in two-qubit states. In: Scientific Reports 9.1 (Feb. 2019), 3030.[153]

- C. Marletto et al. Non-Monogamy of Spatio-Temporal Correlations and the Black Hole Information Loss Paradox. In: Entropy 22.2 (Feb. 2020), 228.[183]

Proceedings:

- F. Piacentini et al. Quantum Measurements in weak coupling regime: from Sequential weak values to Protective measurements. In: Conference on Lasers and Electro-Optics. Optical Society of America, 2018, FF1B.6.[159]

- F. Piacentini et al. Protective measurements: extracting the expectation value by measuring a single particle. In: Quantum Technologies 2018. Vol. 10674. International Society for Optics and Photonics. SPIE, 2018, pp. 75–82.[161]

147

- E. Rebufello et al. Quantum weak-interaction-based measurement: from sequential weak measurement to protective measurement. In: Quantum Communications and Quantum Imaging XVI. Vol. 10771. International Society for Optics and Photonics. SPIE, 2018, pp. 149–164.[165]

- E. Rebufello et al. Experimental realization of robust weak measurements. In: Optical, Opto-Atomic, and Entanglement-Enhanced Precision Metrology II. Vol. 11296. International Society for Optics and Photonics. SPIE, 2020, pp. 302–308[164]

Papers still under peer review:

- E. Rebufello et al. Anomalous weak values via a single photon detection. Submitted (2020)[163]

Book chapters:

- E. Rebufello. Io resto a casa: Un gioco da tavolo. In: Virus Ex-Machina - Scritti metascientifici al tempo del Coronavirus. Mimesis Edizioni, 2020.[228]

7.2 International conferences and summer schools

International conferences:

- Quantum Technology International Conference (QTech) 2018 in Paris (France), 5/9/2018 - 7/9/2018. Oral presentation: *Determining the quantum expectation value by measuring a single photon.*

- Quantum 2019 - From Foundations of Quantum Mechanics to Quantum Information and Quantum Metrology & Sensing in Torino, 26/5/2019 - 31/5/2019. Poster presented: *Quantum entanglement near open time-like curves: theory and experimental simulation.*

- Time Machine Factory (TMF) 2019 in Torino, 22/9/2019 - 25/9/2019. Poster presented: *Quantum entanglement near open time-like curves: theory and experimental simulation.*

- Single Photon Workshop (SPW) 2019 in Milano, 22/10/2019 - 25/10/2019. Poster presented: *Pseudo-density operator reconstruction: the open time-like curve case.*

Summer schools:

- Quantum devices for non-classical light generation and manipulation (Qlight) 2019 in Erice (TP), 30/9/2019 - 4/10/2019. Poster presented: *Towards a standard procedure for the measurement of the multi-photon component in a CW telecom heralded single-photon source.*

7.3   Training activities

Courses attended during the PhD:

- A Machine Epistemology, 20h, Soft skill

- Computer ethics, 20h, Soft skill

- Development and management of data-acquisition systems, 25h, Hard skill

- Experimental modelling: construction of models from experimental data, 33h, Hard skill

- Forensic Metrology (didattica di eccellenza), 20h, Hard skill

- Introduction to quantum optics and quantum information, 20h, Hard skill

- Magnetism in materials and magnetic measurements, 20h, Hard skill

- Time management, 2h, Soft skill

- Chemo-dynamical evolution of the Milky Way, 12h, Hard skill

- COMSOL Day 2018, 8h, Hard skill

- Quantum Communication, 16h, Hard skill

- Search and characterization for extrasolar planets, 16h, Hard skill

- The future of scholarly communication in Europe, 7h, Hard skill

Courses attended during the third edition of the Percorso Formativo 24 CFU a.a. 2019-2020 (DM 616 of 10/8/2017) organized by CIFIS Piemonte (Università degli Studi di Torino, Politecnico di Torino, Università del Piemonte Orientale):

- Philosophical Anthropology, 6 CFU

- Teaching Models and Strategies, Instruction Technology and Educational Research, 6 CFU

- Psychology of the affective and relational aspects in managing the class group, 6 CFU

- Pedagogy of the educational relationship for secondary school, 6 CFU

7.4   Prizes and rewards

- Best poster award at PhD Day 2019 (Metrology PhD, XXXIII cycle)

- Best poster award at PhD Day 2018 (Metrology PhD, XXXIII cycle)

Appendix A

Uhlmann's Fidelity

Uhlmann's Fidelity (Fidelity in the main text) is a measure of how much two quantum states are close to each other. The Fidelity, defined as the maximum of $|\langle\psi|\varphi\rangle|$ over all purifications $|\psi\rangle$ and $|\varphi\rangle$ of two density operators $\hat{\rho}$ and $\hat{\sigma}$, is:

$$F(\hat{\rho}, \hat{\sigma}) = \mathrm{Tr}\sqrt{\sqrt{\hat{\sigma}}\hat{\rho}\sqrt{\hat{\sigma}}} \qquad (A.0.0.1)$$

and has the following properties:

- F is invariant under unitary transformations:

$$F(\hat{U}\hat{\rho}\hat{U}^{\dagger}, \hat{U}\hat{\sigma}\hat{U}^{\dagger}) = F(\hat{\rho}, \hat{\sigma}) \qquad (A.0.0.2)$$

- F is symmetric

$$F(\hat{\rho}, \hat{\sigma}) = F(\hat{\sigma}, \hat{\rho}) \qquad (A.0.0.3)$$

The Fidelity is very widespread both in the experimental field, where it is employed to characterize the states experimentally obtained, and in the theoretical field, thanks to its ties with Bures metric and Bures angle[33], which defines an infinitesimal distance between density matrix operators defining quantum states and a statistical distance between quantum states, respectively.

In the special case of bidimensional states, it is possible to obtain a simpler explicit formula for the Fidelity[33], thanks to the following property of 2x2 matrices: $\forall$ 2x2 matrix M:

$$M^2 - M\,\mathrm{Tr}\,M + \det M = 0 \qquad (A.0.0.4)$$

which implies:

$$(\mathrm{Tr}\,M)^2 = \mathrm{Tr}\,M^2 + 2\det M \qquad (A.0.0.5)$$

Therefore, with $M = \sqrt{\sqrt{\hat{\sigma}}\hat{\rho}\sqrt{\hat{\sigma}}}$, we find:

$$F^2(\hat{\rho}, \hat{\sigma}) = (\mathrm{Tr}\,M)^2 = \mathrm{Tr}(\hat{\rho}\hat{\sigma}) + 2\sqrt{\det\hat{\rho}\det\hat{\sigma}} \qquad (A.0.0.6)$$

which is easier to compute, since it does not contain square roots of operators.

Bibliography

[1]   Max Planck. "Ueber das Gesetz der Energieverteilung im Normalspektrum". In: *Annalen der Physik* 309 (3 1901), pp. 553–563.

[2]   Albert Einstein. "On a heuristic viewpoint concerning the production and transformation of light". In: *Annalen der Physik* 17 (1905), pp. 132–148.

[3]   Gilbert N. Lewis. "The Conservation of Photons". In: *Nature* 118.2981 (Dec. 1926), pp. 874–875. ISSN: 1476-4687. DOI: 10.1038/118874a0. URL: https://doi.org/10.1038/118874a0.

[4]   Niels Bohr. "I. On the constitution of atoms and molecules". In: *The London, Edinburgh, and Dublin Philosophical Magazine and Journal of Science* 26.151 (1913), pp. 1–25. DOI: 10.1080/14786441308634955. eprint: https://doi.org/10.1080/14786441308634955. URL: https://doi.org/10.1080/14786441308634955.

[5]   Johannes Robert Rydberg. *Recherches sur la constitution des spectres d'émission des éléments chimiques.* fre. Vol. Band 23 No 11. Kungliga vetenskapsakademiens handlingar 11. Kungliga Vetenskapsakademien, 1890. URL: https://lup.lub.lu.se/search/ws/files/39556483/rydberg_1889_reduced_archived.pdf.

[6]   Louis De Broglie. "Recherches sur la théorie des Quanta". Theses. Migration - université en cours d'affectation, Nov. 1924. URL: https://tel.archives-ouvertes.fr/tel-00006807.

[7]   Erwin Schrödinger. "An Undulatory Theory of the Mechanics of Atoms and Molecules". In: *Phys. Rev.* 28 (6 Dec. 1926), pp. 1049–1070. DOI: 10.1103/PhysRev.28.1049. URL: https://link.aps.org/doi/10.1103/PhysRev.28.1049.

[8]   Werner Heisenberg. "Über den anschaulichen Inhalt der quantentheoretischen Kinematik und Mechanik". In: *Zeitschrift für Physik* 43 (1927), pp. 172–198.

[9]   John von Neumann. *Mathematische Grundlagen der Quantenmechanik.* Springer, 1932.

[10] Michael E. Peskin and Daniel V. Schroeder. *An Introduction to Quantum Field Theory*. Perseus Books, 1995.

[11] Carlo Rovelli. "Quantum gravity". In: *Scholarpedia* 3.5 (2008). revision #170369, p. 7117. DOI: 10.4249/scholarpedia.7117.

[12] Bureau International des Poids et Mesures. *SI Brochure: The International System of Units (SI)*. Brochure. 2019. URL: https://www.bipm.org/en/publications/si-brochure/.

[13] Dennis D. McCarthy and P. Kenneth Seidelmann. *Time - From Earth Rotation to Atomic Physics*. Wiley-VCH Verlag, 2009. ISBN: 9783527407804.

[14] Wilfrid Poirier et al. "The ampere and the electrical units in the quantum era". In: *Comptes Rendus Physique* 20.1 (2019). The new International System of Units / Le nouveau Système international d'unités, pp. 92–128. ISSN: 1631-0705. DOI: https://doi.org/10.1016/j.crhy.2019.02.003. URL: http://www.sciencedirect.com/science/article/pii/S1631070519300179.

[15] Ian A. Robinson and Stephan Schlamminger. "The watt or Kibble balance: a technique for implementing the new SI definition of the unit of mass". In: *Metrologia* 53.5 (Sept. 2016), A46–A74. DOI: 10.1088/0026-1394/53/5/a46. URL: https://doi.org/10.1088%2F0026-1394%2F53%2F5%2Fa46.

[16] Cesare Rossetti. *Rudimenti di meccanica quantistica*. Levrotto e Bella, 2011.

[17] Ryszard Horodecki et al. "Quantum entanglement". In: *Rev. Mod. Phys.* 81 (2 June 2009), pp. 865–942. DOI: 10.1103/RevModPhys.81.865. URL: https://link.aps.org/doi/10.1103/RevModPhys.81.865.

[18] Albert Einstein, Boris Podolsky, and Nathan Rosen. "Can Quantum-Mechanical Description of Physical Reality Be Considered Complete?" In: *Phys. Rev.* 47 (10 May 1935), pp. 777–780. DOI: 10.1103/PhysRev.47.777. URL: https://link.aps.org/doi/10.1103/PhysRev.47.777.

[19] David Bohm. *Quantum Theory*. Prentice-Hall, 1951.

[20] Giancarlo Ghirardi, Alberto Rimini, and Tullio Weber. "A general argument against superluminal transmission through the quantum mechanical measurement process". In: *Lettere al Nuovo Cimento (1971-1985)* 27.10 (Mar. 1980), pp. 293–298. ISSN: 1827-613X. DOI: 10.1007/BF02817189. URL: https://doi.org/10.1007/BF02817189.

[21] John S. Bell. "On the Einstein Podolsky Rosen paradox". In: *Physics Physique Fizika* 1 (3 Nov. 1964), pp. 195–200. DOI: 10.1103/PhysicsPhysiqueFizika.1.195. URL: https://link.aps.org/doi/10.1103/PhysicsPhysiqueFizika.1.195.

[22]   John F. Clauser et al. "Proposed Experiment to Test Local Hidden-Variable Theories". In: *Phys. Rev. Lett.* 23 (15 Oct. 1969), pp. 880–884. DOI: `10.1103/PhysRevLett.23.880`. URL: `https://link.aps.org/doi/10.1103/PhysRevLett.23.880`.

[23]   Alain Aspect, Jean Dalibard, and Gérard Roger. "Experimental Test of Bell's Inequalities Using Time-Varying Analyzers". In: *Phys. Rev. Lett.* 49 (25 Dec. 1982), pp. 1804–1807. DOI: `10.1103/PhysRevLett.49.1804`. URL: `https://link.aps.org/doi/10.1103/PhysRevLett.49.1804`.

[24]   Marco Genovese. "Research on hidden variable theories: A review of recent progresses". In: *Physics Reports* 413.6 (2005), pp. 319–396. ISSN: 0370-1573. DOI: `https://doi.org/10.1016/j.physrep.2005.03.003`. URL: `http://www.sciencedirect.com/science/article/pii/S037015730500147X`.

[25]   Marissa Giustina et al. "Significant-Loophole-Free Test of Bell's Theorem with Entangled Photons". In: *Phys. Rev. Lett.* 115 (25 Dec. 2015), p. 250401. DOI: `10.1103/PhysRevLett.115.250401`. URL: `https://link.aps.org/doi/10.1103/PhysRevLett.115.250401`.

[26]   Lynden K. Shalm et al. "Strong Loophole-Free Test of Local Realism". In: *Phys. Rev. Lett.* 115 (25 Dec. 2015), p. 250402. DOI: `10.1103/PhysRevLett.115.250402`. URL: `https://link.aps.org/doi/10.1103/PhysRevLett.115.250402`.

[27]   Michael Nielsen and Isaac Chuang. *Quantum Computation and Quantum Information.* Cambridge University Press, 2010.

[28]   John von Neumann. "Wahrscheinlichkeitstheoretischer Aufbau der Quantenmechanik". In: *Nachrichten von der Gesellschaft der Wissenschaften zu Göttingen, Mathematisch-Physikalische Klasse* 1927 (1927), pp. 245–272. URL: `http://eudml.org/doc/59230`.

[29]   Leah Henderson and Vlatko Vedral. "Classical, quantum and total correlations". In: *Journal of Physics A: Mathematical and General* 34.35 (Aug. 2001), pp. 6899–6905. DOI: `10.1088/0305-4470/34/35/315`. URL: `https://doi.org/10.1088%2F0305-4470%2F34%2F35%2F315`.

[30]   Harold Ollivier and Wojciech H. Zurek. "Quantum Discord: A Measure of the Quantumness of Correlations". In: *Phys. Rev. Lett.* 88 (1 Dec. 2001), p. 017901. DOI: `10.1103/PhysRevLett.88.017901`. URL: `https://link.aps.org/doi/10.1103/PhysRevLett.88.017901`.

[31]   Claude Elwood Shannon. "A Mathematical Theory of Communication". In: *Bell System Technical Journal* 27 (3 1948), pp. 379–423.

[32] Thomas Bayes. "LII. An essay towards solving a problem in the doctrine of chances. By the late Rev. Mr. Bayes, F. R. S. communicated by Mr. Price, in a letter to John Canton, A. M. F. R. S". In: *Philosophical Transactions of the Royal Society of London* 53 (1763), pp. 370–418. DOI: 10.1098/rstl. 1763.0053. eprint: https://royalsocietypublishing.org/doi/pdf/10. 1098/rstl.1763.0053. URL: https://royalsocietypublishing.org/doi/abs/10.1098/rstl.1763.0053.

[33] Ingemar Bengstonn and Karol Zyczkowski. *Geometry of Quantum States*. Cambridge University Press, 2008.

[34] Leonard Mandel and Emil Wolf. *Optical Coherence and Quantum Optics*. Cambridge University Press, 1995.

[35] Neil W. Ashcroft and N. D. Mermin. *Solid State Physics*. Holt, Rinehart and Winston, 1976.

[36] Zhi-Pei Liang and Paul C. Lauterbur. *Principles of Magnetic Resonance Imaging: A Signal Processing Perspective*. Wiley-IEEE Press, 2000.

[37] Peter W. Shor. "Algorithms for quantum computation: discrete logarithms and factoring". In: *Proceedings 35th Annual Symposium on Foundations of Computer Science*. 1994, pp. 124–134.

[38] Nicolas Gisin and Rob Thew. "Quantum communication". In: *Nature Photonics* 1.3 (Mar. 2007), pp. 165–171. ISSN: 1749-4893. DOI: 10.1038/nphoton. 2007.22. URL: https://doi.org/10.1038/nphoton.2007.22.

[39] Charles H. Bennett and Gilles Brassard. "Quantum cryptography: Public key distribution and coin tossing". In: *Theoretical Computer Science* 560 (2014). Theoretical Aspects of Quantum Cryptography – celebrating 30 years of BB84, pp. 7–11. ISSN: 0304-3975. DOI: https://doi.org/10. 1016/j.tcs.2014.05.025. URL: http://www.sciencedirect.com/science/article/pii/S0304397514004241.

[40] Artur K. Ekert. "Quantum cryptography based on Bell's theorem". In: *Phys. Rev. Lett.* 67 (6 Aug. 1991), pp. 661–663. DOI: 10.1103/PhysRevLett.67. 661. URL: https://link.aps.org/doi/10.1103/PhysRevLett.67.661.

[41] Charles H. Bennett et al. "Teleporting an unknown quantum state via dual classical and Einstein-Podolsky-Rosen channels". In: *Phys. Rev. Lett.* 70 (13 Mar. 1993), pp. 1895–1899. DOI: 10.1103/PhysRevLett.70.1895. URL: https://link.aps.org/doi/10.1103/PhysRevLett.70.1895.

[42] Dik Bouwmeester et al. "Experimental quantum teleportation". In: *Nature* 390.6660 (Dec. 1997), pp. 575–579. ISSN: 1476-4687. DOI: 10.1038/37539. URL: https://doi.org/10.1038/37539.

[43] Frank Miller. *Telegraphic code to insure privacy and secrecy in the transmission of telegrams*. CM Cornwell, 1882.

[44]   Davide Bacco et al. "Field trial of a three-state quantum key distribution scheme in the Florence metropolitan area". In: *EPJ Quantum Technology* 6.1 (Oct. 2019), p. 5. ISSN: 2196-0763. DOI: 10.1140/epjqt/s40507-019-0075-x. URL: https://doi.org/10.1140/epjqt/s40507-019-0075-x.

[45]   Klaus von Klitzing. "The quantized Hall effect". In: *Rev. Mod. Phys.* 58 (3 July 1986), pp. 519–531. DOI: 10.1103/RevModPhys.58.519. URL: https://link.aps.org/doi/10.1103/RevModPhys.58.519.

[46]   Brian D. Josephson. "Possible new effects in superconductive tunnelling". In: *Physics Letters* 1.7 (1962), pp. 251–253. ISSN: 0031-9163. DOI: https://doi.org/10.1016/0031-9163(62)91369-0. URL: http://www.sciencedirect.com/science/article/pii/0031916362913690.

[47]   Vittorio Giovannetti, Seth Lloyd, and Lorenzo Maccone. "Advances in quantum metrology". In: *Nature Photonics* 5.4 (Apr. 2011), pp. 222–229. ISSN: 1749-4893. DOI: 10.1038/nphoton.2011.35. URL: https://doi.org/10.1038/nphoton.2011.35.

[48]   Vittorio Giovannetti, Seth Lloyd, and Lorenzo Maccone. "Quantum Metrology". In: *Phys. Rev. Lett.* 96 (1 Jan. 2006), p. 010401. DOI: 10.1103/PhysRevLett.96.010401. URL: https://link.aps.org/doi/10.1103/PhysRevLett.96.010401.

[49]   Vittorio Giovannetti, Seth Lloyd, and Lorenzo Maccone. "Quantum-Enhanced Measurements: Beating the Standard Quantum Limit". In: *Science* 306.5700 (2004), pp. 1330–1336. ISSN: 0036-8075. DOI: 10.1126/science.1104149. eprint: https://science.sciencemag.org/content/306/5700/1330.full.pdf. URL: https://science.sciencemag.org/content/306/5700/1330.

[50]   Giorgio Brida, Marco Genovese, and Ivano Ruo Berchera. "Experimental realization of sub-shot-noise quantum imaging". In: *Nature Photonics* 4.4 (Apr. 2010), pp. 227–230. ISSN: 1749-4893. DOI: 10.1038/nphoton.2010.29. URL: https://doi.org/10.1038/nphoton.2010.29.

[51]   Omar El Gawhary et al. "Restoration of s-polarized evanescent waves and subwavelength imaging by a single dielectric slab". In: *New Journal of Physics* 14.5 (May 2012), p. 053025. DOI: 10.1088/1367-2630/14/5/053025. URL: https://doi.org/10.1088/1367-2630/14/5/053025.

[52]   Paolo Aluffi. *Algebra: Chapter 0*. American Mathematical Society, 2009.

[53]   Bengt E. Y. Svensson. "Pedagogical Review of Quantum Measurement Theory with an Emphasis on Weak Measurements". In: *Quanta* 2.1 (2013), pp. 18–49. ISSN: 1314-7374. DOI: 10.12743/quanta.v2i1.12. URL: http://quanta.ws/ojs/index.php/quanta/article/view/12.

[54] Yakir Aharonov, Peter G. Bergmann, and Joel L. Lebowitz. "Time Symmetry in the Quantum Process of Measurement". In: *Phys. Rev.* 134 (6B June 1964), B1410–B1416. DOI: 10.1103/PhysRev.134.B1410. URL: https://link.aps.org/doi/10.1103/PhysRev.134.B1410.

[55] Vladimir B. Braginsky, Yuri I. Vorontsov, and Kip S. Thorne. "Quantum Nondemolition Measurements". In: *Science* 209.4456 (1980), pp. 547–557. ISSN: 0036-8075. DOI: 10.1126/science.209.4456.547. eprint: https://science.sciencemag.org/content/209/4456/547.full.pdf. URL: https://science.sciencemag.org/content/209/4456/547.

[56] Boaz Tamir and Eliahu Cohen. "Introduction to Weak Measurements and Weak Values". In: *Quanta* 2.1 (2013), pp. 7–17. ISSN: 1314-7374. DOI: 10.12743/quanta.v2i1.14. URL: http://quanta.ws/ojs/index.php/quanta/article/view/14.

[57] Yakir Aharonov, David Z. Albert, and Lev Vaidman. "How the result of a measurement of a component of the spin of a spin-1/2 particle can turn out to be 100". In: *Phys. Rev. Lett.* 60 (14 Apr. 1988), pp. 1351–1354. DOI: 10.1103/PhysRevLett.60.1351. URL: https://link.aps.org/doi/10.1103/PhysRevLett.60.1351.

[58] Yakir Aharonov and Lev Vaidman. "The two-state vector formalism: an updated review". In: (2008).

[59] I. M. Duck, Paul M. Stevenson, and E. C. George Sudarshan. "The sense in which a "weak measurement" of a spin-½ particle's spin component yields a value 100". In: *Phys. Rev. D* 40 (6 Sept. 1989), pp. 2112–2117. DOI: 10.1103/PhysRevD.40.2112. URL: https://link.aps.org/doi/10.1103/PhysRevD.40.2112.

[60] Christopher Ferrie and Joshua Combes. "How the Result of a Single Coin Toss Can Turn Out to be 100 Heads". In: *Phys. Rev. Lett.* 113 (12 Sept. 2014), p. 120404. DOI: 10.1103/PhysRevLett.113.120404. URL: https://link.aps.org/doi/10.1103/PhysRevLett.113.120404.

[61] Stephen Parrot. "What do quantum "weak" measurements actually measure?" In: *arXiv* (2009).

[62] Fabrizio Piacentini et al. "Experiment Investigating the Connection between Weak Values and Contextuality". In: *Phys. Rev. Lett.* 116 (18 May 2016), p. 180401. DOI: 10.1103/PhysRevLett.116.180401. URL: https://link.aps.org/doi/10.1103/PhysRevLett.116.180401.

[63] Matthew F. Pusey. "Anomalous Weak Values Are Proofs of Contextuality". In: *Phys. Rev. Lett.* 113 (20 Nov. 2014), p. 200401. DOI: 10.1103/PhysRevLett.113.200401. URL: https://link.aps.org/doi/10.1103/PhysRevLett.113.200401.

[64]   Bengt E. Y. Svensson. "What Is a Quantum-Mechanical "Weak Value" the Value of?" In: *Foundations of Physics* 43.10 (2013). ISSN: 1572-9516. DOI: 10.1007/s10701-013-9740-6. URL: https://doi.org/10.1007/s10701-013-9740-6.

[65]   Lev Vaidman. "Weak value controversy". In: *Philosophical Transactions of the Royal Society A: Mathematical, Physical and Engineering Sciences* 375.2106 (2017), p. 20160395. DOI: 10.1098/rsta.2016.0395. eprint: https://royalsocietypublishing.org/doi/pdf/10.1098/rsta.2016.0395. URL: https://royalsocietypublishing.org/doi/abs/10.1098/rsta.2016.0395.

[66]   Richard Jozsa. "Complex weak values in quantum measurement". In: *Phys. Rev. A* 76 (4 Oct. 2007), p. 044103. DOI: 10.1103/PhysRevA.76.044103. URL: https://link.aps.org/doi/10.1103/PhysRevA.76.044103.

[67]   Onur Hosten and Paul Kwiat. "Observation of the Spin Hall Effect of Light via Weak Measurements". In: *Science* 319.5864 (2008), pp. 787–790. ISSN: 0036-8075. DOI: 10.1126/science.1152697. eprint: https://science.sciencemag.org/content/319/5864/787.full.pdf. URL: https://science.sciencemag.org/content/319/5864/787.

[68]   P. Ben Dixon et al. "Ultrasensitive Beam Deflection Measurement via Interferometric Weak Value Amplification". In: *Phys. Rev. Lett.* 102 (17 Apr. 2009), p. 173601. DOI: 10.1103/PhysRevLett.102.173601. URL: https://link.aps.org/doi/10.1103/PhysRevLett.102.173601.

[69]   Amir Feizpour, Xingxing Xing, and Aephraim M. Steinberg. "Amplifying Single-Photon Nonlinearity Using Weak Measurements". In: *Phys. Rev. Lett.* 107 (13 Sept. 2011), p. 133603. DOI: 10.1103/PhysRevLett.107.133603. URL: https://link.aps.org/doi/10.1103/PhysRevLett.107.133603.

[70]   Matin Hallaji et al. "Weak-value amplification of the nonlinear effect of a single photon". In: *Nature Physics* 13.6 (June 2017), pp. 540–544. ISSN: 1745-2481. DOI: 10.1038/nphys4040. URL: https://doi.org/10.1038/nphys4040.

[71]   Yaron Kedem. "Using technical noise to increase the signal-to-noise ratio of measurements via imaginary weak values". In: *Phys. Rev. A* 85 (6 June 2012), p. 060102. DOI: 10.1103/PhysRevA.85.060102. URL: https://link.aps.org/doi/10.1103/PhysRevA.85.060102.

[72]   Atsushi Nishizawa, Kouji Nakamura, and Masa-Katsu Fujimoto. "Weak-value amplification in a shot-noise-limited interferometer". In: *Phys. Rev. A* 85 (6 June 2012), p. 062108. DOI: 10.1103/PhysRevA.85.062108. URL: https://link.aps.org/doi/10.1103/PhysRevA.85.062108.

[73] David J. Starling et al. "Optimizing the signal-to-noise ratio of a beam-deflection measurement with interferometric weak values". In: *Phys. Rev. A* 80 (4 Oct. 2009), p. 041803. DOI: 10.1103/PhysRevA.80.041803. URL: https://link.aps.org/doi/10.1103/PhysRevA.80.041803.

[74] Grégory Strübi and C. Bruder. "Measuring Ultrasmall Time Delays of Light by Joint Weak Measurements". In: *Phys. Rev. Lett.* 110 (8 Feb. 2013), p. 083605. DOI: 10.1103/PhysRevLett.110.083605. URL: https://link.aps.org/doi/10.1103/PhysRevLett.110.083605.

[75] Christopher Ferrie and Joshua Combes. "Weak Value Amplification is Suboptimal for Estimation and Detection". In: *Phys. Rev. Lett.* 112 (4 Jan. 2014), p. 040406. DOI: 10.1103/PhysRevLett.112.040406. URL: https://link.aps.org/doi/10.1103/PhysRevLett.112.040406.

[76] Holger F. Hofmann et al. "Estimation of a quantum interaction parameter using weak measurements: Theory and experiment". In: *Phys. Rev. A* 86 (4 Oct. 2012), p. 040102. DOI: 10.1103/PhysRevA.86.040102. URL: https://link.aps.org/doi/10.1103/PhysRevA.86.040102.

[77] George C. Knee and Erik M. Gauger. "When Amplification with Weak Values Fails to Suppress Technical Noise". In: *Phys. Rev. X* 4 (1 Mar. 2014), p. 011032. DOI: 10.1103/PhysRevX.4.011032. URL: https://link.aps.org/doi/10.1103/PhysRevX.4.011032.

[78] George C. Knee et al. "Weak-value amplification: state of play". In: *Quantum Measurements and Quantum Metrology* 1 (1Jan. 2016). DOI: https://doi.org/10.1515/qmetro-2016-0006. URL: https://www.degruyter.com/view/journals/qmetro/open-issue/article-10.1515-qmetro-2016-0006/article-10.1515-qmetro-2016-0006.xml.

[79] Shengshi Pang, Justin Dressel, and Todd A. Brun. "Entanglement-Assisted Weak Value Amplification". In: *Phys. Rev. Lett.* 113 (3 July 2014), p. 030401. DOI: 10.1103/PhysRevLett.113.030401. URL: https://link.aps.org/doi/10.1103/PhysRevLett.113.030401.

[80] Lijian Zhang, Animesh Datta, and Ian A. Walmsley. "Precision Metrology Using Weak Measurements". In: *Phys. Rev. Lett.* 114 (21 May 2015), p. 210801. DOI: 10.1103/PhysRevLett.114.210801. URL: https://link.aps.org/doi/10.1103/PhysRevLett.114.210801.

[81] Justin Dressel et al. "Strengthening weak-value amplification with recycled photons". In: *Phys. Rev. A* 88 (2 Aug. 2013), p. 023821. DOI: 10.1103/PhysRevA.88.023821. URL: https://link.aps.org/doi/10.1103/PhysRevA.88.023821.

[82]   Kevin Lyons et al. "Power-Recycled Weak-Value-Based Metrology". In: *Phys. Rev. Lett.* 114 (17 Apr. 2015), p. 170801. DOI: 10.1103/PhysRevLett.114.170801. URL: https://link.aps.org/doi/10.1103/PhysRevLett.114.170801.

[83]   Yi-Tao Wang et al. "Experimental Demonstration of Higher Precision Weak-Value-Based Metrology Using Power Recycling". In: *Phys. Rev. Lett.* 117 (23 Nov. 2016), p. 230801. DOI: 10.1103/PhysRevLett.117.230801. URL: https://link.aps.org/doi/10.1103/PhysRevLett.117.230801.

[84]   Justin Dressel et al. "Colloquium: Understanding quantum weak values: Basics and applications". In: *Rev. Mod. Phys.* 86 (1 Mar. 2014), pp. 307–316. DOI: 10.1103/RevModPhys.86.307. URL: https://link.aps.org/doi/10.1103/RevModPhys.86.307.

[85]   Jeff S. Lundeen et al. "Direct measurement of the quantum wavefunction". In: *Nature* 474.7350 (June 2011), pp. 188–191. ISSN: 1476-4687. DOI: 10.1038/nature10120. URL: https://doi.org/10.1038/nature10120.

[86]   Jeff S. Lundeen and Aephraim M. Steinberg. "Experimental Joint Weak Measurement on a Photon Pair as a Probe of Hardy's Paradox". In: *Phys. Rev. Lett.* 102 (2 Jan. 2009), p. 020404. DOI: 10.1103/PhysRevLett.102.020404. URL: https://link.aps.org/doi/10.1103/PhysRevLett.102.020404.

[87]   Graeme Mitchison, Richard Jozsa, and Sandu Popescu. "Sequential weak measurement". In: *Phys. Rev. A* 76 (6 Dec. 2007), p. 062105. DOI: 10.1103/PhysRevA.76.062105. URL: https://link.aps.org/doi/10.1103/PhysRevA.76.062105.

[88]   Fabrizio Piacentini et al. "Measuring Incompatible Observables by Exploiting Sequential Weak Values". In: *Phys. Rev. Lett.* 117 (17 Oct. 2016), p. 170402. DOI: 10.1103/PhysRevLett.117.170402. URL: https://link.aps.org/doi/10.1103/PhysRevLett.117.170402.

[89]   Guillaume S. Thekkadath et al. "Direct Measurement of the Density Matrix of a Quantum System". In: *Phys. Rev. Lett.* 117 (12 Sept. 2016), p. 120401. DOI: 10.1103/PhysRevLett.117.120401. URL: https://link.aps.org/doi/10.1103/PhysRevLett.117.120401.

[90]   Charles H. Bennett et al. "Purification of Noisy Entanglement and Faithful Teleportation via Noisy Channels". In: *Phys. Rev. Lett.* 76 (5 Jan. 1996), pp. 722–725. DOI: 10.1103/PhysRevLett.76.722. URL: https://link.aps.org/doi/10.1103/PhysRevLett.76.722.

[91] Charles H. Bennett et al. "Mixed-state entanglement and quantum error correction". In: *Phys. Rev. A* 54 (5 Nov. 1996), pp. 3824–3851. DOI: `10.1103/PhysRevA.54.3824`. URL: `https://link.aps.org/doi/10.1103/PhysRevA.54.3824`.

[92] Joseph B. Altepeter, Evan R. Jeffrey, and Paul G. Kwiat. "Photonic State Tomography". In: ed. by P.R. Berman and C.C. Lin. Vol. 52. Advances In Atomic, Molecular, and Optical Physics. Academic Press, 2005, pp. 105–159. DOI: `https://doi.org/10.1016/S1049-250X(05)52003-2`. URL: `http://www.sciencedirect.com/science/article/pii/S1049250X05520032`.

[93] Gregg Jaeger, Michael A. Horne, and Abner Shimony. "Complementarity of one-particle and two-particle interference". In: *Phys. Rev. A* 48 (2 Aug. 1993), pp. 1023–1027. DOI: `10.1103/PhysRevA.48.1023`. URL: `https://link.aps.org/doi/10.1103/PhysRevA.48.1023`.

[94] Vlatko Vedral et al. "Quantifying Entanglement". In: *Phys. Rev. Lett.* 78 (12 Mar. 1997), pp. 2275–2279. DOI: `10.1103/PhysRevLett.78.2275`. URL: `https://link.aps.org/doi/10.1103/PhysRevLett.78.2275`.

[95] Guifré Vidal. "Entanglement monotones". In: *Journal of Modern Optics* 47.2-3 (2000), pp. 355–376. DOI: `10.1080/09500340008244048`. eprint: `https://www.tandfonline.com/doi/pdf/10.1080/09500340008244048`. URL: `https://www.tandfonline.com/doi/abs/10.1080/09500340008244048`.

[96] Matthew J. Donald, Michał Horodecki, and Oliver Rudolph. "The uniqueness theorem for entanglement measures". In: *Journal of Mathematical Physics* 43.9 (2002), pp. 4252–4272. DOI: `10.1063/1.1495917`. eprint: `https://doi.org/10.1063/1.1495917`. URL: `https://doi.org/10.1063/1.1495917`.

[97] Michał Horodecki, Paweł Horodecki, and Ryszard Horodecki. "Limits for Entanglement Measures". In: *Phys. Rev. Lett.* 84 (9 Feb. 2000), pp. 2014–2017. DOI: `10.1103/PhysRevLett.84.2014`. URL: `https://link.aps.org/doi/10.1103/PhysRevLett.84.2014`.

[98] William K. Wootters. "Entanglement of Formation of an Arbitrary State of Two Qubits". In: *Phys. Rev. Lett.* 80 (10 Mar. 1998), pp. 2245–2248. DOI: `10.1103/PhysRevLett.80.2245`. URL: `https://link.aps.org/doi/10.1103/PhysRevLett.80.2245`.

[99] Roland Hildebrand. "Concurrence revisited". In: *Journal of Mathematical Physics* 48.10 (2007), p. 102108. DOI: `10.1063/1.2795840`. eprint: `https://doi.org/10.1063/1.2795840`. URL: `https://doi.org/10.1063/1.2795840`.

[100] Scott Hill and William K. Wootters. "Entanglement of a Pair of Quantum Bits". In: *Phys. Rev. Lett.* 78 (26 June 1997), pp. 5022–5025. DOI: 10.1103/PhysRevLett.78.5022. URL: https://link.aps.org/doi/10.1103/PhysRevLett.78.5022.

[101] Frank Verstraete et al. "A comparison of the entanglement measures negativity and concurrence". In: *Journal of Physics A: Mathematical and General* 34.47 (Nov. 2001), pp. 10327–10332. DOI: 10.1088/0305-4470/34/47/329. URL: https://doi.org/10.1088%2F0305-4470%2F34%2F47%2F329.

[102] Jing Wang et al. "Bounds on multipartite concurrence and tangle". In: *Quantum Information Processing* 15.10 (Oct. 2016), pp. 4211–4218. ISSN: 1573-1332. DOI: 10.1007/s11128-016-1385-x. URL: https://doi.org/10.1007/s11128-016-1385-x.

[103] Guifre Vidal and Reinhard F. Werner. "Computable measure of entanglement". In: *Phys. Rev. A* 65 (3 Feb. 2002), p. 032314. DOI: 10.1103/PhysRevA.65.032314. URL: https://link.aps.org/doi/10.1103/PhysRevA.65.032314.

[104] Michał Horodecki, Paweł Horodecki, and Ryszard Horodecki. "Separability of n-particle mixed states: necessary and sufficient conditions in terms of linear maps". In: *Physics Letters A* 283.1 (2001), pp. 1–7. ISSN: 0375-9601. DOI: https://doi.org/10.1016/S0375-9601(01)00142-6. URL: http://www.sciencedirect.com/science/article/pii/S0375960101001426.

[105] Yichen Huang. "Computing quantum discord is NP-complete". In: *New Journal of Physics* 16.3 (Mar. 2014), p. 033027. DOI: 10.1088/1367-2630/16/3/033027. URL: https://doi.org/10.1088/1367-2630/16/3/033027.

[106] Borivoje Daki ć, Vlatko Vedral, and Časlav Brukner. "Necessary and Sufficient Condition for Nonzero Quantum Discord". In: *Phys. Rev. Lett.* 105 (19 Nov. 2010), p. 190502. DOI: 10.1103/PhysRevLett.105.190502. URL: https://link.aps.org/doi/10.1103/PhysRevLett.105.190502.

[107] Carl W. Helstrom. *Quantum Detection and Estimation Theory*. Academic Press, 1976.

[108] Edward T. Jaynes. *Probability Theory The Logic of Science*. Cambridge University Press, 2003.

[109] Harald Cramér. *Mathematical Methods of Statistics*. Princeton Univ. Press, 1945.

[110] Calyampudi Radhakrishna Rao. "Information and the accuracy attainable in the estimation of statistical parameters". In: *Bull. Calcutta Math. Soc.* (37 1945), pp. 81–91.

[111]   Ronald A. Fisher. "Theory of Statistical Estimation". In: *Mathematical Proceedings of the Cambridge Philosophical Society* 22.5 (1925), pp. 700–725. DOI: `10.1017/S0305004100009580`.

[112]   Erich L. Lehmann and George Casella. *Theory of Point Estimation, Second Edition*. Springer-Verlag, 1998.

[113]   Samuel S. Wilks. *Mathematical Statistics*. John Wiley & Sons., 1962.

[114]   Matteo G. A. Paris. "Quantum Estimation For Quantum Technology". In: *International Journal of Quantum Information* 07.supp01 (2009), pp. 125–137. DOI: `10.1142/S0219749909004839`. eprint: `https://doi.org/10.1142/S0219749909004839`. URL: `https://doi.org/10.1142/S0219749909004839`.

[115]   Luigi Seveso and Matteo G. A. Paris. "Quantum enhanced metrology of Hamiltonian parameters beyond the Cramèr–Rao bound". In: *International Journal of Quantum Information* 18.03 (2020), p. 2030001. DOI: `10.1142/S0219749920300016`. eprint: `https://doi.org/10.1142/S0219749920300016`. URL: `https://doi.org/10.1142/S0219749920300016`.

[116]   Luigi Seveso, Matteo A. C. Rossi, and Matteo G. A. Paris. "Quantum metrology beyond the quantum Cramér-Rao theorem". In: *Phys. Rev. A* 95 (1 Jan. 2017), p. 012111. DOI: `10.1103/PhysRevA.95.012111`. URL: `https://link.aps.org/doi/10.1103/PhysRevA.95.012111`.

[117]   Luigi Seveso and Matteo G. A. Paris. "Estimation of general Hamiltonian parameters via controlled energy measurements". In: *Phys. Rev. A* 98 (3 Sept. 2018), p. 032114. DOI: `10.1103/PhysRevA.98.032114`. URL: `https://link.aps.org/doi/10.1103/PhysRevA.98.032114`.

[118]   Yonina C. Eldar. *Rethinking Biased Estimation: Improving Maximum Likelihood and the Cramér-Rao Bound*. Now Publishers Inc, 2008.

[119]   Steven Kay and Yonina C. Eldar. "Rethinking biased estimation [Lecture Notes]". In: *IEEE Signal Processing Magazine* 25.3 (2008), pp. 133–136. DOI: `10.1109/MSP.2008.918027`.

[120]   Harry L. Van Tree, Kristine L. Bell, and Zhi Tian. *Detection Estimation and Modulation Theory, 2nd edition*. John Willey and Sons Inc., 2013.

[121]   Richard D. Gill and Boris Y. Levit. "Applications of the van Trees inequality: a Bayesian Cramér-Rao bound". In: *Bernoulli* 1.1-2 (1995), pp. 59–79. URL: `https://projecteuclid.org/euclid.bj/1186078362`.

[122]   Hitoshi Inamori, Norbert Lütkenhaus, and Dominic Mayers. "Unconditional security of practical quantum key distribution". In: *The European Physical Journal D* 41.3 (Jan. 2007), p. 599. ISSN: 1434-6079. DOI: `10.1140/epjd/e2007-00010-4`. URL: `https://doi.org/10.1140/epjd/e2007-00010-4`.

[123] Peter Michler. *Quantum Dots for Quantum Information Technologies.* Springer, 2017.

[124] Alan Migdall et al. *Single-Photon Generation and Detection.* Elsevier, 2013.

[125] Ferruccio Pisanello et al. "Room temperature-dipolelike single photon source with a colloidal dot-in-rod". In: *Applied Physics Letters* 96.3 (2010), p. 033101. DOI: 10.1063/1.3291849. eprint: https://doi.org/10.1063/1.3291849. URL: https://doi.org/10.1063/1.3291849.

[126] Sviatoslav Ditalia Tchernij et al. "Single-Photon-Emitting Optical Centers in Diamond Fabricated upon Sn Implantation". In: *ACS Photonics* 4.10 (Oct. 2017), pp. 2580–2586. DOI: 10.1021/acsphotonics.7b00904. URL: https://doi.org/10.1021/acsphotonics.7b00904.

[127] Edward M. Purcell, Henry C. Torrey, and Robert V. Pound. "Resonance Absorption by Nuclear Magnetic Moments in a Solid". In: *Phys. Rev.* 69 (1-2 Jan. 1946), pp. 37–38. DOI: 10.1103/PhysRev.69.37. URL: https://link.aps.org/doi/10.1103/PhysRev.69.37.

[128] David Fattal et al. "Entanglement Formation and Violation of Bell's Inequality with a Semiconductor Single Photon Source". In: *Phys. Rev. Lett.* 92 (3 Jan. 2004), p. 037903. DOI: 10.1103/PhysRevLett.92.037903. URL: https://link.aps.org/doi/10.1103/PhysRevLett.92.037903.

[129] Zhe Y. Ou and Leonard Mandel. "Violation of Bell's Inequality and Classical Probability in a Two-Photon Correlation Experiment". In: *Phys. Rev. Lett.* 61 (1 July 1988), pp. 50–53. DOI: 10.1103/PhysRevLett.61.50. URL: https://link.aps.org/doi/10.1103/PhysRevLett.61.50.

[130] Salvatore Savasta, Giovanna Martino, and Raffaello Girlanda. "Entangled photon pairs from the optical decay of biexcitons". In: *Solid State Communications* 111.9 (1999), pp. 495–500. ISSN: 0038-1098. DOI: https://doi.org/10.1016/S0038-1098(99)00233-1. URL: http://www.sciencedirect.com/science/article/pii/S0038109899002331.

[131] Loïc Rondin et al. "Magnetometry with nitrogen-vacancy defects in diamond". In: *Reports on Progress in Physics* 77.5 (May 2014), p. 056503. DOI: 10.1088/0034-4885/77/5/056503. URL: https://doi.org/10.1088%2F0034-4885%2F77%2F5%2F056503.

[132] Hannes Bernien et al. "Heralded entanglement between solid-state qubits separated by three metres". In: *Nature* 497.7447 (May 2013), pp. 86–90. ISSN: 1476-4687. DOI: 10.1038/nature12016. URL: https://doi.org/10.1038/nature12016.

[133]   Alexios Beveratos et al. "Room temperature stable single-photon source". In: *The European Physical Journal D - Atomic, Molecular, Optical and Plasma Physics* 18.2 (Feb. 2002), pp. 191–196. ISSN: 1434-6079. DOI: 10.1140/epjd/ e20020023. URL: https://doi.org/10.1140/epjd/e20020023.

[134]   Norikazu Mizuochi et al. "Electrically driven single-photon source at room temperature in diamond". In: *Nature Photonics* 6.5 (May 2012), pp. 299– 303. ISSN: 1749-4893. DOI: 10.1038/nphoton.2012.75. URL: https://doi. org/10.1038/nphoton.2012.75.

[135]   Simeon I. Bogdanov et al. "Ultrabright Room-Temperature Sub-Nanosecond Emission from Single Nitrogen-Vacancy Centers Coupled to Nanopatch Antennas". In: *Nano Letters* 18.8 (2018). PMID: 29969274, pp. 4837–4844. DOI: 10.1021/acs.nanolett.8b01415. eprint: https://doi.org/10.1021/ acs.nanolett.8b01415. URL: https://doi.org/10.1021/acs.nanolett. 8b01415.

[136]   Tim Schröder et al. "Ultrabright and efficient single-photon generation based on nitrogen-vacancy centres in nanodiamonds on a solid immersion lens". In: *New Journal of Physics* 13.5 (May 2011), p. 055017. DOI: 10.1088/1367- 2630/13/5/055017. URL: https://doi.org/10.1088%2F1367-2630%2F13% 2F5%2F055017.

[137]   Christian Kurtsiefer et al. "Stable Solid-State Source of Single Photons". In: *Phys. Rev. Lett.* 85 (2 July 2000), pp. 290–293. DOI: 10.1103/PhysRevLett. 85.290. URL: https://link.aps.org/doi/10.1103/PhysRevLett.85. 290.

[138]   Robert Boyd. *Nonlinear Optics, second edition.* Elsevier, 2003.

[139]   Mark Fox. *Quantum Optics.* Oxford University Press, 2006.

[140]   Christophe Couteau. "Spontaneous parametric down-conversion". In: *Contemporary Physics* 59.3 (2018), pp. 291–304. DOI: 10.1080/00107514.2018. 1488463. eprint: https://doi.org/10.1080/00107514.2018.1488463. URL: https://doi.org/10.1080/00107514.2018.1488463.

[141]   Alessio Avella. "Theory of Parametric Down Conversion in Bulk Non-Linear Crystals: An Introduction". In: *Journal of Advanced Physics* 4.3 (2015), pp. 252–262. ISSN: 2168-1996. DOI: doi:10.1166/jap.2015.1192. URL: https://www.ingentaconnect.com/content/asp/jap/2015/00000004/ 00000003/art00016.

[142]   N. Boeuf et al. "Calculating characteristics of noncollinear phase matching in uniaxial and biaxial crystals". In: *Optical Engineering* 39.4 (2000), pp. 1016– 1024. DOI: 10.1117/1.602464. URL: https://doi.org/10.1117/1.602464.

[143] John A. Armstrong et al. "Interactions between Light Waves in a Nonlinear Dielectric". In: *Phys. Rev.* 127 (6 Sept. 1962), pp. 1918–1939. DOI: `10.1103/PhysRev.127.1918`. URL: `https://link.aps.org/doi/10.1103/PhysRev.127.1918`.

[144] Wilhelm Sellmeier. "Ueber die durch die Aetherschwingungen erregten Mitschwingungen der Körpertheilchen und deren Rückwirkung auf die ersteren, besonders zur Erklärung der Dispersion und ihrer Anomalien". In: *Annalen der Physik* 223.11 (1872), pp. 386–403. DOI: `10.1002/andp.18722231105`. eprint: `https://onlinelibrary.wiley.com/doi/pdf/10.1002/andp.18722231105`. URL: `https://onlinelibrary.wiley.com/doi/abs/10.1002/andp.18722231105`.

[145] Kiyoshi Kato and Eiko Takaoka. "Sellmeier and thermo-optic dispersion formulas for KTP". In: *Appl. Opt.* 41.24 (Aug. 2002), pp. 5040–5044. DOI: `10.1364/AO.41.005040`. URL: `http://ao.osa.org/abstract.cfm?URI=ao-41-24-5040`.

[146] David Klyshko. *Photons Nonlinear Optics*. Routledge, 1988. DOI: `https://doi.org/10.1201/9780203743508`.

[147] Andrew Weiner. *Ultrafast Optics*. Wiley, 2009.

[148] Lucien Hardy. "Source of photons with correlated polarisations and correlated directions". In: *Physics Letters A* 161.4 (1992), pp. 326–328. ISSN: 0375-9601. DOI: `https://doi.org/10.1016/0375-9601(92)90554-Y`. URL: `http://www.sciencedirect.com/science/article/pii/037596019290554Y`.

[149] Giorgio Brida et al. "A first test of Wigner function local realistic model". In: *Physics Letters A* 299.2 (2002), pp. 121–124. ISSN: 0375-9601. DOI: `https://doi.org/10.1016/S0375-9601(02)00658-8`. URL: `http://www.sciencedirect.com/science/article/pii/S0375960102006588`.

[150] Paul G. Kwiat et al. "Ultrabright source of polarization-entangled photons". In: *Phys. Rev. A* 60 (2 Aug. 1999), R773–R776. DOI: `10.1103/PhysRevA.60.R773`. URL: `https://link.aps.org/doi/10.1103/PhysRevA.60.R773`.

[151] Yoon-Ho Kim, Sergei P. Kulik, and Yanhua Shih. "Bell-state preparation using pulsed nondegenerate two-photon entanglement". In: *Phys. Rev. A* 63 (6 May 2001), p. 060301. DOI: `10.1103/PhysRevA.63.060301`. URL: `https://link.aps.org/doi/10.1103/PhysRevA.63.060301`.

[152] Enrico Rebufello et al. "Towards a standard procedure for the measurement of the multi-photon component in a CW telecom heralded single-photon source". In: *Metrologia* 56.2 (Feb. 2019), p. 025004. DOI: `10.1088/1681-7575/ab022e`. URL: `https://doi.org/10.1088%2F1681-7575%2Fab022e`.

[153] Salvatore Virzì et al. "Optimal estimation of entanglement and discord in two-qubit states". In: *Scientific Reports* 9.1 (Feb. 2019), p. 3030. ISSN: 2045-2322. DOI: 10.1038/s41598-019-39334-8. URL: https://doi.org/10.1038/s41598-019-39334-8.

[154] Roy J. Glauber. "The Quantum Theory of Optical Coherence". In: *Phys. Rev.* 130 (6 June 1963), pp. 2529–2539. DOI: 10.1103/PhysRev.130.2529. URL: https://link.aps.org/doi/10.1103/PhysRev.130.2529.

[155] Robert Hanbury Brown and Richard Q. Twiss. "LXXIV. A new type of interferometer for use in radio astronomy". In: *The London, Edinburgh, and Dublin Philosophical Magazine and Journal of Science* 45.366 (1954), pp. 663–682. DOI: 10.1080/14786440708520475. eprint: https://doi.org/10.1080/14786440708520475. URL: https://doi.org/10.1080/14786440708520475.

[156] Giorgio Brida et al. "An extremely low-noise heralded single-photon source: A breakthrough for quantum technologies". In: *Applied Physics Letters* 101.22 (2012), p. 221112. DOI: 10.1063/1.4768288. eprint: https://doi.org/10.1063/1.4768288. URL: https://doi.org/10.1063/1.4768288.

[157] Philippe Grangier, Gérard Roger, and Alain Aspect. "Experimental Evidence for a Photon Anticorrelation Effect on a Beam Splitter: A New Light on Single-Photon Interferences". In: *Europhysics Letters (EPL)* 1.4 (Feb. 1986), pp. 173–179. DOI: 10.1209/0295-5075/1/4/004. URL: https://doi.org/10.1209%2F0295-5075%2F1%2F4%2F004.

[158] Stefano Olivares et al. "Quantum tomography of light states by photon-number-resolving detectors". In: *New Journal of Physics* 21.10 (Oct. 2019), p. 103045. DOI: 10.1088/1367-2630/ab4afb. URL: https://doi.org/10.1088%2F1367-2630%2Fab4afb.

[159] Fabrizio Piacentini et al. "Quantum Measurements in weak coupling regime: from Sequential weak values to Protective measurements". In: *Conference on Lasers and Electro-Optics*. Optical Society of America, 2018, FF1B.6. DOI: 10.1364/CLEO_QELS.2018.FF1B.6. URL: http://www.osapublishing.org/abstract.cfm?URI=CLEO_QELS-2018-FF1B.6.

[160] Fabrizio Piacentini et al. "Determining the quantum expectation value by measuring a single photon". In: *Nature Physics* 13.12 (Dec. 2017), pp. 1191–1194. DOI: 10.1038/nphys4223. URL: https://doi.org/10.1038/nphys4223.

[161] Fabrizio Piacentini et al. "Protective measurements: extracting the expectation value by measuring a single particle". In: *Quantum Technologies 2018*. Ed. by Jürgen Stuhler, Andrew J. Shields, and Miles J. Padgett. Vol. 10674. International Society for Optics and Photonics. SPIE, 2018, pp. 75–82. DOI: 10.1117/12.2307692. URL: https://doi.org/10.1117/12.2307692.

[162] Enrico Rebufello. "Misure protettive: un nuovo paradigma della misura quantistica". MA thesis. Università degli Studi di Torino, 2016.

[163] Enrico Rebufello et al. "Anomalous weak values via a single photon detection". In: *submitted* (2020).

[164] Enrico Rebufello et al. "Experimental realization of robust weak measurements". In: *Optical, Opto-Atomic, and Entanglement-Enhanced Precision Metrology II*. Ed. by Selim M. Shahriar and Jacob Scheuer. Vol. 11296. International Society for Optics and Photonics. SPIE, 2020, pp. 302–308. DOI: 10.1117/12.2542097. URL: https://doi.org/10.1117/12.2542097.

[165] Enrico Rebufello et al. "Quantum weak-interaction-based measurement: from sequential weak measurement to protective measurement". In: *Quantum Communications and Quantum Imaging XVI*. Ed. by Ronald E. Meyers, Yanhua Shih, and Keith S. Deacon. Vol. 10771. International Society for Optics and Photonics. SPIE, 2018, pp. 149–164. DOI: 10.1117/12.2319186. URL: https://doi.org/10.1117/12.2319186.

[166] Yakir Aharonov and Lev Vaidman. "Measurement of the Schrödinger wave of a single particle". In: *Physics Letters A* 178.1 (1993), pp. 38–42. ISSN: 0375-9601. DOI: https://doi.org/10.1016/0375-9601(93)90724-E. URL: http://www.sciencedirect.com/science/article/pii/037596019390724E.

[167] Vaidman Lev. "Protective Measurements". In: *in Compendium of Quantum Physics* (2009). DOI: https://doi.org/10.1007/978-3-540-70626-7_153.

[168] Walther Gerlach and Otto Stern. "Der experimentelle Nachweis der Richtungsquantelung im Magnetfeld". In: *Zeitschrift für Physik* 9.1 (Dec. 1922), pp. 349–352. ISSN: 0044-3328. DOI: 10.1007/BF01326983. URL: https://doi.org/10.1007/BF01326983.

[169] Baidyaneth Misra and E. C. George Sudarshan. "The Zeno's paradox in quantum theory". In: *Journal of Mathematical Physics* 18.4 (1977), pp. 756–763. DOI: 10.1063/1.523304. eprint: https://doi.org/10.1063/1.523304. URL: https://doi.org/10.1063/1.523304.

[170] Marco Genovese. "Interpretations of Quantum Mechanics and Measurement Problem". In: *Advanced Science Letters* 3.3 (2010), pp. 249–258. ISSN: 1936-6612. DOI: doi:10.1166/asl.2010.1133. URL: https://www.ingentaconnect.com/content/asp/asl/2010/00000003/00000003/art00001.

[171] Lucien Hardy. "Are quantum states real?" In: *International Journal of Modern Physics B* 27.01n03 (2013), p. 1345012. DOI: 10.1142/S0217979213450124. eprint: https://doi.org/10.1142/S0217979213450124. URL: https://doi.org/10.1142/S0217979213450124.

[172] Matthew F. Pusey, Jonathan Barrett, and Terry Rudolph. "On the reality of the quantum state". In: *Nature Physics* 8.6 (June 2012), pp. 475–478. ISSN: 1745-2481. DOI: 10.1038/nphys2309. URL: https://doi.org/10.1038/nphys2309.

[173] Martin Ringbauer et al. "Measurements on the reality of the wavefunction". In: *Nature Physics* 11.3 (Mar. 2015), pp. 249–254. ISSN: 1745-2481. DOI: 10.1038/nphys3233. URL: https://doi.org/10.1038/nphys3233.

[174] Federica Villa et al. "CMOS Imager With 1024 SPADs and TDCs for Single-Photon Timing and 3-D Time-of-Flight". In: *IEEE Journal of Selected Topics in Quantum Electronics* 20.6 (2014), pp. 364–373.

[175] John R. Taylor. *An introduction to error analysis, 2nd edition.* University science books, 1997.

[176] Fabrizio Piacentini et al. "Genetic quantum measurements". In: *in preparation* (2020).

[177] Melanie Mitchell. *An Introduction to Genetic Algorithms.* MIT Press, 1996.

[178] Yakir Aharonov et al. "Surprising quantum effects". In: *Physics Letters A* 124.4 (1987), pp. 199–203. ISSN: 0375-9601. DOI: https://doi.org/10.1016/0375-9601(87)90619-0. URL: http://www.sciencedirect.com/science/article/pii/0375960187906190.

[179] Jan Dziewior et al. "Universality of local weak interactions and its application for interferometric alignment". In: *Proceedings of the National Academy of Sciences* 116.8 (2019), pp. 2881–2890. ISSN: 0027-8424. DOI: 10.1073/pnas.1812970116. eprint: https://www.pnas.org/content/116/8/2881.full.pdf. URL: https://www.pnas.org/content/116/8/2881.

[180] Fabrizio Piacentini et al. "Investigating the Effects of the Interaction Intensity in a Weak Measurement". In: *Scientific Reports* 8.1 (May 2018), p. 6959. ISSN: 2045-2322. DOI: 10.1038/s41598-018-25156-7. URL: https://doi.org/10.1038/s41598-018-25156-7.

[181] Alessio Avella et al. "Absolute calibration of an EMCCD camera by quantum correlation, linking photon counting to the analog regime". In: *Opt. Lett.* 41.8 (Apr. 2016), pp. 1841–1844. DOI: 10.1364/OL.41.001841. URL: http://ol.osa.org/abstract.cfm?URI=ol-41-8-1841.

[182] Bureau International des Poids et Mesures. *JCGM 101:2008 - Evaluation of measurement data — Supplement 1 to the "Guide to the expression of uncertainty in measurement" — Propagation of distributions using a Monte Carlo method.* 2008. URL: https://www.bipm.org/utils/common/documents/jcgm/JCGM_101_2008_E.pdf.

[183] Chiara Marletto et al. "Non-Monogamy of Spatio-Temporal Correlations and the Black Hole Information Loss Paradox". In: *Entropy* 22.2 (Feb. 2020), p. 228. ISSN: 1099-4300. DOI: 10.3390/e22020228. URL: http://dx.doi.org/10.3390/e22020228.

[184] Chiara Marletto et al. "Theoretical description and experimental simulation of quantum entanglement near open time-like curves via pseudo-density operators". In: *Nature Communications* 10.1 (Jan. 2019), p. 182. DOI: 10.1038/s41467-018-08100-1. URL: https://doi.org/10.1038/s41467-018-08100-1.

[185] Albert Einstein. "Zur Elektrodynamik bewegter Körper". In: *Annalen der Physik* 17.891 (1905).

[186] Wolfgang Pauli. "Relativitätstheorie". In: *Encyklopadie der mathematischen Wissenschaften* 19 (1921).

[187] Dominic Horsman et al. "Can a quantum state over time resemble a quantum state at a single time?" In: *Proceedings of the Royal Society A: Mathematical, Physical and Engineering Sciences* 473.2205 (2017), p. 20170395. DOI: 10.1098/rspa.2017.0395. eprint: https://royalsocietypublishing.org/doi/pdf/10.1098/rspa.2017.0395. URL: https://royalsocietypublishing.org/doi/abs/10.1098/rspa.2017.0395.

[188] Christopher J. Isham. "Quantum logic and the histories approach to quantum theory". In: *Journal of Mathematical Physics* 35.5 (1994), pp. 2157–2185. DOI: 10.1063/1.530544. eprint: https://doi.org/10.1063/1.530544. URL: https://doi.org/10.1063/1.530544.

[189] Joseph F. Fitzsimons, Jonathan A. Jones, and Vlatko Vedral. "Quantum correlations which imply causation". In: *Scientific Reports* 5.1 (Dec. 2015), p. 18281. ISSN: 2045-2322. DOI: 10.1038/srep18281. URL: https://doi.org/10.1038/srep18281.

[190] Ognyan Oreshkov, Fabio Costa, and Časlav Brukner. "Quantum correlations with no causal order". In: *Nature Communications* 3.1 (Oct. 2012), p. 1092. ISSN: 2041-1723. DOI: 10.1038/ncomms2076. URL: https://doi.org/10.1038/ncomms2076.

[191] Donald Marolf. "The black hole information problem: past, present, and future". In: *Reports on Progress in Physics* 80.9 (July 2017), p. 092001. DOI: 10.1088/1361-6633/aa77cc. URL: https://doi.org/10.1088%2F1361-6633%2Faa77cc.

[192] Stephen Hawking and George Ellis. *The Large Scale Structure of Space-Time*. Cambridge University Press, 1973.

[193] Stephen W. Hawking. "Black hole explosions?" In: *Nature* 248.5443 (Mar. 1974), pp. 30–31. DOI: 10.1038/248030a0.

[194] Samuel L. Braunstein and Arun K. Pati. "Quantum Information Cannot Be Completely Hidden in Correlations: Implications for the Black-Hole Information Paradox". In: *Phys. Rev. Lett.* 98 (8 Feb. 2007), p. 080502. DOI: 10.1103/PhysRevLett.98.080502. URL: https://link.aps.org/doi/10.1103/PhysRevLett.98.080502.

[195] Stephen W. Hawking, Malcolm J. Perry, and Andrew Strominger. "Soft Hair on Black Holes". In: *Phys. Rev. Lett.* 116 (23 June 2016), p. 231301. DOI: 10.1103/PhysRevLett.116.231301. URL: https://link.aps.org/doi/10.1103/PhysRevLett.116.231301.

[196] Donald Marolf. "The black hole information problem: past, present, and future". In: *Reports on Progress in Physics* 80.9 (July 2017), p. 092001. DOI: 10.1088/1361-6633/aa77cc. URL: https://doi.org/10.1088%2F1361-6633%2Faa77cc.

[197] William G. Unruh and Robert M. Wald. "Information loss". In: *Reports on Progress in Physics* 80.9 (July 2017), p. 092002. DOI: 10.1088/1361-6633/aa778e. URL: https://doi.org/10.1088%2F1361-6633%2Faa778e.

[198] Sayantan Choudhury and Sudhakar Panda. "Spectrum of cosmological correlation from vacuum fluctuation of stringy axion in entangled de Sitter space". In: *Eur. Phys. J. C* 80 (67 2020).

[199] Sayantan Choudhury, Sudhakar Panda, and Rajinder Singh. "Bell violation in the sky". In: *Eur. Phys. J. C* 77 (60 2017).

[200] Juan Maldacena. "A model with cosmological Bell inequalities". In: *Fortschritte der Physik* 64.1 (2016), pp. 10–23. DOI: 10.1002/prop.201500097. eprint: https://onlinelibrary.wiley.com/doi/pdf/10.1002/prop.201500097. URL: https://onlinelibrary.wiley.com/doi/abs/10.1002/prop.201500097.

[201] Jérôme Martin and Vincent Vennin. "Obstructions to Bell CMB experiments". In: *Phys. Rev. D* 96 (6 Sept. 2017), p. 063501. DOI: 10.1103/PhysRevD.96.063501. URL: https://link.aps.org/doi/10.1103/PhysRevD.96.063501.

[202] Stephen W. Hawking. "Black holes in general relativity". In: *Communications in Mathematical Physics* 25.2 (June 1972), pp. 152–166. ISSN: 1432-0916. DOI: 10.1007/BF01877517. URL: https://doi.org/10.1007/BF01877517.

[203] Stephen W. Hawking. "Breakdown of predictability in gravitational collapse". In: *Phys. Rev. D* 14 (10 Nov. 1976), pp. 2460–2473. DOI: 10.1103/PhysRevD.14.2460. URL: https://link.aps.org/doi/10.1103/PhysRevD.14.2460.

[204]   Stephen W. Hawking. "Information loss in black holes". In: *Phys. Rev. D* 72 (8 Oct. 2005), p. 084013. DOI: 10.1103/PhysRevD.72.084013. URL: https://link.aps.org/doi/10.1103/PhysRevD.72.084013.

[205]   Stephen W. Hawking. "Particle creation by black holes". In: *Communications in Mathematical Physics* 43.3 (Aug. 1975), pp. 199–220. ISSN: 1432-0916. DOI: 10.1007/BF02345020. URL: https://doi.org/10.1007/BF02345020.

[206]   Ben Toner. "Monogamy of non-local quantum correlations". In: *Proceedings of the Royal Society A: Mathematical, Physical and Engineering Sciences* 465.2101 (2009), pp. 59–69. DOI: 10.1098/rspa.2008.0149. eprint: https://royalsocietypublishing.org/doi/pdf/10.1098/rspa.2008.0149. URL: https://royalsocietypublishing.org/doi/abs/10.1098/rspa.2008.0149.

[207]   David Wallace. Why Black Hole Information Loss is Paradoxical. 2017. URL: https://arxiv.org/abs/1710.03783.

[208]   Don N. Page. "Information in black hole radiation". In: *Phys. Rev. Lett.* 71 (23 Dec. 1993), pp. 3743–3746. DOI: 10.1103/PhysRevLett.71.3743. URL: https://link.aps.org/doi/10.1103/PhysRevLett.71.3743.

[209]   Karl Schwarzschild. "Über das Gravitationsfeld eines Massenpunktes nach der Einsteinschen Theorie". In: *Sitzungsberichte der Königlich Preussischen Akademie der Wissenschaften.* 7 (1916), pp. 189–196. URL: https://archive.org/stream/sitzungsberichte1916deutsch#page/188/mode/2up.

[210]   Barrett O'Neill. *The Geometry of Kerr Black Holes.* A K Peters, Wellseley, Massachusetts, 1995.

[211]   Charles W. Misner, Kip S. Thorne, and John A. Wheeler. *Gravitation.* Macmillan, 1973.

[212]   Albert Einstein. "Die Grundlage der allgemeinen Relativitätstheorie". In: *in Das Relativitätsprinzip. Fortschritte der Mathematischen Wissenschaften in Monographien* (1923). DOI: https://doi.org/10.1007/978-3-663-19510-8_7.

[213]   Steven Weinberg. *Gravitation and Cosmology.* John Wiley and sons, 1971.

[214]   Willem J. van Stockum. "IX.—The Gravitational Field of a Distribution of Particles Rotating about an Axis of Symmetry". In: *Proceedings of the Royal Society of Edinburgh* 57 (1938), pp. 135–154. DOI: 10.1017/S0370164600013699.

[215]   Charles Cloukey. "Paradox". In: *Amazing Stories Quarterly* (392 1929).

[216]   Kip S. Thorne. "Lectures on Closed Timelike Curves". In: *in Proceedings of 13th International Conference on General Relativity and Gravitation, Ed.s J. Gleiser, C.N. Kozameh & O.M. Moreschi,* (1993).

[217] David Deutsch. "Quantum mechanics near closed timelike lines". In: *Phys. Rev. D* 44 (10 Nov. 1991), pp. 3197–3217. DOI: `10.1103/PhysRevD.44.3197`. URL: `https://link.aps.org/doi/10.1103/PhysRevD.44.3197`.

[218] Seth Lloyd et al. "Closed Timelike Curves via Postselection: Theory and Experimental Test of Consistency". In: *Phys. Rev. Lett.* 106 (4 Jan. 2011), p. 040403. DOI: `10.1103/PhysRevLett.106.040403`. URL: `https://link.aps.org/doi/10.1103/PhysRevLett.106.040403`.

[219] Seth Lloyd et al. "Quantum mechanics of time travel through post-selected teleportation". In: *Phys. Rev. D* 84 (2 July 2011), p. 025007. DOI: `10.1103/PhysRevD.84.025007`. URL: `https://link.aps.org/doi/10.1103/PhysRevD.84.025007`.

[220] Scott Aaronson and John Watrous. "Closed timelike curves make quantum and classical computing equivalent". In: *Proceedings of the Royal Society A: Mathematical, Physical and Engineering Sciences* 465.2102 (2009), pp. 631–647. DOI: `10.1098/rspa.2008.0350`. eprint: `https://royalsocietypublishing.org/doi/pdf/10.1098/rspa.2008.0350`. URL: `https://royalsocietypublishing.org/doi/abs/10.1098/rspa.2008.0350`.

[221] Doyeol Ahn et al. "Quantum-state cloning in the presence of a closed timelike curve". In: *Phys. Rev. A* 88 (2 Aug. 2013), p. 022332. DOI: `10.1103/PhysRevA.88.022332`. URL: `https://link.aps.org/doi/10.1103/PhysRevA.88.022332`.

[222] Todd A. Brun, Jim Harrington, and Mark M. Wilde. "Localized Closed Timelike Curves Can Perfectly Distinguish Quantum States". In: *Phys. Rev. Lett.* 102 (21 May 2009), p. 210402. DOI: `10.1103/PhysRevLett.102.210402`. URL: `https://link.aps.org/doi/10.1103/PhysRevLett.102.210402`.

[223] Todd A. Brun, Mark M. Wilde, and Andreas Winter. "Quantum State Cloning Using Deutschian Closed Timelike Curves". In: *Phys. Rev. Lett.* 111 (19 Nov. 2013), p. 190401. DOI: `10.1103/PhysRevLett.111.190401`. URL: `https://link.aps.org/doi/10.1103/PhysRevLett.111.190401`.

[224] Xiao Yuan et al. "Replicating the benefits of Deutschian closed timelike curves without breaking causality". In: *npj Quantum Information* 1.1 (Nov. 2015), p. 15007. ISSN: 2056-6387. DOI: `10.1038/npjqi.2015.7`. URL: `https://doi.org/10.1038/npjqi.2015.7`.

[225] Martin Ringbauer et al. "Experimental simulation of closed timelike curves". In: *Nature Communications* 5.1 (June 2014), p. 4145. ISSN: 2041-1723. DOI: `10.1038/ncomms5145`. URL: `https://doi.org/10.1038/ncomms5145`.

[226] Jacques L. Pienaar, Timothy C. Ralph, and Casey R. Myers. "Open Timelike Curves Violate Heisenberg's Uncertainty Principle". In: *Phys. Rev. Lett.* 110 (6 Feb. 2013), p. 060501. DOI: 10.1103/PhysRevLett.110.060501. URL: https://link.aps.org/doi/10.1103/PhysRevLett.110.060501.

[227] Yu. I. Bogdanov et al. "Statistical Estimation of the Efficiency of Quantum State Tomography Protocols". In: *Phys. Rev. Lett.* 105 (1 July 2010), p. 010404. DOI: 10.1103/PhysRevLett.105.010404. URL: https://link.aps.org/doi/10.1103/PhysRevLett.105.010404.

[228] Enrico Rebufello. "Io resto a casa: Un gioco da tavolo". In: *Virus Ex-Machina - Scritti metascientifici al tempo del Coronavirus.* Ed. by V. Marchis and M. Pozzi. Mimesis Edizioni, 2020, pp. 209–220.

This Ph.D. thesis has been typeset by means of the TEX-system facilities. The typesetting engine was pdfLATEX. The document class was `toptesi`, by Claudio Beccari, with option `tipotesi=scudo`. This class is available in every up-to-date and complete TEX-system installation.